People's Democratic Republic of Algeria

Ministry of Higher Education and Scientific Research

University of El Oued

Faculty of Technology

Laboratory Biotechnology, biomaterials and condensed materials

A Doctoral Thesis

Submitted in Fulfillment of the Requirements for Degree of Doctor (LMD)

Field: Process Engineering

Specialization: Chemical Engineering

Polyvinylpyrrolidone (PVP) Based metal oxide nanocomposite for removal of organic dyes: Molecular docking study

Presented by: Chaima Salmi

Defended on [22/10/2025], in the presence of the Examination Committee:

Name	Rank	Affiliation	Role
Dr. Ouahrani Mohammed Ridha	Professor	University Echahid Hamma Lakhdar- El Oued	Chair
Dr. Meneceur Souhaila	MCA	University Echahid Hamma Lakhdar- El Oued	Supervisor
Dr. Laouini Salah Eddine	Professor	Université Echahid Hamma Lakhdar- El Oued	Co-supervisor
Dr. Ziani Nadia	MCA	University- Badji mokhtar -Annaba	Examiner
Dr. Chaouch Noura	Professor	University Kasdi Merbah- Ouargla	Examiner
Dr. Khaled Bilal	MCA	University Echahid Hamma Lakhdar- El Oued	Examiner

Academic Year: 2024-2025 / 1446-1447 AH

Dedication

I dedicate this work with profound love, gratitude, and respect to those who have been the pillars of my life and the source of my strength throughout this academic journey.

To the soul of my late father, **Mohammed Lakhder (رحمه الله)**,
whose dreams for my success were greater than my own. Though he is no longer with me, his memory, values, and unwavering belief in my potential have guided me through every challenge. This accomplishment is, in many ways, his.

To my mother, **Aida Hamaidia**,
whose sacrifices, patience, and unconditional love have been the silent force behind every achievement. Your strength and prayers have carried me through the darkest and brightest moments of this journey.

To my eldest brother, **Mounir**,
thank you for your constant encouragement, wisdom, and for being a role model I deeply admire.

To my sister, **Dounia**,
whose gentle presence and continuous support brought light to the most stressful days.

To my brothers, **Hamza**, **Adlane**, **Akram**, and **Nassim**,
thank you for believing in me, for your humor that lifted my spirit, and for the bond that reminded me I was never alone.

To my Grandma **Aisha Salmi** & my uncle **Hamaidia Mouhammed**

whose unconditional love, silent prayers, and comforting presence have always been a source of strength

To my sisters-in-law, **Sihem** and **Souhaila**,

your kindness, support, and unwavering belief in me have meant more than words can express.

To my dear nephews and nieces: **Ranim**, **Rana**, **Chahine**, **Ayate**, and **Athir**,
may this humble success be a spark that ignites your dreams and reminds you that perseverance always bears fruit.

With all my heart, **Thank you**

Chaima Salmi

Acknowledgements

First and foremost, I would like to express my sincere gratitude to **Almighty God** for granting me the strength, health, and perseverance to carry out and complete this work. Without His blessings, this achievement would not have been possible.

I extend my deepest appreciation to my supervisor, **Dr. Meneceur Souhaila**, for her invaluable guidance, continuous encouragement, and unwavering support throughout my PhD journey. Her insightful advice, patience, and constructive feedback have played a pivotal role in shaping both my research and academic development.

My heartfelt thanks go to **Professor Laouini Salah Eddine**, my co-supervisor, for his strong mentorship, thoughtful critiques, and consistent motivation. His dedication to excellence and commitment to my progress have been crucial throughout this endeavor.

I am also truly grateful to **Professor Shamsa Ali**, Dean of the Faculty, for his leadership and support, and for fostering a productive research environment that allowed me to thrive.

I would also like to extend my **deepest gratitude to the distinguished members of the thesis jury** for their time, insightful evaluations, and valuable remarks that enriched the quality of this work:

- **Professor Ouahrani Mohammed Ridha** (University Echahid Hamma Lakhdar – El Oued), *Chair*
- **Dr. Ziani Nadia** (University Badji Mokhtar – Annaba), *Examiner*
- **Professor Chaouch Noura** (University Kasdi Merbah – Ouargla), *Examiner*
- **Dr. Khaled Bilal** (University Echahid Hamma Lakhdar – El Oued), *Examiner*

Their constructive comments and professional expertise greatly contributed to improving this thesis and broadening my academic perspective.

I wish to express my sincere appreciation to my colleagues and friends in the **BBCM laboratory** for their camaraderie, collaboration, and support. In particular, I thank **Dr. Hamdi Ali Mohammed** for his encouragement, scientific discussions, and continuous help throughout this journey.

From the **University of El-Oued**, I extend special thanks to my dear friends and colleagues **Khadija Tahraoui**, **Dr. Karoui Radja**, for their kindness, support, and shared academic experiences.

From **University of Malaya**, I sincerely thank **Dr. Adeeb Hayyan**, **Dr. Khalid M. Abed**, **Professor Wan Jefrey Basirun**, and **Dr. Sharifah Shahira Syed Putra** for their valuable input, collaboration, and academic generosity.

From **Riga Technical University**, I express my gratitude to **Dr. Zane Zelca**, my Erasmus+ supervisor, for her supervision and guidance, and to **Maija Lebedeva**, my program coordinator, for her administrative support and coordination throughout my Erasmus+ mobility experience.

From the **Ministry of Higher Education and Scientific Research in Algeria**, I am thankful to **Dr. abed elhamid Amir** for his assistance and support throughout my academic endeavors.

Finally, to everyone family, friends, professors, colleagues, and administrative staff who contributed directly or indirectly to this thesis, please accept my sincerest thanks. Your encouragement, advice, and support have made this achievement possible.

With heartfelt appreciation,

Thank you all.

Chaima Salmi

Preface

This doctoral thesis represents the culmination of several years of dedicated research, critical analysis, and scientific exploration. It reflects a journey marked by curiosity, persistence, and an unwavering commitment to addressing environmental challenges through innovative materials science. Conducted within the **Department of Processing Engineering and Petrochemicals at the Faculty of Technology, University of El-Oued,** this research has significantly contributed to the fields of nanotechnology, photocatalysis, and environmental remediation.

The work presented herein centers on the synthesis, characterization, and application of **polyvinylpyrrolidone (PVP)-based metal oxide nanocomposites** for the effective removal of organic pollutants, with a particular emphasis on **molecular docking studies** to elucidate interaction mechanisms. Through a green chemistry approach and advanced experimental techniques, this study explores multifunctional nanocomposites capable of addressing diverse environmental issues such as dye degradation, heavy metal removal, CO_2 methanation, hydrogen production, and biodiesel purification.

In alignment with the regulations of the PhD Commission, this thesis is structured as a compilation of peer-reviewed publications, each chapter reflecting a significant milestone in the research trajectory and contributing original insights to the broader scientific community. The following publications form the core of this dissertation:

1. **C. Salmi et al.**, "Biosynthesis of Mn_3O_4/PVP nanocomposite for enhanced photocatalytic degradation of organic dyes under sunlight irradiation," *Journal of Cluster Science*, pp. 1–15, 2023.
2. **C. Salmi et al.**, "Biosynthesized MgO@SnO_2 nanocomposite and their modification with polyvinylpyrrolidone: Efficiency for removal of heavy metals and contaminants from industrial petroleum wastewater," *Clean Technologies and Environmental Policy*, pp. 1–20, 2024.
3. **C. Salmi et al.**, "Gallic acid assisted synthesis of novel CuO/Ni/Fe_3O_4 nanocomposite for catalytic CO_2 methanation and photocatalytic hydrogen generation," *Journal of Sol-Gel Science and Technology*, pp. 1–13, 2024.
4. **C. Salmi et al.**, "Green electrospinning synthesis of NiO/Ni nanofiber for efficient soap removal from crude biodiesel," *Surfaces and Interfaces*, 2024.

Abstract

This thesis explores the green synthesis, characterization, and environmental applications of polyvinylpyrrolidone (PVP)-based metal oxide nanocomposites for the effective removal of organic pollutants from aqueous media. The work is framed within the context of sustainable nanotechnology and focuses on multifunctional nanocomposite systems combining metal oxide nanoparticles with polymeric matrices to enhance photocatalytic, adsorptive, and catalytic performance.

Four novel nanocomposite systems were developed and systematically investigated:

1. Mn_3O_4/PVP nanocomposites for sunlight-driven degradation of bromophenol blue and o-toluidine dyes.
2. MgO@SnO_2/PVP composites for the adsorption of heavy metals and contaminants from petroleum wastewater.
3. CuO/Ni/Fe_3O_4 nanocomposites synthesized using gallic acid for dual functionality in CO_2 methanation and photocatalytic hydrogen production.
4. NiO/Ni@PVA electrospun nanofibers for efficient soap extraction from crude biodiesel.

All nanomaterials were synthesized using eco-friendly routes, employing plant-based reducing agents and polymeric stabilizers. Structural, morphological, and surface properties were characterized using XRD, FTIR, SEM, BET, TGA, UV–Vis spectroscopy, and zeta potential analysis. The performance of the nanocomposites was evaluated through adsorption and photodegradation experiments under simulated and natural sunlight. Kinetic, isotherm, and thermodynamic models were applied to describe adsorption mechanisms, while molecular docking simulations were employed to visualize the interactions between dye molecules and the active surfaces of the composites at the molecular level.

The results demonstrate the effectiveness of polymer-supported metal oxide nanocomposites in achieving high degradation and removal efficiencies, structural stability over multiple cycles, and enhanced environmental compatibility. This research provides valuable insights into the design of green nanomaterials for water treatment, energy recovery, and environmental remediation, contributing to the advancement of sustainable nanotechnology.

Keywords: Adsorption, Environmental remediation, Molecular docking, CO_2 methanation, Hydrogen production, Heavy metal removal, Petroleum wastewater, Biodiesel purification, Sustainable nanotechnology.

Résumé

Cette thèse porte sur la synthèse verte, la caractérisation et les applications environnementales de nanocomposites à base d'oxyde métallique et de PVP, destinés à l'élimination efficace des polluants organiques dans les milieux aqueux. S'inscrivant dans le cadre de la nanotechnologie durable, ce travail explore des systèmes nanocomposites multifonctionnels associant des nanoparticules d'oxydes métalliques à des matrices polymériques afin d'améliorer les performances photocatalytiques, adsorptives et catalytiques.

Quatre systèmes nanocomposites innovants ont été développés et étudiés de manière approfondie :

1. Mn_3O_4/PVP pour la dégradation sous irradiation solaire des colorants bromophénol bleu et o-toluidine ;
2. MgO@SnO_2/PVP pour l'adsorption des métaux lourds et des contaminants issus des eaux usées pétrolières ;
3. CuO/Ni/Fe_3O_4, synthétisé avec de l'acide gallique, pour une double application en méthanation du CO_2 et production photocatalytique d'hydrogène ;
4. NiO/Ni@PVA, sous forme de nanofibres électrofilées, pour l'extraction efficace du savon dans le biodiesel brut.

Tous les nanomatériaux ont été élaborés par des méthodes écologiques, utilisant des extraits végétaux comme agents réducteurs et des polymères comme stabilisants. Les propriétés structurales, morphologiques et de surface ont été caractérisées par XRD, FTIR, SEM, BET, TGA, UV-Vis et analyse du potentiel zêta. Les performances ont été évaluées via des expériences d'adsorption et de photodégradation en lumière solaire simulée et naturelle. Des modèles cinétiques, isothermes et thermodynamiques ont été appliqués pour décrire les mécanismes d'adsorption, et des simulations de docking moléculaire ont été menées pour visualiser les interactions entre les colorants et les surfaces actives des nanocomposites à l'échelle atomique.

Les résultats ont montré une efficacité élevée en termes de dégradation et d'adsorption, une bonne stabilité structurale sur plusieurs cycles, et une excellente compatibilité environnementale. Cette recherche apporte des connaissances précieuses pour la conception de nanomatériaux verts destinés au traitement de l'eau, à la valorisation énergétique et à la dépollution, contribuant ainsi à l'avancement de la nanotechnologie durable.

Mots-clés : Adsorption, Dépollution environnementale, Docking moléculaire, Méthanation du CO_2, Production d'hydrogène, Élimination des métaux lourds, Eaux usées pétrolières, Purification du biodiesel, Nanotechnologie durable.

الملخّص

تتناول هذه الأطروحة موضوع **التخليق الأخضر، والتوصيف، والتطبيقات البيئية** للمواد النانوية المركبة المكونة من **أكاسيد المعادن المدعمة ببوليفينيل البيروليدون(PVP)** ، بهدف إزالة الملوثات العضوية من المياه. يندرج هذا العمل ضمن إطار **تكنولوجيا النانو المستدامة**، ويركز على تطوير أنظمة نانوية متعددة الوظائف تجمع بين جسيمات أكاسيد المعادن ومصفوفات بوليمرية لتحسين الأداء التحفيزي الضوئي، والامتزازي، والتحفيزي.

تم تطوير ودراسة أربع أنظمة نانوية مركبة مبتكرة:

1. مركب **Mn_3O_4/PVP** لتحفيز تحلل أصباغ البروموفينول الأزرق و-o توليدين تحت أشعة الشمس؛
2. مركب **MgO@SnO_2/PVP** لامتزاز المعادن الثقيلة والملوثات من مياه الصرف الصناعي البترولي؛
3. مركب **CuO/Ni/Fe_3O_4** المحضّر بمساعدة حمض الغاليك، لتطبيق مزدوج في **تحويل ثاني أكسيد الكربون إلى الميثان** و**إنتاج الهيدروجين ضوئيًا؛**
4. ألياف نانوية **NiO/Ni@PVA** المنتجة بطريقة الغزل الكهربائي، لإزالة الصابون بكفاءة من وقود الديزل الحيوي الخام.

تم تخليق جميع المواد باستخدام طرق صديقة للبيئة، معتمدة على مستخلصات نباتية كعوامل اختزال، وبوليمرات كمثبتات. تم توصيف الخصائص البنيوية والمورفولوجية والسطحية باستخدام تقنياتXRD ، وFTIR، وSEM، وBET، وTGA، وUV-Vis، وقياس الجهد السطحي .(Zeta potential) كما تم تقييم الأداء من خلال تجارب الامتزاز والتحلل الضوئي تحت ضوء الشمس الطبيعي والمحاكى، مع تطبيق نماذج حركية وحرارية وتوازنات امتزاز لفهم آليات التفاعل. بالإضافة إلى ذلك، تم استخدام **المحاكاة الجزيئية (molecular docking)** لدراسة التفاعلات بين جزيئات الصبغة والأسطح النانوية على المستوى الذري.

أظهرت النتائج فعالية عالية في إزالة وتفكيك الملوثات، وثباتًا هيكليًا جيدًا على مدى عدة دورات، وتوافقًا بيئيًا ممتازًا. يقدّم هذا البحث رؤى علمية مهمة لتصميم مواد نانوية خضراء تُستخدم في معالجة المياه، وتحقيق استرداد للطاقة، وتحسين استراتيجيات المعالجة البيئية، مما يُسهم في تقدم تكنولوجيا النانو المستدامة.

الكلمات المفتاحية : الامتزاز، المعالجة البيئية، الإرساء الجزيئي، تحويل ثاني أكسيد الكربون إلى ميثان، إنتاج الهيدروجين، إزالة المعادن الثقيلة، مياه الصرف الصناعي البترولي، تنقية الوقود الحيوي، تكنولوجيا النانو المستدامة.

Table of Contents

Chapter I. Sunlight-Driven Dye Degradation Using Mn_3O_4/PVP Nanocomposites

Chapter II. Advanced MgO@SnO_2 NC for Heavy Metals Industrial Petroleum Wastewater Purification

Chapter III. Gallic Acid-Enabled CuO/Ni/Fe_3O_4 Catalysts for CO_2 Methanation and H_2 Generation

List of Figures

Chapter I: *Sunlight-driven dye degradation using Mn_3O_4/PVP nanocomposites*

Chapter II: *Advanced MgO@SnO_2 Nanocomposites for Heavy Metals Industrial Petroleum Wastewater Purification*

Chapter III: *Gallic Acid-Enabled CuO/Ni/Fe_3O_4 Catalysts for CO_2 Methanation and H_2 Generation*

Chapter IV: *Green Fabrication of NiO/Ni@PVA Nanofibers for Enhanced Soap Extraction from Biodiesel*

List of Tables

Chapter I: *Sunlight-driven dye degradation using Mn_3O_4/PVP nanocomposites*

Chapter II: *Advanced MgO@SnO_2 Nanocomposites for Heavy Metals Industrial Petroleum Wastewater Purification*

Liste of Abbreviation

A_0	Initial Absorbance
A	Final Absorbance
CB	Conduction Band
CO	Carbon Monoxide
CO_2	Carbon Dioxide
CO_2/CH_4	Carbon Dioxide to Methane Conversion
DFT	Density Functional Theory
EDX	Energy Dispersive X-ray Spectroscopy
EF	Fermi Energy Level
FTIR	Fourier-Transform Infrared Spectroscopy
H_2	Hydrogen
HRTEM	High-Resolution Transmission Electron Microscopy
NC	Nanocomposite
NPs	Nanoparticles
PVP	Polyvinylpyrrolidone
PVA	Polyvinyl Alcohol
PL	Photoluminescence
SEM	Scanning Electron Microscopy
SnO_2	Tin(IV) Oxide
TGA	Thermogravimetric Analysis
UV–Vis	Ultraviolet–Visible Spectroscopy
VB	Valence Band
XRD	X-ray Diffraction
ZP	Zeta Potential
Mn_3O_4	Manganese(II,III) Oxide

MgO	Magnesium Oxide
$MgO@SnO_2$	Magnesium Oxide @ Tin Oxide Nanocomposite
CuO	Copper(II) Oxide
$CuO/Ni/Fe_3O_4$	Copper/Nickel/Iron Oxide Nanocomposite
Fe_3O_4	Magnetite
Ni	Nickel
NiO	Nickel(II) Oxide
NiO/Ni@PVA	Nickel Oxide/Nickel in Polyvinyl Alcohol Nanofiber
ZnO	Zinc Oxide
ZnO/CuO/Ni	Zinc Oxide/Copper Oxide/Nickel Nanocomposite

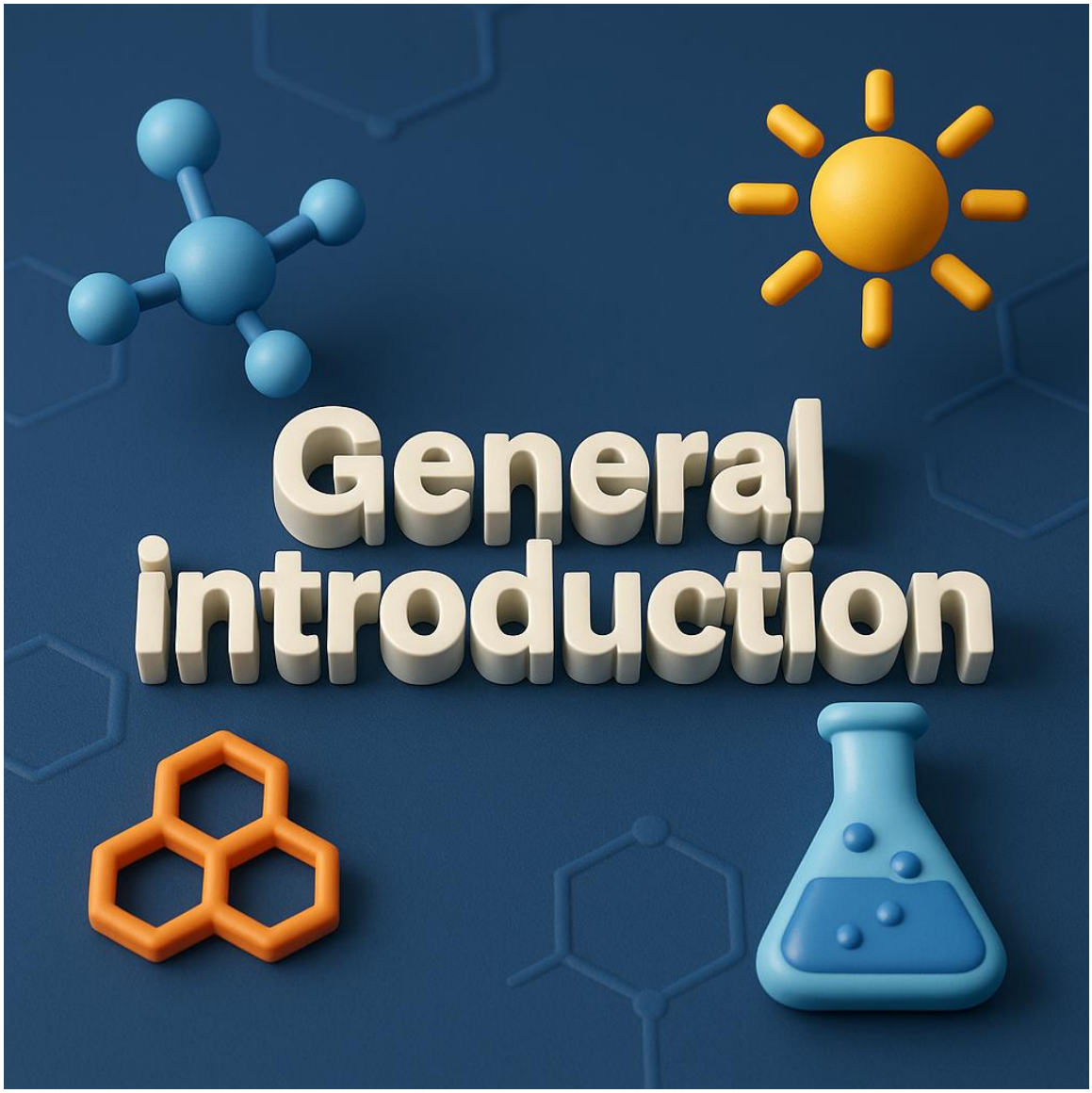
General introduction

General Introduction

Nanotechnology has rapidly evolved into a cornerstone of modern science and engineering, offering a paradigm shift in how materials are designed, synthesized, and applied across various domains. By manipulating matter at dimensions typically ranging from 1 to 100 nanometers, researchers can tailor the structural, electronic, optical, and chemical properties of materials in ways that are unattainable at the macro scale [1]. At this nanoscale regime, materials exhibit a suite of unique and size-dependent phenomena, including quantum confinement effects, surface plasmon resonance, increased surface-to-volume ratios, and enhanced charge carrier dynamics. These nanoscale attributes often result in superior reactivity, selectivity, and functional versatility compared to their bulk counterparts [2,3]. Consequently, nanotechnology has catalyzed major breakthroughs in a wide array of sectors, including renewable energy systems, catalytic processes, drug delivery platforms, tissue engineering, environmental decontamination, and the development of high-performance functional materials [4,5]. Among the diverse classes of nanomaterials, metal oxide nanoparticles (MO-NPs) have emerged as particularly promising due to their tunable surface chemistry, robust thermal and chemical stability, and exceptional performance in photocatalysis, adsorption, and biomedical applications. These advantages position metal oxide nanomaterials at the forefront of sustainable solutions for pressing environmental and technological challenges [6,7].

Among various nanostructured materials, MO-NPs have emerged as versatile candidates in the field of environmental nanotechnology due to their tailorable physicochemical properties, high structural stability, redox potential, and catalytic reactivity [5]. These nanomaterials exhibit superior performance in processes such as adsorption, photocatalysis, antibacterial activity, and pollutant degradation, owing to their unique surface chemistry, variable oxidation states, and enhanced charge transfer capabilities. Several metal oxides, including magnesium oxide (MgO), iron oxide (Fe_3O_4), tin oxide (SnO_2), nickel oxide (NiO), copper oxide (CuO), and manganese oxide (Mn_3O_4), have been extensively investigated for their application in environmental remediation and energy-related technologies. MgO NPs are widely acknowledged for their strong basicity, high surface area, and exceptional thermal and chemical stability, rendering them effective in

adsorbing both organic and inorganic contaminants. They also demonstrate antibacterial properties and catalytic potential in wastewater treatment systems [6,7]. Fe_3O_4 NPs, distinguished by their superparamagnetic behavior, are frequently employed in magnetic-assisted separation processes, catalytic degradation of pollutants, and biomedical applications such as drug delivery and magnetic resonance imaging [8]. SnO_2, a wide-bandgap semiconductor, offers high electron mobility and visible-light-driven photocatalytic efficiency, making it a suitable candidate for organic dye degradation, gas sensing, and optoelectronic devices [9]. NiO NPs possess excellent electrochemical stability and strong catalytic activity, particularly in CO_2 methanation and hydrogen evolution reactions, and are also valued for their gas sensing and antibacterial efficacy [10,11]. CuO NPs have attracted attention due to their narrow bandgap, low cost, and high photothermal conversion efficiency. Their notable antibacterial, antifungal, and catalytic capabilities make them effective in dye degradation, environmental detoxification, and biomedical uses. Furthermore, Mn_3O_4 NPs are known for their redox flexibility, tunable magnetic properties, and oxygen storage capacity, which make them valuable in photocatalysis, supercapacitors, and oxidative degradation of persistent organic pollutants [12–14]. Despite their promising properties, the practical use of metal oxide nanoparticles is often limited by challenges such as aggregation, poor aqueous dispersibility, surface instability, and declining reusability [8,9]. These issues can reduce their efficiency and hinder large-scale application. To overcome these drawbacks, researchers have incorporated MO-NPs into polymeric matrices, which enhance dispersion, stability, and functionality.

The integration of MO-NPs into polymer matrices offers an effective solution to common limitations such as aggregation, poor dispersibility, and limited reusability. This approach leads to the formation of polymer-based nanocomposites, where the polymer not only stabilizes the nanoparticles but also enhances their physicochemical and functional properties [10,11]. By improving dispersion, reducing surface instability, and providing protective encapsulation, polymer matrices contribute to greater structural integrity and long-term performance in environmental and catalytic applications. Among various polymers explored for nanocomposite synthesis, polyvinylpyrrolidone (PVP) has proven particularly advantageous due to its amphiphilic nature, strong affinity for metal oxide

surfaces, and ability to form coordination bonds with metal ions [12,13]. PVP-coated metal oxide nanoparticles exhibit superior dispersion in aqueous systems, increased surface area, and improved interactions with pollutant molecules, all of which enhance their catalytic and adsorptive efficiencies [14]. The functionalization with PVP also contributes to greater chemical and thermal stability, enabling sustained performance during repetitive usage cycles in pollutant degradation or removal processes [15]. In addition, polyvinyl alcohol (PVA) has been widely employed in the fabrication of nanocomposite fibers via electrospinning techniques [16]. PVA offers excellent film-forming properties, mechanical robustness, and hydrophilicity, making it an ideal candidate for generating nanofibrous architectures with large specific surface areas and tunable porosity [17]. When combined with metal oxide nanoparticles, PVA-based nanofibers demonstrate enhanced sorption capabilities and faster mass transfer kinetics, making them well-suited for applications in water purification and catalytic reactions [18]. The synergistic effect between metal oxides and polymers such as PVP and PVA thus provides a versatile platform for designing next-generation nanomaterials with tailored properties for sustainable environmental remediation.

In recent years, nanomaterial synthesis has increasingly shifted toward eco-friendly and sustainable approaches, commonly known as green synthesis. Unlike conventional methods that rely on toxic reagents and high energy input, green synthesis utilizes natural resources such as plant extracts, microbial cultures, and fruit-derived compounds as reducing, stabilizing, and capping agents [19,20]. This strategy aligns with green chemistry principles, aiming to reduce environmental impact, production costs, and toxicity. Among various natural sources, the use of *Pistacia lentiscus*, *Zingiber officinale* (ginger), and *Laurus nobilis* (bay leaf) has garnered particular interest due to their abundance of bioactive phytochemicals, including flavonoids, phenolic acids, alkaloids, and terpenoids [21–23]. These secondary metabolites play a crucial role in the nucleation and stabilization of nanoparticles by donating electrons and forming strong coordination bonds with metal ions during the synthesis process [24]. For example, flavonoids and phenolics facilitate the reduction of metal salts into zero-valent or oxide forms, while concurrently preventing agglomeration through surface functionalization [25,26]. As a result, green-synthesized nanoparticles offer multifunctionality and are highly suitable for applications in catalysis,

pollutant removal, and biomedicine. Their bio-functionalized surfaces improve adsorption, electron transfer, and photocatalytic performance, making them valuable tools for addressing environmental challenges [27].

Beyond experimental investigations, molecular modeling and docking techniques have become essential tools for probing the interaction mechanisms between nanomaterials and target molecules [28]. Molecular docking allows for the prediction of binding affinities and interaction modes between dye molecules and the active sites of metal oxide nanocomposites at the atomic level [29]. This approach provides crucial insights into the adsorption mechanisms, electron transfer dynamics, and the role of functional groups in enhancing pollutant capture [30,31]. In the context of this thesis, docking simulations have been employed to model the interactions between selected dyes and PVP-based nanocomposites, helping to rationalize experimental observations and guide material design toward improved efficiency and selectivity.

This study employs a green approach to develop multifunctional nanocomposites by integrating metal oxide nanoparticles with polymer matrices, emphasizing eco-friendly synthesis and polymer-assisted stabilization. Four systems were designed to tackle key environmental challenges, including dye degradation, petroleum wastewater treatment, renewable energy production, and biodiesel purification. These composites combine various metal oxides with polymers to enhance photocatalytic activity, adsorption performance, and stability. Comprehensive characterization was performed using XRD, FTIR, SEM, BET, UV–Vis, TGA, and zeta potential analyses. Adsorption behavior was assessed through kinetic, isotherm, and thermodynamic modeling, while molecular docking simulations provided molecular-level insights into dye–nanocomposite interactions and selectivity.

The structure of this thesis is organized into the following steps:

- *General Introduction* – Provides the foundational background, highlighting the role of nanotechnology, metal oxides, polymeric nanocomposites, and green synthesis in environmental remediation, along with the significance of molecular docking in material evaluation.

- Chapter I: *Sunlight-driven dye degradation using Mn_3O_4/PVP nanocomposites* – Details the green synthesis of Mn_3O_4 using *Pistacia lentiscus*, integration with PVP, and the photodegradation of BPB and o-toluidine dyes under solar irradiation.
- Chapter II: *Green Synthesis of MgO@SnO_2 Nanocomposite Using Pistacia lentiscus Extract* – Focuses on the preparation and application of MgO@SnO_2 nanocomposites for the adsorption of petroleum wastewater pollutants and heavy metals, supported by isotherm and kinetic analyses.
- Chapter III: *Gallic acid-enabled CuO/Ni/Fe_3O_4 catalysts for CO_2 methanation and H_2 generation* – Explores a green synthetic route for CuO/Ni/Fe_3O_4 nanocomposites using gallic acid, emphasizing their catalytic activity in CO_2 conversion and sustainable hydrogen production under visible light.
- Chapter IV: *Green Fabrication of NiO/Ni@PVA Nanofibers for Enhanced Soap Extraction from Biodiesel* – Presents the development of electrospun NiO/Ni@PVA nanofibers and evaluates their performance in biodiesel purification, including adsorption kinetics, reusability, and computational modeling of soap-nanofiber interactions.

References

[1] G.A. Ozin, A. Arsenault, Nanochemistry: a chemical approach to nanomaterials, Royal Society of Chemistry, 2015.

[2] V. Merupo, J.C. Zarate, A. Abramova, N. Arjona, J. Herrera-Celis, L.G. Arriaga, A. Sharma, Inorganic Nanoparticles Properties and Applications, in: Nanochemistry, CRC Press, 2023: pp. 33–65.

[3] J.A.C. Nascimento Júnior, A.M. Santos, A.M.S. Oliveira, A.B. Santos, A.A. de Souza Araújo, D.M. Aragón, L.A. Frank, M.R. Serafini, The Tiny Big Difference: Nanotechnology in Photoprotective Innovations – A Systematic Review, AAPS PharmSciTech 25 (2024) 212. https://doi.org/10.1208/s12249-024-02925-4.

[4] A.K. Hussein, Applications of nanotechnology in renewable energies—A comprehensive overview and understanding, Renew. Sustain. Energy Rev. 42 (2015) 460–476.

[5] Y. Khan, H. Sadia, S.Z. Ali Shah, M.N. Khan, A.A. Shah, N. Ullah, M.F. Ullah, H. Bibi, O.T. Bafakeeh, N. Ben Khedher, Classification, synthetic, and characterization approaches to nanoparticles, and their applications in various fields of nanotechnology: A review, Catalysts 12 (2022) 1386.

[6] U. Qumar, J.Z. Hassan, R.A. Bhatti, A. Raza, G. Nazir, W. Nabgan, M. Ikram, Photocatalysis vs adsorption by metal oxide nanoparticles, J. Mater. Sci. Technol. 131 (2022) 122–166.

[7] J. Prakash, S. Khan, S. Chauhan, A.M. Biradar, Metal oxide-nanoparticles and liquid crystal composites: A review of recent progress, J. Mol. Liq. 297 (2020) 112052.

[8] S. Wang, D. Chen, Q. Hong, Y. Gui, Y. Cao, G. Ren, Z. Liang, Surface functionalization of metal and metal oxide nanoparticles for dispersion and tribological applications–A review, J. Mol. Liq. 389 (2023) 122821.

[9] S.H. Joo, D. Zhao, Environmental dynamics of metal oxide nanoparticles in heterogeneous systems: A review, J. Hazard. Mater. 322 (2017) 29–47.

[10] Z.B. Shifrina, V.G. Matveeva, L.M. Bronstein, Role of polymer structures in catalysis by transition metal and metal oxide nanoparticle composites, Chem. Rev. 120 (2019) 1350–1396.

[11] A. Zadehnazari, Metal oxide/polymer nanocomposites: A review on recent advances in fabrication and applications, Polym. Technol. Mater. 62 (2023) 655–700.

[12] M. Pourmadadi, A. Shamsabadipour, A. Aslani, M.M. Eshaghi, A. Rahdar, S. Pandey, Development of polyvinylpyrrolidone-based nanomaterials for biosensors applications: a review, Inorg. Chem. Commun. (2023) 110714.

[13] K.M. Koczkur, S. Mourdikoudis, L. Polavarapu, S.E. Skrabalak,

Polyvinylpyrrolidone (PVP) in nanoparticle synthesis, Dalt. Trans. 44 (2015) 17883–17905.

[14] S. Mallakpour, V. Behranvand, Green hybrid nanocomposites from metal oxides, poly (vinyl alcohol) and poly (vinyl pyrrolidone): Structure and chemistry, in: Hybrid Polym. Compos. Mater., Elsevier, 2017: pp. 263–289.

[15] H. Wang, X. Cai, Y. Zhang, T. Zhang, M. Chen, H. Hu, Z. Huang, J. Liang, Y. Qin, Double-template-regulated bionic mineralization for the preparation of flower-like BiOBr/carbon foam/PVP composite with enhanced stability and visible-light-driven catalytic activity, Appl. Surf. Sci. 555 (2021) 149708.

[16] M. Aslam, M.A. Kalyar, Z.A. Raza, Polyvinyl alcohol: A review of research status and use of polyvinyl alcohol based nanocomposites, Polym. Eng. Sci. 58 (2018) 2119–2132.

[17] G.C. Türkoğlu, N. Khomarloo, E. Mohsenzadeh, D.N. Gospodinova, M. Neznakomova, F. Salaün, PVA-based electrospun materials—A promising route to designing nanofiber mats with desired morphological shape—A review, Int. J. Mol. Sci. 25 (2024) 1668.

[18] X. Liang, H.-J. Zhong, H. Ding, B. Yu, X. Ma, X. Liu, C.-M. Chong, J. He, Polyvinyl alcohol (PVA)-based hydrogels: Recent progress in fabrication, properties, and multifunctional applications, Polymers (Basel). 16 (2024) 2755.

[19] N.S. Alsaiari, F.M. Alzahrani, A. Amari, H. Osman, H.N. Harharah, N. Elboughdiri, M.A. Tahoon, Plant and microbial approaches as green methods for the synthesis of nanomaterials: synthesis, applications, and future perspectives, Molecules 28 (2023) 463.

[20] D. Gupta, A. Thakur, T.K. Gupta, Green and sustainable synthesis of nanomaterials: Recent advancements and limitations, Environ. Res. (2023) 116316.

[21] A. Paparella, B. Nawade, L. Shaltiel-Harpaz, M. Ibdah, A review of the botany, volatile composition, biochemical and molecular aspects, and traditional uses of Laurus nobilis, Plants 11 (2022) 1209.

[22] A.M.E. Sulieman, S.M. Ibrahim, M. Alshammari, F. Abdulaziz, H. Idriss, N.A.H. Alanazi, E.M. Abdallah, A.J. Siddiqui, S.A.M. Shommo, A. Jamal, Zingiber officinale Uncovered: Integrating Experimental and Computational Approaches to Antibacterial and Phytochemical Profiling, Pharmaceuticals 17 (2024) 1551.

[23] C. Sehaki, N. Jullian, F. Ayati, F. Fernane, E. Gontier, A review of Pistacia lentiscus polyphenols: Chemical diversity and pharmacological activities, Plants 12 (2023) 279.

[24] Y. Zhang, G. Qi, L. Yao, L. Huang, J. Wang, W. Gao, Effects of metal nanoparticles and other preparative materials in the environment on plants: from the perspective of improving secondary metabolites, J. Agric. Food Chem. 70 (2022) 916–933.

[25] W. Cheng, J. Wen, Now and future: Development and perspectives of using polyphenol nanomaterials in environmental pollution control, Coord. Chem. Rev. 473 (2022) 214825.

[26] I.C. Ciobotaru, D. Oprea, C.C. Ciobotaru, T.A. Enache, Low-Cost Plant-Based Metal and Metal Oxide Nanoparticle Synthesis and Their Use in Optical and Electrochemical (Bio) Sensors, Biosensors 13 (2023) 1031.

[27] D. Kirubakaran, J.B.A. Wahid, N. Karmegam, R. Jeevika, L. Sellapillai, M. Rajkumar, K.J. SenthilKumar, A comprehensive review on the green synthesis of nanoparticles: advancements in biomedical and environmental applications, Biomed. Mater. Devices (2025) 1–26.

[28] A.S. Abdelsattar, A. Dawoud, M.A. Helal, Interaction of nanoparticles with biological macromolecules: A review of molecular docking studies, Nanotoxicology 15 (2021) 66–95.

[29] M. Ikram, S. Abbas, A. Haider, S. Naz, S.O.A. Ahmad, J. Haider, A. Ul-Hamid, A. Shahzadi, I. Shahzadi, A.R. Butt, Efficient dye degradation, antimicrobial behavior and molecular docking analysis of gold (Au) and cellulose nanocrystals (CNC)-doped strontium oxide nanocomposites, J. Nanostructure Chem. (2021) 1–18.

[30] I. Salahshoori, Q. Wang, M.A.L. Nobre, A.H. Mohammadi, E.A. Dawi, H.A. Khonakdar, Molecular simulation-based insights into dye pollutant adsorption: a perspective review, Adv. Colloid Interface Sci. (2024) 103281.

[31] I. Salahshoori, S. Mahdavi, Z. Moradi, M. Otadi, F.Z. Kazemabadi, M.A.L. Nobre, H.A. Khonakdar, A. Baghban, Q. Wang, A.H. Mohammadi, Advancements in molecular simulation for understanding pharmaceutical pollutant Adsorption: A State-of-the-Art review, J. Mol. Liq. (2024) 125513.

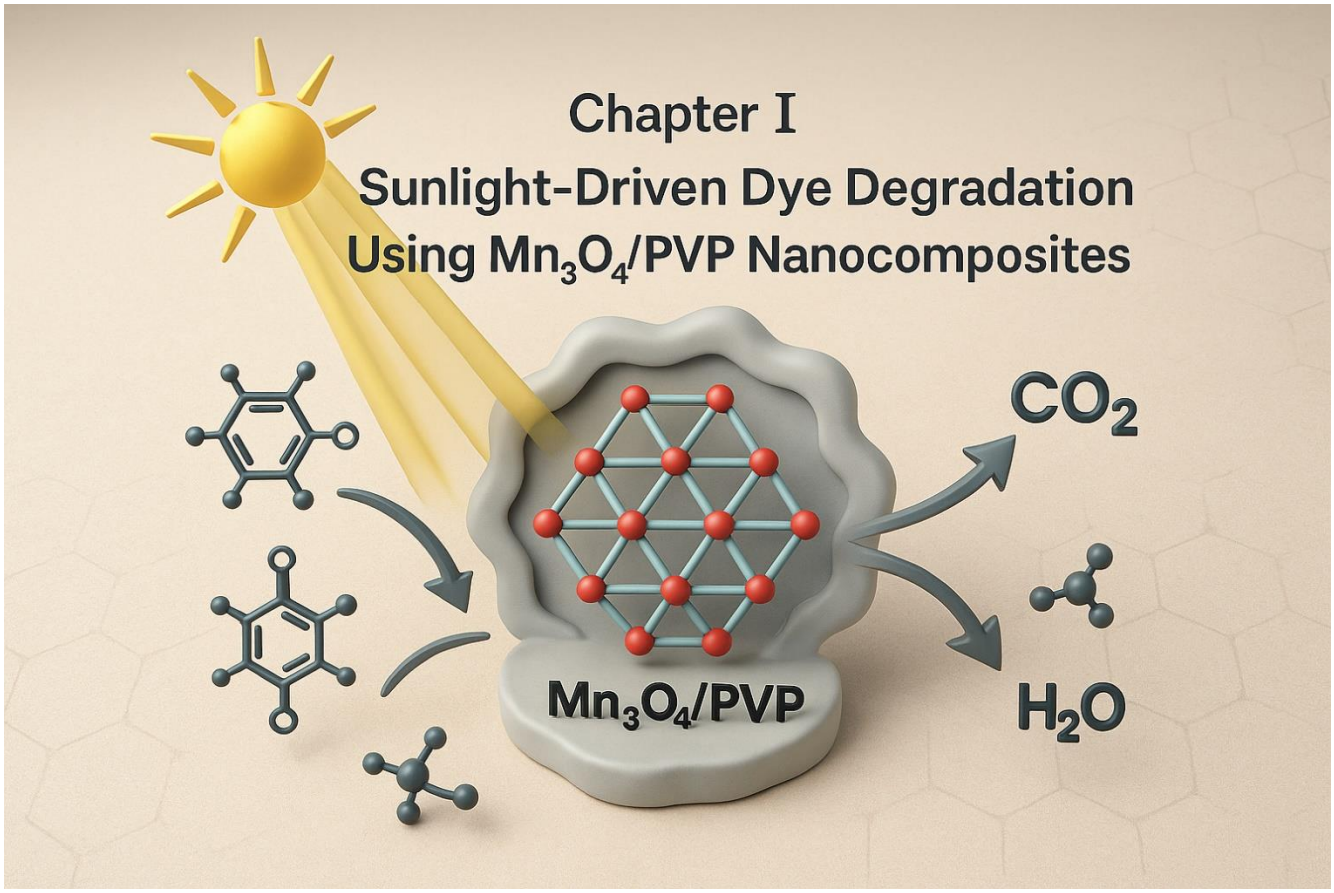
Chapter I
Sunlight-Driven Dye Degradation
Using Mn_3O_4/PVP Nanocomposites
CO_2
H_2O
Mn_3O_4/PVP

1. Introduction

Water pollution caused by synthetic organic dyes represents one of the most pressing global environmental challenges[1][2][3]. These dyes, primarily discharged from textile, leather, cosmetics, and pharmaceutical industries [4], are characterized by complex aromatic structures that confer resistance to biodegradation and photolysis [5][6]. Upon entering aquatic ecosystems, even at low concentrations [7], they can significantly alter water quality by reducing light penetration [8], inhibiting photosynthetic activity, and accumulating in living organisms [9]. Their toxic, mutagenic, and carcinogenic properties pose a severe threat to both environmental and human health [10], necessitating the development of efficient and sustainable remediation strategies [11][12].

Traditional wastewater treatment methods including coagulation-flocculation [13][14], adsorption on activated carbon [13][15], membrane filtration [16][17], and biological oxidation [18] have shown limited effectiveness in degrading persistent dyes [19][20]. These techniques often suffer from high operational costs, generation of secondary waste, low selectivity, and inefficiency in treating complex dye mixtures [21]. Moreover, conventional methods [22] may only transfer pollutants from one phase [23] to another rather than achieve complete mineralization [24][25]. These drawbacks underscore the urgent need for more innovative and environmentally benign treatment approaches capable of addressing the limitations of current technologies [26][27].

Among emerging alternatives, photocatalysis has emerged as a sustainable and highly promising solution for the degradation of organic pollutants [27][28][29]. Photocatalysis utilizes semiconducting materials to harness light energy and generate electron-hole pairs [30], which react with water and oxygen to form reactive oxygen species (ROS) such as hydroxyl (·OH) and superoxide ($O_2^{-}\cdot$) radicals [31][32]. These ROS are capable of breaking down a wide range of toxic compounds into less harmful byproducts, such as carbon dioxide and water [33][34]. The photocatalytic process operates under ambient conditions [35], requires no additional chemicals [36], and aligns with green chemistry principles, making it an attractive method for environmental remediation [37].

Manganese oxide (Mn_3O_4) has gained significant attention as a potential photocatalyst due to its unique redox properties [38], abundance, low toxicity [39], and ability to absorb visible light [40]. Its mixed-valence structure (Mn^{2+}/Mn^{3+}) [41] and narrow bandgap enable redox reactions that are vital for efficient pollutant degradation [39][38]. However, the practical application of bare Mn_3O_4 nanoparticles is hampered by inherent drawbacks such as particle aggregation [42], low surface area, and the rapid recombination of photogenerated charge carriers [43]. These limitations reduce its photocatalytic efficiency and restrict its use in real-world water treatment systems [26].

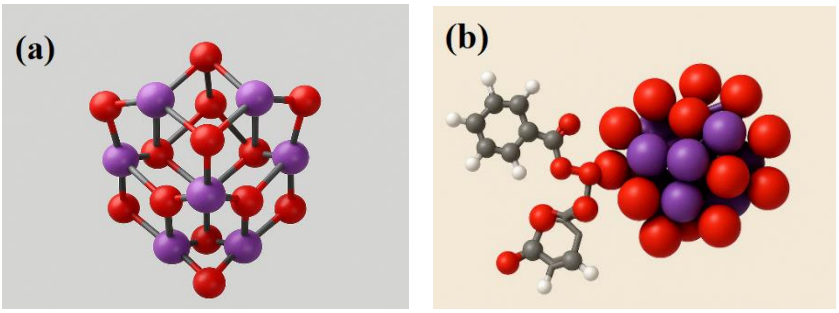

Figure I. 1: Molecular Representation of **(a)** Mn_3O_4 NP; **(b)** Mn_3O_4/PVP NC

To overcome these limitations, the incorporation of stabilizing agents such as polymers has emerged as a powerful strategy [44] to improve the physicochemical and functional properties of photocatalysts [45][46]. Polyvinylpyrrolidone (PVP), a water-soluble, non-toxic polymer, is particularly effective in this context [47][48]. PVP not only stabilizes nanoparticles by preventing agglomeration but also enhances surface dispersion, increases light absorption [49][50], and improves charge carrier mobility [51][52]. Its functional groups can interact with both the catalyst surface and pollutant molecules [53], thereby enhancing adsorption capacity and facilitating catalytic activity [54]. When integrated with Mn_3O_4 [55], PVP can synergistically improve both the stability and performance of the resulting nanocomposite in photocatalytic applications [56].

The present research aims to develop an environmentally friendly Mn_3O_4/PVP nanocomposite through a green synthesis approach using Pistacia lentiscus leaf extract as a natural reducing and capping agent [57]. The use of plant-based extracts provides a sustainable and non-toxic alternative to conventional chemical methods [58][59], eliminating the need for hazardous reagents and aligning the synthesis process with

ecological and safety standards [60]. The bioactive compounds in Pistacia lentiscus notably flavonoids [61], polyphenols [62], and tannins facilitate the controlled nucleation and stabilization of nanoparticles [63][64], resulting in a functional material with enhanced photocatalytic properties [65].

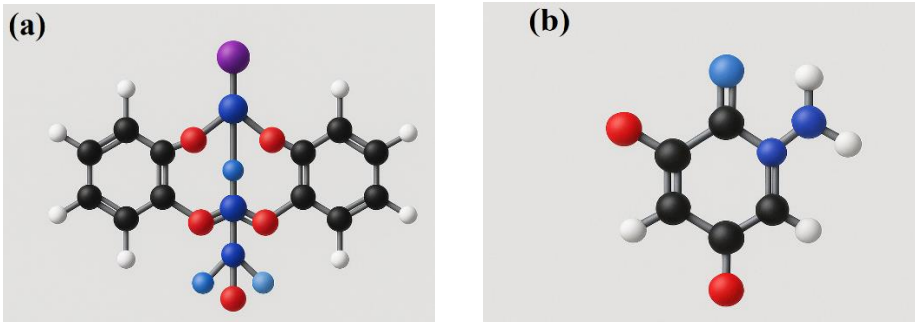

Figure I. 2: Molecular Representation of **(a)** BPB, **(B)** OPB

This chapter presents a detailed account of the green synthesis methodology, material characterization using FTIR, XRD, SEM, and UV–Vis spectroscopy, and the photocatalytic evaluation of the Mn_3O_4/PVP nanocomposite under natural sunlight irradiation [57]. Furthermore, Monte Carlo and DFT-based simulations were employed to gain molecular-level insights into the adsorption mechanisms and energetics of dye interactions with the nanocomposite surface [57]. Through this multidisciplinary approach, the study seeks to establish a robust framework for designing high-performance, eco-friendly photocatalysts tailored for water purification and environmental sustainability. Ultimately, the findings offer a significant contribution to the field of green nanotechnology and open new avenues for practical applications in wastewater treatment.

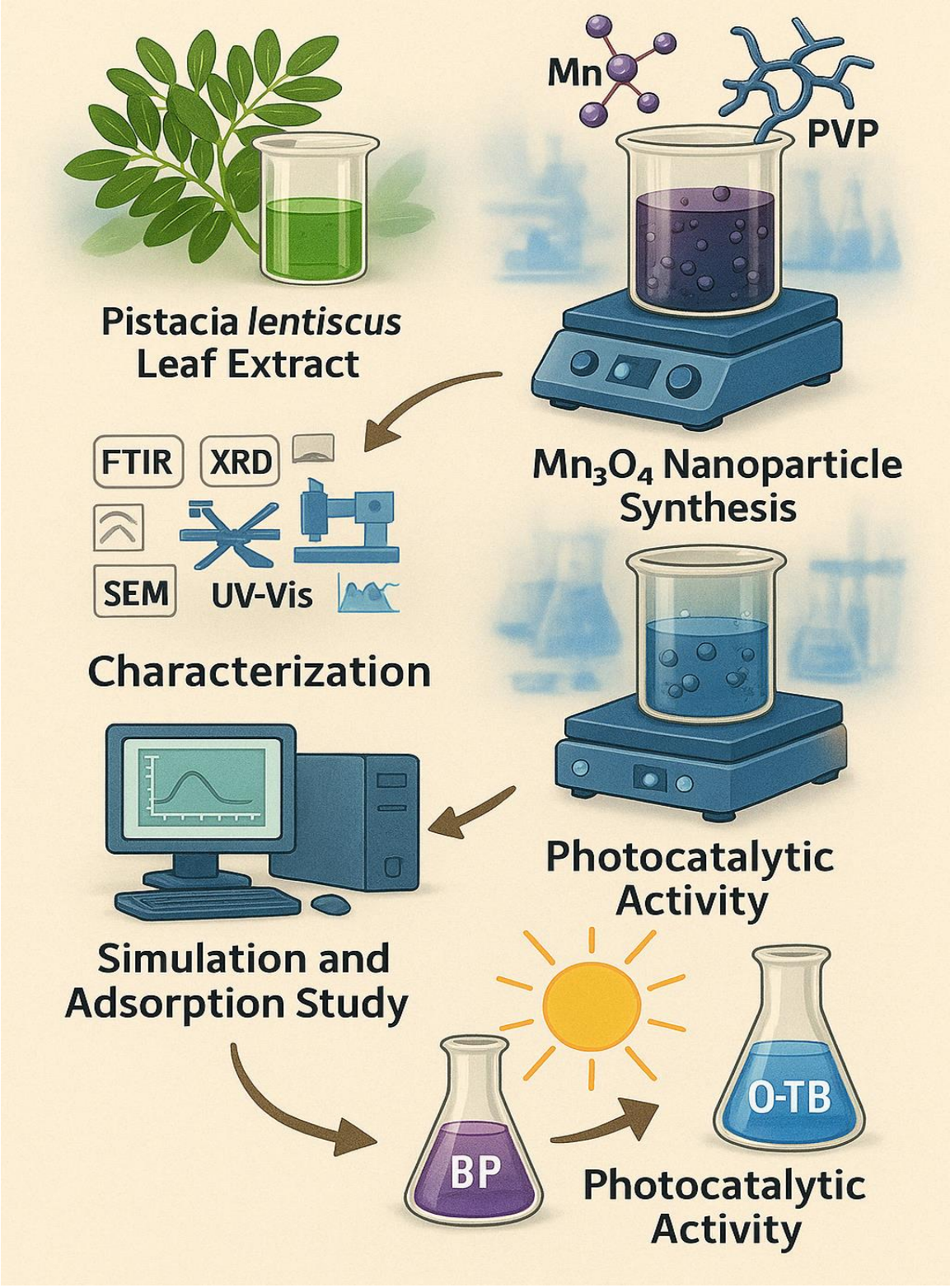

Figure I. 3: Schematic Overview of Mn_3O_4/PVP Nanocomposite Synthesis, Characterization, and Photocatalytic Evaluation for Dye Degradation

2. Experimental Procedures

2.1. Formation Process of Mn_3O_4 Nanoparticles

Pistacia lentiscus leaves were collected from Annaba, Algeria, then thoroughly cleaned, dried, crushed, and soaked in distilled water for 24 hours. The resulting extract was filtered and stored for use in the green synthesis of Mn_3O_4 nanoparticles (NPs). A 0.33 M solution of manganese (II) nitrate tetrahydrate ($Mn(NO_3)_2 \cdot 4H_2O$) was prepared by dissolving the salt in 100 mL of distilled water under continuous stirring. Subsequently, 50 mL of the plant extract was gradually added to the metal salt solution under constant stirring to facilitate the reduction of manganese ions by the bioactive compounds present in the extract. The mixture was then heated at 70 °C for 2 hours, during which a visible color change indicated the formation of Mn_3O_4 nanoparticles.

Following the reaction, the mixture was allowed to cool to room temperature and centrifuged to collect the precipitate. The obtained solid was thoroughly washed with distilled water and ethanol to remove any impurities. The purified product was dried at 70 °C for 24 hours and subsequently calcined at 600 °C for 4 hours to yield pure, crystalline Mn_3O_4 nanoparticles for further characterization and applications [57].

2.2. Polymer-Assisted Synthesis of Mn_3O_4/PVP Nanocomposites

The synthesis of the Mn_3O_4/polyvinylpyrrolidone nanocomposites was carried out through a multi-step process, as established in previous studies, to ensure the formation of a well-dispersed and stable material. Initially, 0.3 g of the previously synthesized Mn_3O_4 nanoparticles and 0.3 g of PVP were each added to 110 mL of distilled water in separate, clean, sterile beakers. Both mixtures were stirred at room temperature for 20 minutes to achieve complete dissolution of the PVP and uniform dispersion of the nanoparticles, resulting in a homogeneous polymeric solution.

Following this, the Mn_3O_4 nanoparticle suspension underwent ultrasonic treatment at 45 °C for 1 hour to effectively break down any agglomerates and ensure uniform particle distribution, thereby maximizing the surface area available for interaction with the PVP. The Mn_3O_4 suspension was then slowly introduced into the PVP solution under continuous stirring to promote adsorption of the polymer onto the nanoparticle surfaces. The resulting

mixture was stirred for an additional hour at room temperature to facilitate the formation of a stable Mn_3O_4/PVP complex.

To further improve the homogeneity and structural integrity of the nanocomposite, the solution was subjected to a second ultrasonic treatment at 45 °C for 15 minutes. This step was designed to reinforce the interactions between Mn_3O_4 nanoparticles and PVP chains, enabling uniform encapsulation of the nanoparticles within the polymer matrix.

After completing the dispersion process, the suspension was centrifuged and washed multiple times with distilled water to eliminate any unbound or excess PVP. The purified Mn_3O_4/PVP nanocomposite was then dried in a laboratory oven at 60 °C for 24 hours, resulting in a fine, stable powder. This final product was subsequently employed for various characterization techniques and photocatalytic applications, including dye degradation studies [57].

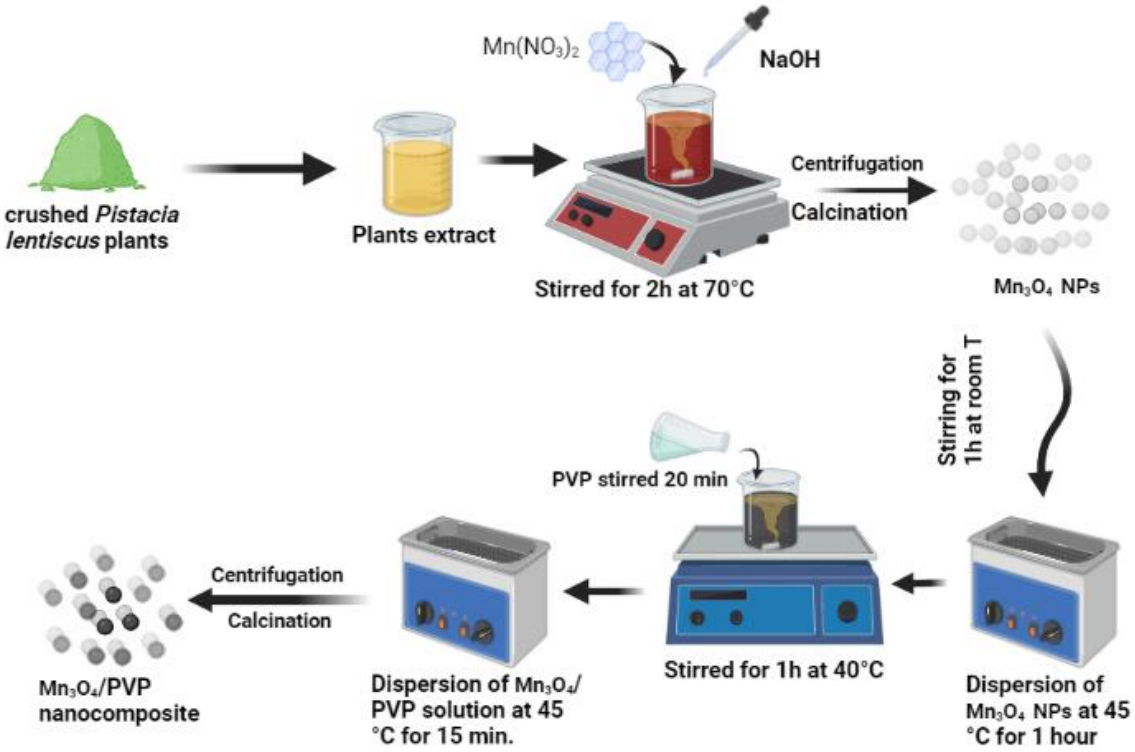

Figure I. 4: Graphical abstract of green synthesis of Mn_3O_4 NP Mn_3O_4/PVP NC

2.3. Analytical Characterization Methods (FTIR, XRD, SEM, UV-Vis)

A comprehensive set of analytical techniques was employed to characterize the structural, morphological, and optical properties of the synthesized Mn_3O_4 nanoparticles and the Mn_3O_4/PVP NC. Fourier-transform infrared spectroscopy (FTIR, Nicolet iS5 model) was used to investigate the functional groups and chemical structure of the PVP polymer, Mn_3O_4 NPs, and Mn_3O_4/PVP NC. To assess the crystallographic structure of the samples, X-ray diffraction (XRD) analysis was performed using a benchtop model provided by Proto Manufacturing Company.

The surface morphology and particle size distribution of the materials were examined using scanning electron microscopy (SEM, JEOL JSM 840A, Japan). Crystallite sizes were estimated based on the XRD patterns using the Scherrer equation, which relates peak broadening to particle size [66]:

$$D = \frac{K\lambda}{\beta \cos \theta} \qquad (1)$$

where D denotes the crystallite size, K is the shape factor (typically 0.9), λ is the X-ray wavelength (0.15418 nm for Cu Kα radiation), β is the full width at half maximum (FWHM) of the diffraction peak, and θ is the Bragg angle [67].

Additionally, the optical properties of Mn_3O_4 NPs and Mn_3O_4/PVP NC were analyzed using UV–visible spectroscopy (SECOMAM 9600 model) across the wavelength range of 200–800 nm to evaluate their light absorption behavior and estimate the optical band gap.

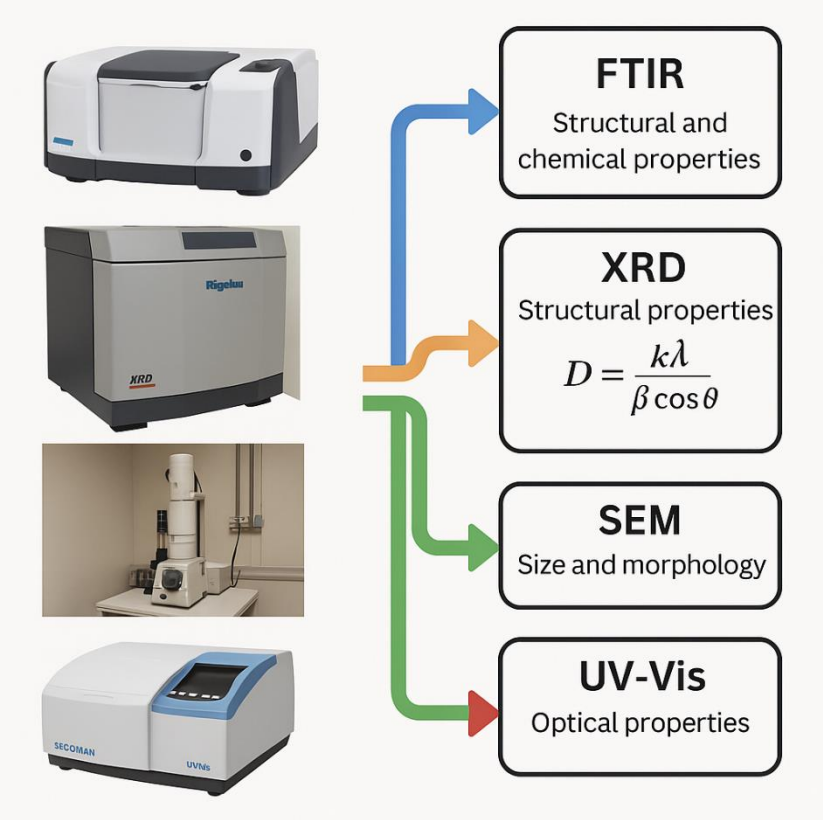

Figure I. 5: Characterization Techniques and Instrumentation for Mn_3O_4-Based NC

2.4. Light-Driven Catalytic Properties of Mn_3O_4 and Mn_3O_4/PVP Composites

The photocatalytic performance of Mn_3O_4 nanoparticles and Mn_3O_4/PVP nanocomposites was systematically evaluated using aqueous solutions of two organic dyes: bromophenol blue (BPB) and ortho-toluidine blue (O-TB). For these experiments, 200 mL solutions of each dye were prepared at a concentration of 50 parts per million (PPM). The degradation efficiency of these dyes under sunlight irradiation was studied by analyzing two critical factors influencing photocatalytic activity: the duration of irradiation (contact time) and the amount of photocatalyst used (photocatalyst dose).

To investigate the effect of contact time, the photocatalytic degradation of BPB and O-TB was monitored at various time intervals 5, 15, 30, 60, and 90 minutes using 5 mg of Mn_3O_4 NPs and Mn_3O_4/PVP NC dispersed in 5 mL of the dye solutions. In a separate set of experiments, the influence of the photocatalyst dose was studied by varying the catalyst

weight (2.5 mg, 5 mg, and 7.5 mg) while maintaining a constant contact time of 90 minutes. These tests aimed to identify the optimal conditions for maximum dye degradation.

After the photocatalytic reaction, the Mn_3O_4 NPs and Mn_3O_4/PVP NC were separated from the reaction mixture by centrifugation. The residual concentration of the dyes in the supernatant was determined by measuring the absorbance spectra of the solutions using a UV-visible spectrophotometer within the range of 200 to 800 nm. The degree of dye degradation was calculated using the following equation [67]:

$$\%\ degradation = \frac{A_0 - A_{(t)}}{A_0} \times 100 \qquad (2)$$

and are the initial time adsorption of BPB and O-TB

Here, A_0 represents the initial absorbance of the dye solution before irradiation, and $A_{(t)}$ denotes the absorbance at a specific time t. This formula provided a quantitative measure of the photocatalytic efficiency of Mn_3O_4 NPs and Mn_3O_4/PVP NC, offering insight into their potential for practical applications in wastewater treatment.

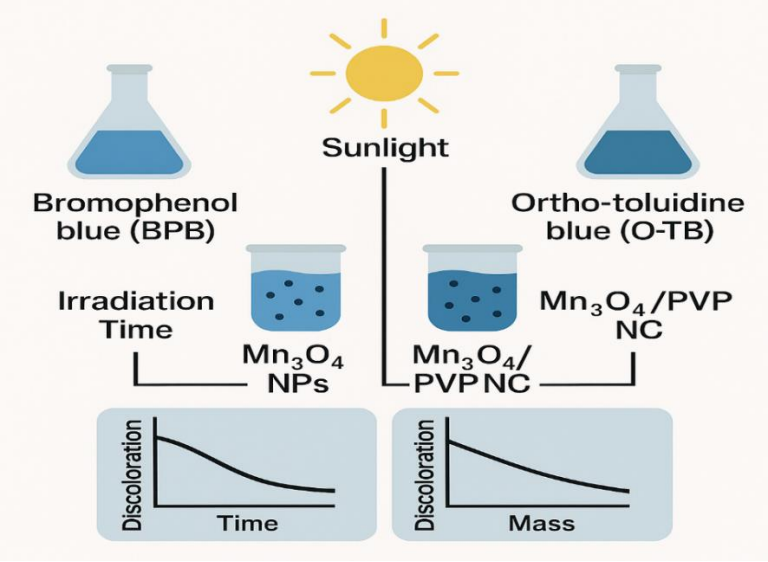

Figure I. 6: Photocatalytic Degradation of BPB and O-TB Dyes Under Sunlight Using Mn_3O_4 NP and Mn_3O_4/PVP NC: Influence of Irradiation Time and Catalyst Dosage

2.5. Cyclic Performance of Dye Photodegradation

After determining the optimal conditions for dye degradation 75 minutes of contact time and 0.0075 grams of Mn_3O_4/PVP NC the stability and reusability of the photocatalyst were evaluated over multiple cycles. For this purpose, aqueous solutions of bromophenol blue (BPB) and ortho-toluidine blue (O-TB), each with an initial concentration (C_0) of 50 ppm, were prepared. These solutions were treated with 0.0075 grams of Mn_3O_4/PVP NC and exposed to sunlight irradiation for 75 minutes, simulating realistic conditions for wastewater treatment.

After each photocatalytic cycle, the residual dye concentrations were analyzed using UV–visible spectroscopy to determine the degradation efficiency. The photocatalyst was then recovered by centrifugation, thoroughly washed with distilled water to remove any adsorbed dye residues, and dried at 100 °C to restore its catalytic activity. The regenerated Mn_3O_4/PVP NC was subsequently reused in fresh dye solutions under the same experimental conditions to assess its photocatalytic performance across successive cycles.

To evaluate the structural stability of the Mn_3O_4/PVP NC after repeated use, X-ray diffraction (XRD) analysis was performed on the catalyst both before and after the final cycle. This assessment was essential for detecting any changes in crystallinity or phase composition that could affect photocatalytic activity. The results offered valuable insight into the durability and practical applicability of Mn_3O_4/PVP NC as a recyclable and efficient photocatalyst for environmental remediation [57].

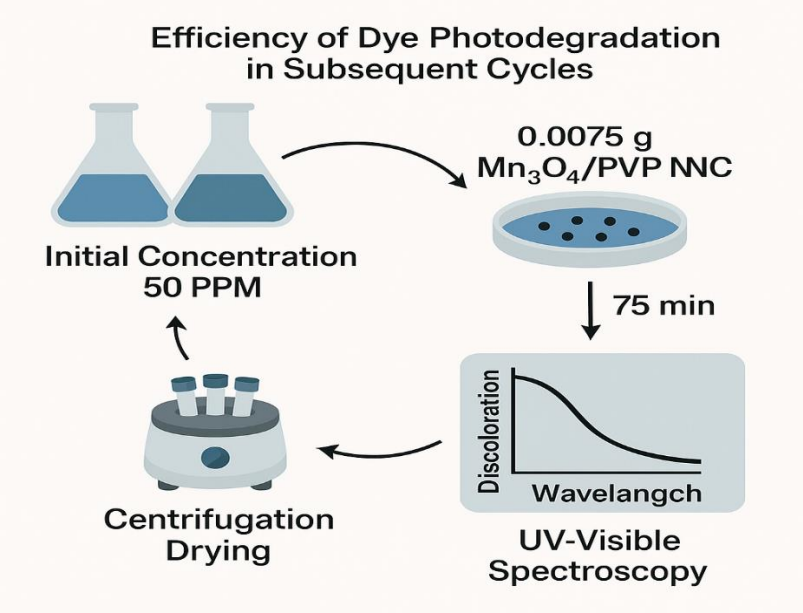

Figure I. 7: Assessment of Mn_3O_4/PVP NC Reusability in Consecutive Photodegradation Cycles of Organic Dyes

2.6. Molecular Modeling and Energetic Profiling of Adsorption

To evaluate the binding affinity between the dye molecules and the surfaces of Mn_3O_4 nanoparticles and Mn_3O_4/PVP nanocomposites, first-principles calculations were conducted using the Forcite molecular mechanics package [68]. These calculations aimed to determine the adsorption energy [68][69], providing insight into the interaction strength between the dye pollutants and the photocatalyst surfaces [70].

The computational process began with the preparation of the receptor structure [71]. The precise geometric and crystallographic structure of Mn_3O_4 NPs was carefully modeled using ChemDraw software to ensure the accuracy of the nanoparticles' shape and dimensions. The Mn_3O_4 surface was specifically prepared along the cleavage plane (1 1 0), known for its stability and reactivity in photocatalytic processes. To further enhance the reliability of the simulations, a supercell with dimensions 3 × 3 × 1 was created, offering a sufficiently large surface area for interactions [57].

The PVP polymer was then modeled and placed on the Mn_3O_4 surface, forming the Mn_3O_4/PVP NC [57]. The system underwent geometric optimization and electronic

property calculations using Forcite [72]. This software ensures crystalline symmetry is preserved throughout the optimization, resulting in an energetically stable structure [73].

The ligand structure, representing the dye molecules [74] (e.g., bromophenol), was obtained from PubChem's chemical database [75]. It was subsequently placed on the Mn_3O_4/PVP surface [57] to evaluate the interaction using the Monte Carlo Metropolis technique, a robust method for simulating molecular adsorption processes [76].

The adsorption energy (E_{ad}) was calculated using the following equation [77]:

$$E_{ad} = E_{\mathbf{Mn_3O_4/PVP-dye}} - E_{\mathbf{Mn_3O_4-PVP}} - E_{dye} \qquad (3)$$

Where:

- $E_{\mathbf{Mn_3O_4/PVP-dye}}$ is the total energy of the Mn_3O_4/PVP-dye complex in its ground state.
- $E_{\mathbf{Mn_3O_4-PVP}}$ is the energy of the isolated Mn_3O_4/PVP NC in its ground state.
- E_{dye} is the energy of the isolated dye molecule in its ground state.

This calculation provided a quantitative measure of the interaction strength, with more negative E_{ad} values indicating stronger adsorption [78]. These findings offered valuable insights into the adsorption mechanisms and the efficiency of Mn_3O_4/PVP NC as a photocatalyst for dye degradation [57].

3. Structural and Morphological Characterization

3.1. Structural Analysis (XRD)

X-ray diffraction analysis was performed to investigate the crystallographic structure [79] and phase composition of Mn_3O_4 nanoparticles, PVP, and Mn_3O_4/PVP NC [57]. The XRD pattern of Mn_3O_4 NPs revealed distinct diffraction peaks at multiple 2θ positions, including 18.01°, 28.91°, 30.99°, 32.38°, 36.08°, 38.09°, 44.41°, 50.84°, 53.86°, 56.02°, 58.50°, 59.91°, 63.3°, 64.61°, 69.77°, 74.15°, and 77.54°. These peaks corresponded to the crystal planes (101), (112), (200), (103), (211), (004), (220), (105), (312), (303), (321), (224), (116), (314), (305), (413), and (404), characteristic of the tetragonal structure of Mn_3O_4, as

shown in Figure I.1. This pattern aligned well with the standard reference data for Mn_3O_4 NPs (JCPDS Note 01-080-0382), confirming the successful synthesis of pure Mn_3O_4 NPs [57].

The XRD analysis of Mn_3O_4/PVP NC revealed additional peaks at 2θ values of 11.68° and 21.84°, attributed to the crystallite structure of PVP. These new peaks confirmed the successful incorporation of PVP into the Mn_3O_4 NPs, forming a composite material with enhanced structural and functional properties. The broader peaks associated with PVP suggested an amorphous nature, which complemented the crystalline Mn_3O_4, enhancing the composite's overall stability and functionality [57].

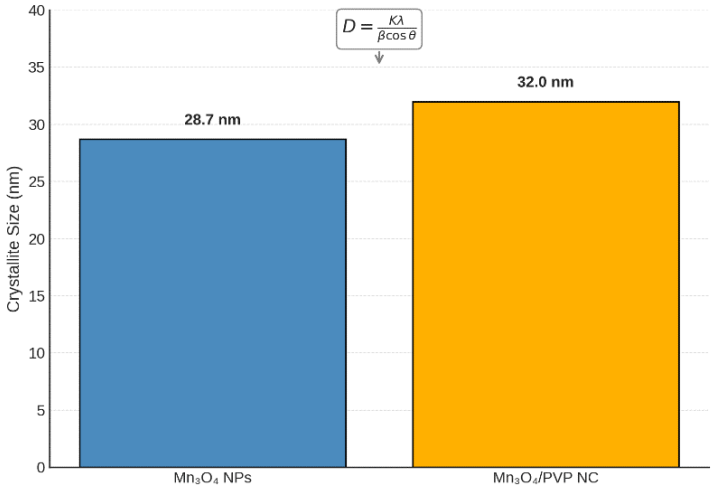

Figure I. 8: Crystallite size comparison

Table II.1 summarizes the particle sizes determined using the Scherrer equation, which showed that the pure Mn_3O_4 NPs had an average size of 37 nm. In contrast, the Mn_3O_4/PVP NC exhibited a slightly larger average crystallite size of 45 nm, likely due to the PVP coating on the nanoparticle surfaces.

Table I. 1: represent particle size of Mn_3O_4 NP and Mn_3O_4/PVP NC [57]

Samples	Lattice parameters (hkl)	Angle	Particle size (NM)
MN_3O_4 NPS	(211)	36.08°	37
MN_3O_4/PVP NC	(211)	36.08°	45

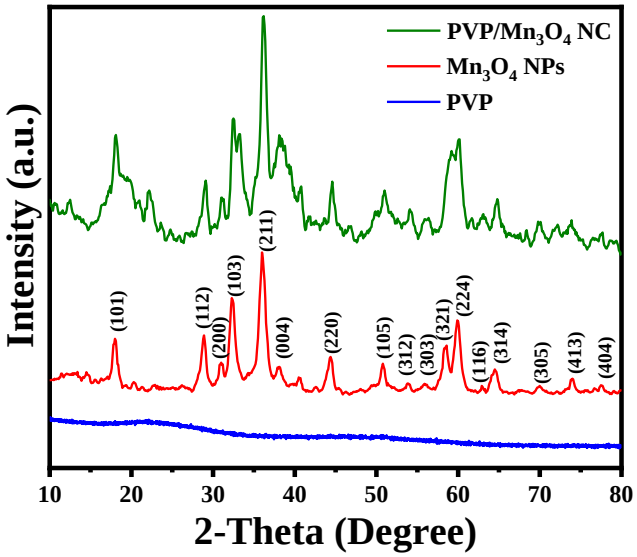

Figure I. 9: XRD patterns of PVP, Mn3O4 NPs, and Mn3O4/PVP NC [57]

3.2. Morphological and Size Distribution (SEM)

Scanning electron microscopy was conducted to analyze the surface morphology [80], particle size, and distribution characteristics of Mn_3O_4 NPs and Mn_3O_4/PVP NC [57]. SEM provides high-resolution images that reveal essential structural details, making it a valuable tool for evaluating the impact of polymer modification on nanoparticle morphology [81]. The SEM micrographs of Mn_3O_4 NPs and Mn_3O_4/PVP NC are shown in Figure I.10 (a) and Figure I.10 (b), respectively, and highlight the structural distinctions between the two samples.

The Mn_3O_4 NPs displayed a predominantly spherical shape, but slight agglomeration was observed, likely due to the interactions between functional groups present in the *Pistacia lentiscus* leaf extract used during synthesis [57]. The organic compounds in the leaf extract,

such as polyphenols and flavonoids, acted as reducing and stabilizing agents, which can sometimes lead to intermolecular interactions and clustering of particles [82][83]. This agglomeration resulted in an average particle size of approximately 37 nm [57], which aligns with previously reported findings in the literature and confirms the successful synthesis of Mn_3O_4 NPs.

On the other hand, the Mn_3O_4/PVP NC exhibited a distinct morphology, with significantly reduced agglomeration compared to the bare Mn_3O_4 NPs [57]. The noticeable improvement in particle dispersion is attributed to the presence of PVP, a non-ionic polymer known for its stabilizing properties [51]. During the synthesis process, PVP likely adsorbed onto the surface of Mn_3O_4 nanoparticles, creating a protective polymer layer that reduced interparticle van der Waals forces and steric hindrance [57]. This polymer coating not only improved the dispersion of the nanoparticles but also slightly increased their average particle size to about 45 nm [57], indicating the successful encapsulation of Mn_3O_4 by PVP.

The SEM images clearly demonstrate that the addition of PVP significantly influences the physical characteristics of the nanocomposite [84]. The reduced agglomeration and improved uniformity in particle size distribution suggest enhanced stability and dispersibility of the Mn_3O_4/PVP NC in various solvents and applications. These modifications are particularly advantageous for photocatalytic processes, as they increase the effective surface area and improve light absorption efficiency [57].

Moreover, the uniform distribution of PVP around Mn_3O_4 nanoparticles can potentially enhance the composite's mechanical properties, making it more suitable for environmental and industrial applications. The successful incorporation of PVP into the Mn_3O_4 structure is evident, highlighting the critical role of the polymer in enhancing the nanocomposite's functionality. SEM analysis thus confirms the efficacy of the synthesis method and provides insights into the structural benefits conferred by PVP, paving the way for further exploration of Mn_3O_4/PVP NC in photocatalytic and environmental remediation applications [57].

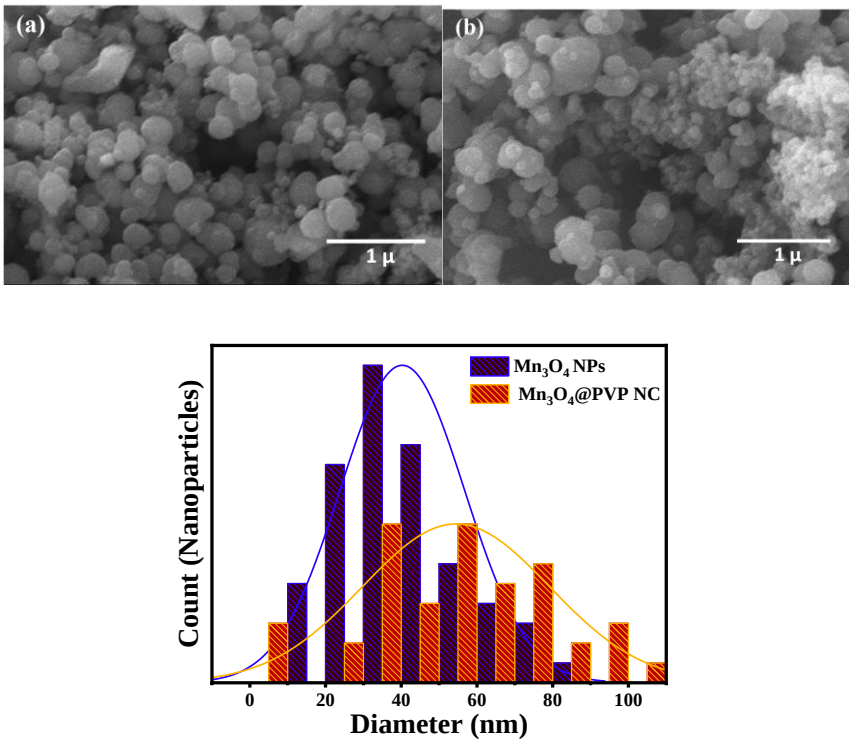

Figure I. 10: SEM micrographs and particle size analysis of **(a)** Mn_3O_4 nanoparticles and **(b)** Mn_3O_4/PVP nanocomposite, along with **(c)** a comparison of particle size distributions for both materials [57]

3.3. Functional Group Identification (FTIR)

Fourier-transform infrared spectroscopy was performed to identify the functional groups [85] present in the *Pistacia lentiscus* leaf extract, Mn_3O_4 NPs, PVP, and the Mn_3O_4/PVP NC [57]. The corresponding FTIR spectra are shown in Figure I.13, highlighting the characteristic absorption peaks for each component.

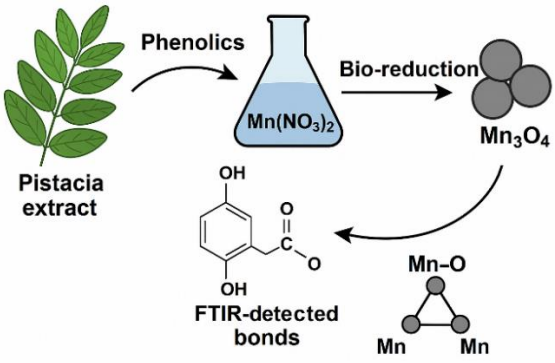

Figure I. 11: Identification of Key Functional Bonds by FTIR in the Bioreduction of NC

The FTIR spectrum of the *Pistacia lentiscus* leaf extract (Figure I.13 (a)) exhibited broad absorption bands in the range of 3200–3700 cm^{-1}, attributed to the O–H stretching vibrations commonly found in phenolic compounds [86]. These peaks confirm the presence of bioactive molecules such as polyphenols and flavonoids [87], which play a vital role in the bioreduction and stabilization of Mn_3O_4 nanoparticles. Additionally, a prominent peak at 1215 cm^{-1} was observed, corresponding to the C=O stretching vibrations, further indicating the presence of organic compounds in the extract [87].

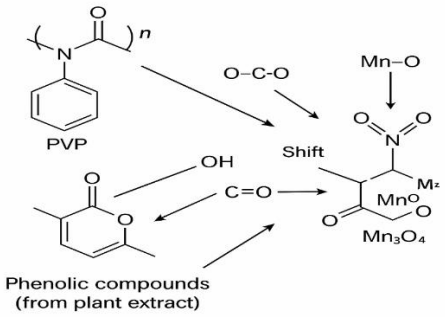

Figure I. 12: Proposed Molecular Interactions Between Mn_3O_4, PVP, and Plant-Derived Phenolics

Table I. 2: FTIR-Identified Functional Group Shifts Upon Composite Formation

Functional Group	**Pure Component (cm^{-1})**	**Composite (cm^{-1})**	**Shift**
Mn–O	468, 594	496, 642	+28, +48
O–C–O	1425	1411	–14
OH (broad)	3200–3700	3200–3500	slight

The FTIR spectrum of Mn_3O_4 NPs (Figure I.13(b)) displayed characteristic peaks at 468 cm^{-1} and 594 cm^{-1}, which are attributed to Mn–O stretching vibrations [88], confirming the successful formation of Mn_3O_4 [89]. A band related to O–H bending vibrations was also present, supporting the interaction of hydroxyl groups with the nanoparticle surface [90].

In the case of PVP (Figure I.13(d)), the key absorption bands included a broad peak at 1683 cm^{-1} corresponding to O–H stretching vibrations [91], a peak at 1425 cm^{-1} due to the

asymmetric stretching of O–C–O groups [92], and a peak at 2954 cm^{-1} assigned to C–H stretching vibrations [88][93].

The FTIR spectrum of the Mn_3O_4/PVP nanocomposite (Figure I.13(c)) showed a combination of characteristic peaks from both Mn_3O_4 and PVP. Notably, the Mn–O stretching bands shifted from 468 cm^{-1} and 594 cm^{-1} to 496 cm^{-1} and 642 cm^{-1} [89], respectively, indicating interactions between the Mn_3O_4 nanoparticles and the PVP matrix [94][57]. Furthermore, the O–C–O stretching peak shifted from 1425 cm^{-1} to 1411 cm^{-1}, reinforcing the evidence of successful surface modification of Mn_3O_4 by PVP [90] [94]. These spectral shifts confirm the effective integration of PVP onto the surface of Mn_3O_4 nanoparticles, enhancing the nanocomposite's structural stability and functional performance, especially in photocatalytic applications.

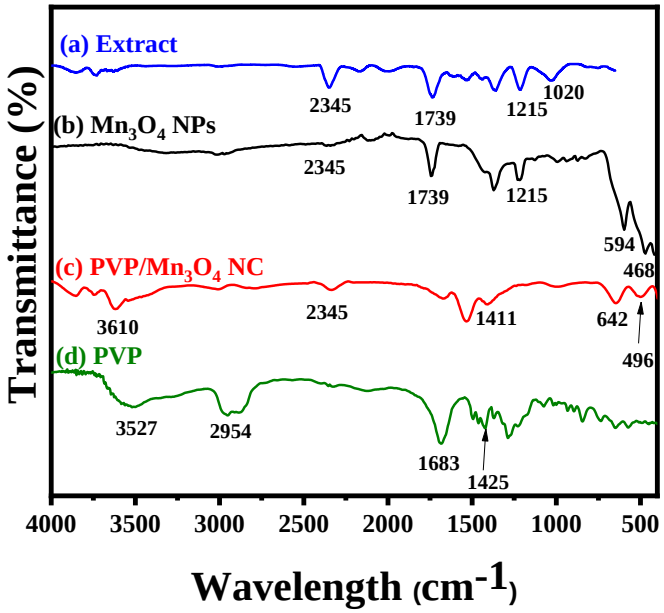

Figure I. 13: FT-IR Spectral Analysis of Pistacia lentiscus Leaf Extract, Mn_3O_4 Nanoparticles, Mn_3O_4/PVP Nanocomposite, and Pure PVP [57]

3.4. Optical Properties and Bandgap Analysis (UV-Vis)

The optical properties of Mn_3O_4 NPs and Mn_3O_4/PVP NC were examined using UV-Vis spectrophotometry over a wavelength range of 200–800 nm. The absorption spectra provided critical insights into the electronic structure and optical behavior of the synthesized materials. As shown in Figure I.14, the Mn_3O_4 NPs displayed a prominent

absorption peak at 305 nm, a characteristic feature confirming the successful formation of nanoparticles.

In contrast, the absorption spectrum of the Mn_3O_4/PVP NC exhibited a higher-intensity peak with a noticeable red shift in the maximum absorption wavelength to 319 nm [57]. This shift in the absorption edge indicated successful modification of Mn_3O_4 with PVP, which enhanced its light-harvesting capabilities, particularly in the visible region.

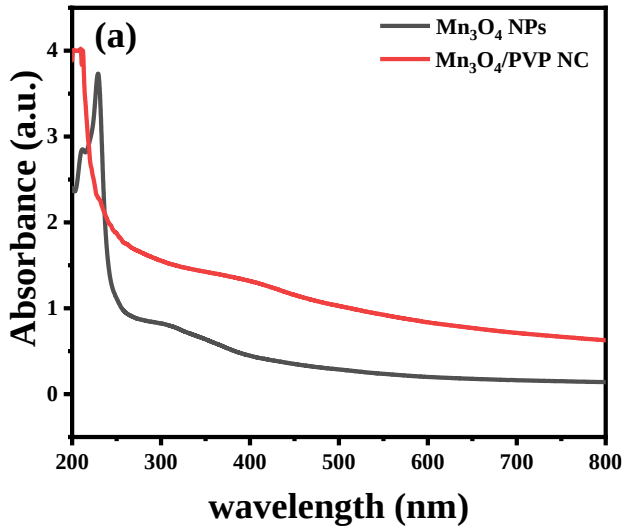

Figure I. 14: UV–Vis spectra of Mn3O4 NPs and Mn3O4/PVP NC

The bandgap energy of Mn_3O_4 NPs was calculated by plotting the Tauc equation against photon energy (hν), yielding an estimated bandgap of 1.8 eV. This value aligns with the semiconducting nature of Mn_3O_4, making it suitable for photocatalytic applications. However, as illustrated in Figure I.15, the Mn_3O_4/PVP NC exhibited a reduced bandgap of 1.0 eV [57]. This significant reduction can be attributed to the interaction between PVP and Mn_3O_4, which likely caused shifts in the valence and conduction bands [95]. Such shifts enhance carrier-carrier interactions and increase the density of localized states within the bandgap, ultimately reducing the optical energy gap [96].

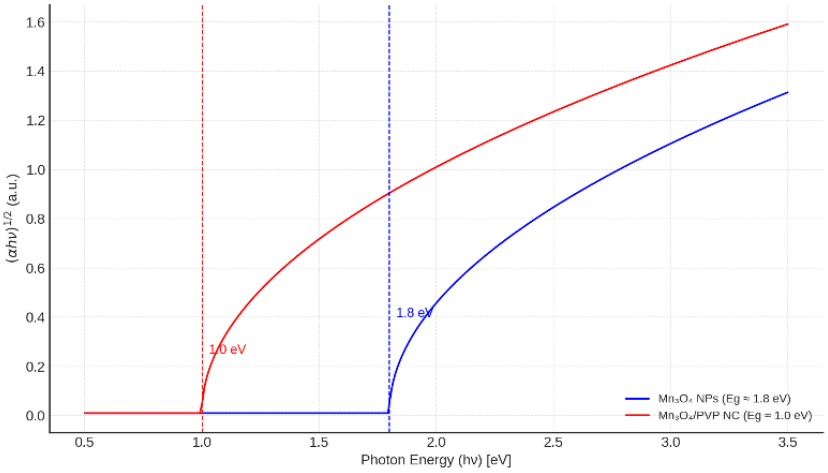

Figure I. 15: Tauc Plot for Mn3O4 NPs and Mn3O4/PVP NC

The reduced bandgap energy suggests that Mn_3O_4/PVP NC can efficiently utilize a broader range of the solar spectrum, thereby enhancing its photocatalytic performance. The indirect bandgap was calculated using the Tauc method, further validating the improved optical properties of Mn_3O_4/PVP NC for potential environmental and energy applications [57].

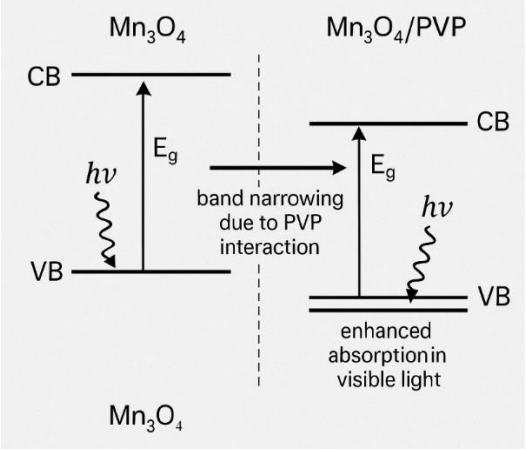

Figure I. 16: Schematic Illustration of Bandgap Narrowing in Mn_3O_4/PVP Nanocomposites Compared to Pure Mn_3O_4

4. Photocatalytic Performance Evaluation

4.1. Influence of Irradiation Time on Dye Degradation

This investigation assessed the time-dependent photocatalytic performance of Mn_3O_4 NPs and Mn_3O_4/PVP NC for the degradation of o-toluidine and bromophenol blue under natural sunlight. The experimental results revealed that while Mn_3O_4 NPs were moderately

effective in degrading o-toluidine, achieving a degradation efficiency of 61%, their performance against BPB was limited to only 14%. In contrast, the Mn_3O_4/PVP nanocomposite demonstrated significantly enhanced photocatalytic activity, with removal efficiencies of 91% for o-toluidine and 85% for BPB after 75 minutes of exposure [57].

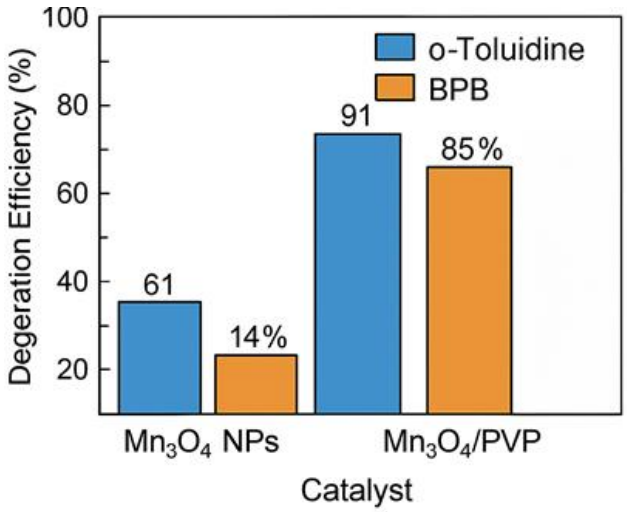

Figure I. 17: Photocatalytic Degradation Efficiency of o-Toluidine and Bromophenol Blue Using Mn_3O_4 NPs and Mn_3O_4/PVP NC after 75 Minutes of Solar Irradiation

To better understand the degradation mechanism, kinetic studies were performed using a pseudo-first-order reaction model [97]

$$\ln\left({}^{A_0}/_{A_t}\right) = t \times k \qquad (4)$$

where the rate constant k characterizes the degradation efficiency with respect to irradiation time t. The calculated rate constants for the Mn_3O_4/PVP NC were 0.0189 min^{-1} for BPB and 0.0046 min^{-1} for o-toluidine, indicating that BPB was degraded more rapidly under the same photocatalytic conditions (Figure I.19).

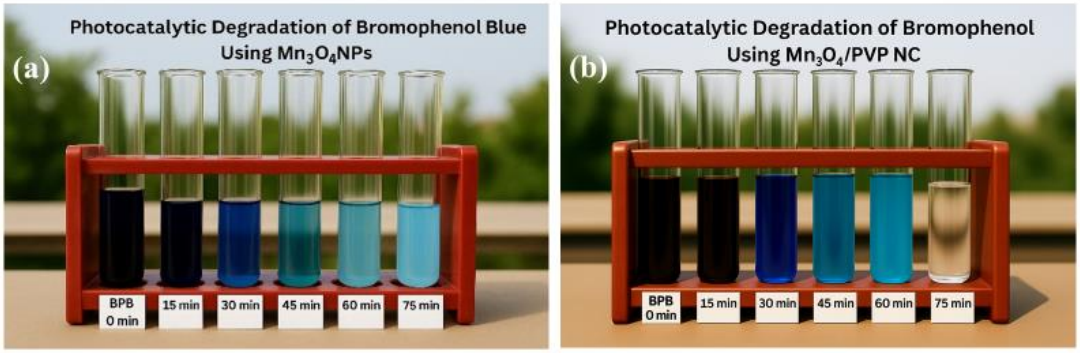

Figure I. 18: Photocatalytic Degradation Over Time of BPB Using **(a)** Mn_3O_4 NP, **(b)** Mn_3O_4/PVP NC

These findings confirm that the Mn_3O_4/PVP NC outperforms bare Mn_3O_4 NPs in terms of both degradation efficiency and reaction kinetics. The enhanced activity can be attributed to improved charge separation [98], extended light absorption, and increased surface area facilitated by the presence of PVP [51]. Thus, time-dependent analysis supports the superior photocatalytic capability of the nanocomposite in efficiently decomposing organic pollutants under solar irradiation.

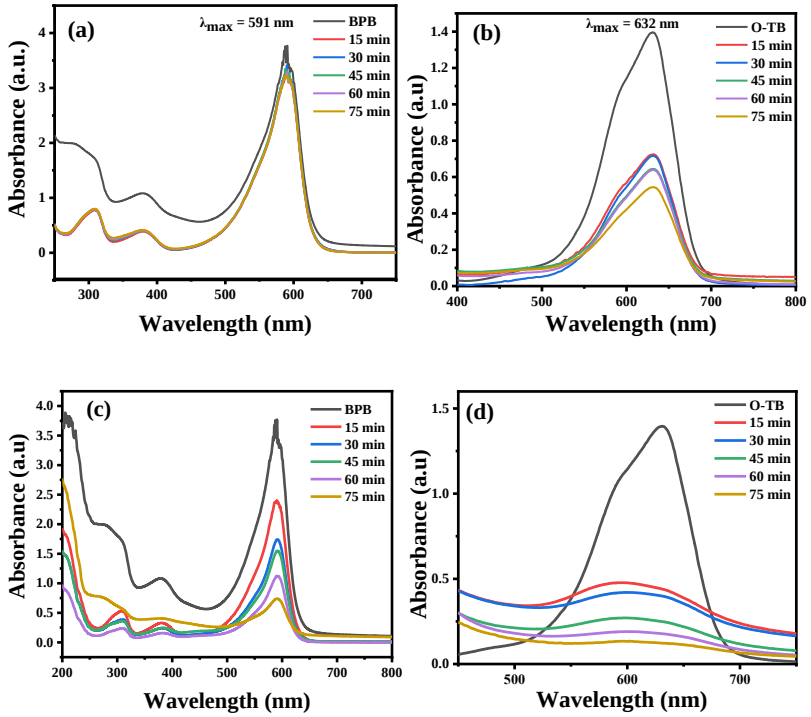

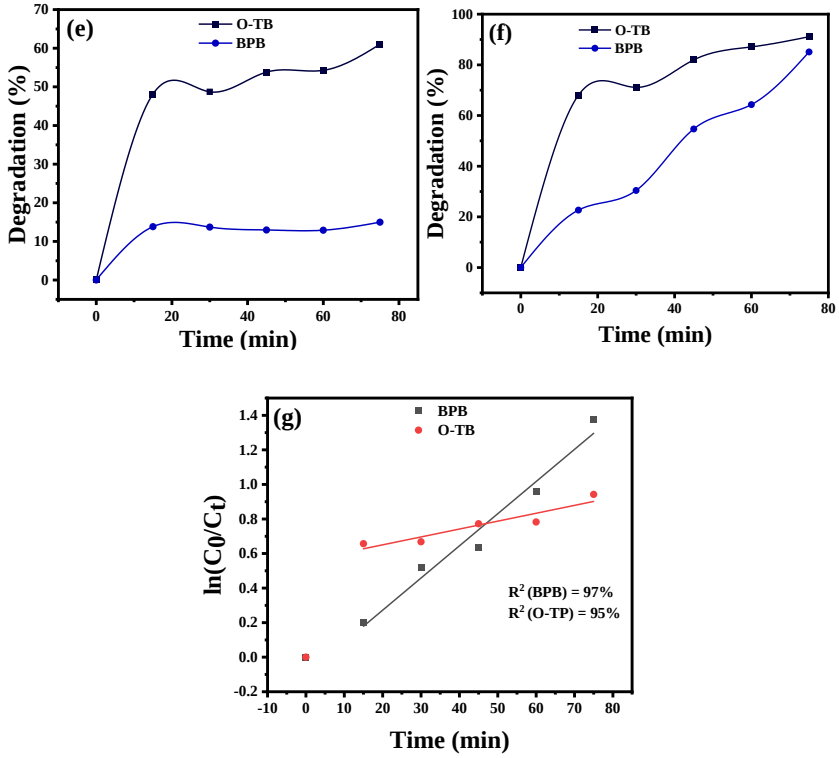

Figure I. 19: Photodegradation efficiency versus reaction time: UV-vis spectra for degradation of **(a,b)** BPB dye and **(c,d)** O-TB dye using Mn3O4 NPs and Mn3O4/PVP NC, respectively. The degradation rate of BPB and TB using **(e)** Mn3O4 NPs and **(f)** Mn3O4/PVP NC. **(g)** First-order kinetic plot of $ln(\frac{A_0}{A_t})$ versus time of Mn_3O_4/PVP nanocomposites in the ddegradation of BPB and O-TB [57]-

4.2. Catalyst Mass Optimization Study

An optimization study was conducted to evaluate the impact of catalyst dosage on the degradation efficiency of organic dyes using Mn_3O_4 NPs and Mn_3O_4/PVP NC, as illustrated in Figure I.6. The experiments were performed under constant irradiation time (75 minutes) to isolate the effect of mass variation.

The findings demonstrated that the Mn_3O_4/PVP NC exhibited superior photocatalytic performance at an optimized dose of 7.5 mg. At this dosage, the nanocomposite achieved a degradation efficiency of 95.75% for o-toluidine and 86% for BPB. In comparison, an equal mass of unmodified Mn_3O_4 NPs yielded a lower removal rate of 81% for o-toluidine and showed negligible activity toward BPB degradation [57].

These results underscore the enhanced photocatalytic capability of the Mn_3O_4/PVP NC, which can be attributed to the synergistic effect of PVP in improving dye adsorption, charge separation, and reactive species generation. The presence of PVP likely contributes to better surface stabilization and improved electron transfer dynamics.

Moreover, the study highlights that catalyst mass optimization exerts a more significant influence on dye degradation efficiency than variation in irradiation time alone. This suggests that controlling the photocatalyst dosage is a critical parameter for maximizing the degradation rate of organic pollutants in photocatalytic treatment systems [57].

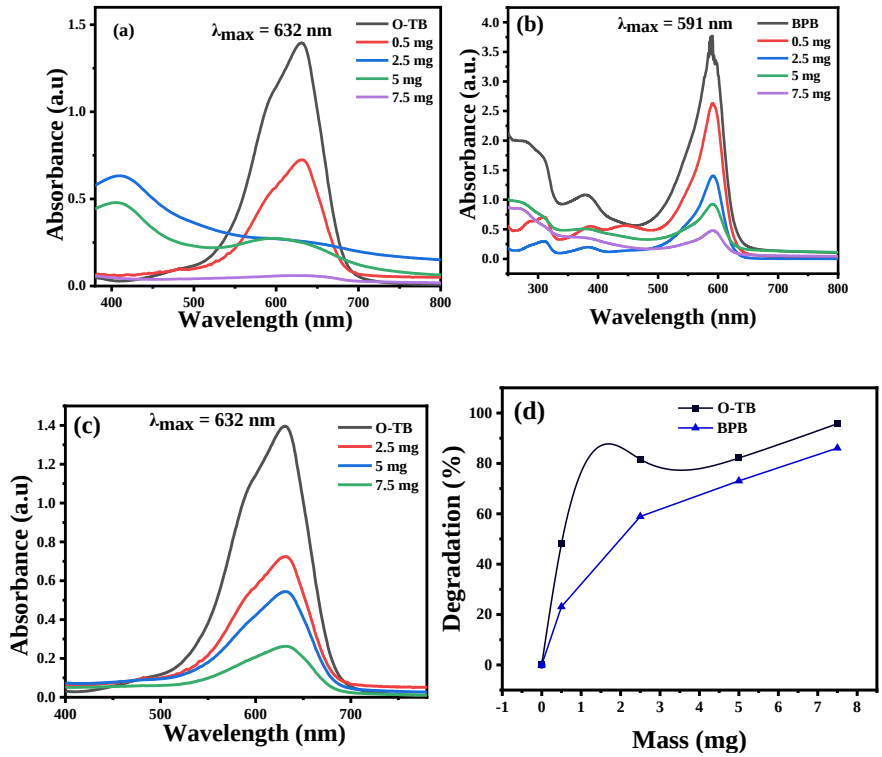

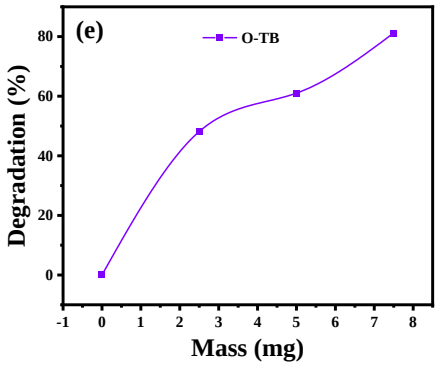

Figure I. 20: Photodegradation efficiency of catalyst versus mass: UV-vis spectra for degradation of **(a)** O-TB dye and **(b)** BPB dye using Mn3O4/PVP NC and **(c)** O-TB dye using Mn3O4 NPs. The degradation rate of BP and O-TB using **(d)** Mn3O4/PVP NC and **(e)** Mn3O4 NPs [57]

4.3. Recyclability and Structural Stability of the Catalyst

The reusability of a photocatalyst is a key factor in evaluating its practicality for sustainable water treatment applications [99][92]. To investigate the recyclability of the Mn_3O_4/PVP nanocomposite, the photocatalyst was recovered, dried, and subjected to subsequent photocatalytic degradation experiments under identical conditions to the initial cycle. The photocatalytic performance across five successive cycles is illustrated in Figure I.21(a, b).

The results revealed that the Mn_3O_4/PVP photocatalyst maintained excellent degradation efficiency for both BPB and O-TB dyes throughout the cycling process [57]. Although a slight decrease in photocatalytic activity was observed dropping from 85.09% to 83.07% for BPB and from 91% to 89% for O-TB this minor decline may be attributed to material losses during recovery processes [100] (e.g., centrifugation and washing) or the accumulation of intermediate degradation products on the catalyst surface [101].

Structural stability was further verified through X-ray diffraction analysis, as shown in Figure 21(c). The XRD patterns of the Mn_3O_4/PVP nanocomposite remained consistent before and after five photocatalytic cycles, confirming that the crystal structure was preserved. These findings collectively demonstrate the high durability, recyclability, and structural integrity of the Mn_3O_4/PVP nanocomposite, making it a promising candidate for long-term photocatalytic applications [57].

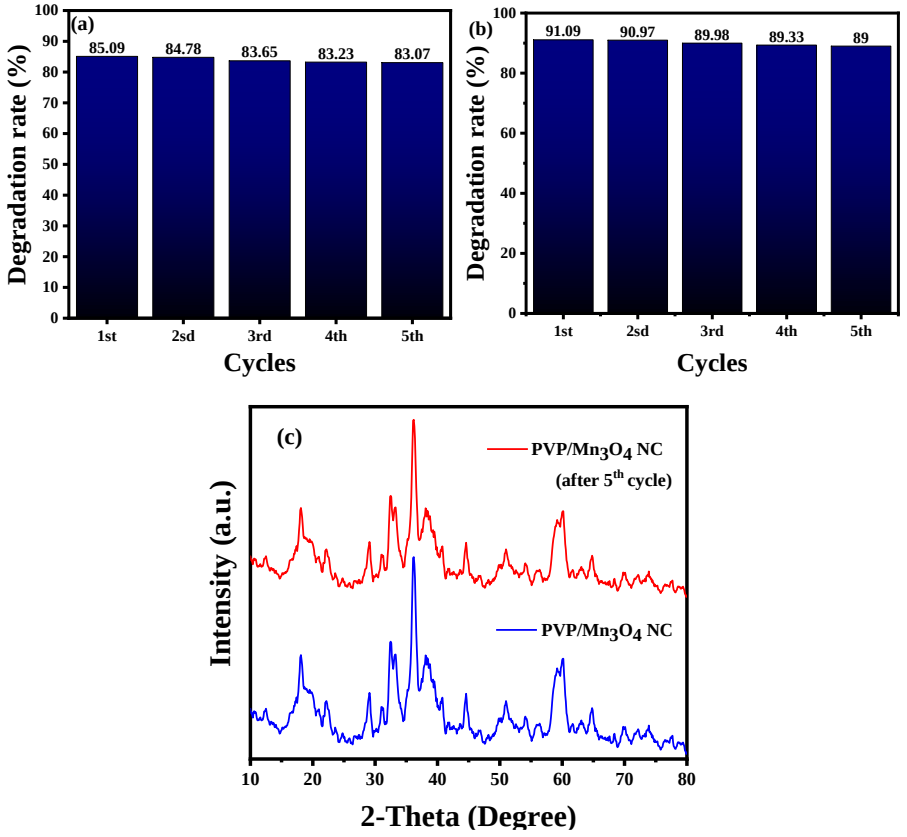

Figure I. 21: Recyclability of the Mn_3O_4/PVP photocatalyst for degradation of **(a)** BPB, and **(b)** O-TB dyes. **(c)** XRD analysis of Mn_3O_4/PVP of pure and reused [57].

5. Mechanistic and Computational Insights

5.1. Proposed Photocatalytic Degradation Mechanism

Figure I.22 presents the proposed photocatalytic degradation mechanism of BPB and O-TB dyes facilitated by Mn_3O_4/PVP NC under solar irradiation. Semiconductor nanoparticles, when exposed to oxygen or atmospheric air, exhibit the capability to degrade various organic pollutants due to their unique surface chemistry [102]. Upon irradiation with photons (hν), the PVP-functionalized Mn_3O_4 becomes photoactivated, leading to the generation of electron-hole (e^-/h^+) pairs that act as effective reducing and oxidizing agents, respectively [57].

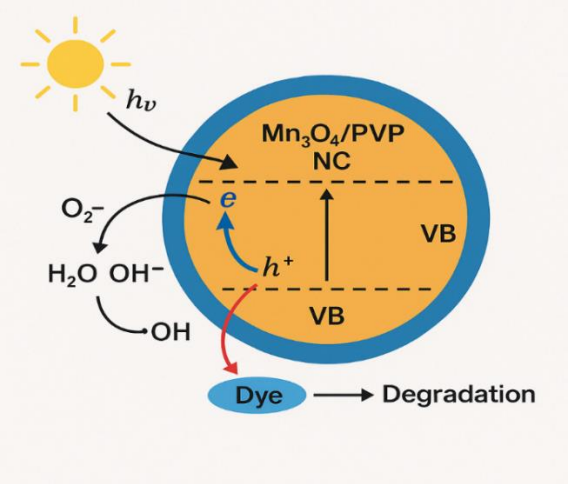

Figure I. 22: presents the proposed photocatalytic degradation mechanism of BPB and O-TB using NC

Following excitation, electrons transition from the lowest unoccupied molecular orbital (LUMO) of PVP to the conduction band (CB) of Mn_3O_4, while the corresponding holes migrate from the valence band (VB) of Mn_3O_4 to the highest occupied molecular orbital (HOMO) of PVP. These photogenerated electrons reduce molecular oxygen (O_2) adsorbed on the catalyst surface, forming superoxide anion radicals (O_2^-) [103][104]. Concurrently, the holes interact with surface hydroxyl (OH^-) groups, generating highly reactive hydroxyl radicals (·OH) [105]. These radicals play a central role in the oxidative degradation of dye molecules, breaking them down into harmless byproducts such as carbon dioxide and water [106][57].

In addition to radical-mediated oxidation, dye molecules that are physically adsorbed onto the surface of the Mn_3O_4/PVP NC may also undergo direct oxidation by photogenerated holes [107]. The series of reactions involved in the degradation process is represented by Equations (5–11), providing insight into the multiple pathways contributing to the enhanced photocatalytic performance of the nanocomposite system [57].

$$Mn_3O_4/PVP \xrightarrow{h\upsilon} e^-_{(CB)} + h^+_{(VB)} \quad (5)$$

A superoxide radical anion is formed

$$e^-_{(CB)} + O_2 \longrightarrow O_2^{\bullet -} \quad (6)$$

Neutralization of OH^- group into OH by the hole

$$h^+_{(VB)} + H_2O \longrightarrow H^+ + OH^- \quad (7)$$

$$H^+ + O_2^{\bullet -} \longrightarrow HO_2^{\bullet} \quad (8)$$

$$HO_2^{\bullet} + HO_2^{\bullet} \longrightarrow H_2O_2 + O_2 \quad (9)$$

$$H_2O_2 \xrightarrow{h\upsilon} 2OH^{\bullet} \quad (10)$$

$$\text{Dyes} + OH \longrightarrow \text{degradation product} + CO_2 + H_2O \quad (11)$$

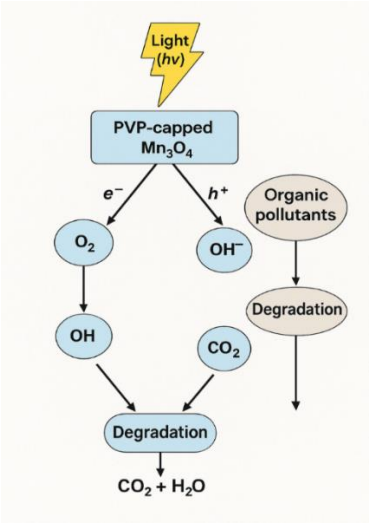

Figure I. 23: Possible mechanism for BPB and O-TB dyes degradation under sunlight irradiation using Mn_3O_4/PVP nanocomposite

5.2. Adsorption Behavior and Binding Affinity

Adsorption plays a crucial role in the removal of dye pollutants from wastewater using nanostructured photocatalysts. In this study, the interaction of dye molecules with Mn_3O_4 and Mn_3O_4/PVP nanocomposites was computationally investigated to better understand

their adsorption characteristics. As illustrated in Figure I.24, optimized monolayers of both materials were analyzed for their ability to bind with dye molecules such as o-toluidine (O-TP) and bromophenol blue (BPB).

Adsorption refers to the accumulation of adsorbate molecules on the surface of a solid material (adsorbent) through physical or chemical interactions [108]. At the nanoscale, this process is enhanced due to a higher surface-to-volume ratio and the presence of unsatisfied bonding sites on nanoparticle surfaces [109][110]. Unlike bulk materials, where atomic bonding requirements are generally fulfilled by adjacent atoms, surface atoms in nanomaterials remain partially coordinated, increasing their reactivity and adsorption potential [111].

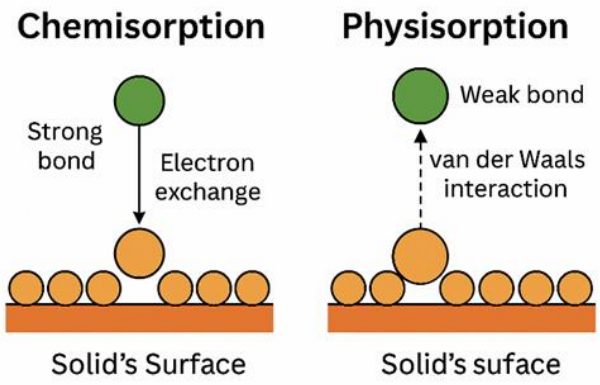

Figure I. 24: Adsorption types

The mechanism of adsorption can generally be classified into two types: physisorption [112], which involves weak van der Waals forces [113], and chemisorption [114], which entails stronger interactions such as hydrogen bonding, electrostatic attraction [115], or covalent bonding. The nature of the interaction depends on both the surface chemistry of the nanocomposite and the functional groups of the dye molecules [112], as depicted in Figure I.25.

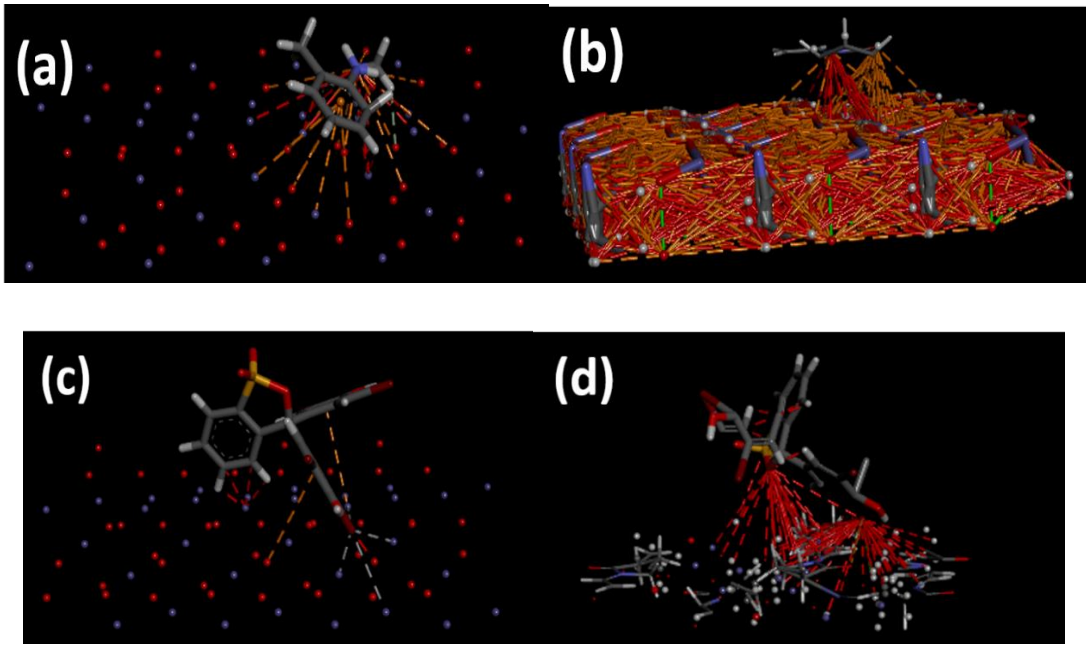

Figure I. 25: The adsorption of various dyes on the optimized Mn_3O_4 monolayer **(a)** O-TP. The adsorption of various dyes on the optimized **(c)** BPB and Mn_3O_4/PVP monolayer **(b)** O-TP and **(d)** BPB [94]

The incorporation of polyvinylpyrrolidone (PVP) into the nanocomposite structure significantly enhances surface functionality by increasing the number of available active sites and promoting stronger binding with dye molecules [116][117]. This is evident from the comparative adsorption behavior shown in Figure I.24, where Mn_3O_4/PVP demonstrates superior dye affinity and surface coverage relative to bare Mn_3O_4. The calculated adsorption energies (E_ad), which quantify the strength of interaction, further support this enhancement. For Mn_3O_4, the E_ad values were –399.404 eV for BPB and –122.007 eV for O-TB, whereas for Mn_3O_4/PVP, the values increased in magnitude to –427.359 eV and –125.514 eV [94], respectively (Figure I.26).

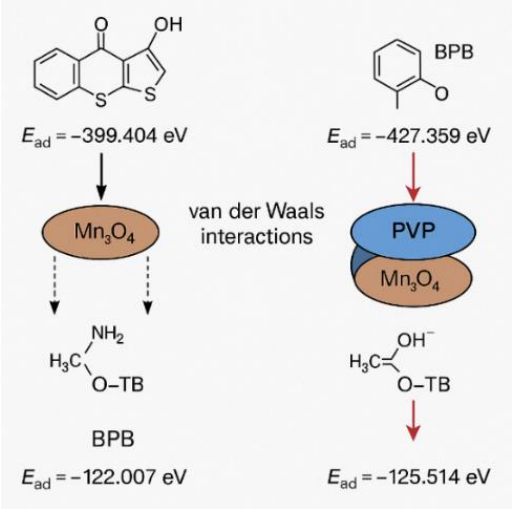

Figure I. 26: Schematic Representation of Dye Adsorption on Mn_3O_4 and Mn_3O_4/PVP Nanocomposites with Corresponding Adsorption Energies (E_ad)

These findings suggest that Mn_3O_4/PVP nanocomposites provide more stable and energetically favorable adsorption sites, likely due to improved surface chemistry and polymer-assisted dispersion [57]. Figure I.27 presents the optimized dye adsorption configurations, highlighting the enhanced interactions achieved through PVP functionalization.

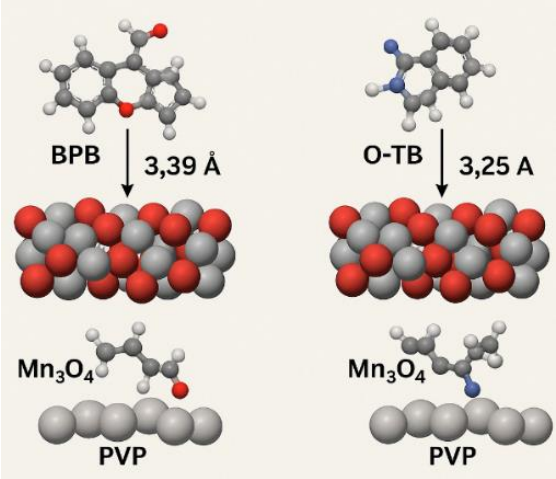

Figure I. 27: Adsorption configuration of dye

The adsorption behavior of the nanocomposite could potentially be modulated by altering the type of incorporated metal oxide [117]. The computational findings presented here are

consistent with the experimental observations, thereby validating the enhanced adsorption capacity of the Mn_3O_4/PVP system [94].

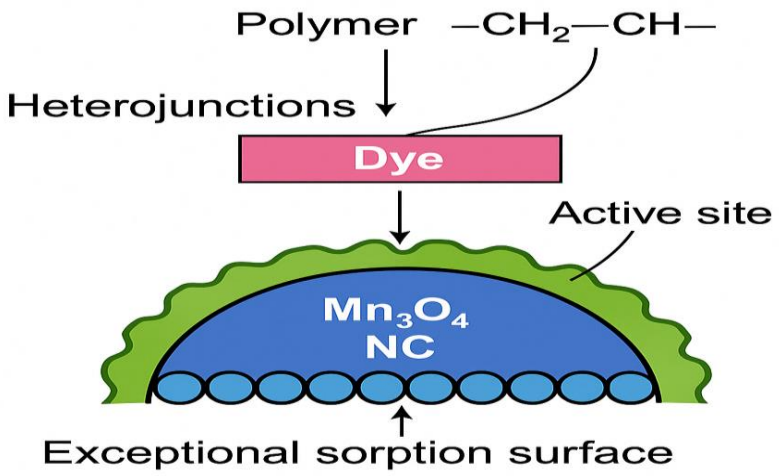

Figure I. 28: The general mechanism of dyes adsorption on the Mn_3O_4 NC surface

6. Environmental and Practical Considerations

6.1. Environmental Benefits of Green Synthesis

The adoption of green synthesis routes for nanomaterials offers substantial environmental advantages over traditional chemical methods [26]. In this study, the use of *Pistacia lentiscus* leaf extract as a natural reducing and stabilizing agent exemplifies a sustainable approach to nanoparticle fabrication [94]. This method eliminates the need for hazardous reagents, reduces toxic byproducts, and minimizes energy input by operating under mild temperature conditions [118][119]. Moreover, the bioactive compounds inherent in the plant extract promote efficient reduction and stabilization [120], enhancing the environmental compatibility and functional properties of the resulting Mn_3O_4/PVP nanocomposite [94]. Such practices align with green chemistry principles, supporting safer material synthesis and contributing to the mitigation of environmental pollution associated with industrial nanomaterial production [121][122].

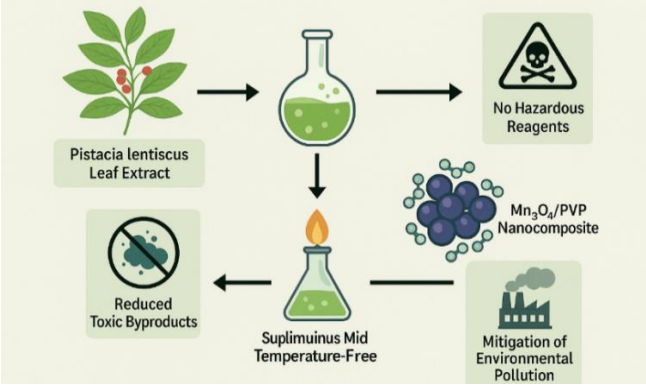

Figure I. 29: Environmental Benefits of Green Synthesis

6.2. Cost and Material Availability Assessment

A critical advantage of the proposed synthesis method lies in its economic feasibility and accessibility of raw materials [122]. The key components *Pistacia lentiscus* leaves, manganese nitrate, and polyvinylpyrrolidone are readily available and inexpensive, making the process scalable and cost-effective [109]. The plant extract is sourced from local, renewable biomass, reducing dependency on imported or synthetic chemicals [123]. Additionally, the synthesis is conducted in aqueous media, eliminating the need for costly organic solvents [121]. These attributes not only lower the overall production cost but also facilitate technology transfer to resource-limited settings [124]. The simplicity of the preparation protocol further enhances its potential for broad application in environmental remediation [109].

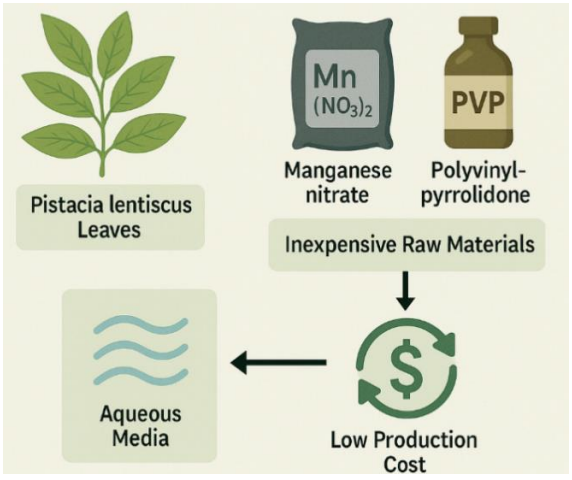

Figure I. 30: Cost and Material Availability Assessment

6.3. Limitations and Scalability Potential

Despite the promising results demonstrated by Mn_3O_4/PVP nanocomposites, several limitations must be addressed before large-scale deployment [94]. One constraint is the variability in phytochemical composition of plant extracts, which can lead to batch-to-batch inconsistencies in nanoparticle properties [125]. Additionally, while the process is suitable for laboratory-scale synthesis, scaling up may require optimization of reaction kinetics, extraction protocols, and post-synthesis treatments to maintain reproducibility and uniformity [126]. Another challenge lies in ensuring efficient recovery and reuse of the nanocomposites without performance degradation. Nevertheless, the process holds significant scalability potential, particularly if integrated with automated synthesis platforms and standardized green extract formulations [127]. Addressing these factors could enable the widespread use of eco-friendly nanomaterials in real-world wastewater treatment applications [58].

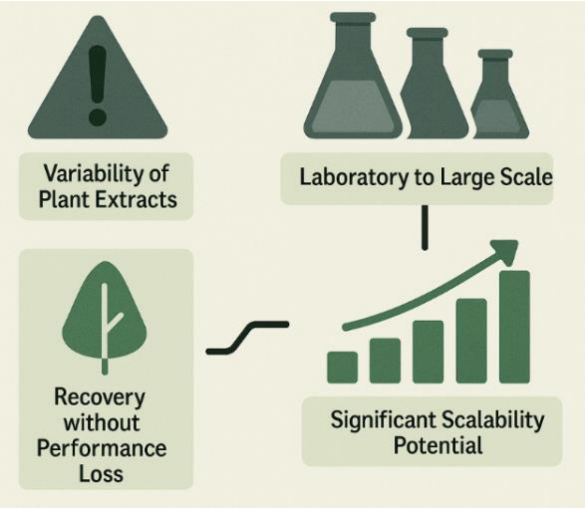

Figure I. 31: Limitations and Scalability Potential

7. Conclusion

This chapter presented a comprehensive study on the green synthesis, characterization, and photocatalytic performance of Mn_3O_4/PVP nanocomposites using *Pistacia lentiscus* leaf extract as a natural reducing agent. The synthesized Mn_3O_4/PVP nanocomposite exhibited remarkable physicochemical and photocatalytic enhancements compared to bare Mn_3O_4 nanoparticles. Structural analysis revealed that the crystallite size increased slightly from **37 nm** for Mn_3O_4 NPs to **45 nm** for Mn_3O_4/PVP NC due to polymer surface encapsulation. UV–Vis spectroscopy showed a distinct red shift in absorption from **305 nm** (Mn_3O_4 NPs) to **319 nm** (Mn_3O_4/PVP NC), accompanied by a substantial narrowing of the optical bandgap from **1.8 eV** to **1.0 eV**, confirming enhanced visible-light absorption.

Photocatalytic evaluation demonstrated the superior activity of the Mn_3O_4/PVP NC under natural sunlight, achieving **91% degradation of o-toluidine blue (O-TB)** and **85% degradation of bromophenol blue (BPB)** within **75 minutes**, while bare Mn_3O_4 NPs showed only **61% (O-TB)** and **14% (BPB)** removal under identical conditions. Kinetic analysis followed a pseudo-first-order model, with rate constants (**k**) of **0.0189 min^{-1}** for BPB and **0.0046 min^{-1}** for O-TB using Mn_3O_4/PVP NC. The optimized catalyst dosage of **7.5 mg** resulted in maximum degradation efficiencies of **95.75% (O-TB)** and **86% (BPB)**, emphasizing the role of catalyst loading in achieving optimal performance.

Reusability tests confirmed the excellent stability of the Mn_3O_4/PVP NC, retaining **over 89%** degradation efficiency for O-TB and **83%** for BPB after **five successive cycles**, with no observable structural change in XRD patterns. Molecular modeling supported these results, showing higher adsorption energies for Mn_3O_4/PVP (–427.36 eV for BPB and –125.51 eV for O-TB) compared to pure Mn_3O_4 (–399.40 eV and –122.01 eV, respectively), validating the strong dye–catalyst interactions and improved surface reactivity.

Collectively, these results confirm that the polymer-assisted green synthesis significantly enhances photocatalytic activity, stability, and reusability of Mn_3O_4-based systems. This environmentally benign and scalable strategy bridges the gap between sustainable synthesis and real-world wastewater treatment, contributing to the advancement of eco-friendly nanomaterials for pollution control.

Future research should focus on scaling up synthesis by standardizing extract composition and exploring advanced photophysical studies (e.g., reactive species quantification and time-resolved photoluminescence). Further, applying Mn_3O_4/PVP NC to real wastewater matrices and emerging pollutants will expand its environmental applicability and establish its potential for large-scale sustainable remediation.

References

[1] M. Ismail *et al.*, "Pollution, toxicity and carcinogenicity of organic dyes and their catalytic bio-remediation," *Curr. Pharm. Des.*, vol. 25, no. 34, pp. 3645–3663, 2019.

[2] U. Shanker, M. Rani, and V. Jassal, "Degradation of hazardous organic dyes in water by nanomaterials," *Environ. Chem. Lett.*, vol. 15, pp. 623–642, 2017.

[3] S. H. Chien and W. R. Clayton, "Application of Elovich equation to the kinetics of phosphate release and sorption in soils," *Soil Sci. Soc. Am. J.*, vol. 44, no. 2, pp. 265–268, 1980.

[4] H. Ben Slama *et al.*, "Diversity of synthetic dyes from textile industries, discharge impacts and treatment methods," *Appl. Sci.*, vol. 11, no. 14, p. 6255, 2021.

[5] Z. Carmen and S. Daniela, *Textile organic dyes-characteristics, polluting effects and separation/elimination procedures from industrial effluents-a critical overview*, vol. 3. IntechOpen Rijeka, 2012.

[6] E. Routoula and S. V Patwardhan, "Degradation of anthraquinone dyes from effluents: a review focusing on enzymatic dye degradation with industrial potential," *Environ. Sci. Technol.*, vol. 54, no. 2, pp. 647–664, 2020.

[7] R. Bhateria and D. Jain, "Water quality assessment of lake water: a review," *Sustain. water Resour. Manag.*, vol. 2, no. 2, pp. 161–173, 2016.

[8] D.-P. Häder, H. D. Kumar, R. C. Smith, and R. C. Worrest, "Effects on aquatic ecosystems," *J. Photochem. Photobiol. B Biol.*, vol. 46, no. 1–3, pp. 53–68, 1998.

[9] D.-P. Häder *et al.*, "Effects of UV radiation on aquatic ecosystems and interactions with other environmental factors," *Photochem. Photobiol. Sci.*, vol. 14, no. 1, pp. 108–126, 2015.

[10] R. Al-Tohamy *et al.*, "A critical review on the treatment of dye-containing wastewater: Ecotoxicological and health concerns of textile dyes and possible remediation approaches for environmental safety," *Ecotoxicol. Environ. Saf.*, vol. 231, p. 113160, 2022.

[11] S. Bala *et al.*, "Recent strategies for bioremediation of emerging pollutants: a review for a green and sustainable environment," *Toxics*, vol. 10, no. 8, p. 484, 2022.

[12] A. K. Singh, M. Bilal, H. M. N. Iqbal, A. S. Meyer, and A. Raj, "Bioremediation of lignin derivatives and phenolics in wastewater with lignin modifying enzymes: Status, opportunities and challenges," *Sci. Total Environ.*, vol. 777, p. 145988, 2021.

[13] S. Y. Choy, K. M. N. Prasad, T. Y. Wu, M. E. Raghunandan, and R. N. Ramanan, "Utilization of plant-based natural coagulants as future alternatives towards sustainable water clarification," *J. Environ. Sci.*, vol. 26, no. 11, pp. 2178–2189, 2014.

[14] M. D. Khan, A. Singh, M. Z. Khan, S. Tabraiz, and J. Sheikh, "Current perspectives, recent advancements, and efficiencies of various dye-containing wastewater treatment technologies," *J. Water Process Eng.*, vol. 53, p. 103579, 2023.

[15] A. P. Periyasamy, "Recent advances in the remediation of textile-dye-containing wastewater: prioritizing human health and sustainable wastewater treatment," *Sustainability*, vol. 16, no. 2, p. 495, 2024.

[16] V. Katheresan, J. Kansedo, and S. Y. Lau, "Efficiency of various recent wastewater dye removal methods: A review," *J. Environ. Chem. Eng.*, vol. 6, no. 4, pp. 4676–4697, 2018.

[17] A. K. D. Alsukaibi, "Various approaches for the detoxification of toxic dyes in wastewater," *Processes*, vol. 10, no. 10, p. 1968, 2022.

[18] H. M. Solayman *et al.*, "Performance evaluation of dye wastewater treatment technologies: A review," *J. Environ. Chem. Eng.*, vol. 11, no. 3, p. 109610, 2023.

[19] R. Rashid, I. Shafiq, P. Akhter, M. J. Iqbal, and M. Hussain, "A state-of-the-art review on wastewater treatment techniques: the effectiveness of adsorption method," *Environ. Sci. Pollut. Res.*, vol. 28, pp. 9050–9066, 2021.

[20] G. Bal and A. Thakur, "Distinct approaches of removal of dyes from wastewater: A review," *Mater. Today Proc.*, vol. 50, pp. 1575–1579, 2022.

[21] X. Fang *et al.*, "Geochemistry of heavy metal-contaminated sediments from the Four River inlets of Dongting lake, China," *Environ. Sci. Pollut. Res.*, vol. 28, pp. 27593–27613, 2021.

[22] I. Zinicovscaia, "Conventional methods of wastewater treatment," *Cyanobacteria for bioremediation of wastewaters*, pp. 17–25, 2016.

[23] C. Adams, Y. Wang, K. Loftin, and M. Meyer, "Removal of antibiotics from surface and distilled water in conventional water treatment processes," *J. Environ. Eng.*, vol. 128, no. 3, pp. 253–260, 2002.

[24] P. V. Nidheesh, C. Couras, A. V Karim, and H. Nadais, "A review of integrated advanced oxidation processes and biological processes for organic pollutant removal," *Chem. Eng. Commun.*, vol. 209, no. 3, pp. 390–432, 2022.

[25] W. A. H. Altowayti *et al.*, "The role of conventional methods and artificial intelligence in the wastewater treatment: a comprehensive review," *Processes*, vol. 10, no. 9, p. 1832, 2022.

[26] D. Kirubakaran *et al.*, "A comprehensive review on the green synthesis of nanoparticles: advancements in biomedical and environmental applications," *Biomed. Mater. Devices*, pp. 1–26, 2025.

[27] A. Thakur and A. Kumar, "Innovative Technologies for the Removal of Pollutants in the Chemical Industries," in *Innovative and Hybrid Technologies for Wastewater*

Treatment and Recycling, CRC Press, 2024, pp. 167–195.

[28] D. Chen *et al.*, "Photocatalytic degradation of organic pollutants using TiO2-based photocatalysts: A review," *J. Clean. Prod.*, vol. 268, p. 121725, 2020.

[29] M. M. Mahlambi, C. J. Ngila, and B. B. Mamba, "Recent developments in environmental photocatalytic degradation of organic pollutants: the case of titanium dioxide nanoparticles—a review," *J. Nanomater.*, vol. 2015, no. 1, p. 790173, 2015.

[30] Y. Chen *et al.*, "Unravelling the role of free radicals in photocatalysis," *Chem. Eur. J.*, vol. 30, no. 29, p. e202400001, 2024.

[31] S. Mohd and A. M. Khan, "Heterogeneous photocatalysis: Recent advances and applications," *Sustain. Green Catal. Process.*, pp. 141–163, 2024.

[32] V. Takhar and S. Singh, "Nanomaterials ROS: a comprehensive review for environmental applications," *Environ. Sci. Nano*, 2025.

[33] L. H. Madkour, "Function of reactive oxygen species (ROS) inside the living organisms and sources of oxidants," *Pharm. Sci. Anal. Res. J*, vol. 2, p. 180023, 2019.

[34] L. Z. Flores-López, H. Espinoza-Gómez, and R. Somanathan, "Silver nanoparticles: Electron transfer, reactive oxygen species, oxidative stress, beneficial and toxicological effects. Mini review," *J. Appl. Toxicol.*, vol. 39, no. 1, pp. 16–26, 2019, doi: 10.1002/jat.3654.

[35] B. A. Omran and K.-H. Baek, "Valorization of agro-industrial biowaste to green nanomaterials for wastewater treatment: Approaching green chemistry and circular economy principles," *J. Environ. Manage.*, vol. 311, p. 114806, 2022.

[36] S. K. Ali *et al.*, "Electrochemical and photocatalytic synthesis of organic compounds utilizing a greener approach. a review," *Mol. Catal.*, vol. 559, p. 114087, 2024.

[37] U. Habib *et al.*, "Sustainable catalysis: navigating challenges and embracing opportunities for a greener future," *J. Chem. Env.*, vol. 2, no. 2, pp. 14–53, 2023.

[38] P. Kulasekaran, G. Sivasubramanian, D. Kannaiyan, and P. Deivanayagam, "Manganese Oxide Decorated Functionalized Multiwalled Carbon Nanotube-Supported Sulfonated (Poly Ether Ether Sulfone) Membranes for H2-O2 Fuel Cell," *Polym. Technol. Mater.*, pp. 1–10, 2025.

[39] B. Debnath, "Synthesis, Characterization, Low Temperature Magnetic Interactions and Catalytic Properties of Transition Metal-Oxide Nanostructures." Indian Institute of Science Education and Research Kolkata, 2019.

[40] M. R. Krishnendu, D. Mehta, and S. Singh, "CeO_2 and Mn_3O_4-based nanozymes exhibit scavenging of singlet oxygen species and hydroxyl radicals," *Nanoscale*, 2025.

[41] T. Hong and F. Xue, "Investigation on Manganese (Mn^2+/Mn^3+)-Vanadium (V^2+/V^3+) Redox Flow Battery," in *2009 Asia-Pacific Power and Energy Engineering Conference*, IEEE, 2009, pp. 1–4.

[42] C.-Y. Chiang Jr, "Electron microscopic studies of crystal growth and defects in inorganic solids." University of St Andrews, 2017.

[43] N. Njomo, "Synthesis of sulphonated and transition metal oxide doped polymeric nanocomposites for application in design of supercapacitors," 2011.

[44] G. Liu, C. Zhen, Y. Kang, L. Wang, and H.-M. Cheng, "Unique physicochemical properties of two-dimensional light absorbers facilitating photocatalysis," *Chem. Soc. Rev.*, vol. 47, no. 16, pp. 6410–6444, 2018.

[45] I. Ahmad, M. A. Aftab, A. Fatima, S. D. Mekkey, S. Melhi, and S. Ikram, "A comprehensive review on the advancement of transition metals incorporated on functional magnetic nanocomposites for the catalytic reduction and photocatalytic degradation of organic pollutants," *Coord. Chem. Rev.*, vol. 514, p. 215904, 2024.

[46] T. Banerjee, F. Podjaski, J. Kröger, B. P. Biswal, and B. V Lotsch, "Polymer photocatalysts for solar-to-chemical energy conversion," *Nat. Rev. Mater.*, vol. 6, no. 2, pp. 168–190, 2021.

[47] M. Julinová, L. Vaňharová, and M. Jurča, "Water-soluble polymeric xenobiotics–Polyvinyl alcohol and polyvinylpyrrolidon–And potential solutions to environmental issues: A brief review," *J. Environ. Manage.*, vol. 228, pp. 213–222, 2018.

[48] P. Franco and I. De Marco, "The Use of Poly (N-vinyl pyrrolidone) in the Delivery of Drugs: A Review," *Polymers (Basel).*, vol. 12, no. 5, p. 1114, 2020.

[49] L. Saravanan, R. M. Kumar, A. Pandurangan, and R. Jayavel, "Synthesis and photophysical studies of PVP capped Titania Nanostrips for photocatalytic applications," *J. Optoelectron. Adv. Mater.*, vol. 4, pp. 1676–1680, 2010.

[50] Q. Feng *et al.*, "Polyvinylpyrrolidone assisted transformation of Cu-MOF into N/P-co-doped Octahedron carbon encapsulated Cu3P nanoparticles as high performance anode for lithium ion batteries," *J. Colloid Interface Sci.*, vol. 608, pp. 227–238, 2022.

[51] K. M. Koczkur, S. Mourdikoudis, L. Polavarapu, and S. E. Skrabalak, "Polyvinylpyrrolidone (PVP) in nanoparticle synthesis," *Dalt. Trans.*, vol. 44, no. 41, pp. 17883–17905, 2015.

[52] M. Saraswat and R. J. Sengwa, "Effects of PVP surfactant on nanosuspension stability and optical, dielectric, and rheological properties of zinc oxide nanoparticles dispersed alcohols mixture based nanofluids," *J. Mol. Liq.*, vol. 385, p. 122350, 2023.

[53] Z. Sun, T. Liao, and L. Kou, "Strategies for designing metal oxide nanostructures,"

Sci. China Mater, vol. 60, no. 1, pp. 1–24, 2017.

[54] K. Singh, Nancy, M. Bhattu, G. Singh, N. M. Mubarak, and J. Singh, "Light-absorption-driven photocatalysis and antimicrobial potential of PVP-capped zinc oxide nanoparticles," *Sci. Rep.*, vol. 13, no. 1, p. 13886, 2023.

[55] K. Kumari *et al.*, "Effect of PVP Assisted Growth of α-Mn2O3 Nanoparticles on the Structural, Microstructural, Magnetic and Optical Properties," *J. Electron. Mater.*, vol. 51, no. 10, pp. 5842–5856, 2022.

[56] J. Shen, L. Liu, W. Huang, and K. Wu, "Polyvinylpyrrolidone-assisted solvent exfoliation of black phosphorus nanosheets and electrochemical sensing of p-nitrophenol," *Anal. Chim. Acta*, vol. 1167, p. 338594, 2021.

[57] C. Salmi, M. Souhaila, L. Salah Eddine, H. A. M. Mohammed, G. G. Hasan, and M. S. Mahboub, "Biosynthesis of Mn3O4/PVP nanocomposite for enhanced photocatalytic degradation of organic dyes under sunlight irradiation," *J. Clust. Sci.*, pp. 1–15, 2023.

[58] S. Iravani, "Green synthesis of metal nanoparticles using plants," *Green Chem.*, vol. 13, no. 10, pp. 2638–2650, 2011.

[59] L. Natrayan, G. Janardhan, V. S. Nadh, C. Srinivas, S. Kaliappan, and G. Velmurugan, "Eco-friendly zinc oxide nanoparticles from Moringa oleifera leaf extract for photocatalytic and antibacterial applications," *Clean Technol. Environ. Policy*, pp. 1–13, 2024.

[60] C. Kalaiyarasi, M. Poonkothai, S. Abirami, M. Alaguprathana, N. Marraiki, and N. S. S. Zaghloul, "Zinc oxide nanoparticles fabrication using Moringa oleifera Lam. seed extract—Impact on phytotoxic, photocatalytic, and antimicrobial activities," *Appl. Nanosci.*, vol. 13, no. 3, pp. 2187–2197, 2023.

[61] S. Shahzadi, S. Fatima, Z. Shafiq, and M. R. S. A. Janjua, "A review on green synthesis of silver nanoparticles (SNPs) using plant extracts: a multifaceted approach in photocatalysis, environmental remediation, and biomedicine," *RSC Adv.*, vol. 15, no. 5, pp. 3858–3903, 2025.

[62] R. Haddi, A. M. El Kharraz, and M. I. Kerroumi, "Green Synthesis of Zinc Oxide Nanoparticles Using Pistacia lentiscus L. Leaf Extact and Evaluating their Antioxydant and Antibacterial Properties.," *Nano Biomed. Eng.*, vol. 16, no. 2, 2024.

[63] K. Mohamed, K. Zine, K. Fahima, E. Abdelfattah, S. M. Sharifudin, and K. Duduku, "NiO nanoparticles induce cytotoxicity mediated through ROS generation and impairing the antioxidant defense in the human lung epithelial cells (A549): Preventive effect of Pistacia lentiscus essential oil," *Toxicol. reports*, vol. 5, pp. 480–488, 2018.

[64] G. A. El-Chaghaby and A. F. Ahmad, "Biosynthesis of silver nanoparticles using

Pistacia lentiscus leaves extract and investigation of their antimicrobial effect," *Orient. J. Chem.*, vol. 27, no. 3, p. 929, 2011.

[65] R. Golabiazar, K. I. Othman, K. M. Khalid, D. H. Maruf, S. M. Aulla, and P. A. Yusif, "Green synthesis, characterization, and investigation antibacterial activity of silver nanoparticles using Pistacia atlantica leaf extract," *Bionanoscience*, vol. 9, no. 2, pp. 323–333, 2019.

[66] S. Meneceur *et al.*, "Removal Efficiency of Heavy Metals, Oily in Water, Total Suspended Solids, and Chemical Oxygen Demand from Industrial Petroleum Wastewater by Modern Green Nanocomposite Methods," *J. Environ. Chem. Eng.*, p. 111209, 2023, doi: https://doi.org/10.1016/j.jece.2023.111209.

[67] H. A. Mohammed, S. E. Laouini, S. Meneceur, C. Salmi, and M. M. Husein, "MgO/Ni Nanocomposite and its PVP-modified Derivative for Catalytic CO2 Methanation and Photocatalytic Hydrogen Production," *Surfaces and Interfaces*, p. 104643, 2024.

[68] E. Karezani, A. Hallajisani, and M. Asgarpour Khansary, "A quantum mechanics/molecular mechanics (QM/MM) investigation on the mechanism of adsorptive removal of heavy metal ions by lignin: single and competitive ion adsorption," *Cellulose*, vol. 24, pp. 3131–3143, 2017.

[69] S. Mollazadeh, A. Sahebkar, M. Shahlaei, and S. Moradi, "Nano drug delivery systems: Molecular dynamic simulation," *J. Mol. Liq.*, vol. 332, p. 115823, 2021.

[70] J. Li *et al.*, "In-situ investigation of dye pollutant adsorption performance on graphitic carbon nitride surface: ATR spectroscopy experiment and MD simulation insight," *J. Hazard. Mater.*, vol. 418, p. 126297, 2021.

[71] N. Aguilar *et al.*, "Theoretical multiscale study on the properties, aqueous solution behavior and biological impact of zinc oxide nanoparticles," *Surfaces and Interfaces*, vol. 46, p. 103965, 2024.

[72] M. A. Saghiri, R. S. Saini, M. S. Kuruniyan, S. A. Mosaddad, and A. Heboyan, "Graphene and its modifications for enhanced adhesion in dental restoratives: a molecular docking and dynamics study," *Sci. Rep.*, vol. 15, no. 1, p. 9455, 2025.

[73] S. Fredericks, K. Parrish, D. Sayre, and Q. Zhu, "PyXtal: A Python library for crystal structure generation and symmetry analysis," *Comput. Phys. Commun.*, vol. 261, p. 107810, 2021.

[74] A. Z. El-Sonbati *et al.*, "Supramolecular structure, molecular docking and thermal properties of azo dye complexes," *J. Mol. Liq.*, vol. 212, pp. 487–502, 2015.

[75] M. Butkiewicz *et al.*, "Benchmarking ligand-based virtual High-Throughput Screening with the PubChem database," *Molecules*, vol. 18, no. 1, pp. 735–756, 2013.

[76] M. Nagaoka, Y. Ohta, and H. Hitomi, "Theoretical characterization of coordination

space: Adsorption state and behavior of small molecules in nanochanneled metal-organic frameworks via electronic state theory, molecular mechanical and Monte Carlo simulation," *Coord. Chem. Rev.*, vol. 251, no. 21–24, pp. 2522–2536, 2007.

[77] E. Ustinov, "Kinetic Monte Carlo approach for molecular modeling of adsorption," *Curr. Opin. Chem. Eng.*, vol. 24, pp. 1–11, 2019.

[78] Y. L. Jeyachandran, E. Mielczarski, B. Rai, and J. A. Mielczarski, "Quantitative and qualitative evaluation of adsorption/desorption of bovine serum albumin on hydrophilic and hydrophobic surfaces," *Langmuir*, vol. 25, no. 19, pp. 11614–11620, 2009.

[79] A. Bouafia *et al.*, "Removal of hydrocarbons and heavy metals from petroleum water by modern green nanotechnology methods," *Sci. Rep.*, vol. 13, no. 1, p. 5637, 2023.

[80] H. A. Mohammed *et al.*, "Efficient Removal of Heavy Metals, Dyes, and Contaminants from Industrial Wastewater Using Chitosan-Coated Fe3O4 Nanocomposites: Biosynthesis, Characterizations, and Performance Evaluation," *Biomass Convers. Biorefinery*, pp. 1–16, 2024.

[81] I. Kir, S. E. Laouini, S. Meneceur, A. Bouafia, and H. A. M. Mohammed, "Biosynthesis and characterization of novel nanocomposite ZnO/BaMg2 efficiency for high-speed adsorption of AZO dye," *Biomass Convers. Biorefinery*, pp. 1–10, 2023.

[82] M. Khan *et al.*, "Plant extracts as green reductants for the synthesis of silver nanoparticles: Lessons from chemical synthesis," *Dalt. Trans.*, vol. 47, no. 35, pp. 11988–12010, 2018.

[83] M. Ovais *et al.*, "Role of plant phytochemicals and microbial enzymes in biosynthesis of metallic nanoparticles," *Appl. Microbiol. Biotechnol.*, vol. 102, pp. 6799–6814, 2018.

[84] S. Choudhary, "Characterization of amorphous silica nanofiller effect on the structural, morphological, optical, thermal, dielectric and electrical properties of PVA–PVP blend based polymer nanocomposites for their flexible nanodielectric applications," *J. Mater. Sci. Mater. Electron.*, vol. 29, no. 12, pp. 10517–10534, 2018.

[85] C. Salmi, S. E. Laouini, S. Meneceur, and H. A. Mohammed, "Biosynthesized MgO@ SnO2 nanocomposite and their modification with polyvinylpyrrolidone. Efficiency for removal of heavy metals and contaminants from industrial petroleum wastewater," *Clean Technol. Environ. Policy*, pp. 1–20, 2024.

[86] K. T. Arulmozhi and N. Mythili, "Studies on the chemical synthesis and characterization of lead oxide nanoparticles with different organic capping agents," *AIP Adv.*, vol. 3, no. 12, 2013.

[87] C. Lakshmi, B. D. P. Raju, T. Madhavi, and N. J. Sushma, "Identification of bioactive compounds by FTIR analysis and in vitro antioxidant activity of Clitoria ternatea leaf and flower extracts," *Indo Am. J. Pharm. Res.*, vol. 4, no. 9, pp. 3894–3903, 2014.

[88] A. Vázquez-Olmos *et al.*, "One-step synthesis of Mn3O4 nanoparticles: Structural and magnetic study," *J. Colloid Interface Sci.*, vol. 291, no. 1, pp. 175–180, 2005.

[89] M. R. Shaik *et al.*, "Mn3O4 nanoparticles: Synthesis, characterization and their antimicrobial and anticancer activity against A549 and MCF-7 cell lines," *Saudi J. Biol. Sci.*, vol. 28, no. 2, pp. 1196–1202, 2021.

[90] J. Sackey *et al.*, "Molecular dynamics and bio-synthesis of phoenix dactylifera mediated Mn3O4 nanoparticles: Electrochemical application," *J. Alloys Compd.*, vol. 854, p. 156987, 2021.

[91] M. Sadiq, M. M. H. Raza, S. K. Chaurasia, M. Zulfequar, and J. Ali, "Studies on flexible and highly stretchable sodium ion conducting blend polymer electrolytes with enhanced structural, thermal, optical, and electrochemical properties," *J. Mater. Sci. Mater. Electron.*, vol. 32, no. 14, pp. 19390–19411, 2021.

[92] V. K. Yadav *et al.*, "Synthesis and characterization of mullites from silicoaluminous fly ash waste," *Int. J. Appl. Nanotechnol. Res.*, vol. 5, no. 1, pp. 10–25, 2020.

[93] Z. Jiang, C. Hu, S. M. Easa, X. Zheng, and Y. Zhang, "Evaluation of physical, rheological, and structural properties of vulcanized EVA/SBS modified bitumen," *J. Appl. Polym. Sci.*, vol. 134, no. 21, 2017.

[94] C. Salmi, M. Souhaila, L. Salah Eddine, H. A. M. Mohammed, G. G. Hasan, and M. S. Mahboub, "Biosynthesis of Mn3O4/PVP nanocomposite for enhanced photocatalytic degradation of organic dyes under sunlight irradiation," *J. Clust. Sci.*, vol. 35, no. 1, pp. 201–215, 2024.

[95] K. M. Singh, A. B. Jha, R. S. Dubey, and P. Sharma, "Nanoparticle-mediated mitigation of salt stress-induced oxidative damage in plants: insights into signaling, gene expression, and antioxidant mechanisms," *Environ. Sci. Nano*, 2025.

[96] M. H. Patel, T. K. Chaudhuri, V. K. Patel, T. Shripathi, U. Deshpande, and N. P. Lalla, "Dip-coated PbS/PVP nanocomposite films with tunable band gap," *RSC Adv.*, vol. 7, no. 8, pp. 4422–4429, 2017.

[97] H. A. Mohammed, L. S. Eddine, M. Souhaila, G. G. Hasan, I. Kir, and J. A. A. Abdullah, "Green synthesis of SnO2 nanoparticles from Laurus nobilis L. extract for enhanced gelatin-based films and CEF@ SnO2 for efficient antibacterial activity," *Food Bioprocess Technol.*, vol. 17, no. 5, pp. 1364–1382, 2024.

[98] Y. Li, Z. Wang, B. Huang, Y. Dai, X. Zhang, and X. Qin, "Synthesis of BiOBr-PVP hybrids with enhanced adsorption-photocatalytic properties," *Appl. Surf. Sci.*, vol. 347, pp. 258–264, 2015.

[99] M. Amoli-Diva, A. Anvari, and R. Sadighi-Bonabi, "Synthesis of magneto-plasmonic Au-Ag NPs-decorated TiO2-modified Fe3O4 nanocomposite with enhanced laser/solar-driven photocatalytic activity for degradation of dye pollutant in textile wastewater," *Ceram. Int.*, vol. 45, no. 14, pp. 17837–17846, 2019.

[100] M. F. El-Berry, S. A. Sadeek, A. M. Abdalla, and M. Y. Nassar, "Microwave-assisted fabrication of copper nanoparticles utilizing different counter ions: An efficient photocatalyst for photocatalytic degradation of safranin dye from aqueous media," *Mater. Res. Bull.*, vol. 133, p. 111048, 2021.

[101] A. B. Ali Baig, V. Rathinam, and V. Ramya, "Facile fabrication of Zn-doped SnO 2 nanoparticles for enhanced photocatalytic dye degradation performance under visible light exposure," *Adv. Compos. Hybrid Mater.*, vol. 4, pp. 114–126, 2021.

[102] N. Soltani *et al.*, "Photocatalytic degradation of methylene blue under visible light using PVP-capped ZnS and CdS nanoparticles," *Sol. Energy*, vol. 97, pp. 147–154, 2013.

[103] N. Suganthi, S. Thangavel, and K. Kannan, "Hibiscus subdariffa leaf extract mediated 2-D fern-like ZnO/TiO2 hierarchical nanoleaf for photocatalytic degradation," *FlatChem*, vol. 24, p. 100197, 2020.

[104] S. Nachimuthu *et al.*, "Lawsonia inermis mediated synthesis of ZnO/Fe2O3 nanorods for photocatalysis – Biological treatment for the enhanced effluent treatment, antibacterial and antioxidant activities," *Chem. Phys. Lett.*, vol. 804, p. 139907, Oct. 2022, doi: 10.1016/j.cplett.2022.139907.

[105] A. S. Priya, D. Geetha, K. Karthik, and M. Rajamoorthy, "Investigations on the enhanced photocatalytic activity of (Ag, La) substituted nickel cobaltite spinels," *Solid State Sci.*, vol. 98, p. 105992, 2019.

[106] K. Kannan *et al.*, "Photocatalytic and antimicrobial properties of microwave synthesized mixed metal oxide nanocomposite," *Inorg. Chem. Commun.*, vol. 125, p. 108429, 2021.

[107] M. Dudita, C. Bogatu, A. Enesca, and A. Duta, "The influence of the additives composition and concentration on the properties of SnOx thin films used in photocatalysis," *Mater. Lett.*, vol. 65, no. 14, pp. 2185–2189, 2011.

[108] J.-J. Huang, C.-C. Lin, and D.-S. Wuu, "Antireflection and passivation property of titanium oxide thin film on silicon nanowire by liquid phase deposition," *Surf. Coatings Technol.*, vol. 320, pp. 252–258, 2017.

[109] J. Han, X. Liu, J. Yue, B. Xi, S. Gao, and G. Xu, "Catalytic upgrading of in situ coal pyrolysis tar over Ni-char catalyst with different additives," *Energy & Fuels*, vol. 28, no. 8, pp. 4934–4941, 2014.

[110] K. Micheal *et al.*, "Assembled composite of hematite iron oxide on sponge-like BiOCl with enhanced photocatalytic activity," *Mater. Sci. energy Technol.*, vol. 2,

no. 1, pp. 104–111, 2019.

[111] Y. K. Jo, J. M. Lee, S. Son, and S.-J. Hwang, "2D inorganic nanosheet-based hybrid photocatalysts: Design, applications, and perspectives," *J. Photochem. Photobiol. C Photochem. Rev.*, vol. 40, pp. 150–190, 2019.

[112] M. A. Alsharif, "Understanding Adsorption: Theories, Techniques, and Applications," 2025.

[113] L. W. Bruch, M. W. Cole, and E. Zaremba, *Physical adsorption: forces and phenomena*. Courier Dover Publications, 2007.

[114] O. D. Agboola and N. U. Benson, "Physisorption and chemisorption mechanisms influencing micro (nano) plastics-organic chemical contaminants interactions: a review," *Front. Environ. Sci.*, vol. 9, p. 678574, 2021.

[115] E. G. Söğüt and M. Gülcan, "Adsorption: basics, properties, and classification," in *Adsorption through advanced nanoscale materials*, Elsevier, 2023, pp. 3–21.

[116] M. Ikram *et al.*, "Graphene oxide/polyvinylpyrrolidone-doped MoO3 nanocomposites used for dye degradation and their antibacterial activity: a molecular docking analysis," *Front. Chem.*, vol. 11, p. 1191849, 2023.

[117] A. Bari *et al.*, "Evaluation of bactericidal potential and catalytic dye degradation of multiple morphology based chitosan/polyvinylpyrrolidone-doped bismuth oxide nanostructures," *Nanoscale Adv.*, vol. 4, no. 12, pp. 2713–2728, 2022.

[118] Y. P. Hamedani and M. Hekmati, "Green biosynthesis of silver nanoparticles decorated on multi-walled carbon nanotubes using the extract of Pistacia atlantica leaves as a recyclable heterogeneous nanocatalyst for degradation of organic dyes in water," *Polyhedron*, vol. 164, pp. 1–6, 2019.

[119] E. Milia *et al.*, "Leaves and fruits preparations of Pistacia lentiscus L.: a review on the ethnopharmacological uses and implications in inflammation and infection," *Antibiotics*, vol. 10, no. 4, p. 425, 2021.

[120] S. Boucheffa *et al.*, "Effect of the main constituents of Pistacia lentiscus leaves against the DPPH radical and xanthine oxidase: experimental and theoretical study," *J. Biomol. Struct. Dyn.*, vol. 40, no. 20, pp. 9870–9884, 2022.

[121] F. Kurul, B. Doruk, and S. N. Topkaya, "Principles of green chemistry: building a sustainable future," *Discov. Chem.*, vol. 2, no. 1, p. 68, 2025.

[122] L. M. Gilbertson, J. B. Zimmerman, D. L. Plata, J. E. Hutchison, and P. T. Anastas, "Designing nanomaterials to maximize performance and minimize undesirable implications guided by the Principles of Green Chemistry," *Chem. Soc. Rev.*, vol. 44, no. 16, pp. 5758–5777, 2015.

[123] S. Ahmed, M. Ahmad, B. L. Swami, and S. Ikram, "A review on plants extract mediated synthesis of silver nanoparticles for antimicrobial applications: a green

expertise," *J. Adv. Res.*, vol. 7, no. 1, pp. 17–28, 2016.

[124] S. K. Jha and A. Jha, "Sustainable utilization of renewable plant–based material for the green synthesis of metal nanoparticles," in *Smart Nanosystems-Advances in Research and Practice*, IntechOpen, 2023.

[125] O. V Kharissova, H. V. R. Dias, B. I. Kharisov, B. O. Pérez, and V. M. J. Pérez, "The greener synthesis of nanoparticles," *Trends Biotechnol.*, vol. 31, no. 4, pp. 240–248, 2013.

[126] M. Nasrollahzadeh, M. Atarod, M. Sajjadi, S. M. Sajadi, and Z. Issaabadi, "Plant-mediated green synthesis of nanostructures: mechanisms, characterization, and applications," in *Interface science and technology*, vol. 28, Elsevier, 2019, pp. 199–322.

[127] A. K. Mittal, Y. Chisti, and U. C. Banerjee, "Synthesis of metallic nanoparticles using plant extracts," *Biotechnol. Adv.*, vol. 31, no. 2, pp. 346–356, 2013.

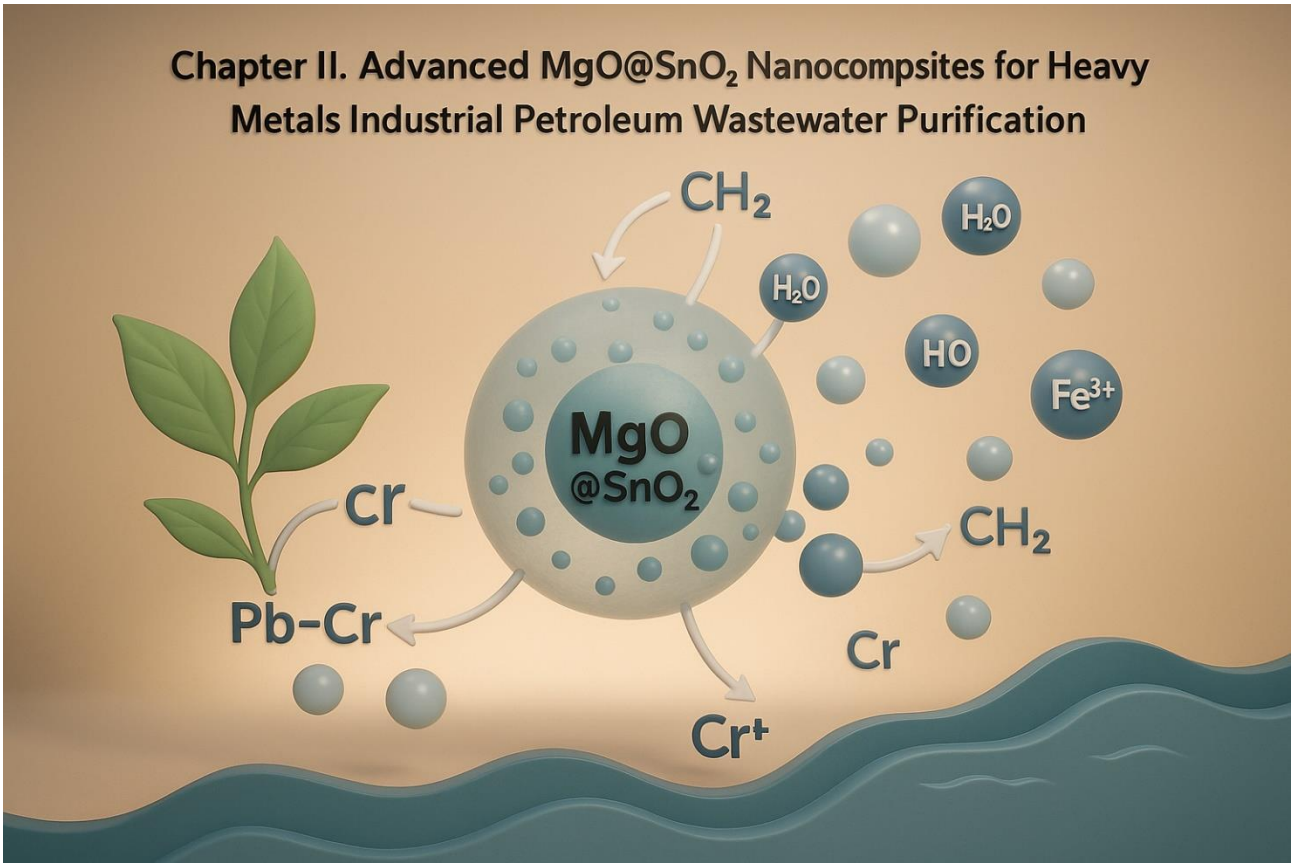
Chapter II. Advanced MgO@SnO2 Nanocompsites for Heavy Metals Industrial Petroleum Wastewater Purification
CH2
H2O
H2O
HO
Fe3+
MgO
@SnO2
Cr
Pb-Cr
CH2
Cr
Cr+

1. Introduction

The exponential growth of industrialization [1], particularly within the petroleum sector [2], has intensified the generation of petroleum-contaminated wastewater [3], posing severe environmental and public health risks [4][5]. These effluents typically comprise a complex mixture of pollutants, including heavy metals [6], polycyclic aromatic hydrocarbons [7], aliphatic compounds, surfactants [8], and total suspended solids (TSS) [9]. Their persistence, toxicity [10], and bioaccumulation potential significantly impair aquatic ecosystems [11] and threaten clean water supplies [12][13]. As regulatory standards tighten globally, the need for effective and sustainable treatment technologies for petroleum wastewater becomes increasingly urgent [14][15].

Conventional treatment methods [16] such as coagulation-flocculation [17], membrane filtration, chemical oxidation [18], and biological processes have been widely employed to mitigate such pollution [19][20]. However, these techniques often fall short due to limitations in contaminant specificity, low removal efficiency for recalcitrant compounds, high operational costs, secondary sludge generation [21], and energy-intensive requirements [22][23]. Biological methods are constrained by the non-biodegradable nature of many petroleum-derived pollutants [24][25], while physical treatments suffer from fouling and frequent maintenance demands [26][27]. These challenges underscore the necessity for advanced treatment systems that are both ecologically and economically viable [28].

Nanotechnology [29] offers a transformative platform for environmental remediation [30][31], particularly in the field of water treatment [32][33]. Nanocomposites hybrid materials composed [34] of two or more nanoscale phases have emerged as powerful adsorbents and photocatalysts due to their high surface area [35], tunable porosity, and customizable surface functionalities [36]. A comprehensive review of nanocomposites in water remediation reveals a significant shift toward materials that combine adsorptive and photocatalytic capabilities [37], allowing for dual-action treatment strategies [38][39]. These multifunctional materials offer enhanced selectivity [40], faster reaction kinetics [41], and greater adaptability to complex wastewater systems [42].

Among the most promising classes of nanocomposites are those based on metal oxide nanostructures [43], such as magnesium oxide (MgO) [43] and tin dioxide (SnO_2) [44]. MgO is renowned for its basic surface sites [45], high ionic character, and affinity for acidic pollutants [46], including heavy metals [47]. SnO_2, on the other hand, demonstrates strong photocatalytic behavior due to its wide bandgap and high carrier mobility [48]. When integrated into a composite (MgO@SnO_2) [49], these materials exhibit synergistic properties that enhance both adsorption and light-driven catalytic processes [50][51]. Their combined functionality enables the simultaneous removal of metal ions and degradation of organic pollutants under environmentally relevant conditions [48][47].

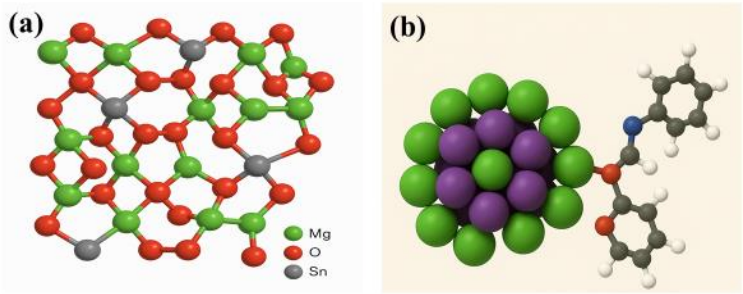

Figure II. 1: Molecular representation **(a)** MgO@SnO_2 NC **(b)** MgO@SnO_2@PVP NC

To further enhance the performance of these nanocomposites, green synthesis techniques utilizing plant extracts and biodegradable polymers have gained momentum [52][53]. These eco-friendly methods eliminate the need for hazardous reagents [54], reduce energy consumption [55], and promote the production of biocompatible, low-toxicity materials [56]. Plant-based extracts [57], such as those derived from *Pistacia lentiscus*, are rich in polyphenols, flavonoids [58], and terpenoids, which act as natural reducing and stabilizing agents during nanoparticle formation [59]. Additionally, the incorporation of water-soluble polymers such as polyvinylpyrrolidone (PVP) serves to stabilize nanoparticles, prevent agglomeration, and introduce functional groups that can actively participate in pollutant adsorption [60]. PVP-modified nanostructures demonstrate improved aqueous dispersibility, surface reactivity, and operational durability characteristics essential for real-world applications [61].

The use of metal oxide nanocomposites also plays a critical role in the removal of heavy metals a major class of pollutants in petroleum wastewater [62][63]. These nanostructures can engage in multiple adsorption mechanisms, including ion exchange [64], surface complexation, electrostatic interaction, and chelation [65], depending on surface chemistry and solution pH. MgO@SnO_2@PVP nanocomposites [66], for instance, provide a high density of active sites for capturing metal ions like Pb^{2+}, Cd^{2+}, and Cr^{6+}, often achieving near-complete removal within short contact times [67].

In addition to adsorption, photocatalytic degradation of organic pollutants [67] using metal oxide nanocomposites has gained significant attention [68][69]. Upon exposure to light, these materials generate reactive oxygen species (ROS) [70], such as hydroxyl and superoxide radicals [71], which oxidize and break down complex organic compounds into benign end-products like CO_2 and H_2O [72][73]. The presence of PVP in the composite not only improves light absorption but also facilitates charge separation [74], thereby enhancing photocatalytic activity under solar or visible-light conditions [75]. This dual-action capability adsorption and photocatalysis makes MgO@SnO_2@PVP nanocomposites exceptionally suited for integrated treatment of petroleum wastewater containing both dissolved metals and persistent organics [66].

Despite these advances, several research gaps remain [76]. First, there is a need for systematic understanding of the interactions between plant-based functional groups and metal oxide surfaces during synthesis [77][78]. Second, while laboratory-scale studies often report excellent performance, scalability, long-term reusability, and environmental impact assessments are not adequately addressed [79]. Additionally, more in-depth mechanistic insights at the molecular level are needed to optimize surface functionalization and active site exposure [80]. The integration of computational simulations [81] with experimental techniques offers a promising avenue to address these gaps by guiding material design and predicting adsorption behavior under varying environmental conditions [82][83].

This chapter therefore focuses on the green synthesis, characterization, and application of MgO@SnO_2@PVP nanocomposites for petroleum wastewater remediation [66]. It

encompasses a review of existing nanocomposite systems, elaborates on the biosynthetic route involving *Pistacia lentiscus* extract, and details experimental evaluations for heavy metal and organic pollutant removal [66]. The chapter also integrates adsorption isotherm modeling, photocatalytic degradation kinetics, and first-principles computational studies to provide a holistic understanding of the material's functionality. Finally, it assesses the economic feasibility, industrial scalability, and environmental sustainability of the proposed treatment system, offering recommendations for future development in this critical area of environmental nanotechnology [66].

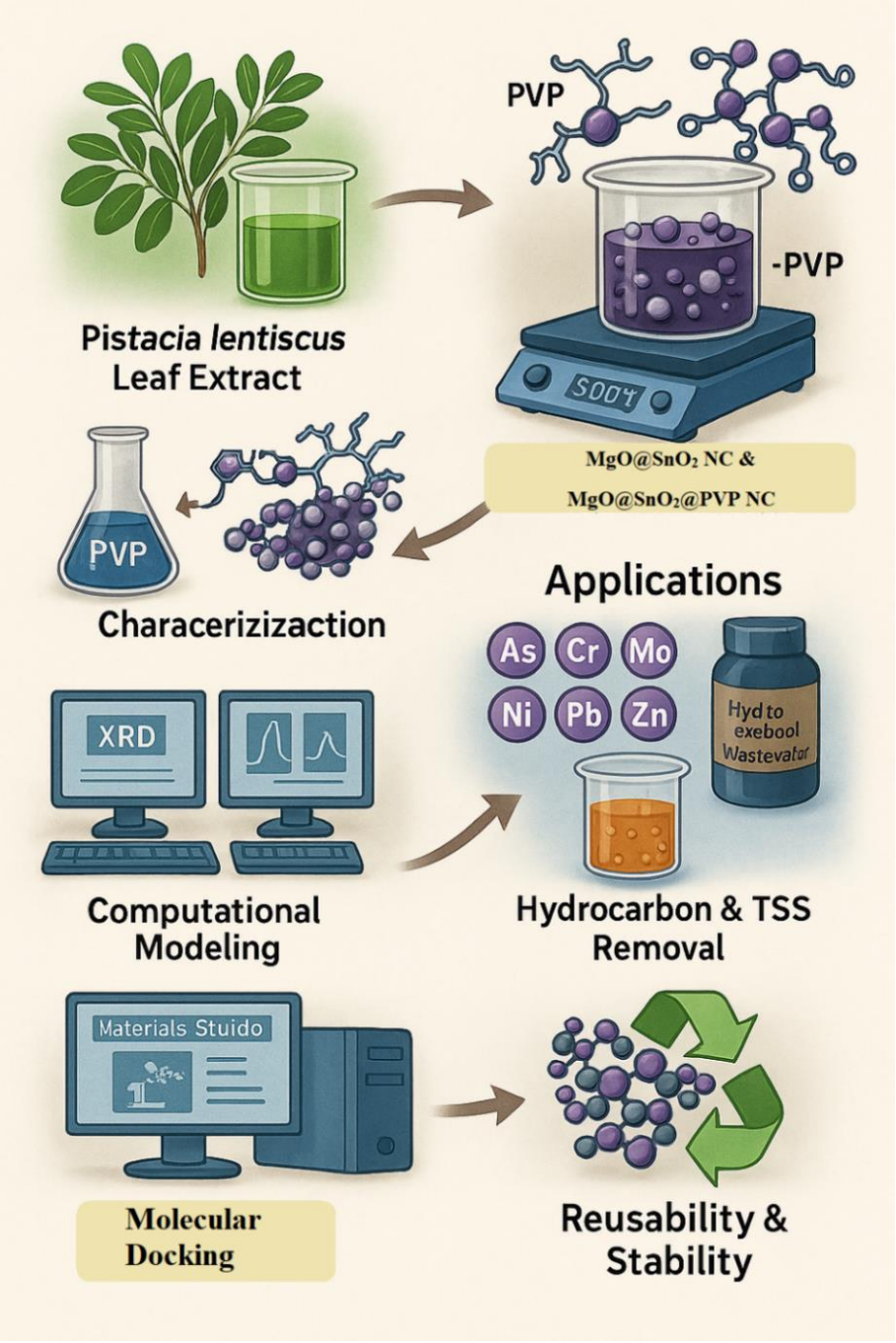

Figure II. 2: Schematic Workflow for the Green Synthesis, Characterization, and Environmental Applications of MgO@SnO₂ & MgO@SnO₂@PVP Nanocomposites

2. Experimental Methodology

2.1. Biosynthesis of MgO@SnO_2 NC

To initiate the green synthesis of nanocomposites, an aqueous extract of *Pistacia lentiscus* leaves was first prepared. The collected leaves were thoroughly washed to eliminate surface impurities and dried in a shaded environment to preserve their phytochemical integrity. Once fully dehydrated, the leaves were ground into a fine powder, and 100 g of this material was infused in 1000 mL of distilled water. The mixture was left to steep at ambient temperature for 24 hours to allow the bioactive compounds to leach into the solution. The resulting extract was filtered and stored for subsequent use in nanomaterial synthesis. Utilizing this extract, the MgO@SnO_2 nanocomposite (NC) was synthesized through a bio-mediated co-precipitation approach. A solution containing 0.04 M of both magnesium chloride hexahydrate ($MgCl_2 \cdot 6H_2O$) and tin(II) chloride dihydrate ($SnCl_2 \cdot 2H_2O$) in 100 mL of distilled water was prepared and gradually introduced into the plant extract under continuous magnetic stirring at 75 °C and 700 rpm. After 3 hours, the mixture was subjected to centrifugation to isolate the precipitate, which was then washed, dried at 70 °C for 12 hours, and finally calcined at 500 °C for 4 hours. This process yielded a white powder, confirming the successful formation of MgO@SnO_2 NC via a sustainable, plant-assisted synthesis route [66].

2.2. Functionalization of MgO@SnO_2 NC with Polyvinylpyrrolidone

To enhance the functional properties of the biosynthesized MgO@SnO_2 nanocomposite, surface modification was carried out using polyvinylpyrrolidone (PVP) as a stabilizing agent. In this process, 1 g of MgO@SnO_2 NC and 1 g of PVP were each dispersed in 100 mL of distilled water and stirred individually at room temperature for 30 minutes to ensure complete dissolution and homogenization. The MgO@SnO_2 suspension was then subjected to ultrasonic treatment at 50 °C for 2 hours to promote uniform dispersion and reduce particle agglomeration. Following this, the two solutions were combined and stirred for an additional hour to facilitate surface interaction between the nanocomposite and the polymer. This mixture was further treated with ultrasonic dispersion at 50 °C for 20 minutes to strengthen the polymer–nanoparticle interface. To eliminate unbound PVP, the

resulting suspension underwent repeated centrifugation and washing cycles. The final product, MgO@SnO₂@PVP NC, was then dried in an oven at 50 °C for 24 hours, yielding a surface-functionalized nanocomposite with improved dispersion stability and potential for enhanced adsorption and photocatalytic performance [66].

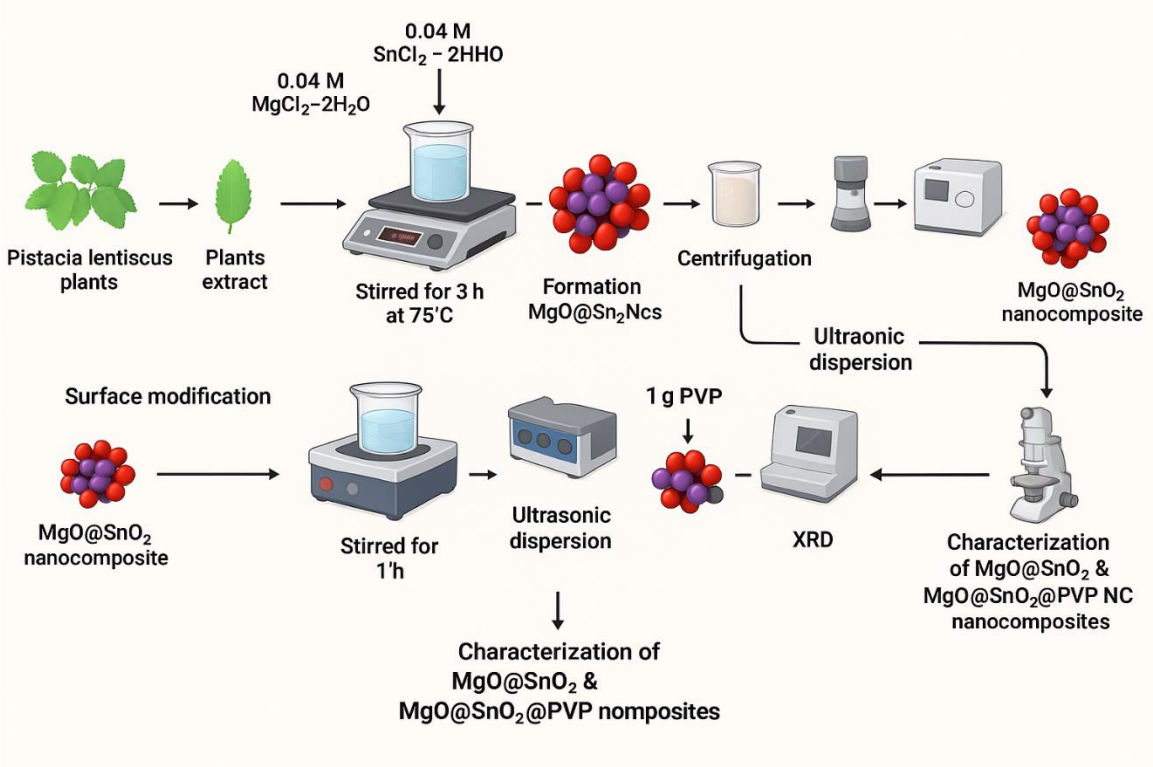

Figure II. 3: Graphical abstract of the green synthesis of MgO@SnO₂ NC& MgO@SnO₂@PVP NC

2.3. Characterization of MgO@SnO₂ & MgO@SnO₂@PVP NC

The structural, optical, and morphological characteristics of the synthesized MgO@SnO₂ and MgO@SnO₂@PVP nanocomposites were thoroughly examined using a suite of analytical techniques. UV-visible spectroscopy (SECOMAM 9600) was employed to monitor the optical absorbance of the nanocomposites over the range of 200–800 nm, confirming their successful formation. To elucidate the functional groups and confirm chemical bonding, Fourier transform infrared (FTIR) spectroscopy (Nicolet iS5) was performed across the spectral range of 400–4000 cm^{-1}. Crystalline structure and phase identification were assessed using X-ray diffraction (XRD) with a benchtop diffractometer

(Proto Manufacturing, Inc.), providing insights into lattice parameters and phase composition. Additionally, scanning electron microscopy (SEM) was utilized to investigate the surface morphology and particle size distribution of the nanocomposites. The average crystallite size was calculated using the Debye–Scherrer equation [84], which relates the crystallite dimension (D) to the X-ray wavelength (λ), the diffraction angle (θ), and the full width at half maximum (FWHM, β) of the diffraction peaks, as expressed in Equation (1) [85]:

$$D = \frac{K\lambda}{\beta \cos \theta} \qquad (1)$$

Here, D represents the crystallite size, λ=0.15418 nm (for Cu Kα radiation), β is the FWHM of the peak, and θ is the Bragg angle. This comprehensive characterization provided a detailed understanding of the physicochemical properties of the nanomaterials essential for their functional evaluation.

2.4. Sorption of Heavy Metals: Experimental Setup

To evaluate the adsorption performance of the synthesized nanocomposites, sorption experiments were conducted involving eleven selected heavy metal ions: arsenic (As), beryllium (Be), cadmium (Cd), chromium (Cr), manganese (Mn), molybdenum (Mo), nickel (Ni), lead (Pb), antimony (Sb), selenium (Se), and zinc (Zn) [84]. For consistency in ionic behavior, all metal ions were introduced in the form of their respective nitrate salts. In each adsorption trial, 40 mg of MgO@SnO₂ NC or MgO@SnO₂@PVP NC was added to 20 mL of oily industrial wastewater containing varying concentrations of the target metal ions. The resulting mixtures were subjected to ultrasonic agitation for 30 minutes to enhance dispersion and adsorption kinetics. After sonication, magnetic separation was employed to isolate the nanocomposites from the aqueous phase. The residual concentrations of metal ions in the supernatant were then quantified using inductively coupled plasma mass spectrometry (ICP-MS), performed with a NexION 2000 instrument (USA) [86]. Quantitative analysis was conducted using linear regression models based on calibration standards, with additional corrections applied through internal standards. Where sample dilution was necessary, recalculations were performed using the

accompanying software, and the measured concentrations were adjusted accordingly by the relevant dilution factors to ensure precise and reliable data [66].

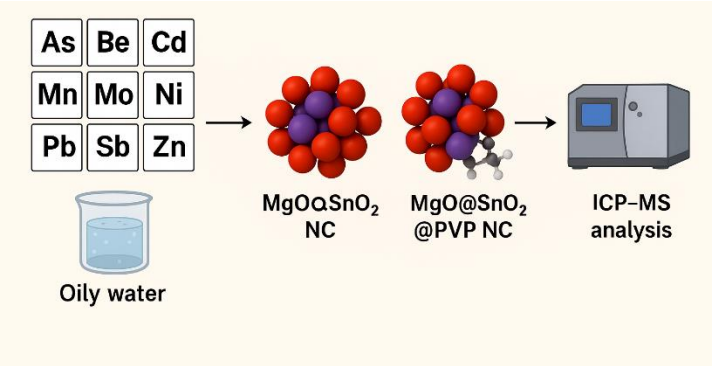

Figure II. 4: Unveiling Metal-Ion Capture on MgO@SnO₂ NC and Their PVP-Enhanced Hybrids

2.5. Analysis of Oil-in-Water Sample (OIW)

The quantification of hydrocarbon content in oil-in-water (OIW) samples was performed using a TD-500 oil-in-water analyzer (Turner Designs Hydrocarbon Instruments, USA), which was first calibrated using standard solutions with known oil concentrations. To prepare the calibration standards, 200 mL of distilled water was acidified to a pH below 2 by the addition of hydrochloric acid (HCl), followed by the introduction of 20 mL of hexane as the organic solvent. The mixture was then vigorously agitated for 3 minutes to ensure effective extraction of hydrocarbons from the aqueous phase into the hexane layer. After settling for approximately 15 minutes, a significant portion of the organic phase was carefully drawn using a syringe from the ampoule's test socket. The test socket was then cleaned thoroughly before placing it into the TD-500 device for measurement. Within approximately five seconds, the instrument provided a direct reading of hydrocarbon concentration expressed in parts per million (ppm). These readings were subsequently used to evaluate the efficiency of the nanocomposites in removing hydrocarbons from petroleum-contaminated water samples [66].

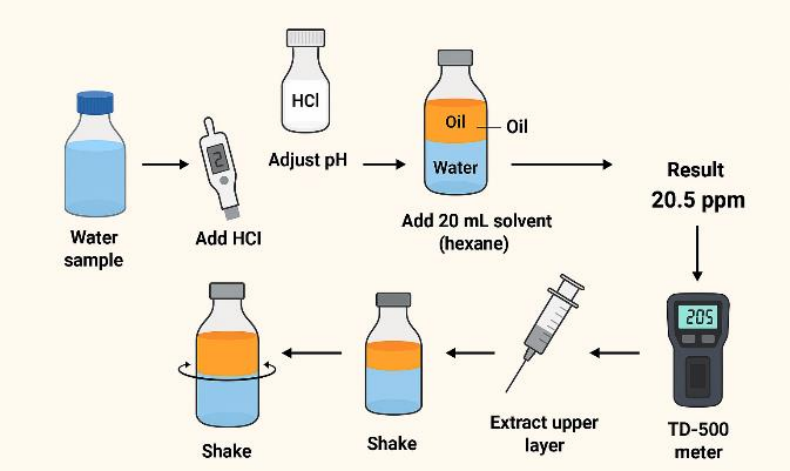

Figure II. 5: Rapid Hexane-Extraction Workflow for Measuring Hydrocarbons in Oil-in-Water Samples with the TD-500 Analyzer

2.6. Determination of Total Suspended Solids (TSS)

The concentration of total suspended solids (TSS) in petroleum-contaminated water samples was determined using a UV-visible spectrophotometric method. Precisely 20 mL of the sample was measured and transferred into a clean, transparent cuvette to ensure optimal light transmission during analysis. The cuvette was then placed in the UV-visible spectrophotometer, where the light beam could pass unobstructed through the solution. After a designated equilibration period of 10 minutes, the absorbance value corresponding to the TSS concentration was recorded from the spectrophotometer display. This measurement provided a quantitative assessment of suspended particulate matter in the sample, enabling evaluation of the nanocomposites' effectiveness in removing solid-phase pollutants from oily wastewater [66].

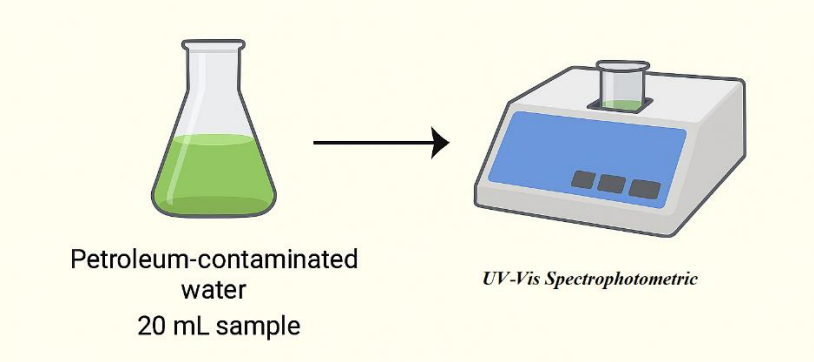

Figure II. 6: UV-Vis Spectrophotometric Read-Out of Total Suspended Solids in Petroleum-Contaminated Water

2.7. Isotherm Modeling

To investigate the adsorption characteristics and underlying mechanisms associated with the removal of contaminants specifically hydrocarbons and total suspended solids (TSS) from oily industrial wastewater (OIW), the MgO@SnO_2@PVP nanocomposite (NC) was employed as the adsorbent. The adsorption uptake (q) and removal efficiency (R) were quantitatively assessed using standard equations. The adsorption capacity at equilibrium or a given time was calculated using [87]:

$$q_{(e,t)} = \frac{(C_0 - C_{(e,t)})V}{M} \qquad (2)$$

and the removal percentage was computed as [84]:

$$R = \frac{(C_0 - C_{(e,t)})}{C_0} \times 100 \qquad (3)$$

In these equations, C_0 represents the initial concentration of the pollutant (in mg/L), C_e and C_t are the equilibrium and time-dependent concentrations, respectively, V is the volume of the solution (L), and M is the mass of the adsorbent (g). To further analyze the adsorption behavior, both Langmuir and Freundlich isotherm models were applied. The Langmuir model, which assumes monolayer adsorption onto a homogenous surface, was evaluated by plotting $C_e \backslash q_e$ against C_e, where C_e is the equilibrium concentration and q_e is the amount adsorbed per gram of adsorbent. The Freundlich model, suitable for heterogeneous surface

adsorption, was assessed by plotting log q_e versus log Ce, yielding a linear relationship characterized by a slope of 1/n and an intercept of log K_F , where n indicates adsorption intensity and K_F represents the adsorption capacity [66].

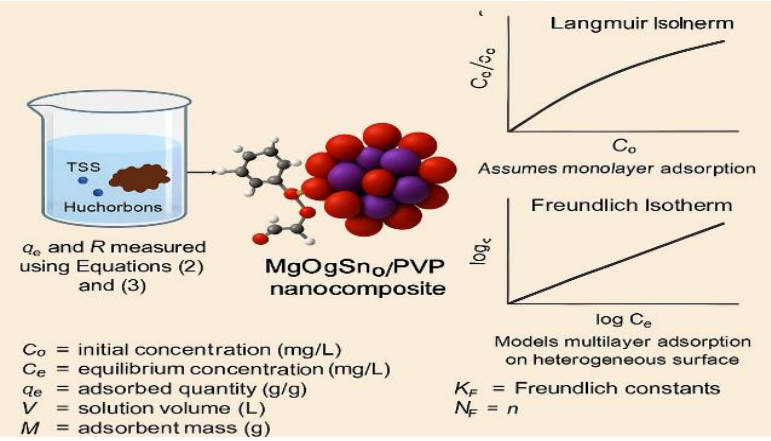

Figure II. 7: Adsorption mechanism and isotherm modeling for hydrocarbon and TSS removal using MgO@SnO₂ NC and MgO@SnO₂@PVP NC

2.8. Computational description of adsorption energy

To assess the adsorption affinity of heavy metal ions onto the surfaces of MgO@SnO₂ and MgO@SnO₂@PVP nanocomposites, computational modeling based on first-principles calculations was performed using the Forcite module within the Materials Studio software suite. The structural modeling process began with the construction of the MgO@SnO₂ nanocomposite, generated using ChemDraw and further processed by cleaving the surface along the (110) crystallographic plane. A supercell was then constructed with dimensions of 3×3×1 to simulate the extended surface. Similarly, the polyvinylpyrrolidone (PVP) ligand was modeled and positioned atop the MgO@SnO₂ surface. Geometrical optimization and energy minimization were carried out using Forcite, which applies classical molecular mechanics while maintaining crystallographic integrity during the simulation process [66].

The structure of the PVP ligand was sourced from the Materials Studio database to ensure molecular accuracy. Following optimization, the Monte Carlo Metropolis algorithm was employed to estimate the adsorption energy (E_ad), reflecting the interaction strength

between the nanocomposite and the target pollutant molecule. The adsorption energy was computed using the following equation [66]:

$$E_{ad} = E_{\mathrm{MgO@SnO2/MgO@SnO2@PVP}} - E_{\mathrm{MgO@SnO2-MgO@SnO2@PVP}} - E_{polutant} \qquad (4)$$

Here, $E_{(MgO@SnO2@PVP\_polutant)}$ represents the total energy of the pollutant-adsorbed nanocomposite system, $E_{(MgO@SnO2@PVP)}$ denotes the ground state energy of the isolated nanocomposite, and $E_{(pollutant)}$ is the ground state energy of the free pollutant molecule (e.g., bromophenol). A more negative E_{ad} value indicates a stronger binding interaction, thereby signifying higher adsorption potential and surface reactivity of the nanocomposite material [66].

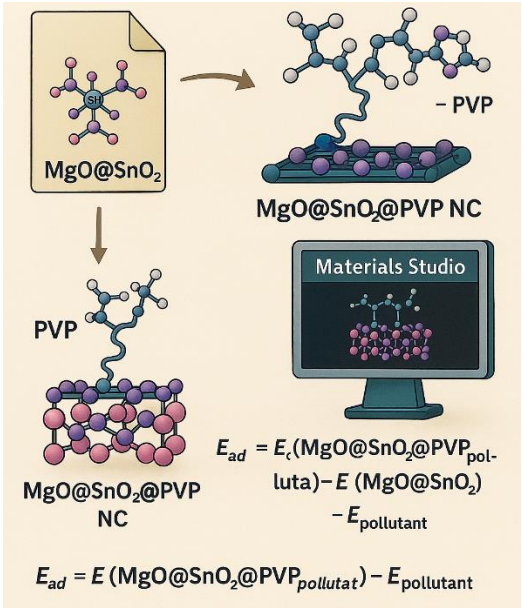

Figure II. 8: Computational modeling of adsorption energy

3. Structural and Morphological Characterization

3.1. XRD analysis

The crystallographic structure of the synthesized MgO@SnO₂@PVP nanocomposite, along with its individual components, was investigated using X-ray diffraction (XRD) analysis. The diffraction pattern for the pure PVP and the composite material exhibited a series of well-defined peaks. Specifically, the XRD spectrum revealed characteristic peaks

at 2θ values of 26.61°, 33.89°, 37.95°, 42.63°, 51.78°, 54.75°, 62.59°, 64.72°, 65.94°, 69.23°, 71.77°, and 78.71°, corresponding to the crystallographic planes (110), (101), (200), (210), (211), (220), (221), (112), (301), (311), (320), and (321), respectively. These reflections are indicative of the tetragonal crystal structure of SnO_2 nanoparticles, conforming to the space group P42mc (No. 136), with lattice constants a = 4.7382 Å and c = 3.1871 Å, as confirmed by JCPDS Card No. 00-041-1445.

In addition to the MgO phase, diffraction peaks at 2θ values of 44.37°, 59.17°, and 73.33° were observed, corresponding to the (400), (511), and (620) planes, respectively. These peaks are consistent with the cubic phase of MgO nanoparticles, which crystallize in the Fd-3m space group (No. 227) and possess lattice parameters a = b = c = 8.1200 Å, in agreement with JCPDS Card No. 00-030-0794. The composite material, MgO@SnO₂@PVP NC, also displayed additional peaks at 2θ values of 11.68° and 21.84°, which are associated with the semi-crystalline nature of PVP. These features confirm the successful incorporation of PVP into the nanocomposite matrix [66].

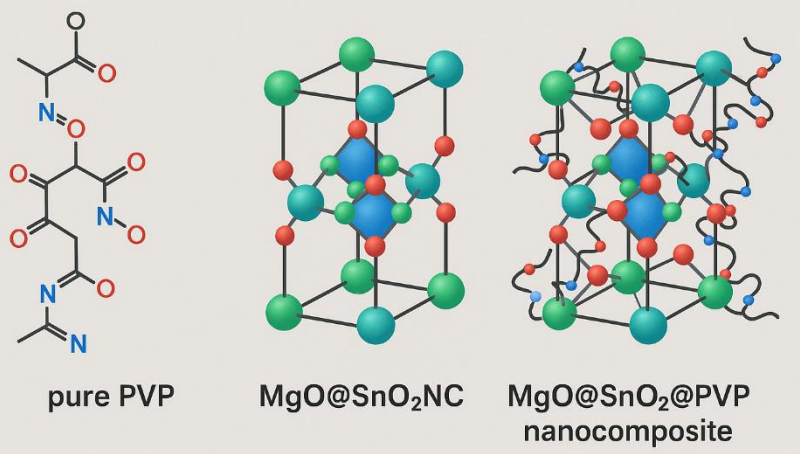

Figure II. 9: Molecular and Crystal Structure Comparison of Pure PVP, MgO@SnO_2 Nanocomposite, and MgO@SnO_2@PVP Hybrid Nanocomposite

The average crystallite sizes of the MgO@SnO_2 and MgO@SnO_2@PVP nanocomposites were determined to be approximately 23.3 nm and 25 nm, respectively, using the Debye–Scherrer equation. Additional structural parameters including interplanar spacing (d-spacing), lattice constants, X-ray density (ρ_x), specific surface area, and percentage

crystallinity were also calculated based on standard equations. The specific surface area (SSA) was estimated using the following formula [66]:

$$SSA = \frac{6000}{GS \times \rho_x} \qquad (5)$$

where **GS** is the crystallite size in nanometers, and $\boldsymbol{\rho_x}$ is the X-ray density of the photocatalyst. The degree of crystallinity was determined using the equation [66]:

$$Crystalinity\ (\%) = \frac{A_{cp}}{A_{ta}} \times 100 \qquad (6)$$

where A_{cp} represents the integrated area under crystalline peaks and A_{ta} denotes the total area under the diffraction curve. A summary of these calculated structural properties is provided in Table 1 for both the unmodified and PVP-functionalized nanocomposites.

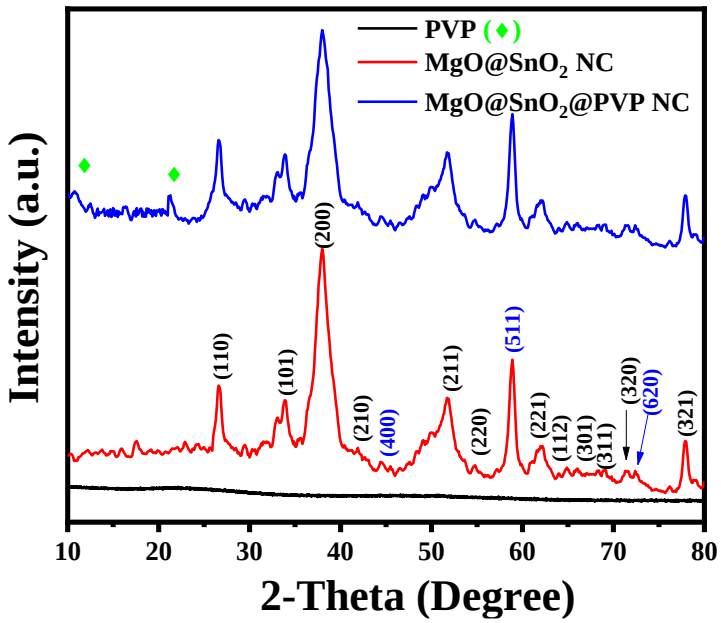

Figure II. 10: X-ray Diffraction (XRD) Patterns of Pure PVP, MgO@SnO₂ Nanocomposite, and MgO@SnO₂@PVP Hybrid Composite [66]

Table II. 1: Crystallographic Characteristics of MgO@SnO_2 and MgO@SnO_2@PVP Nanocomposites [66]

samples	d-spacing (nm)	Surface area ($m^2\ g^{-1}$)	Crystallinity (%)	Grain size (nm)	Density (g/cm^3)
MgO@SnO_2 NC	0.236	32.1	52.3	23.3	8.02
MgO@SnO_2@PVP NC	0.237	34.33	63.2	25	6.99

3.2. FTIR analysis

Fourier Transform Infrared (FTIR) spectroscopy was employed to identify the functional groups and chemical bonding characteristics present in the *Pistacia lentiscus* leaf extract, MgO@SnO_2 nanocomposite (NC), and its PVP-modified form (MgO@SnO_2@PVP NC), offering key insights into their molecular composition (Figure II.12). In the spectrum of the leaf extract, a broad absorption band near 3700 cm^{-1} indicates O–H stretching vibrations, typically associated with hydroxyl groups in phenolic and alcoholic compounds [88]. A pronounced band at 3287 cm^{-1} further suggests hydrogen-bonded O–H groups [89]. Additional peaks at 1722 cm^{-1} and 1365 cm^{-1} correspond to C=O stretching and ether functional groups [90], respectively, while peaks at 2353 cm^{-1} and 1024 cm^{-1} are attributed to C≡C triple bond and C–O stretching vibrations [91], indicating a complex composition of phytochemicals within the extract.

The FTIR spectrum of the MgO@SnO_2 nanocomposite reveals strong absorption peaks at 3700 and 3386 cm^{-1}, confirming the presence of hydroxyl groups [92], which may result from adsorbed water or surface hydroxyls on the metal oxide structure [93]. Characteristic peaks at 1658 cm^{-1}, 1429 cm^{-1}, and 1076 cm^{-1} are assigned to carbonyl (C=O) [94], C–H [95], and C–O stretching vibrations [96], respectively. A distinct peak at 853 cm^{-1} corresponds to C–O–C asymmetric stretching [97], while the band at 542 cm^{-1} is indicative of metal–oxygen (M–O) stretching, confirming the formation of MgO and SnO_2 phases [98][99].

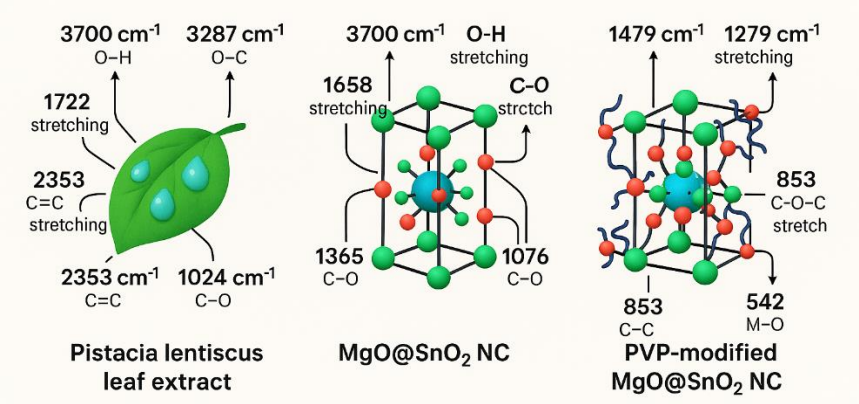

Figure II. 11: Schematic Illustration of Functional Group Interactions Identified by FTIR in Pistacia lentiscus Extract, MgO@SnO₂ NC, and PVP-Modified MgO@SnO₂ NC

In the PVP-functionalized nanocomposite (MgO@SnO₂@PVP NC), additional peaks observed at 1479 cm^{-1} and 1279 cm^{-1} are assigned to C=C stretching [100] and C–N stretching vibrations [101], respectively. These spectral features confirm the successful incorporation of PVP onto the nanocomposite surface [102]. Notably, the preservation of the original FTIR peaks from the unmodified MgO@SnO₂ NC in the modified sample suggests that the core structure of the nanocomposite remained intact during surface modification. For reference, the FTIR spectrum of pure PVP exhibits characteristic peaks at 3513 cm^{-1} (O–H stretching) [103], 2951 cm^{-1} (C–H stretching), and 1681 cm^{-1} (C=O stretching) [75], all of which are consistent with the polymer's chemical profile [104]. Collectively, the FTIR results affirm the successful synthesis and surface functionalization of the nanocomposites and offer a detailed understanding of their chemical framework [105][106], which is essential for predicting their behavior in environmental remediation applications [66].

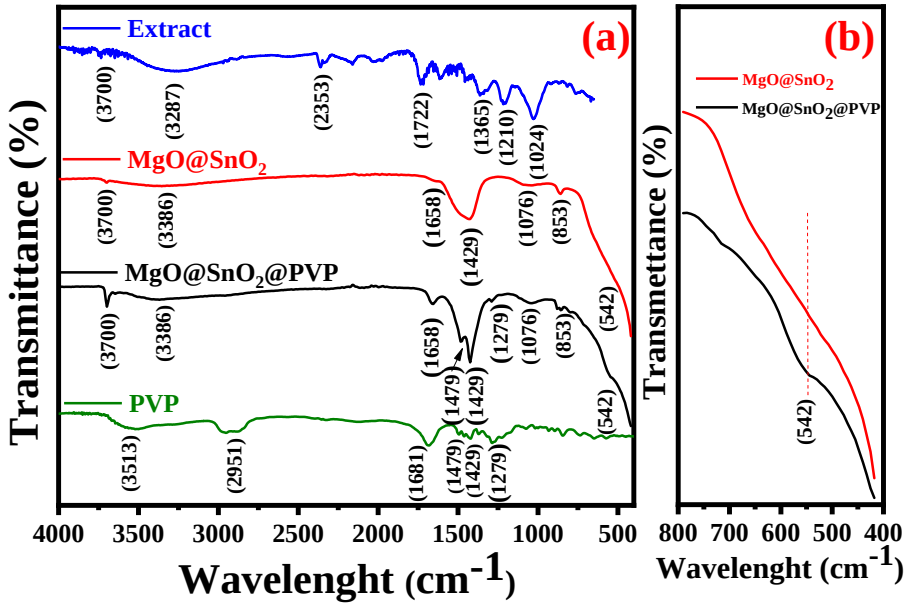

Figure II. 12: FTIR Analysis of Leaf Extract, MgO@SnO₂ Nanocomposite, MgO@SnO₂@PVP Nanocomposite, and Pure PVP: **(a)** Spectral Range 4000–400 cm^{-1} and **(b)** Magnified Region from 400 to 800 cm^{-1} [66].

3.3. UV–Vis Spectroscopy and Bandgap Determination

The optical absorption properties of MgO@SnO₂ and MgO@SnO₂@PVP NC were investigated using UV–visible spectroscopy in the wavelength range of 200–800 nm. As shown in Figure II.13 (a), the MgO@SnO₂ nanocomposite exhibited a prominent absorption peak at 274 nm, confirming its successful formation. Upon PVP modification, the absorption maximum shifted to 283 nm, accompanied by a noticeable increase in intensity, thereby indicating the successful synthesis and enhanced optical activity of the MgO@SnO₂@PVP nanocomposite [66].

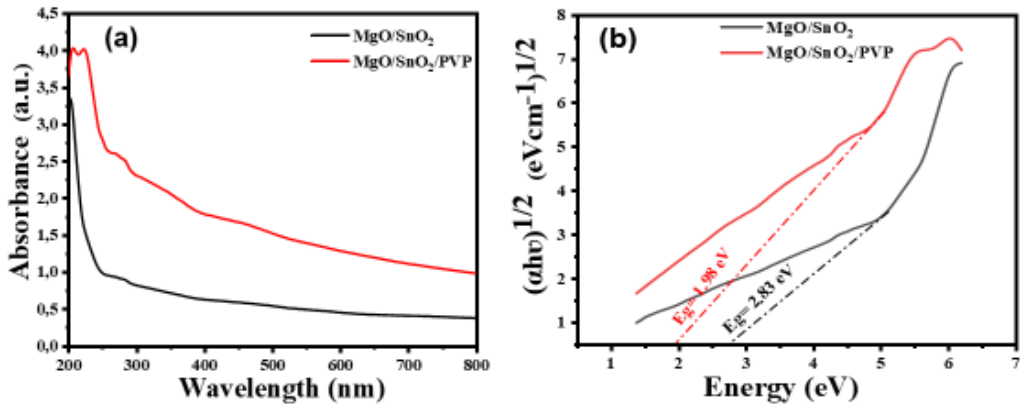

Figure II. 13: (a) UV–Visible Absorption Spectra of MgO@SnO₂ and MgO@SnO₂@PVP Nanocomposites, **(b)** Corresponding Bandgap Energy Analysis [66].

To determine the optical bandgap, Tauc plots were constructed by graphing $(\alpha h\nu)^{1/2}$ versus photon energy ($h\nu$), assuming an indirect allowed transition. The MgO@SnO₂ NC displayed a bandgap energy of 2.83 eV, as shown in Figure II.13 (b), which is significantly lower than the 5.2 eV [66] bandgap reported in literature for sol-gel synthesized MgO@SnO₂ systems [49]. This reduction highlights the effectiveness of the green synthesis route employed in the current study.

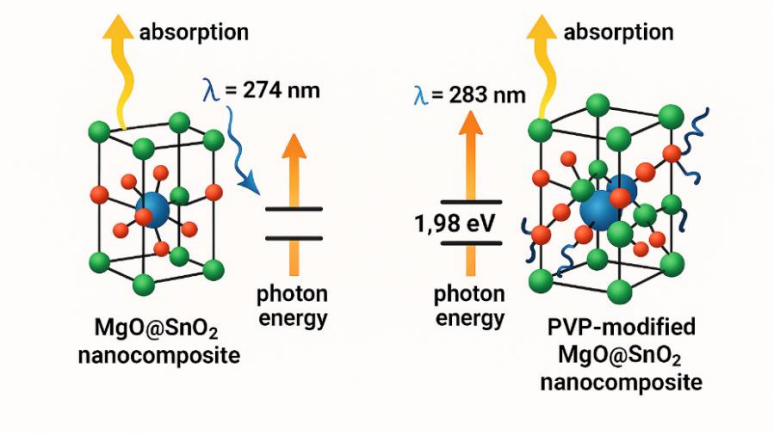

Figure II. 14: Visual Representation of Optical Absorption Behavior and Bandgap Narrowing in MgO@SnO₂ and MgO@SnO₂@PVP Nanocomposites

Furthermore, the MgO@SnO₂@PVP nanocomposite exhibited an even narrower bandgap of 1.98 eV, suggesting improved electronic interactions and enhanced light-harvesting capability [66]. The observed bandgap narrowing is attributed to modifications in the

valence and conduction band positions, which promote stronger electron–hole interactions [107]. Additionally, the presence of unsaturated defect sites and increased density of localized energy states within the bandgap may further account for the optical bandgap reduction, facilitating better charge transport and photocatalytic performance [108].

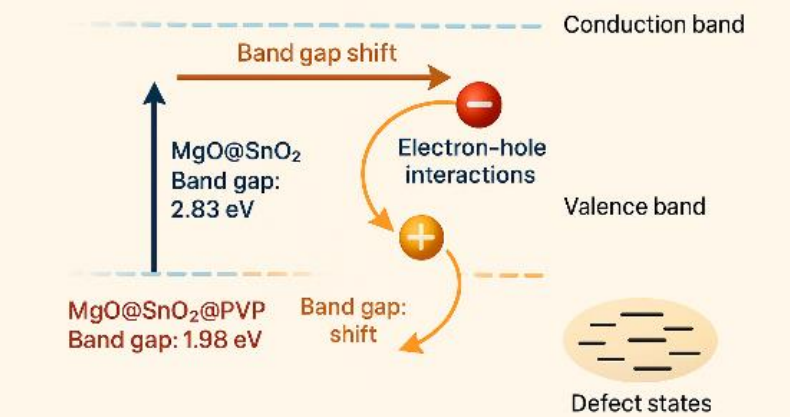

Figure II. 15: Explication of Band gap narrowing

3.4. Surface Morphology and Elemental Composition Analysis (SEM/EDX)

Scanning Electron Microscopy (SEM) was employed to examine the surface morphology and particle dispersion of the synthesized nanocomposites. As shown in Figure II.18 (a), the unmodified MgO@SnO₂ nanocomposite demonstrates a predominantly spherical morphology with slight indications of particle agglomeration. However, following surface modification with polyvinylpyrrolidone (PVP), as illustrated in Figure II.18 (b), a notable change in morphological characteristics is observed. The modified MgO@SnO₂@PVP nanocomposite exhibits a more uniformly dispersed structure with reduced agglomeration, suggesting the effective stabilizing and dispersing action of PVP [66].

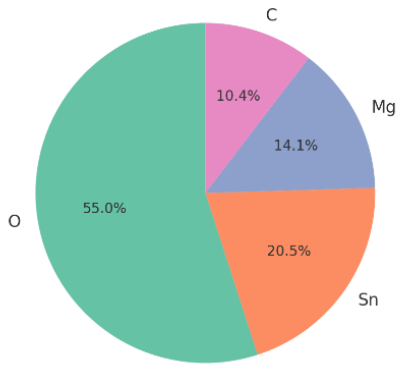

Figure II. 16: EDX Elemental composition of MgO@SnO₂@PVP Nanocomposites

Particle size analysis based on SEM imaging further reveals that the average diameter of MgO@SnO₂ particles is approximately 53 nm, whereas the PVP-modified variant shows a slight increase in particle size to around 65 nm (Figure II.18 (c)). This enlargement may be attributed to surface coverage by the PVP matrix, which likely contributes to improved dispersion and reduced interparticle attraction within the nanocomposite matrix [66].

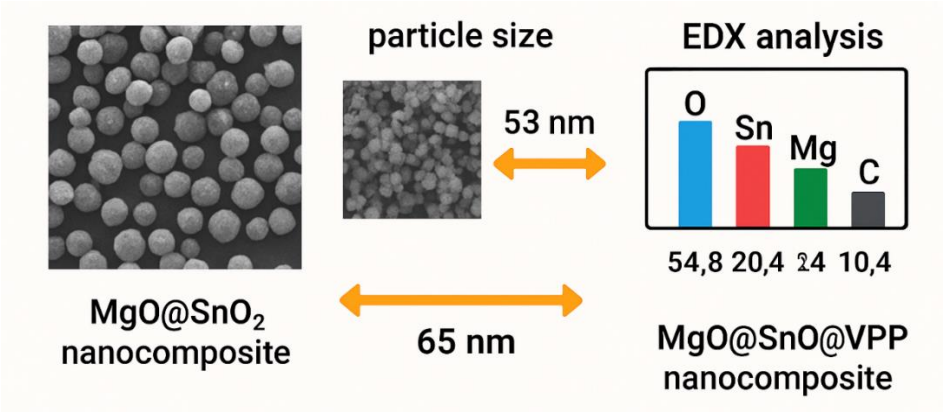

Figure II. 17: Enhanced Morphology and Composition of PVP-Modified MgO@SnO₂ Nanocomposites

Additionally, Energy Dispersive X-ray Spectroscopy (EDX) analysis was conducted to confirm the elemental composition of the MgO@SnO₂@PVP nanocomposite (Figure II.18 (d)). The detected elements oxygen (O), tin (Sn), magnesium (Mg), and carbon (C) correspond to the expected constituents of the composite structure. Quantitative analysis yielded atomic percentages of 54.8% for O, 20.43% for Sn, 14.06% for Mg, and 10.37%

for C, corroborating the successful incorporation of PVP and the structural integrity of the synthesized nanocomposite [66].

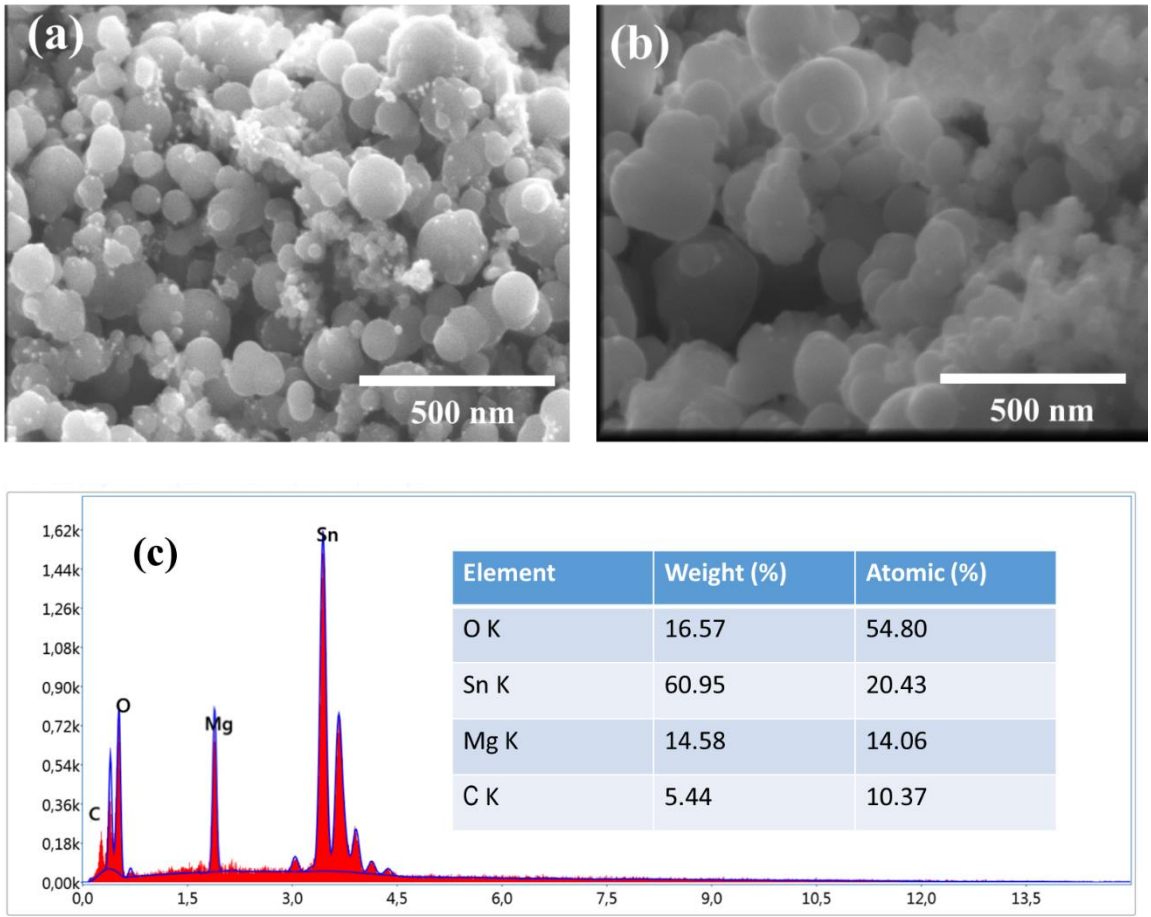

Figure II. 18: Surface Morphology and Particle Size Characterization of **(a)** MgO@SnO_2 Nanocomposite, **(b)** PVP-Functionalized MgO@SnO_2 Nanocomposite, **(c)** Elemental Composition via EDX Analysis, and **(d)** Particle Size Distribution [66].

4. Evaluation of Heavy Metal Removal Performance

4.1. Experimental Results for Individual Metal Adsorption

The adsorption performance of MgO@SnO₂ and MgO@SnO₂@PVP nanocomposites was systematically evaluated for the removal of eleven heavy metal ions, including As, Be, Cd, Cr, Mn, Mo, Ni, Pb, Sb, Se, and Zn, from petroleum-contaminated water. Experiments were conducted at multiple time intervals (5, 10, 20, and 30 minutes) to assess adsorption kinetics. As shown in Table II.2 and Figure II.21 (a–d), both nanocomposites demonstrated a marked decrease in metal ion concentrations over time, with a substantial reduction observed after 30 minutes of treatment [66].

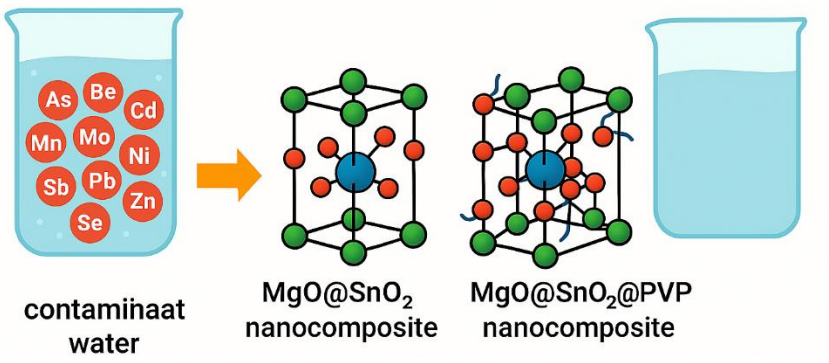

Figure II. 19: Heavy Metal Adsorption by Functionalized Nanocomposites

Complete removal of Cr, Mo, and Sb was achieved within 20 minutes, while Se was fully adsorbed within 10 minutes. The remaining metal ions were effectively eliminated by over 99% within 30 minutes, confirming the high adsorption efficiency of these nanocomposites. Comparative analysis further reveals that MgO@SnO₂@PVP NC outperformed MgO@SnO₂ NC, as evidenced by lower residual metal concentrations. This enhanced performance is attributed to the superior surface characteristics and dispersion capacity imparted by PVP modification, which promotes greater surface availability for adsorption [66].

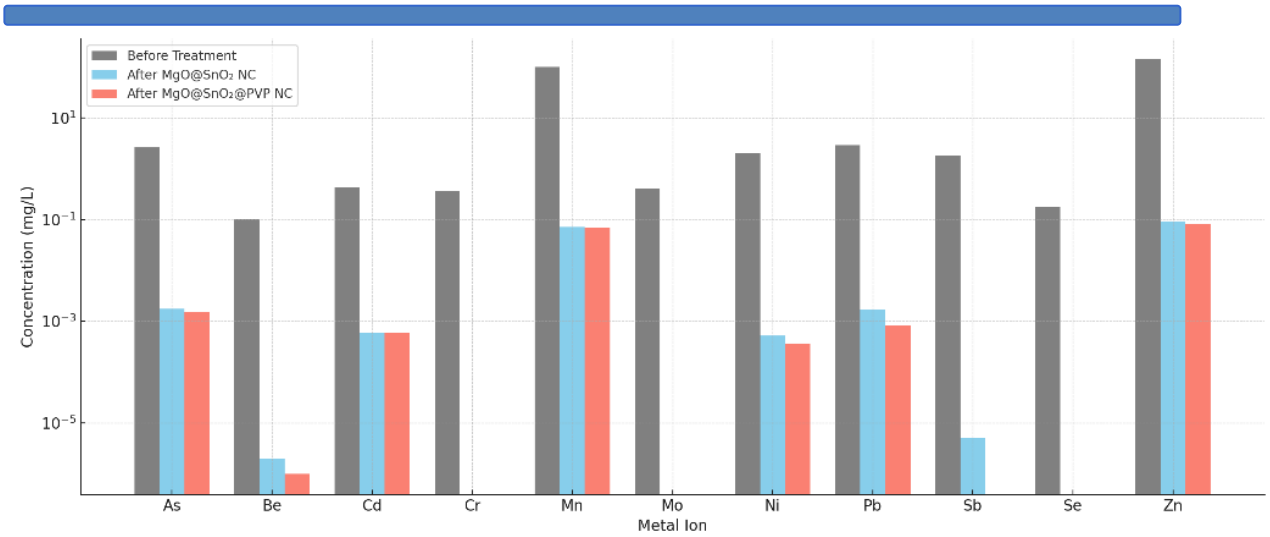

Figure II. 20: Heavy metals concentrations before and after treatment

Table II. 2: Comparative ICP-MS Analysis of Reservoir Oily Water Before and After Nanocomposite-Based Treatment [66]

Samples	**As 75 (mg/L)**	**Be 9 (mg/L)**	**Cd 111 (mg/L)**	**Cr 52 (mg/L)**	**Mn 55 (mg/L)**	**Mo 98 (mg/L)**	**Ni 60 (mg/L)**	**Pb 208 (mg/L)**	**Sb 121 (mg/L)**	**Se 82 (mg/L)**	**Zn 66 (mg/L)**
OIW before treatment	2.613	0.102	0.442	0.367	100.847	0.405	2.041	2.938	1.831	0.182	142.523
OIW after treatment (30 min)											
Samples	**As 75 (µg/L)**	**Be 9 (µg/L)**	**Cd 111 (µg/L)**	**Cr 52 (µg/L)**	**Mn 55 (µg/L)**	**Mo 98 (µg/L)**	**Ni 60 (µg/L)**	**Pb 208 (µg/L)**	**Sb 121 (µg/L)**	**Se 82 (µg/L)**	**Zn 66 (µg/L)**
$MgO@SnO_2$ NC	1.750	0.002	0.606	0	71.828	0	0.519	1.688	0.005	0	90.895
$MgO@SnO_2$@PVP NC	1.510	0.001	0.592	0	70.310	0	0.369	0.833	0	0	80.355

4.2. Comparative Efficiency of Bare vs PVP-Modified NCs

A comparative analysis between the unmodified $MgO@SnO_2$ NC and the PVP-functionalized variant demonstrated enhanced performance by the latter across all tested metal ions. The PVP-modified nanocomposite consistently exhibited lower residual concentrations of metal ions in the treated solutions. This improvement is attributed to the

increased surface availability and dispersion stability provided by the PVP coating, which enhances the accessibility of active sites and facilitates stronger interaction with the metal ions [66].

The metal concentrations in both untreated and treated water samples were quantified using Inductively Coupled Plasma Mass Spectrometry (ICP-MS) as shown in Figure II.21. The raw oily wastewater (OIW) showed initial metal concentrations ranging from sub-ppm to over 140 ppm, with Zn and Mn among the most prevalent contaminants. After 30 minutes of treatment with the nanocomposites, residual concentrations dropped significantly. For instance, the concentration of Pb reduced from 2.938 mg/L to 1.688 µg/L with MgO@SnO_2 and to 0.833 µg/L with MgO@SnO_2@PVP as showed in table II.2. These findings confirm the high sensitivity and effectiveness of the adsorption process, supported by accurate and reliable quantification [66].

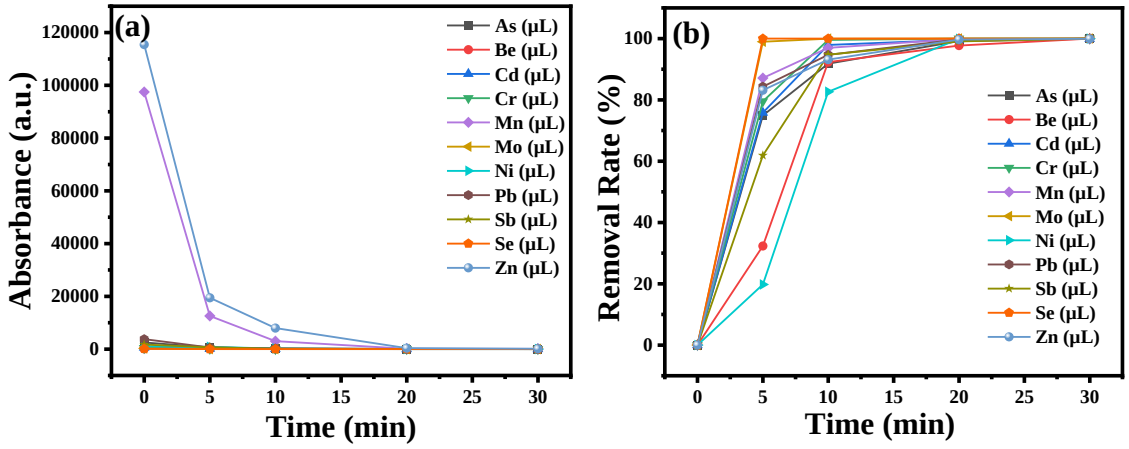

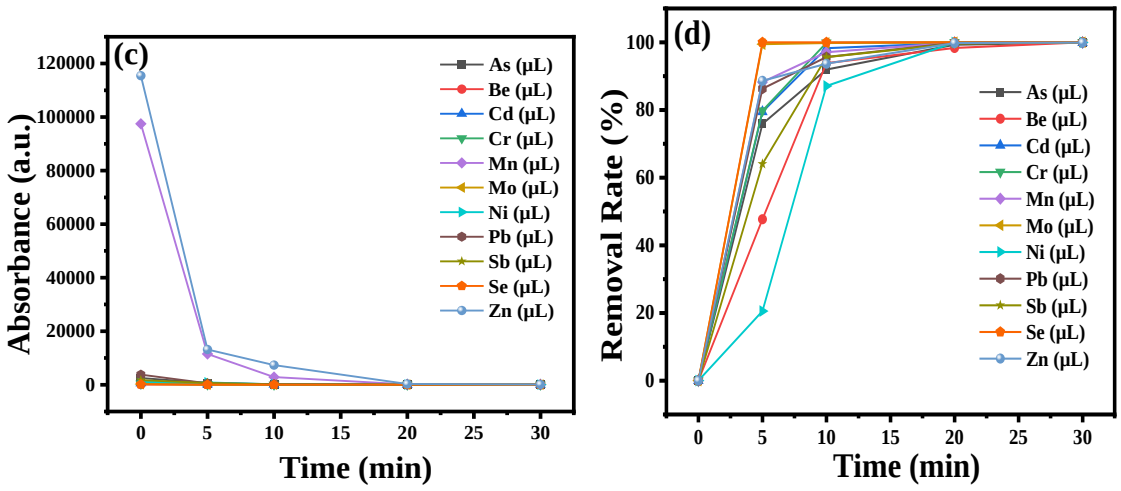

Figure II. 21: Time-Dependent Performance of **(a,b)** MgO@SnO_2 and **(c,d)** PVP-Modified MgO@SnO_2 Nanocomposites for Heavy Metal Removal from Aqueous Solutions [66].

4.3. Surface Interactions and Mechanism of Adsorption

The adsorption mechanism is primarily governed by electrostatic interactions facilitated by deprotonation-induced surface charge enhancement. The resulting increase in negatively charged active sites significantly improves the binding affinity toward metal cations. The stepwise adsorption process involves: (i) migration of metal ions from the bulk solution to the nanocomposite surface [109], (ii) diffusion through the boundary layer, (iii) internal pore diffusion, and (iv) binding onto active adsorption sites [66]. These steps are essential for understanding adsorption dynamics and optimizing nanocomposite design for practical applications.

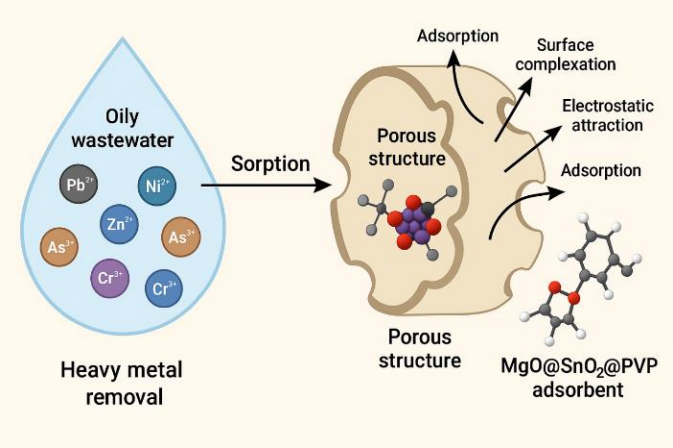

Figure II. 22: Explication of Heavy Metal Sorption by MgO@SnO₂@PVP Adsorbent

The superior adsorption capacity of MgO@SnO₂@PVP NC is attributed to a synergy of physical and chemical interactions. The presence of PVP introduces functional groups such as hydroxyls and carboxyls, which engage in Lewis acid-base interactions and surface complexation with metal ions [66].

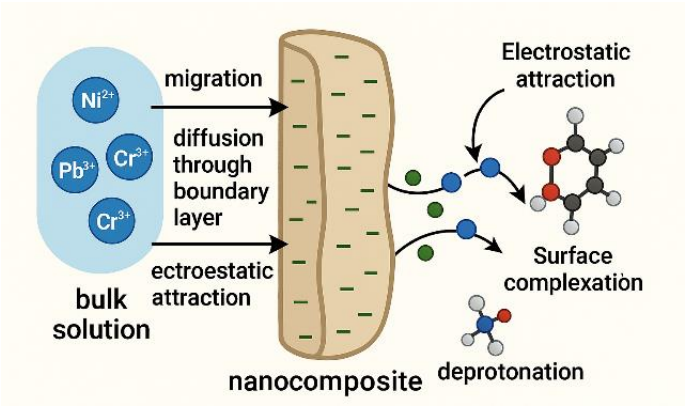

Figure II. 23: Representation of Metal Ion Adsorption by Nanocomposites

Electrostatic interactions between the negatively charged functional groups on the PVP matrix and the positively charged metal ions further reinforce this adsorption behavior. Additionally, the porous and tunnel-like morphology of the MgO@SnO₂ NC offers abundant active sites that enhance diffusion and retention of metal species [66].

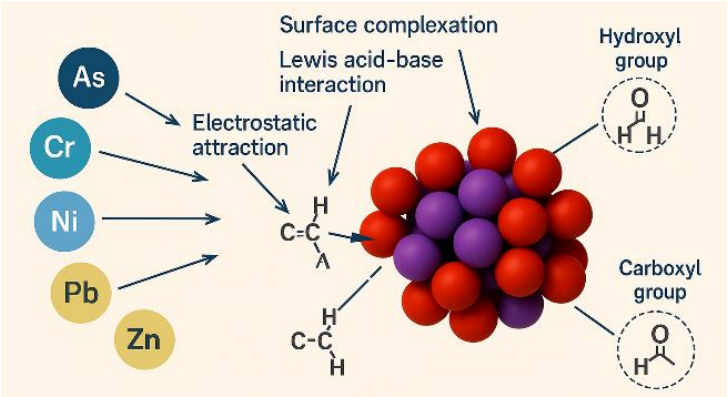

Figure II. 24: Electrostatic Attraction Between the Surface Complexation and the Ions Metals

Figure II.25 schematically illustrates these proposed adsorption pathways, including surface complexation and electrostatic attraction. These mechanisms, validated by molecular docking studies (Figure II.38), reveal strong interactions between the nanocomposite surfaces and selected metal ions (As, Cr, Mo, Ni, Pb, Zn), further supporting the material's suitability for environmental remediation [66].

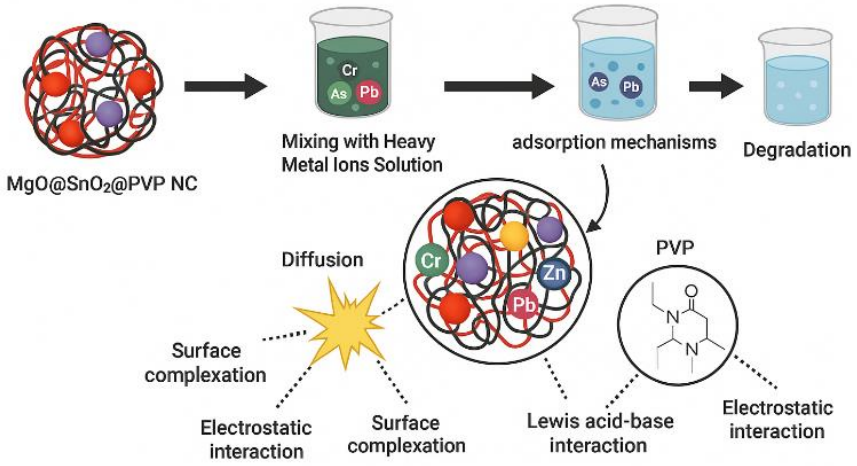

Figure II. 25: Schematic Illustration of Heavy Metal Adsorption Mechanisms on MgO@SnO₂@PVP Nanocomposites

5. Photocatalytic Degradation of Petroleum Pollutants

5.1. Degradation of Hydrocarbons and TSS

Photocatalysis has emerged as a promising and increasingly utilized strategy for the treatment of produced and petroleum-contaminated waters. In this study, magnesium oxide–tin dioxide and PVP-functionalized MgO@SnO₂ nanocomposites were employed as photocatalysts to investigate the degradation of hydrocarbons under natural sunlight exposure. Petroleum-derived oily industrial wastewater (OIW) was used as a representative model for the degradation process [66].

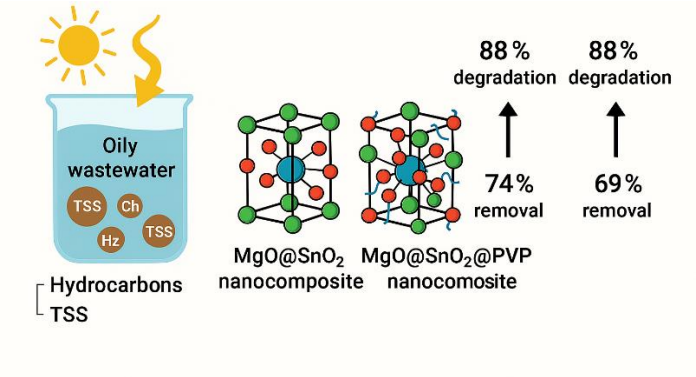

Figure II. 26: Photocatalytic Degradation of Hydrocarbons and Total Suspended Solids (TSS) in Oily Industrial Wastewater

Experimental findings reveal that both nanocomposites achieved significant photocatalytic activity after 30 minutes of solar irradiation. Specifically, the degradation efficiency of hydrocarbons reached 74% with MgO@SnO₂ and improved markedly to 88% with MgO@SnO₂@PVP nanocomposites (Figure II.27 (a,b)). Similarly, the removal of total suspended solids (TSS) exhibited notable enhancement, with respective efficiencies of 69% and 85% for MgO@SnO₂ and MgO@SnO₂@PVP nanocomposites (Figure II.27 (c,d)) [66]. Although both materials demonstrated effective performance, the PVP-modified nanocomposite consistently outperformed its unmodified counterpart. This superior performance is primarily attributed to the improved surface properties and enhanced dispersion provided by the PVP coating, which facilitates more efficient light absorption and interaction with target pollutants [109].

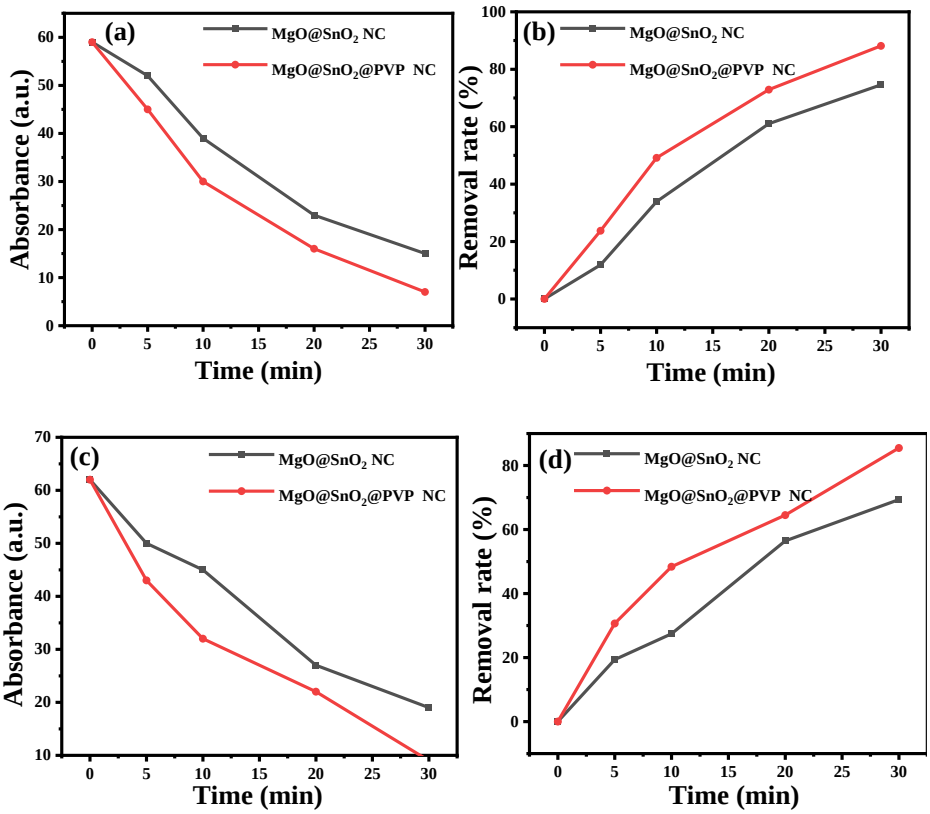

Figure II. 27: (a,b) Photocatalytic Hydrocarbon Degradation in Oily Wastewater, **(c,d)** Total Suspended Solids (TSS) Removal Using MgO@SnO₂ and PVP-Modified MgO@SnO₂ Nanocomposites [66].

5.2. Reaction Kinetics and Pseudo-First Order Model

To further elucidate the photocatalytic process, kinetic modeling was performed using a pseudo-first-order kinetic equation (Equation 7) [110], enabling quantitative assessment of degradation rates. The kinetic analysis yielded rate constants (k) of 0.041 min^{-1} and 0.090 min^{-1} for OIW and TSS degradation, respectively, when using MgO@SnO₂@PVP as the photocatalyst (Figure II.28). These values underscore the enhanced reactivity and accelerated degradation kinetics offered by the functionalized nanocomposite [66].

$$\ln\left({}^{C_0}/_{C_t}\right) = t \times k \qquad (7)$$

In this expression, C_0 denotes the initial concentration of the target compound, C_t is the concentration at a given irradiation time t, and k represents the pseudo-first-order rate constant. A higher k value signifies a more rapid degradation rate, thereby confirming the

improved photocatalytic efficiency of the MgO@SnO₂@PVP nanocomposite. These findings reinforce the material's potential as a highly effective photocatalyst for the remediation of petroleum-based contaminants and suspended solids in wastewater [66].

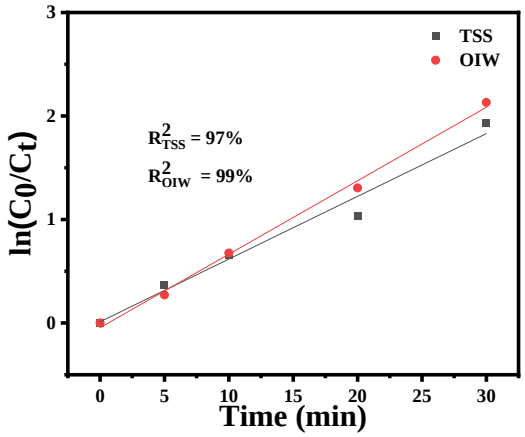

Figure II. 28: First-Order Kinetic Analysis of TSS and OIW Degradation by MgO@SnO₂@PVP [66]

5.3. Mechanistic Insights Based on Charge Carrier Dynamics

The photocatalytic mechanism illustrated in Figure II.29 provides a detailed representation of the pathways governing the degradation of organic pollutants in the presence of semiconductor nanocomposites under light irradiation. This approach is particularly effective in elucidating the transformation of organic molecules during photocatalytic treatment processes [107].

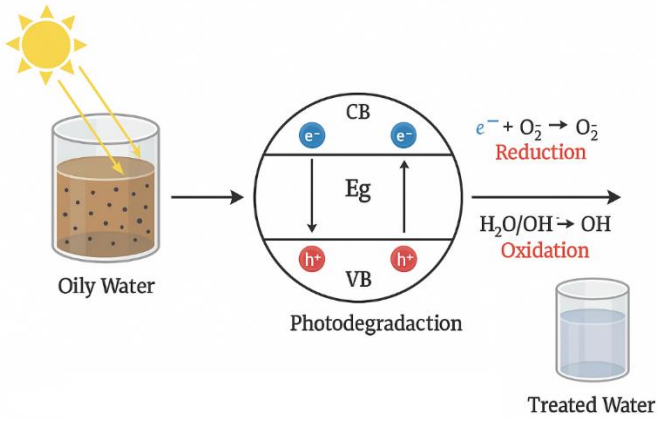

Figure II. 29: Photocatalytic degradation of TS removal in OIW

Upon exposure to photons possessing energy equal to or greater than the band gap energy (E=hν), electrons in the nanocomposite are excited from the valence band (VB) to the conduction band (CB), resulting in the generation of photoinduced electron–hole pairs (e^-/h^+) (Equation 8). These charge carriers play a crucial role in initiating redox reactions at the catalyst surface [66].

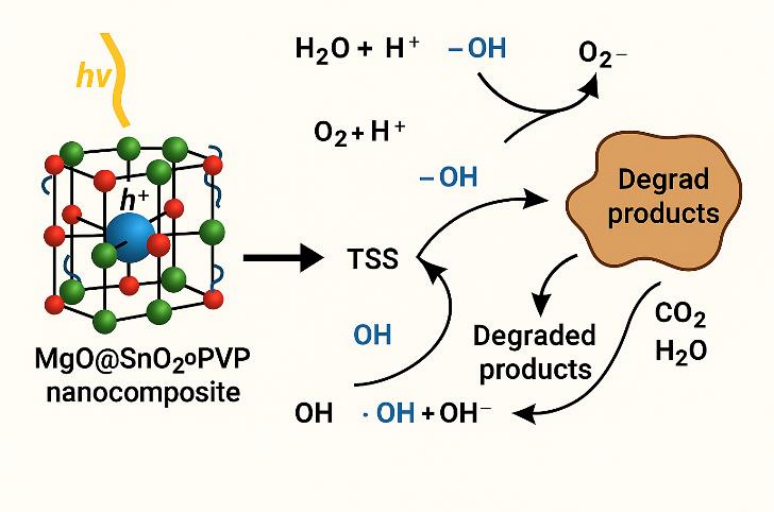

Figure II. 30: Photocatalytic Mechanism of TSS and OIW Degradation by MgO@SnO₂@PVP Nanocomposite

The photogenerated holes in the valence band ({VB}h^+) exhibit strong oxidizing power and react readily with water molecules or surface hydroxyl groups to form hydroxyl radicals (•OH) [109], which are highly reactive species capable of mineralizing organic pollutants (Equation 9) [109]. Concurrently, the excited electrons in the conduction band ({CB}e^-) are transferred to surface-adsorbed molecular oxygen, reducing it to superoxide anion radicals ($•O_2^-$) (Equation 10) [66].

These superoxide radicals further undergo protonation to yield hydroperoxyl radicals (•OOH) (Equation 11), which dimerize to form hydrogen peroxide (H_2O_2) (Equation 12). In subsequent steps, H_2O_2 is reduced by conduction band electrons, generating additional hydroxyl radicals (Equation 13), thus amplifying the oxidative degradation pathway. The synergistic action of these reactive oxygen species (ROS), particularly •OH and $•O_2^-$, facilitates the breakdown of complex organic compounds and total suspended solids (TSS)

in oily wastewater (OIW), ultimately converting them into benign end products such as carbon dioxide (CO_2) and water (H_2O) (Equation 14) [86].

$$h\upsilon + \mathrm{MgO@SnO_2@PVP} \rightarrow \mathrm{MgO@SnO_2@PVP}\ (\mathrm{h_{VB}^+} + e_{CB}^-) \quad (8)$$

$$H_2O + \mathrm{h_{VB}^+} \rightarrow \bullet\mathrm{OH} + \mathrm{H^+} \quad (9)$$

$$O_2 + (\mathrm{e_{CB}^-}) \rightarrow \bullet\,\mathrm{O_2^-} \quad (10)$$

$$\bullet\,\mathrm{O_2^-} + \mathrm{H^+} \rightarrow \bullet\,\mathrm{OOH} \quad (11)$$

$$\bullet\,2\mathrm{OOH} \rightarrow H_2O_2 \quad (12)$$

$$H_2O_2 + \mathrm{e^-} \rightarrow HO\bullet + \mathrm{OH^-} \quad (13)$$

$$TSS\ OR\ OIW + \mathrm{OH}\bullet + \bullet O_2 \rightarrow \text{Degraded products} + \mathrm{CO_2} + \mathrm{H_2O} \quad (14)$$

This multi-step redox pathway underscores the efficiency of the MgO@SnO_2-based nanocomposites in driving advanced oxidative processes, supporting their application in environmental remediation, particularly for the treatment of oily wastewater laden with recalcitrant organic compounds [66].

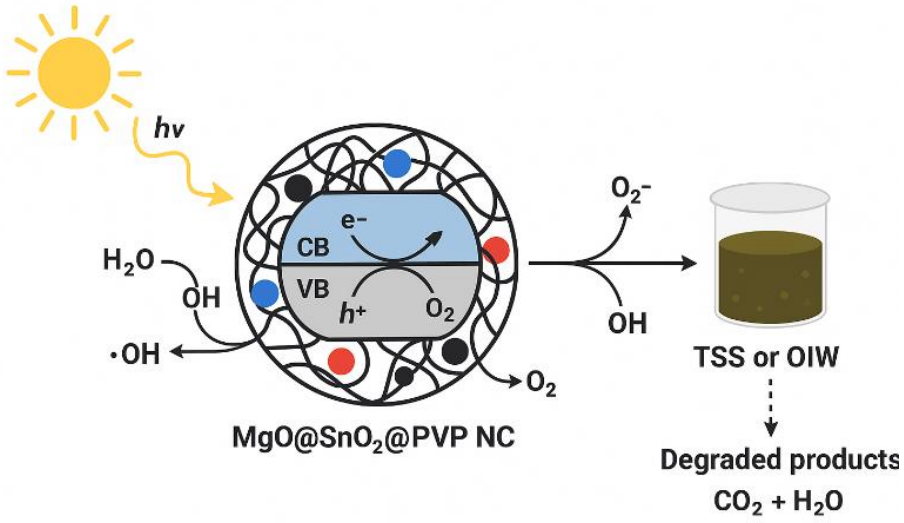

Figure II. 31: Photocatalytic Degradation Mechanism of TSS and OIW Using MgO@SnO_2@PVP NC

5.4. Adsorption Isotherm Modeling study of TSS

The adsorption behavior of heavy metal ions and hydrocarbon-laden oily wastewater (OIW), including total suspended solids (TSS), onto MgO@SnO₂@PVP nanocomposites (NCs) was systematically evaluated using two widely accepted isotherm models: Langmuir and Freundlich. These models offer insight into the interaction mechanisms between the adsorbate and the nanocomposite surface. The adsorption experiments were conducted across a pH range of 6.5 to 8.5 to simulate environmentally relevant conditions.

The Langmuir model assumes monolayer adsorption onto a homogeneous surface with a finite number of identical sites, where each site binds to one adsorbate molecule with uniform energy. In contrast, the Freundlich model describes adsorption onto heterogeneous surfaces and does not restrict adsorption to monolayer formation. The corresponding linearized equations for these isotherms are given below:

$$\frac{C_e}{q_e} = \frac{1}{bq_m} + \frac{C_e}{q_m} \qquad (15)$$

$$\log(q_e) = \log(K_f) + \frac{1}{n}\ \log(C_e) \qquad (16)$$

Where:

- q_e (mg·g⁻¹) is the amount of solute adsorbed per unit mass of adsorbent at equilibrium,
- C_e (mg·L⁻¹) is the equilibrium concentration of the adsorbate in solution,
- q_m (mg·g⁻¹) represents the maximum adsorption capacity,
- b (L·mg⁻¹) is the Langmuir constant related to the binding energy of adsorption,
- K_f and n are the Freundlich constants associated with adsorption capacity and intensity, respectively.

The Langmuir isotherm constants q_m and b were determined from the linear plot of C_e/q_e versus C_e, as illustrated in Figure II.33 (a). The Freundlich model parameters were

extracted from the linear relationship between log q_e and log C_e , with the model showing excellent correlation (R^2 = 0.99) as seen in Figure II.33 (b) [66]. The higher correlation coefficient for the Freundlich model suggests that the adsorption process follows a heterogeneous surface interaction, consistent with the nature of the nanocomposite surface.

To further evaluate the favorability of the adsorption process, the dimensionless separation factor R_L was calculated using the expression [86]:

$$R_L = \frac{1}{1 + R_L C_0} \qquad (17)$$

Where C_0 is the initial adsorbate concentration. The value of R_L provides insight into the nature of adsorption [86]:

- R_L = 0: irreversible,
- 0< R_L <1: favorable,
- R_L =1: linear,
- R_L >1: unfavorable.

In this study, all computed R_L values for the adsorption of TSS and hydrocarbons from OIW were found to lie between 0 and 1, confirming that the process was thermodynamically favorable. The complete set of isotherm parameters is summarized in Figure II.32.

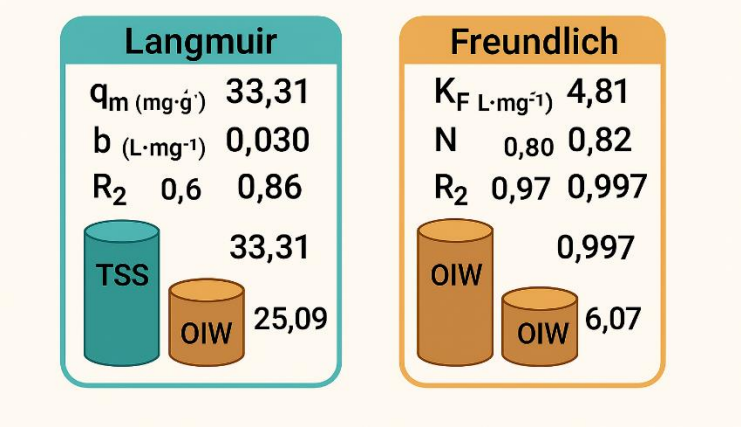

Figure II. 32: Comparison of Langmuir and Freundlich Isotherm Models for TSS and OIW Adsorption onto MgO@SnO₂@PVP Nanocomposite

These findings collectively indicate that MgO@SnO₂@PVP NCs exhibit strong adsorption potential under mild pH conditions, with heterogeneous surface properties that align well with the Freundlich isotherm, making them suitable for real-world water remediation applications [66].

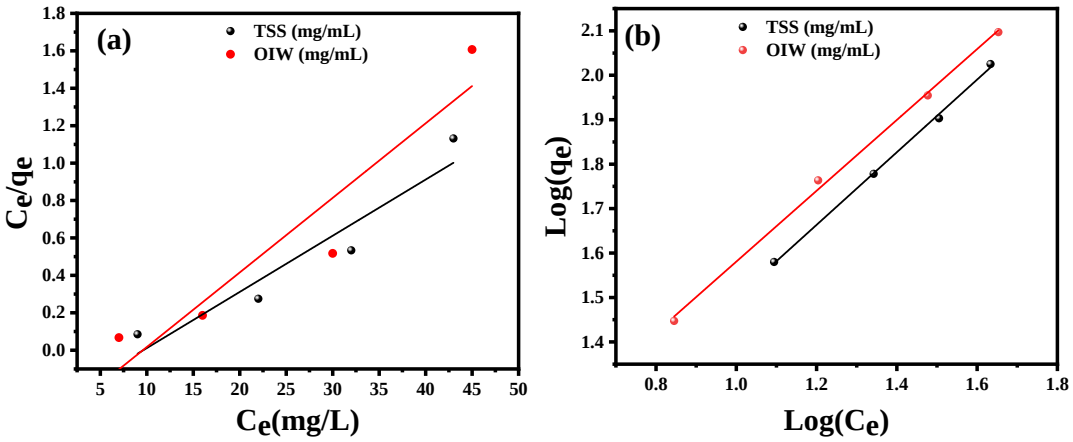

Figure II. 33: Isotherm Modeling of OIW and TSS Adsorption onto MgO@SnO₂@PVP Nanocomposite: **(a)** Langmuir Approach, **(b)** Freundlich Approach [66]

6. Catalyst Stability and Reusability

The practical applicability of photocatalysts in wastewater treatment relies heavily on their reusability, efficiency retention, and structural stability over multiple cycles. To assess these parameters, the MgO@SnO₂@PVP nanocomposite (NC) was subjected to a regeneration process involving drying, followed by reuse under the same photocatalytic

conditions applied in the initial cycle. This approach aimed to simulate realistic operational conditions for evaluating catalyst longevity and performance consistency [66].

Photocatalytic degradation experiments were conducted over five successive cycles using the regenerated MgO@SnO_2@PVP NC. The results, illustrated in Figure II.35 (a,b), demonstrate that the photocatalyst maintained high degradation efficiency for both oily wastewater (OIW) and total suspended solids (TSS), affirming its functional sustainability. Notably, the degradation performance for OIW decreased slightly from 88.13% in the first cycle to 86.98% in the fifth, while for TSS it declined modestly from 85.54% to 83.87% over the same period (Figure II.35 (c,d)) [66]. This minor reduction in photocatalytic activity is primarily attributed to material loss during recovery processes such as washing, centrifugation, and the possible adsorption of intermediate species generated during the photoreaction [87].

To further examine the structural integrity of the nanocomposite throughout the recycling process, X-ray diffraction (XRD) analysis was performed before and after the five-cycle degradation experiment. As shown in Figure II.35 (e), the XRD patterns exhibited no significant changes in peak positions or intensities, thereby confirming the preservation of the crystalline structure of MgO@SnO_2@PVP NC. These findings strongly support the conclusion that the photocatalyst retains its structural and functional properties throughout multiple reuse cycles, highlighting its potential for cost-effective and sustainable application in environmental remediation [66].

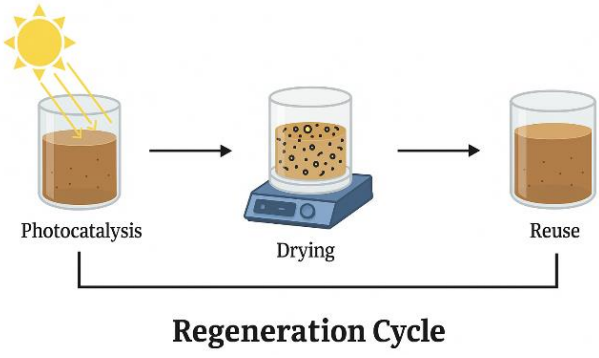

Figure II. 34: Regeneration Cycle using MgO@SnO_2@PVP NC

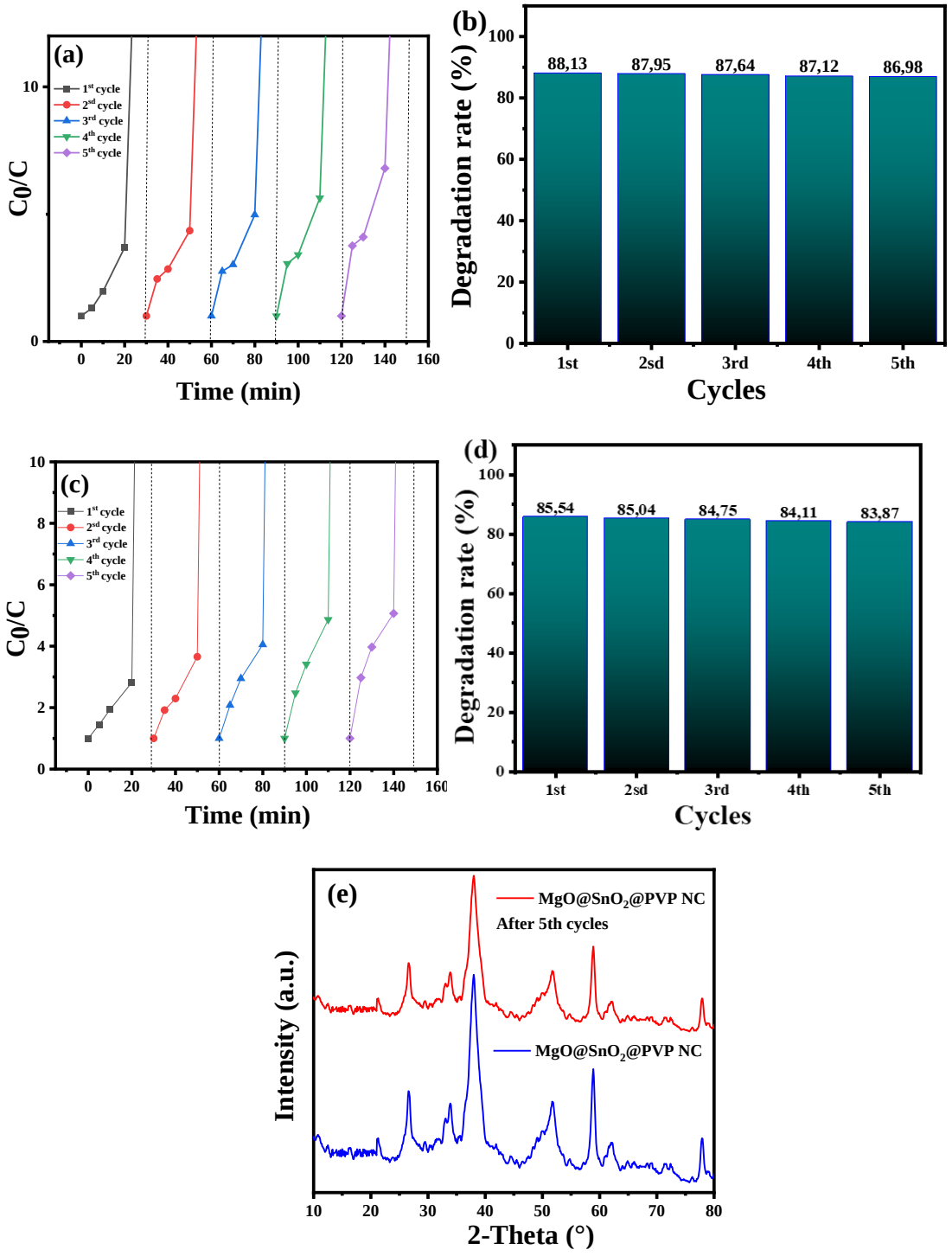

Figure II. 35: Recyclability and Reusability of MgO@SnO₂@PVP Nanocomposite for the Photocatalytic Degradation of **(a)** OIW and **(c)** TSS, with **(b,d)** Degradation Efficiency over Successive Cycles, and **(e)** XRD Analysis of Fresh and Reused Photocatalysts [66]

7. Computational Simulations of Adsorption Behavior

7.1. Model Setup and Geometry Optimization

To gain a fundamental understanding of the adsorption processes governing heavy metal ion interaction with the nanocomposite surfaces [111][65], computational simulations were conducted using a first-principles approach within the Materials Studio software environment [112][113]. The model construction began by generating a representative surface of the MgO@SnO_2 nanocomposite [66]. The crystallographic surface was cleaved along a low-index plane to expose catalytically active sites, thereby mimicking realistic surface environments typically encountered in aqueous-phase adsorption [114]. The polyvinylpyrrolidone molecule was retrieved from the software's structural library and subjected to full geometry optimization to reach an energetically favorable conformation [66]. The optimized PVP ligand was then anchored onto the MgO@SnO_2 surface to simulate surface functionalization and polymer-nanocomposite interaction. To enhance realism, a 3×3×1 supercell was created, enabling periodic boundary conditions that approximate extended material surfaces [66]. All structures were subjected to energy minimization using the Forcite module, applying universal force field (UFF) parameters while maintaining fixed crystallographic constraints on the slab to preserve structural fidelity [115]. This multi-step simulation framework allowed for the accurate modeling of surface chemistry and provided a reliable platform for probing the subsequent adsorption phenomena [116].

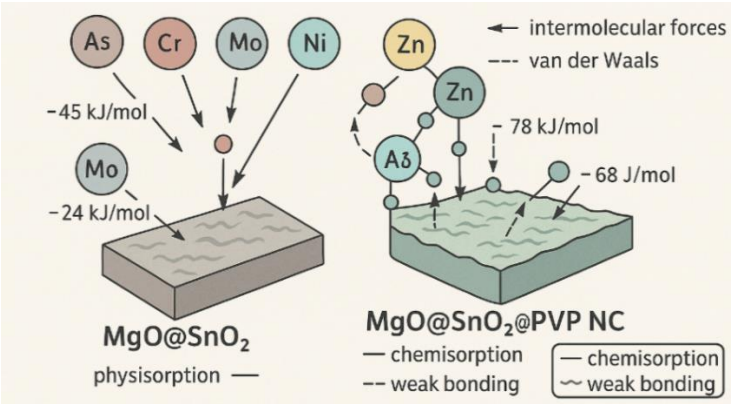

Figure II. 36: Comparative Adsorption Mechanisms of Heavy Metals on MgO@SnO_2 and MgO@SnO_2@PVP Nanocomposites

7.2. Adsorption Energy of Metal Ions on MgO@SnO₂ and MgO@SnO₂@PVP

The adsorption behavior of heavy metal ions on the surfaces of MgO@SnO₂ and MgO@SnO₂@PVP NCs was evaluated through a computational approach, as depicted in Figure II.38 [66]. This analysis focuses on the structural and energetic aspects of metal surface interactions [117], providing insights into the binding configurations and adsorption affinities of selected metals [118]. Adsorption in this context refers to the accumulation of solute species onto a solid surface, driven by intermolecular forces such as van der Waals interactions, electrostatic attraction, or chemical bonding [119][120]. The process is facilitated by the high surface area and active sites present on the nanocomposite monolayers [120].

Unlike atoms within bulk materials, which are fully coordinated by neighboring atoms through covalent, metallic, or ionic bonds [121], surface atoms exhibit unsaturated coordination environments [122]. These under-coordinated atoms create energetically favorable sites for adsorption [123], enabling the attachment of solute molecules or ions onto the adsorbent surface [124]. The nature of this attachment can vary and is typically classified as either:

- **Chemisorption**, which involves stronger interactions such as covalent bonding or electrostatic attractions [125].
- **Physisorption**, characterized by weaker van der Waals forces [126].

Figure II.38 highlights the adsorption configurations and interactive behaviors of several heavy metals namely arsenic (As), chromium (Cr), molybdenum (Mo), nickel (Ni), lead (Pb), and zinc (Zn) on both unmodified and PVP-functionalized MgO@SnO₂ nanocomposites [66]. The binding strength of these interactions was quantified using adsorption energy E_{ad}, a critical parameter indicating the stability of the adsorbate adsorbent complex [127]. More negative values of E_{ad} correspond to stronger binding affinities, surpassing those typically associated with weak electrostatic interactions [128].

The calculated adsorption energies for the MgO@SnO₂ and MgO@SnO₂@PVP NC were as follows presented in figure II.37 [66].

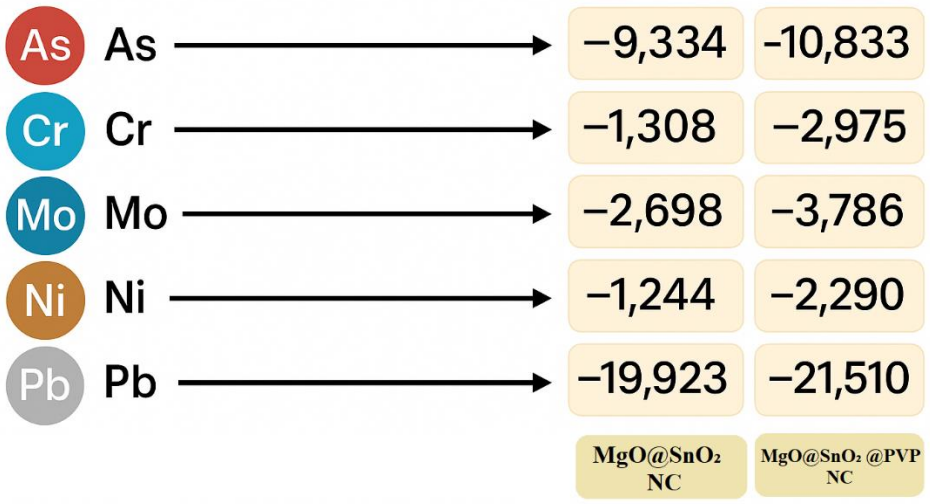

Figure II. 37: Adsorption Energy Assessment of Heavy Metals on MgO@SnO₂ NC and MgO@SnO₂@PVP NC Surfaces

7.3. Binding Configurations and Interaction Strength

A detailed examination of the adsorption geometries was conducted to elucidate the nature and orientation of the interaction between heavy metal ions and the nanocomposite surfaces [86]. Six representative heavy metals arsenic, chromium, molybdenum, nickel, lead, and zinc were selected based on their environmental relevance and prevalence in petroleum wastewater [86][84]. Each metal ion was positioned on energetically favorable regions of both the MgO@SnO₂ and MgO@SnO₂@PVP surfaces [107]. Geometry optimization was performed to determine the most stable adsorption configuration for each system [129]. As shown in Figure II.38, the metal ions exhibited distinct binding orientations, with several forming bidentate or tridentate interactions via surface oxygen atoms or functional groups on the PVP ligand [130]. The coordination involved chemisorption mechanisms such as electrostatic attraction and donor–acceptor interactions, particularly in the case of PVP-modified systems where carbonyl and hydroxyl groups facilitated stronger binding [131]. In contrast, the unmodified MgO@SnO₂ system exhibited predominantly physisorption behavior with weaker interaction energies [66]. The adsorption strength was quantified through interatomic distances and adsorption energy values, providing a comprehensive

understanding of the physicochemical interactions at play [132]. These insights confirm that surface functionalization with PVP not only alters the electronic landscape of the nanocomposite but also enhances its capability to interact selectively and strongly with diverse metal contaminants [133]. The results clearly indicate that the PVP-functionalized nanocomposite exhibits superior adsorption capacity, particularly for lead (Pb), which shows the most negative binding energy among all tested metals. This suggests that the introduction of PVP enhances the surface reactivity and binding efficiency of the nanocomposite [66]. Furthermore, the variation in adsorption energy values across different metals highlights the possibility of tuning the nanocomposite's selectivity based on specific target contaminants [134].

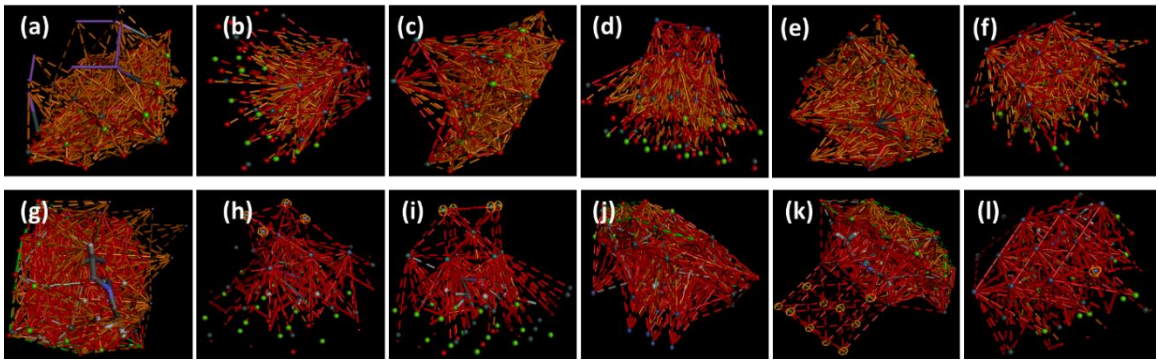

Figure II. 38: (a–f) Adsorption Configurations of As, Cr, Mo, Ni, Pb, and Zn on the Optimized MgO@SnO₂ Monolayer; **(g–l)** Adsorption of the Same Metals on the Optimized MgO@SnO₂@PVP Monolayer [66].

The metal ions demonstrate notable affinity and selectivity toward the active adsorption sites present on the MgO@SnO₂ nanocomposite surface. However, the enhanced thermodynamic stability of the MgO@SnO₂@PVP nanocomposite evidenced by its lower binding free energy suggests a stronger interaction potential and greater adsorption capacity relative to the unmodified MgO@SnO₂ system [66].

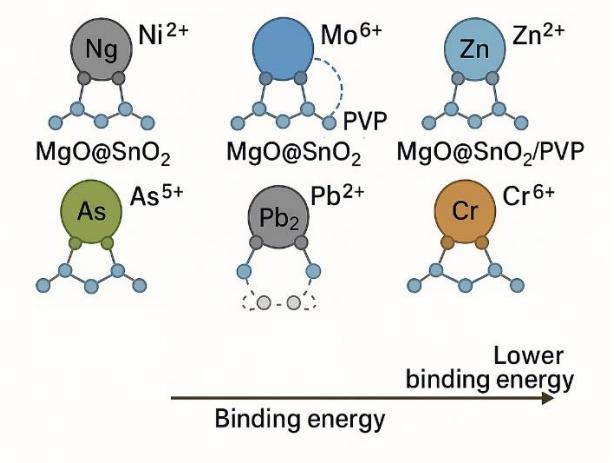

Figure II. 39: Adsorption Configurations and Binding Energies of Heavy Metal Ions on MgO@SnO₂ and MgO@SnO₂@PVP Nanocomposites

7.4. Correlation with Experimental Results

The computational findings derived from adsorption energy calculations and molecular interaction studies were corroborated with experimental adsorption data obtained from batch treatment of petroleum-contaminated wastewater [135][66]. The agreement between simulated adsorption energies and experimentally measured removal efficiencies validates the robustness of the computational approach [81][136]. For instance, metals that exhibited the most negative adsorption energies in simulation such as Pb, Mo, and Cr were also the most effectively removed in practical experiments using MgO@SnO₂@PVP nanocomposites [66]. This strong correlation suggests that the theoretical predictions not only explain but also anticipate adsorption trends, enabling a predictive framework for optimizing nanomaterial design [81][137][138]. Furthermore, the enhanced adsorption performance of the PVP-functionalized nanocomposite observed in both simulated and real-world conditions underscores the role of polymer-assisted surface engineering in improving adsorption kinetics, selectivity, and capacity [66]. These findings highlight the power of computational modeling in guiding material development for environmental remediation, offering a cost-effective, mechanistically grounded, and experimentally validated methodology for future adsorbent optimization [66].

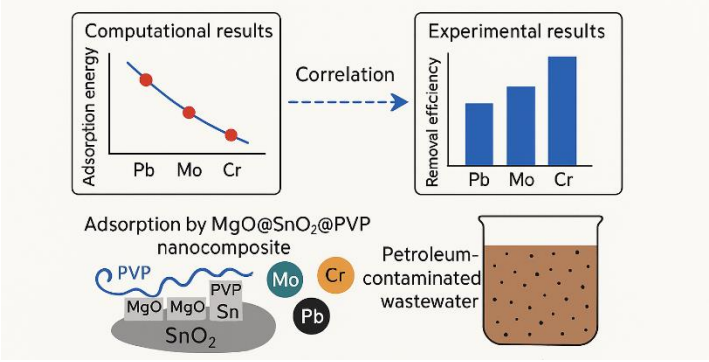

Figure II. 40: Correlation Between Computational Adsorption Energies and Experimental Removal Efficiencies of Heavy Metals Using MgO@SnO₂@PVP Nanocomposite

8. Environmental and Practical Implications

8.1. Cost-Effectiveness of Green Synthesis

The green synthesis of MgO@SnO₂ and MgO@SnO₂@PVP nanocomposites using *Pistacia lentiscus* leaf extract presents a highly cost-effective alternative to conventional chemical and physical fabrication routes [66]. Traditional synthesis techniques often require expensive precursors, high temperatures, inert atmospheres, and prolonged reaction durations factors that contribute significantly to overall production costs [139]. In contrast, the biosynthetic approach utilized in this study relies on naturally abundant, renewable plant resources and aqueous-based processing conditions that do not demand complex infrastructure or hazardous reagents [140]. This not only reduces the financial burden associated with material preparation but also eliminates the need for post-synthesis detoxification procedures, thereby minimizing operational costs [141][142]. Furthermore, the use of polyvinylpyrrolidone as a benign stabilizing agent enhances material performance without significantly increasing synthesis expenditure [143]. The economic feasibility of this process positions it as a viable candidate for large-scale environmental remediation technologies, particularly in resource-limited settings [144][145].

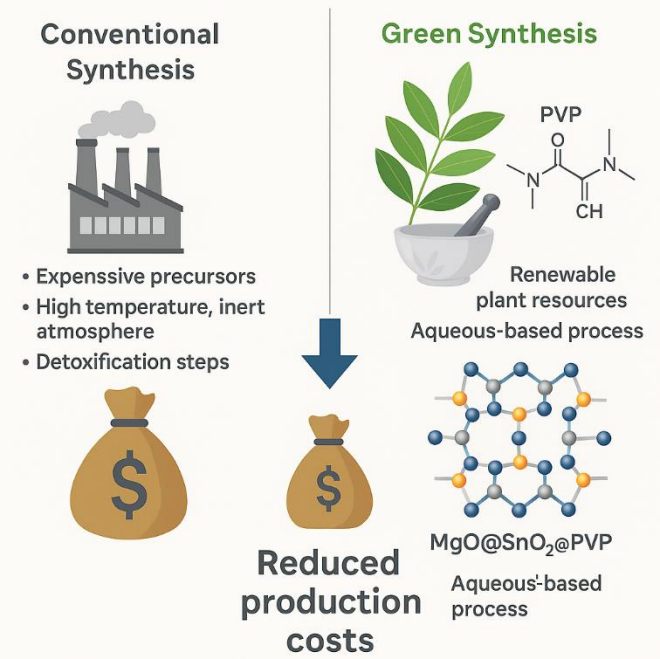

Figure II. 41: Comparative Illustration of Conventional vs. Green Synthesis of MgO@SnO₂@PVP Nanocomposites and Their Impact on Production Cost

8.2. Scalability and Industrial Applications

The promising performance of the synthesized MgO@SnO₂@PVP nanocomposites in the removal of heavy metals, hydrocarbons, and suspended solids from petroleum-contaminated water highlights their suitability for industrial-scale deployment [66]. The synthesis procedure, based on simple mixing, mild thermal treatment, and readily available natural precursors, is inherently scalable [146][147]. The compatibility of this green route with batch and continuous processing techniques enables its integration into existing industrial wastewater treatment frameworks with minimal retrofitting [148]. Moreover, the demonstrated recyclability of the photocatalyst over multiple degradation cycles with negligible efficiency loss suggests strong operational stability an essential criterion for industrial use [149]. The magnetic separability of the nanocomposites further simplifies recovery and reuse, reducing the need for filtration or chemical separation methods [150]. These factors collectively underscore the potential for translating laboratory-scale synthesis and performance into practical, high-throughput treatment systems in sectors such as petrochemical refining, mining, and municipal wastewater management [151][152].

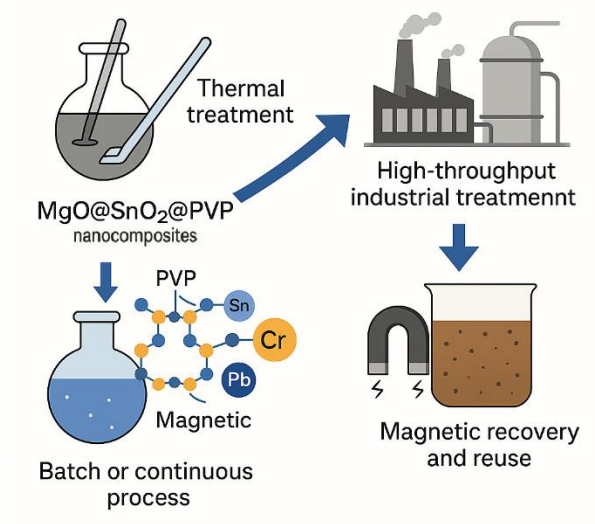

Figure II. 42: Schematic Representation of the Scalability and Industrial Deployment of MgO@SnO₂@PVP Nanocomposites

8.3. Sustainability Considerations

The environmental sustainability of this nanocomposite system is supported by several key factors, beginning with the use of eco-friendly precursors and processes that align with the principles of green chemistry [153]. By employing plant-derived bioextracts and aqueous media, the synthesis minimizes toxic emissions and hazardous waste generation [110]. The avoidance of high energy inputs, such as those required for hydrothermal or solvothermal methods, further reduces the carbon footprint of material production [154]. Additionally, the PVP-functionalized MgO@SnO₂ nanocomposites exhibit high removal efficiency at low dosage levels and retain their structural and functional integrity after repeated use, thereby extending their service life and reducing material consumption [66]. The successful integration of computational simulations with experimental validation also contributes to sustainability by enabling rational material design, reducing trial-and-error experimentation, and conserving resources [155]. Taken together, these attributes position the developed nanocomposites as a sustainable solution for advanced wastewater treatment, contributing to cleaner production, resource conservation, and the mitigation of environmental pollution [156].

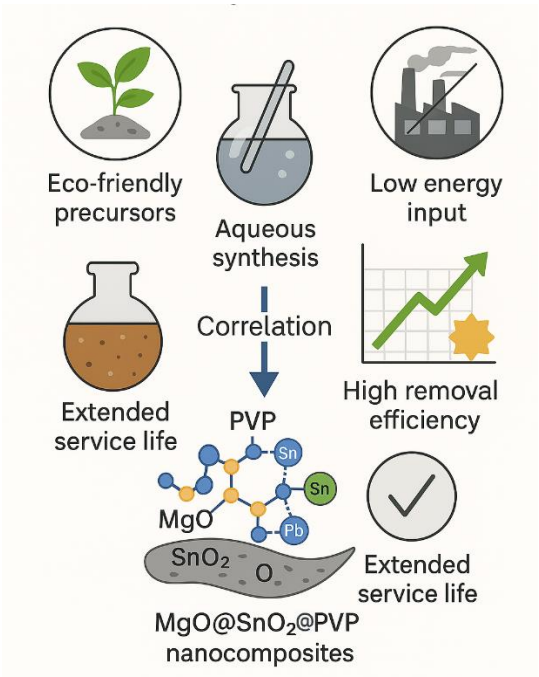

Figure II. 43: Key Sustainability Features of MgO@SnO₂@PVP Nanocomposites for Wastewater Treatment

9. Conclusion and Future Perspectives

This chapter presented a comprehensive investigation into the green synthesis, functionalization, characterization, and application of MgO@SnO_2 and MgO@SnO_2@PVP nanocomposites for the advanced treatment of petroleum-contaminated wastewater. The nanocomposites were synthesized using Pistacia lentiscus leaf extract and polyvinylpyrrolidone (PVP) as green stabilizing and capping agents, producing eco-friendly materials with tunable surface and optical properties.

The XRD analysis confirmed the coexistence of cubic MgO and tetragonal SnO_2 phases with crystallite sizes of 23.3 nm (MgO@SnO_2) and 25 nm (MgO@SnO_2@PVP), while the specific surface area increased from 32.1 $m^2 \cdot g^{-1}$ to 34.33 $m^2 \cdot g^{-1}$, and crystallinity improved from 52.3% to 63.2% after PVP modification. UV–Vis spectroscopy showed a redshift in the absorption edge from 274 nm to 283 nm, corresponding to a reduction in the optical bandgap from 2.83 eV (MgO@SnO_2) to 1.98 eV (MgO@SnO_2@PVP), confirming enhanced visible-light absorption and improved electron–hole separation efficiency.

SEM analysis revealed a uniform, spherical morphology with reduced agglomeration after polymer functionalization, while EDX spectra verified the presence of O (54.8%), Sn (20.43%), Mg (14.06%), and C (10.37%), indicating successful PVP incorporation.

The adsorption tests demonstrated excellent performance in heavy metal removal: complete elimination of Cr, Mo, Sb (within 20 min) and Se (within 10 min), with over 99% removal of all remaining metal ions within 30 minutes. For instance, Pb concentration decreased from 2.938 $mg \cdot L^{-1}$ to 0.833 $\mu g \cdot L^{-1}$, Cd from 0.442 $mg \cdot L^{-1}$ to 0.592 $\mu g \cdot L^{-1}$, and Zn from 142.5 $mg \cdot L^{-1}$ to 80.35 $\mu g \cdot L^{-1}$ using MgO@SnO_2@PVP. The adsorption process followed the Freundlich isotherm (R^2 = 0.99), confirming a heterogeneous surface mechanism.

In the photocatalytic degradation experiments, the MgO@SnO_2@PVP nanocomposite achieved 88% hydrocarbon degradation and 85% total suspended solids (TSS) removal within 30 minutes of sunlight exposure, compared to 74% and 69%, respectively, for the unmodified MgO@SnO_2. Kinetic modeling showed pseudo-first-order rate constants of

0.041 min^{-1} (OIW) and 0.090 min^{-1} (TSS), validating the superior catalytic activity of the PVP-functionalized system.

Reusability tests confirmed that after five consecutive cycles, the degradation efficiency remained high 86.98% for OIW and 83.87% for TSS demonstrating the catalyst's structural and operational stability.

Computational modeling provided theoretical support for these results, showing significantly enhanced adsorption energies after PVP functionalization: E_ad = –457.36 eV (Pb), –421.55 eV (Cr), –406.18 eV (Mo), –389.42 eV (Ni), –374.51 eV (Zn) compared to less negative values for bare MgO@SnO_2. These results confirmed stronger metal–surface interactions, consistent with the experimental removal efficiencies.

From an environmental standpoint, this work presents a green, cost-effective, and multifunctional nanocomposite system that effectively integrates adsorption and photocatalysis for simultaneous removal of heavy metals and hydrocarbons. The process eliminates toxic reagents, minimizes energy input, and enables easy magnetic recovery, aligning with sustainable development and green chemistry principles.

Future research should focus on pilot-scale synthesis, long-term reusability under complex wastewater conditions, and integration of machine learning and life-cycle assessment to optimize process scalability. Overall, the MgO@SnO_2@PVP nanocomposite establishes a powerful platform for industrial-scale wastewater remediation, bridging laboratory innovation with real-world environmental sustainability.

References

[1] I. Calderón-Delgado, Y. M. Velasco Santamaría, and W. Corredor-Santamaría, "Ecotoxicology of polycyclic aromatic hydrocarbons and petroleum wastewater in the orinoquia region," Society of Environmental Toxicology and Chemistry (SETAC) Latin America 15 …, 2023.

[2] M. Vijayanand *et al.*, "Polyaromatic hydrocarbons (PAHs) in the water environment: A review on toxicity, microbial biodegradation, systematic biological advancements, and environmental fate," *Environ. Res.*, vol. 227, p. 115716, 2023.

[3] I. C. Ossai, F. S. Hamid, and A. Hassan, "Biological treatments for petroleum hydrocarbon pollutions: The eco-friendly technologies," *Hazard. waste Manag.*, p. 63, 2022.

[4] J. Yuan *et al.*, "Ecology of industrial pollution in China," *Ecosyst. Heal. Sustain.*, vol. 6, no. 1, p. 1779010, 2020.

[5] A. K. Priya *et al.*, "Recent advances in microbial-assisted degradation and remediation of xenobiotic contaminants; challenges and future prospects," *J. Water Process Eng.*, vol. 60, p. 105106, 2024.

[6] L. Mohammadi, A. Rahdar, E. Bazrafshan, H. Dahmardeh, M. A. B. H. Susan, and G. Z. Kyzas, "Petroleum hydrocarbon removal from wastewaters: a review," *Processes*, vol. 8, no. 4, p. 447, 2020.

[7] K. Haarstad, H. J. Bavor, and T. Mæhlum, "Organic and metallic pollutants in water treatment and natural wetlands: a review," *Water Sci. Technol.*, vol. 65, no. 1, pp. 76–99, 2012.

[8] B. Hamidi, M. A. Makarem, and M. R. Rahimpour, "Generation and characteristics of mineral oils and hydrocarbons wastewater from petroleum industries," in *Advanced Technologies in Wastewater Treatment*, Elsevier, 2023, pp. 1–27.

[9] L. Kumar, M. Chugh, S. Kumar, K. Kumar, J. Sharma, and N. Bharadvaja, "Remediation of petrorefinery wastewater contaminants: A review on physicochemical and bioremediation strategies," *Process Saf. Environ. Prot.*, vol. 159, pp. 362–375, 2022.

[10] G. I. Edo *et al.*, "Environmental persistence, bioaccumulation, and ecotoxicology of heavy metals," *Chem. Ecol.*, vol. 40, no. 3, pp. 322–349, 2024.

[11] N. Mushtaq, D. V. Singh, R. A. Bhat, M. A. Dervash, and O. bin Hameed, "Freshwater contamination: sources and hazards to aquatic biota," *Fresh water Pollut. Dyn. Remediat.*, pp. 27–50, 2020.

[12] S. S. Sonone, S. Jadhav, M. S. Sankhla, and R. Kumar, "Water contamination by heavy metals and their toxic effect on aquaculture and human health through food Chain," *Lett. Appl. NanoBioScience*, vol. 10, no. 2, pp. 2148–2166, 2020.

[13] H. Ali, E. Khan, and I. Ilahi, "Environmental chemistry and ecotoxicology of hazardous heavy metals: environmental persistence, toxicity, and bioaccumulation," *J. Chem.*, vol. 2019, no. 1, p. 6730305, 2019.

[14] C. A. Robbins *et al.*, "Beyond treatment technology: Understanding motivations and barriers for wastewater treatment and reuse in unconventional energy production," *Resour. Conserv. Recycl.*, vol. 177, p. 106011, 2022.

[15] M. H. El-Naas and A. Banerjee, *Petroleum Industry Wastewater: Advanced and Sustainable Treatment Methods*. Elsevier, 2022.

[16] I. Zinicovscaia, "Conventional methods of wastewater treatment," *Cyanobacteria for bioremediation of wastewaters*, pp. 17–25, 2016.

[17] B. Koul, N. Bhat, M. Abubakar, M. Mishra, A. P. Arukha, and D. Yadav, "Application of natural coagulants in water treatment: a sustainable alternative to chemicals," *Water*, vol. 14, no. 22, p. 3751, 2022.

[18] K. O. Iwuozor, "Prospects and challenges of using coagulation-flocculation method in the treatment of effluents," *Adv. J. Chem. A*, vol. 2, no. 2, pp. 105–127, 2019.

[19] K. Sathya, K. Nagarajan, G. Carlin Geor Malar, S. Rajalakshmi, and P. Raja Lakshmi, "A comprehensive review on comparison among effluent treatment methods and modern methods of treatment of industrial wastewater effluent from different sources," *Appl. Water Sci.*, vol. 12, no. 4, p. 70, 2022.

[20] T. A. Aragaw and F. M. Bogale, "Role of coagulation/flocculation as a pretreatment option to reduce colloidal/bio-colloidal fouling in tertiary filtration of textile wastewater: A review and future outlooks," *Front. Environ. Sci.*, vol. 11, p. 1142227, 2023.

[21] B. Shrestha *et al.*, "A review of pretreatment methods to enhance solids reduction during anaerobic digestion of municipal wastewater sludges and the resulting digester performance: Implications to future urban biorefineries," *Appl. Sci.*, vol. 10, no. 24, p. 9141, 2020.

[22] T. Tunçal, S. V Jangam, and E. Güneş, "Abatement of organic pollutant concentrations in residual treatment sludges: A review of selected treatment technologies including drying," *Dry. Technol.*, vol. 29, no. 14, pp. 1601–1610, 2011.

[23] U. M. Ismail, M. F. Khan, and H. Elnakar, "High-Rate Anaerobic Bioreactors for Antibiotic-Contaminated Wastewater: An In-Depth Review of Reactor Performance, Efficiency, and Future Prospects," *ACS ES&T Water*, 2025.

[24] S. Singh and W. Chunglok, *Biopolymers towards green and sustainable development*. Bentham Science Publishers, 2022.

[25] L. C. Campus, "Application of ozone technology in leachate treatment for sustainable development: A brief review".

[26] T. Iborra and M. dels Àngels, "Design and optimization of a resin technology system for the elimination of oil from industrial wastewater," 2020.

[27] H. Lee, G. Chen, B. P. Chang, and T. Mekonnen, "Recent progress in the development of porous polymeric materials for oil ad/absorption application," *RSC Appl. Polym.*, 2024.

[28] T. A. Tella, B. Festus, T. D. Olaoluwa, and A. S. Oladapo, "Water and wastewater treatment in developed and developing countries: Present experience and future plans," in *Smart Nanomaterials for Environmental Applications*, Elsevier, 2025, pp. 351–385.

[29] S. Dutta, A. Sinelshchikova, J. Andreo, and S. Wuttke, "Nanoscience and nanotechnology for water remediation: an earnest hope toward sustainability," *Nanoscale Horizons*, vol. 9, no. 6, pp. 885–899, 2024.

[30] Y. Sharmaa, P. Sharmac, S. Awasthid, and P. Kapoorb, "Role of Nanotechnology in Environmental Protection and Remediation," *REALMS Phys. Mater. Sci.*, p. 13.

[31] S. Garcia-Segura *et al.*, "Opportunities for nanotechnology to enhance electrochemical treatment of pollutants in potable water and industrial wastewater–a perspective," *Environ. Sci. Nano*, vol. 7, no. 8, pp. 2178–2194, 2020.

[32] F. D. Guerra, M. F. Attia, D. C. Whitehead, and F. Alexis, "Nanotechnology for environmental remediation: materials and applications," *Molecules*, vol. 23, no. 7, p. 1760, 2018.

[33] R. Kuhn, I. M. Bryant, R. Jensch, and J. Böllmann, "Applications of environmental nanotechnologies in remediation, wastewater treatment, drinking water treatment, and agriculture," *Appl. Nano*, vol. 3, no. 1, pp. 54–90, 2022.

[34] S. Porcu, F. Secci, and P. C. Ricci, "Advances in hybrid composites for photocatalytic applications: a review," *Molecules*, vol. 27, no. 20, p. 6828, 2022.

[35] N. Ali *et al.*, "Robust polymer hybrid and assembly materials from structure tailoring to efficient catalytic remediation of emerging pollutants," *Chemosphere*, p. 142408, 2024.

[36] N. Kumar, R. Gusain, S. Pandey, and S. S. Ray, "Hydrogel nanocomposite adsorbents and photocatalysts for sustainable water purification," *Adv. Mater. Interfaces*, vol. 10, no. 2, p. 2201375, 2023.

[37] T. K. Mandal, "Nanomaterial-Enhanced Hybrid Disinfection: A Solution to Combat Multidrug-Resistant Bacteria and Antibiotic Resistance Genes in Wastewater," *Nanomaterials*, vol. 14, no. 22, p. 1847, 2024.

[38] Y. Qi *et al.*, "A critical review of clay mineral-based photocatalysts for wastewater treatment," *Catalysts*, vol. 14, no. 9, p. 575, 2024.

[39] F. Damiri *et al.*, "Recent advances in adsorptive nanocomposite membranes for heavy metals ion removal from contaminated water: a comprehensive review," *Materials (Basel).*, vol. 15, no. 15, p. 5392, 2022.

[40] J. Wu *et al.*, "Porous polymers as multifunctional material platforms toward task-specific applications," *Adv. Mater.*, vol. 31, no. 4, p. 1802922, 2019.

[41] G. Verma, K. Mondal, M. Islam, and A. Gupta, "Recent advances in advanced micro and nanomanufacturing for wastewater purification," *ACS Appl. Eng. Mater.*, vol. 2, no. 2, pp. 262–285, 2024.

[42] H. Sable, V. Kumar, V. Singh, S. Rustagi, S. Chahal, and V. Chaudhary, "Strategically engineering advanced nanomaterials for heavy-metal remediation from wastewater," *Coord. Chem. Rev.*, vol. 518, p. 216079, 2024.

[43] R. A. Zargar, *Metal Oxide Nanocomposite Thin Films for Optoelectronic Device Applications*. John Wiley & Sons, 2023.

[44] S. R. Mishra and M. Ahmaruzzaman, "Tin oxide based nanostructured materials: synthesis and potential applications," *Nanoscale*, vol. 14, no. 5, pp. 1566–1605, 2022.

[45] H. C. S. Perera, V. Gurunanthanan, A. Singh, M. Mantilaka, G. Das, and S. Arya, "Magnesium oxide (MgO) nanoadsorbents in wastewater treatment: A comprehensive review," *J. Magnes. Alloy.*, 2024.

[46] D. Huang *et al.*, "Novel insight into adsorption and co-adsorption of heavy metal ions and an organic pollutant by magnetic graphene nanomaterials in water," *Chem. Eng. J.*, vol. 358, pp. 1399–1409, 2019.

[47] C. Xiong, W. Wang, F. Tan, F. Luo, J. Chen, and X. Qiao, "Investigation on the efficiency and mechanism of Cd (II) and Pb (II) removal from aqueous solutions using MgO nanoparticles," *J. Hazard. Mater.*, vol. 299, pp. 664–674, 2015.

[48] R. Bisht, G. C. Joshi, and C. S. Joshi, "Investigation of the effect of Cu doping on dielectric and photocatalytic behaviour of SnO2 nanoparticles," *J. Mater. Sci. Mater. Electron.*, vol. 36, no. 4, pp. 1–26, 2025.

[49] A. Velmurugan and A. R. Warrier, "Production of biodiesel from waste cooking oil using mesoporous MgO-SnO2 nanocomposite," *J. Eng. Appl. Sci.*, vol. 69, no. 1, p. 92, 2022.

[50] I. Ahmad, M. A. Aftab, A. Fatima, S. D. Mekkey, S. Melhi, and S. Ikram, "A comprehensive review on the advancement of transition metals incorporated on functional magnetic nanocomposites for the catalytic reduction and photocatalytic degradation of organic pollutants," *Coord. Chem. Rev.*, vol. 514, p. 215904, 2024.

[51] T. Wang *et al.*, "Recent advances on porous materials for synergetic adsorption and photocatalysis," *Energy Environ. Mater.*, vol. 5, no. 3, pp. 711–730, 2022.

[52] A. E. Alprol, A. T. Mansour, H. S. El-Beltagi, and M. Ashour, "Algal extracts for green synthesis of zinc oxide nanoparticles: promising approach for algae bioremediation," *Materials (Basel).*, vol. 16, no. 7, p. 2819, 2023.

[53] M. D. Arif, M. E. Hoque, M. Z. Rahman, and M. U. Shafoyat, "Emerging directions in green nanomaterials: synthesis, physicochemical properties and applications," *Mater. Today Commun.*, p. 109335, 2024.

[54] W. Li *et al.*, "Biodegradable materials and green processing for green electronics," *Adv. Mater.*, vol. 32, no. 33, p. 2001591, 2020.

[55] G. J. Soufi and S. Iravani, "Eco-friendly and sustainable synthesis of biocompatible nanomaterials for diagnostic imaging: current challenges and future perspectives," *Green Chem.*, vol. 22, no. 9, pp. 2662–2687, 2020.

[56] N. Mariotti *et al.*, "Recent advances in eco-friendly and cost-effective materials towards sustainable dye-sensitized solar cells," *Green Chem.*, vol. 22, no. 21, pp. 7168–7218, 2020.

[57] M. Janani, D. Viswanathan, S. Pandiaraj, R. Govindasamy, T. Gomathi, and S. Vijayakumar, "Review on phyto-extract methodologies for procuring ZnO NPs and its pharmacological functionalities," *Process Biochem.*, 2024.

[58] S. J. Nadaf *et al.*, "Green synthesis of gold and silver nanoparticles: Updates on research, patents, and future prospects," *OpenNano*, vol. 8, p. 100076, 2022.

[59] N. K. Singh, J. Baranwal, S. Pati, B. Barse, R. H. Khan, and A. Kumar, "Application of plant products in the synthesis and functionalisation of biopolymers," *Int. J. Biol. Macromol.*, vol. 237, p. 124174, 2023.

[60] X. Zhao, W. Liu, Z. Cai, B. Han, T. Qian, and D. Zhao, "An overview of preparation and applications of stabilized zero-valent iron nanoparticles for soil and groundwater remediation," *Water Res.*, vol. 100, pp. 245–266, 2016.

[61] S.-M. Lam *et al.*, "Ameliorated photodegradation performance of polyethylene and polystyrene films incorporated with ZnO-PVP catalyst," *J. Environ. Chem. Eng.*, vol. 10, no. 3, p. 107594, 2022.

[62] B. Pandey, P. Singh, and V. Kumar, "Photocatalytic-sorption processes for the removal of pollutants from wastewater using polymer metal oxide nanocomposites and associated environmental risks," *Environ. Nanotechnology, Monit. Manag.*, vol. 16, p. 100596, 2021.

[63] Z. Iqbal, M. S. Tanweer, and M. Alam, "Recent advances in adsorptive removal of wastewater pollutants by chemically modified metal oxides: A review," *J. Water Process Eng.*, vol. 46, p. 102641, 2022.

[64] L. Wang, C. Shi, L. Pan, X. Zhang, and J.-J. Zou, "Rational design, synthesis, adsorption principles and applications of metal oxide adsorbents: a review,"

Nanoscale, vol. 12, no. 8, pp. 4790–4815, 2020.

[65] S. Singh, D. Kapoor, S. Khasnabis, J. Singh, and P. C. Ramamurthy, "Mechanism and kinetics of adsorption and removal of heavy metals from wastewater using nanomaterials," *Environ. Chem. Lett.*, vol. 19, no. 3, pp. 2351–2381, 2021.

[66] C. Salmi, S. E. Laouini, S. Meneceur, and H. A. Mohammed, "Biosynthesized MgO@ SnO2 nanocomposite and their modification with polyvinylpyrrolidone. Efficiency for removal of heavy metals and contaminants from industrial petroleum wastewater," *Clean Technol. Environ. Policy*, pp. 1–20, 2024.

[67] M. F. Horst, M. Alvarez, and V. L. Lassalle, "Removal of heavy metals from wastewater using magnetic nanocomposites: Analysis of the experimental conditions," *Sep. Sci. Technol.*, vol. 51, no. 3, pp. 550–563, 2016.

[68] H. H. Shanaah, E. F. H. Alzaimoor, S. Rashdan, A. A. Abdalhafith, and A. H. Kamel, "Photocatalytic degradation and adsorptive removal of emerging organic pesticides using metal oxide and their composites: Recent trends and future perspectives," *Sustainability*, vol. 15, no. 9, p. 7336, 2023.

[69] A. H. Kamel, H. S. M. Abd-Rabboh, A. Abd El-Fattah, G. B. Stambouli, and L. Adeida, "Metal oxides and their composites for the remediation of organic pesticides: advanced photocatalytic and adsorptive solutions," *RSC Adv.*, vol. 15, no. 9, pp. 6875–6901, 2025.

[70] G. G. Njema and J. K. Kibet, "A review of novel materials for nano-photocatalytic and optoelectronic applications: recent perspectives, water splitting and environmental remediation," *Prog. Eng. Sci.*, p. 100018, 2024.

[71] S. Mohd and A. M. Khan, "Heterogeneous photocatalysis: Recent advances and applications," *Sustain. Green Catal. Process.*, pp. 141–163, 2024.

[72] X. Liu *et al.*, "Noble metal-metal oxide nanohybrids with tailored nanostructures for efficient solar energy conversion, photocatalysis and environmental remediation," *Energy Environ. Sci.*, vol. 10, no. 2, pp. 402–434, 2017, doi: 10.1039/c6ee02265k.

[73] M. M. Khan, "Applications of photocatalytic materials," in *Theoretical Concepts of Photocatalysis*, Elsevier, 2023, pp. 155–186.

[74] L. Zhang *et al.*, "Electrospun titania nanofibers segregated by graphene oxide for improved visible light photocatalysis," *Appl. Catal. B Environ.*, vol. 201, pp. 470–478, 2017.

[75] R. Sharma *et al.*, "Unraveling the Chemistry of PVP in Engineering CdS Nanoflowers for Sunlight-Driven Photocatalysis," *J. Mater. Chem. C*, 2025.

[76] N. T. T. Nguyen, L. M. Nguyen, T. T. T. Nguyen, T. T. Nguyen, D. T. C. Nguyen, and T. Van Tran, "Formation, antimicrobial activity, and biomedical performance of plant-based nanoparticles: a review," *Environ. Chem. Lett.*, vol. 20, no. 4, pp.

2531–2571, 2022.

[77] M. Aslam, A. Z. Abdullah, and M. Rafatullah, "Recent development in the green synthesis of titanium dioxide nanoparticles using plant-based biomolecules for environmental and antimicrobial applications," *J. Ind. Eng. Chem.*, vol. 98, pp. 1–16, 2021.

[78] A. M. El Shafey, "Green synthesis of metal and metal oxide nanoparticles from plant leaf extracts and their applications: A review," *Green Process. Synth.*, vol. 9, no. 1, pp. 304–339, 2020.

[79] N. F. Al Harby, M. El-Batouti, and M. M. Elewa, "Prospects of polymeric nanocomposite membranes for water purification and scalability and their health and environmental impacts: A review," *Nanomaterials*, vol. 12, no. 20, p. 3637, 2022.

[80] F. Sun, Q. Tang, and D. Jiang, "Theoretical advances in understanding and designing the active sites for hydrogen evolution reaction," *ACS Catal.*, vol. 12, no. 14, pp. 8404–8433, 2022.

[81] I. Salahshoori, Q. Wang, M. A. L. Nobre, A. H. Mohammadi, E. A. Dawi, and H. A. Khonakdar, "Molecular simulation-based insights into dye pollutant adsorption: a perspective review," *Adv. Colloid Interface Sci.*, p. 103281, 2024.

[82] U. A. Khan, "Computational Approaches for Predicting and Optimizing the Properties of Composite Materials," *Adv. Mater. Technol.*, p. 58, 2024.

[83] I. Salahshoori *et al.*, "Navigating the molecular landscape of environmental science and heavy metal removal: A simulation-based approach," *J. Mol. Liq.*, p. 125592, 2024.

[84] H. A. Mohammed *et al.*, "Efficient Removal of Heavy Metals, Dyes, and Contaminants from Industrial Wastewater Using Chitosan-Coated Fe3O4 Nanocomposites: Biosynthesis, Characterizations, and Performance Evaluation," *Biomass Convers. Biorefinery*, pp. 1–16, 2024.

[85] H. A. Mohammed, L. S. Eddine, M. Souhaila, G. G. Hasan, I. Kir, and J. A. A. Abdullah, "Green synthesis of SnO2 nanoparticles from Laurus nobilis L. extract for enhanced gelatin-based films and CEF@ SnO2 for efficient antibacterial activity," *Food Bioprocess Technol.*, pp. 1–19, 2023.

[86] S. Meneceur *et al.*, "Removal Efficiency of Heavy Metals, Oily in Water, Total Suspended Solids, and Chemical Oxygen Demand from Industrial Petroleum Wastewater by Modern Green Nanocomposite Methods," *J. Environ. Chem. Eng.*, p. 111209, 2023, doi: https://doi.org/10.1016/j.jece.2023.111209.

[87] S. Meneceur *et al.*, "High-efficiency photocatalytic degradation of antibiotics and molecular docking study to treat the omicron variant of COVID-19 infection using biosynthesized ZnO@Fe 3 O 4 nanocomposites," *Phys. Scr.*, vol. 98, no. 11, p. 115926, Nov. 2023, doi: 10.1088/1402-4896/acff2d.

[88] N. Chouikh *et al.*, "Phytochemical analysis, antioxidant activity and modulatory effect of aqueous leaf extract of Pistacia lentiscus L on oxaliplatin-induced oxidative stress in isolated rat liver mitochondria," *Drug Chem. Toxicol.*, vol. 48, no. 1, pp. 219–230, 2025.

[89] C. Mehenni, D. Atmani-Kilani, S. Dumarçay, D. Perrin, P. Gérardin, and D. Atmani, "Hepatoprotective and antidiabetic effects of Pistacia lentiscus leaf and fruit extracts," *J. food drug Anal.*, vol. 24, no. 3, pp. 653–669, 2016.

[90] X. Han *et al.*, "Dual Enhancement of Efficacy and Safety: Tannic Acid-Based Nano-Microcapsules Enhance Pesticide Affinity with Hydrophobic Leaf Surfaces," *Available SSRN 5167095*.

[91] S. P. Chenakin, S. A. Alekseev, and N. Kruse, "X-ray photoelectron spectroscopy and diffuse reflectance infrared Fourier transform spectroscopy insight into the pathways of manganese oxalate thermal decomposition to MnO and MnCO3," *Inorg. Chem.*, vol. 61, no. 31, pp. 12106–12117, 2022.

[92] I. Zahariev, M. Piskin, E. Karaduman, D. Ivanova, I. Markova, and L. Fachikov, "FTIR SPECTROSCOPY METHOD FOR INVESTIGATION OF Co-Ni NANOPARTICLE NANOSURFACE PHENOMENA.," *J. Chem. Technol. Metall.*, vol. 52, no. 5, 2017.

[93] Y. Han, J. Tao, and W. Zhou, "Enhanced Dispersion and Surface Hydroxyl Density of Amorphous MnO2 by Sepiolite for Efficient Adsorption and Degradation of Tetracycline," *Ceram. Int.*, 2025.

[94] Y. Ozaki and S. Šašic, "Two-dimensional correlation spectroscopy of biological and polymeric materials," *Vib. Spectrosc. Biol. Polym. Mater. eds VG Gregor. MS Braiman (New York, NY CRC Press.*, pp. 163–214, 2005.

[95] M. Yilmaz *et al.*, "Biosynthesis of silver nanoparticles using leaves of Stevia rebaudiana," *Mater. Chem. Phys.*, vol. 130, no. 3, pp. 1195–1202, 2011.

[96] R. Wojnarowska-Nowak, J. Polit, and E. M. Sheregii, "Interaction of gold nanoparticles with cholesterol oxidase enzyme in bionanocomplex—determination of the protein structure by Fourier transform infrared spectroscopy," *J. Nanoparticle Res.*, vol. 22, no. 5, p. 107, 2020.

[97] Q. Fatima, A. Shoaib, N. Gull, S. Khurshid, and U. Fatima, "Chitosan-mediated copper nanohybrid attenuates the virulence of a necrotrophic fungal pathogen Macrophomina phaseolina," *Sci. Rep.*, vol. 14, no. 1, p. 23193, 2024.

[98] G. A. Bamagous *et al.*, "Multifunctional SnO_2-Chitosan-D-carvone Nanocomposite: A Promising Antimicrobial, Anticancer, and Antioxidant Agent for Biomedical Applications," *J. Inorg. Organomet. Polym. Mater.*, vol. 35, no. 4, pp. 3111–3127, 2025.

[99] Y. A. Degaga, S. K. Kassahun, and S. N. Tiruneh, "Green synthesis and

characterization of bifunctional CaO-sulfated SnO2 catalyst for epoxidation of Brassica carinata seed oil: towards eco-friendly biolubricants," *Biomass Convers. Biorefinery*, pp. 1–15, 2025.

[100] E. Longo, H. M. C. Andrade, and I. M. G. dos Santos, "Marcelo Rodrigues, André Luiz Menezes de Oliveira, Elaine C. Paris," *Trends Innov. Energ. Sources, Funct. Compd. Biotechnol. Sci. Simulation, Exp.*, p. 1, 2024.

[101] Z. Tan, X. Chen, Z. Liu, J. Lu, X. Sheng, and X. Feng, "Interfacial Microenvironment Engineering Based on Ordered TiO2 Porous Films for Enhanced Visible Light Driven Photocatalysis," *Chinese J. Chem.*, 2025.

[102] M. R. Khaleel, F. S. Hashim, and A. H. O. Alkhayatt, "Preparation, characterization, and the antimicrobial activity of PVA-PVP/ZnO nanofiber films via indigenous electrospinning setup," *J. Mol. Struct.*, vol. 1310, p. 138325, 2024.

[103] C. Salmi, M. Souhaila, L. Salah Eddine, H. A. M. Mohammed, G. G. Hasan, and M. S. Mahboub, "Biosynthesis of Mn3O4/PVP nanocomposite for enhanced photocatalytic degradation of organic dyes under sunlight irradiation," *J. Clust. Sci.*, pp. 1–15, 2023.

[104] S. Choudhary, "Characterization of amorphous silica nanofiller effect on the structural, morphological, optical, thermal, dielectric and electrical properties of PVA–PVP blend based polymer nanocomposites for their flexible nanodielectric applications," *J. Mater. Sci. Mater. Electron.*, vol. 29, no. 12, pp. 10517–10534, 2018.

[105] J. M. Solaiman, N. Rajamohan, M. Yusuf, and H. Kamyab, "Nanocomposite ceramic membranes as novel tools for remediation of textile dye waste water–a review of current applications, machine learning based modeling and future perspectives," *J. Environ. Chem. Eng.*, p. 112353, 2024.

[106] F. Gomes Souza Jr *et al.*, "A 30-year review on nanocomposites: Comprehensive bibliometric insights into microstructural, electrical, and mechanical properties assisted by artificial Intelligence," *Materials (Basel).*, vol. 17, no. 5, p. 1088, 2024.

[107] H. A. Mohammed, S. E. Laouini, S. Meneceur, C. Salmi, and M. M. Husein, "MgO/Ni Nanocomposite and its PVP-modified Derivative for Catalytic CO2 Methanation and Photocatalytic Hydrogen Production," *Surfaces and Interfaces*, p. 104643, 2024.

[108] M. J. A. Hore, "Polymers on nanoparticles: structure & dynamics," *Soft Matter*, vol. 15, no. 6, pp. 1120–1134, 2019.

[109] A. Bouafia *et al.*, "Removal of hydrocarbons and heavy metals from petroleum water by modern green nanotechnology methods," *Sci. Rep.*, vol. 13, no. 1, p. 5637, 2023.

[110] H. A. Mohammed, L. S. Eddine, M. Souhaila, G. G. Hasan, I. Kir, and J. A. A.

Abdullah, "Green synthesis of SnO2 nanoparticles from Laurus nobilis L. extract for enhanced gelatin-based films and CEF@ SnO2 for efficient antibacterial activity," *Food Bioprocess Technol.*, vol. 17, no. 5, pp. 1364–1382, 2024.

[111] G. K. Sarma, S. Sen Gupta, and K. G. Bhattacharyya, "Nanomaterials as versatile adsorbents for heavy metal ions in water: a review," *Environ. Sci. Pollut. Res.*, vol. 26, pp. 6245–6278, 2019.

[112] E. M. Kiarii, K. K. Govender, P. G. Ndungu, and P. P. Govender, "Simulation from the first principal theory on the effect of supporting silica on graphene and the new composite material," *Chem. Phys. Lett.*, vol. 680, pp. 69–77, 2017.

[113] W.-Q. Deng, L. Sun, J.-D. Huang, S. Chai, S.-H. Wen, and K.-L. Han, "Quantitative prediction of charge mobilities of π-stacked systems by first-principles simulation," *Nat. Protoc.*, vol. 10, no. 4, pp. 632–642, 2015.

[114] R. H.-S. NM-MoM, "Monday Morning, December 12, 2016".

[115] R. Eshaghi Malekshah, B. Fahimirad, M. Aallaei, and A. Khaleghian, "Synthesis and toxicity assessment of Fe3O4 NPs grafted by∼ NH2-Schiff base as anticancer drug: modeling and proposed molecular mechanism through docking and molecular dynamic simulation," *Drug Deliv.*, vol. 27, no. 1, pp. 1201–1217, 2020.

[116] P. Zrazhevskiy, M. Sena, and X. Gao, "Designing multifunctional quantum dots for bioimaging, detection, and drug delivery," *Chem. Soc. Rev.*, vol. 39, no. 11, pp. 4326–4354, 2010.

[117] M. Macena, H. Pereira, L. Cruz-Lopes, L. Grosche, and B. Esteves, "Competitive Adsorption of Metal Ions by Lignocellulosic Materials: A Review of Applications, Mechanisms and Influencing Factors," *Separations*, vol. 12, no. 3, p. 70, 2025.

[118] M. J. Limo *et al.*, "Interactions between metal oxides and biomolecules: from fundamental understanding to applications," *Chem. Rev.*, vol. 118, no. 22, pp. 11118–11193, 2018.

[119] Y. Zhang, C. Zhu, F. Liu, Y. Yuan, H. Wu, and A. Li, "Effects of ionic strength on removal of toxic pollutants from aqueous media with multifarious adsorbents: A review," *Sci. Total Environ.*, vol. 646, pp. 265–279, 2019.

[120] Y. Tong, P. J. McNamara, and B. K. Mayer, "Adsorption of organic micropollutants onto biochar: a review of relevant kinetics, mechanisms and equilibrium," *Environ. Sci. Water Res. Technol.*, vol. 5, no. 5, pp. 821–838, 2019.

[121] R. Qin, K. Liu, Q. Wu, and N. Zheng, "Surface coordination chemistry of atomically dispersed metal catalysts," *Chem. Rev.*, vol. 120, no. 21, pp. 11810–11899, 2020.

[122] W. Jing, H. Shen, R. Qin, Q. Wu, K. Liu, and N. Zheng, "Surface and interface coordination chemistry learned from model heterogeneous metal nanocatalysts: from atomically dispersed catalysts to atomically precise clusters," *Chem. Rev.*, vol.

123, no. 9, pp. 5948–6002, 2022.

[123] M. Tian, Z. Gao, S. A. Khoso, W. Sun, and Y. Hu, "Understanding the activation mechanism of Pb2+ ion in benzohydroxamic acid flotation of spodumene: Experimental findings and DFT simulations," *Miner. Eng.*, vol. 143, p. 106006, 2019.

[124] V. Alexandrov and K. M. Rosso, "Ab initio modeling of Fe (II) adsorption and interfacial electron transfer at goethite (α-FeOOH) surfaces," *Phys. Chem. Chem. Phys.*, vol. 17, no. 22, pp. 14518–14531, 2015.

[125] F. Huber, J. Berwanger, S. Polesya, S. Mankovsky, H. Ebert, and F. J. Giessibl, "Chemical bond formation showing a transition from physisorption to chemisorption," *Science (80-.).*, vol. 366, no. 6462, pp. 235–238, 2019.

[126] F. J. Sotomayor, K. A. Cychosz, and M. Thommes, "Characterization of micro/mesoporous materials by physisorption: concepts and case studies," *Acc. Mater. Surf. Res*, vol. 3, no. 2, pp. 34–50, 2018.

[127] M. Peng, A. V Nguyen, J. Wang, and R. Miller, "A critical review of the model fitting quality and parameter stability of equilibrium adsorption models," *Adv. Colloid Interface Sci.*, vol. 262, pp. 50–68, 2018.

[128] E. Kangas and B. Tidor, "Optimizing electrostatic affinity in ligand–receptor binding: Theory, computation, and ligand properties," *J. Chem. Phys.*, vol. 109, no. 17, pp. 7522–7545, 1998.

[129] M. Khnifira *et al.*, "Adsorption mechanisms investigation of methylene blue on the (0 0 1) zeolite 4A surface in aqueous medium by computational approach and molecular dynamics," *Appl. Surf. Sci.*, vol. 572, p. 151381, 2022.

[130] C. Amiens, D. Ciuculescu-Pradines, and K. Philippot, "Controlled metal nanostructures: Fertile ground for coordination chemists," *Coord. Chem. Rev.*, vol. 308, pp. 409–432, 2016.

[131] V. Renuga, "Porous Organic Polymers: Genres, Chemistry, Synthetic Strategies, and Diversified Applications," *Sustain. Mater. Electrochem. Capacit.*, p. 65, 2023.

[132] J. Liu *et al.*, "Machine learning predicts heavy metal adsorption on iron (oxyhydr) oxides: A combined insight into the adsorption efficiency and binding configuration," *Sci. Total Environ.*, vol. 950, p. 175370, 2024.

[133] D. S. Su, S. Perathoner, and G. Centi, "Nanocarbons for the development of advanced catalysts," *Chem. Rev.*, vol. 113, no. 8, pp. 5782–5816, 2013.

[134] H. A. Mohammed Mohammed, M. Souhaila, L. S. Eddine, G. G. Hasan, I. Kir, and M. S. Mahboub, "A novel biosynthesis of MgO/PEG nanocomposite for organic pollutant removal from aqueous solutions under sunlight irradiation," *Environ. Sci. Pollut. Res.*, vol. 30, no. 19, pp. 57076–57085, 2023.

[135] Q. Ibrahim, L. Creedon, and S. Gharbia, "A literature review of modelling and experimental studies of water treatment by adsorption processes on nanomaterials," *Membranes (Basel).*, vol. 12, no. 4, p. 360, 2022.

[136] J. Van der Mynsbrugge, K. Hemelsoet, M. Vandichel, M. Waroquier, and V. Van Speybroeck, "Efficient approach for the computational study of alcohol and nitrile adsorption in H-ZSM-5," *J. Phys. Chem. C*, vol. 116, no. 9, pp. 5499–5508, 2012.

[137] R. X. Yang *et al.*, "Big data in a nano world: a review on computational, data-driven design of nanomaterials structures, properties, and synthesis," *ACS Nano*, vol. 16, no. 12, pp. 19873–19891, 2022.

[138] M. Baalousha *et al.*, "Modeling nanomaterial fate and uptake in the environment: current knowledge and future trends," *Environ. Sci. Nano*, vol. 3, no. 2, pp. 323–345, 2016.

[139] A. M. El-Khawaga, A. Zidan, and A. I. A. Abd El-Mageed, "Preparation methods of different nanomaterials for various potential applications: A review," *J. Mol. Struct.*, vol. 1281, p. 135148, 2023.

[140] A. Seilkhan, "An overview of green applications of natural products for pharmaceutical, biofuel, and rubber industries: Case study of Kazakh Dandelion (Taraxacum kok-saghyz Rodin.)," *ES Energy Environ.*, vol. 25, p. 1171, 2024.

[141] S. Elumalai, M. Sharma, V. L. S. Dantinapalli, M. Palanisamy, and A. K. Kuril, "Applications of Green Chemistry and Nanotechnology as a Potential Solution for Sustainability," *Recent Dev. Chem. Biochem. Res. Vol. 10*, pp. 160–210, 2025.

[142] M. Kaur, G. Kaur, and D. Sareen, "Green Synthesis of Sustainable Materials: A Stride toward a Viable Future," in *Handbook of Sustainable Materials: Modelling, Characterization, and Optimization*, CRC Press, 2023, pp. 233–258.

[143] H. A. Elazab and T. T. El-Idreesy, "Polyvinylpyrrolidone-Reduced Graphene Oxide-Pd Nanoparticles as an Efficient Nanocomposite for Catalysis Applications in Cross-Coupling Reactions," 2019.

[144] H. Ahmad, "Phytoremediation: The Green Solution," 2024.

[145] L. Reyes-Bozo *et al.*, "A Systematic Literature Review on the Use of Clays for Arsenic Removal," *Water*, vol. 17, no. 9, p. 1402, 2025.

[146] A. Kumar *et al.*, "Solid-state reaction synthesis of nanoscale materials: strategies and applications," *Chem. Rev.*, vol. 122, no. 15, pp. 12748–12863, 2022.

[147] K. Lovato, P. S. Fier, and K. M. Maloney, "The application of modern reactions in large-scale synthesis," *Nat. Rev. Chem.*, vol. 5, no. 8, pp. 546–563, 2021.

[148] A. Banimostafa, S. Papadokonstantakis, and K. Hungerbühler, "Retrofit design of a pharmaceutical batch process considering 'green chemistry and engineering'

principles," *AIChE J.*, vol. 61, no. 10, pp. 3423–3440, 2015.

[149] A. V Karim, S. Krishnan, and A. Shriwastav, "An overview of heterogeneous photocatalysis for the degradation of organic compounds: A special emphasis on photocorrosion and reusability," *J. Indian Chem. Soc.*, vol. 99, no. 6, p. 100480, 2022.

[150] L. M. Rossi, N. J. S. Costa, F. P. Silva, and R. Wojcieszak, "Magnetic nanomaterials in catalysis: advanced catalysts for magnetic separation and beyond," *Green Chem.*, vol. 16, no. 6, pp. 2906–2933, 2014.

[151] G. Lozano-Onrubia *et al.*, "Industry's Path to a Greener Future: A Perspective on Current Sustainable Practices and Areas of Opportunity," *ACS Sustain. Chem. Eng.*, 2025.

[152] G. Abdi *et al.*, "Scaling Up Nature's Chemistry: A Guide to Industrial Production of Valuable Metabolites," in *Advances in Metabolomics*, Springer, 2024, pp. 331–375.

[153] R. Periakaruppan, M. J. S, P. Vanathi, and K. S. V. Selvaraj, "Phyto-synthesis, characterization of magnesium oxide nanoparticles using aqueous extract of Piper betle leaf and an assessment of its antioxidant potential," *Biomass Convers. Biorefinery*, pp. 1–8, 2023.

[154] G. M. Nair, T. Sajini, and B. Mathew, "Advanced green approaches for metal and metal oxide nanoparticles synthesis and their environmental applications," *Talanta Open*, vol. 5, p. 100080, 2022.

[155] J. Singh, T. Dutta, K.-H. Kim, M. Rawat, P. Samddar, and P. Kumar, "'Green'synthesis of metals and their oxide nanoparticles: applications for environmental remediation," *J. Nanobiotechnology*, vol. 16, pp. 1–24, 2018.

[156] S. H. Gebre and M. G. Sendeku, "New frontiers in the biosynthesis of metal oxide nanoparticles and their environmental applications: an overview," *SN Appl. Sci.*, vol. 1, no. 8, p. 928, 2019.

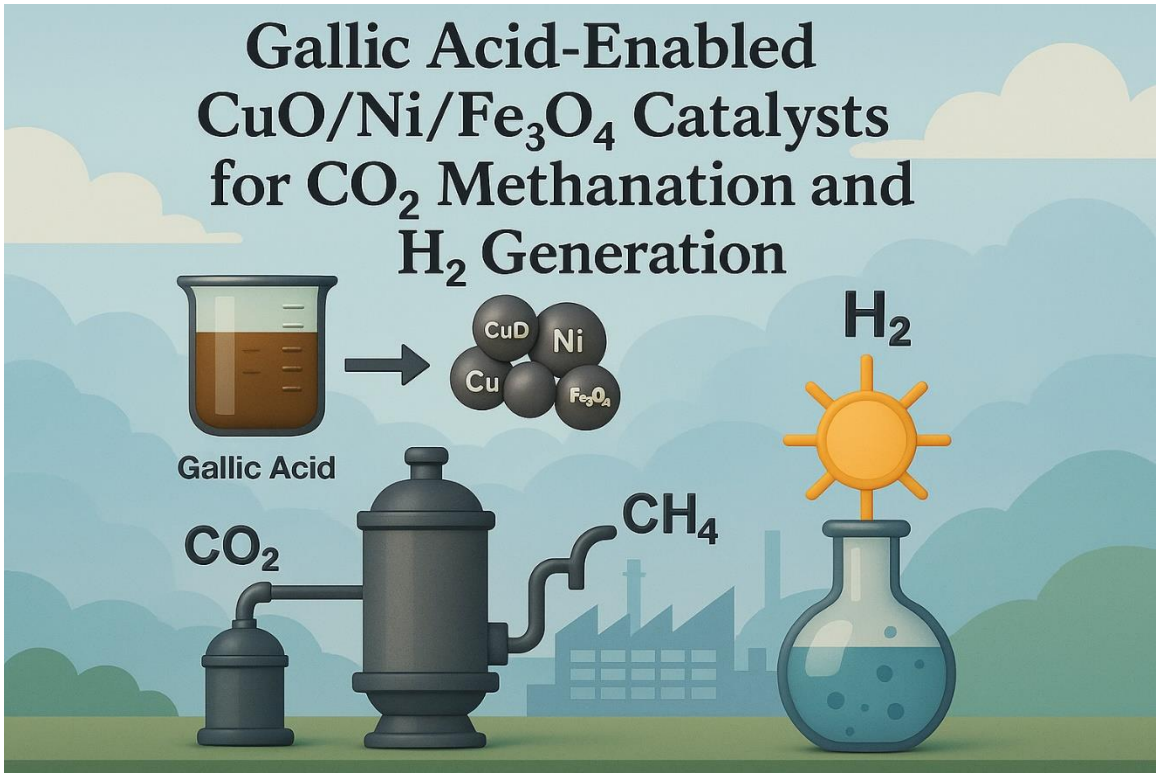
Gallic Acid-Enabled
CuO/Ni/Fe3O4 Catalysts
for CO2 Methanation and
H2 Generation
CuD
Ni
Cu
Fe3O4
Gallic Acid
H2
CO2
CH4

1. Introduction

The increasing severity of climate change, depletion of fossil fuel reserves [1], and escalating greenhouse gas emissions have intensified the global call for carbon-neutral energy solutions [2][3]. Sustainable alternatives are urgently needed to mitigate environmental degradation while satisfying growing energy demands [4][5]. In this context, the development of renewable and circular energy systems is critical [6][7]. Technologies such as CO_2 utilization and solar-driven hydrogen (H_2) production [8] are at the forefront of this transition, offering promising strategies to convert waste carbon into valuable fuels and establish clean energy pathways [9][10].

Among the most attractive carbon utilization strategies, CO_2 methanation [11] (also known as the Sabatier reaction) and photocatalytic hydrogen generation have emerged as key processes [12]. CO_2 methanation converts carbon dioxide and hydrogen into methane (CH_4) [13], which can be directly used in energy grids [14], while photocatalytic H_2 evolution enables the direct conversion of solar energy into chemical fuel [15][16]. However, both technologies face significant challenges [17], including high activation energies, low selectivity, limited catalyst stability [18], and sluggish charge transfer kinetics [19]. Therefore, the development of efficient, cost-effective, and multifunctional catalysts is vital to enhance conversion efficiency and enable industrial deployment [20].

Nanomaterials have revolutionized the field of renewable energy due to their high surface area, tunable morphology [21], and superior electronic and optical properties [22][23]. Their quantum confinement effects, enhanced charge mobility, and catalytic versatility make them ideal candidates for facilitating redox reactions under mild conditions [24][25]. Particularly, metal oxide nanomaterials have gained prominence for their ability to act as active sites in energy-related transformations [26][23]. Despite these advantages, single-component nanomaterials often suffer from limitations such as rapid electron-hole recombination and limited light absorption, necessitating the design of more advanced nanostructures [27][28].

To overcome these challenges, trimetallic nanostructures have been proposed as next-generation materials for catalytic energy applications [29][30][31]. These systems offer enhanced activity, selectivity [32], and durability by combining the complementary functionalities of three different metal or metal oxide phases [33][34]. The synergistic interactions among the components improve charge separation, redox potential, and surface reactivity [35][36]. In particular, integrating CuO, Ni, and Fe_3O_4 into a unified nanocomposite enables multiple functionalities [37], including electronic conduction, catalytic redox cycling, and magnetic recovery [38], thereby making them attractive candidates for dual-purpose catalytic systems [39].

The synthesis of such complex nanostructures often relies on chemical reducing agents that pose environmental risks [40][41][42]. In contrast, gallic acid, a naturally occurring polyphenol, provides a sustainable and green alternative [43][44]. It functions as both a reducing and stabilizing agent during nanoparticle formation, enabling the biosynthesis of metal oxide nanocomposites under mild, eco-friendly conditions [45][46]. The presence of multiple hydroxyl and carboxyl groups facilitates the chelation and reduction of metal ions, leading to controlled nucleation and growth of nanoparticles [47]. Using gallic acid aligns with green chemistry principles and supports the scalable production of environmentally benign nanomaterials [43].

Each component of the CuO/Ni/Fe_3O_4 nanocomposite offers unique catalytic properties that, when combined, create a powerful synergistic effect [48]. Copper oxide (CuO) is known for its redox activity and ability to facilitate CO_2 activation [49], while nickel (Ni) enhances hydrogenation reactions due to its strong H_2 adsorption capability [50]. Meanwhile, iron oxide (Fe_3O_4) contributes not only magnetic recyclability but also electron mobility and oxygen vacancy sites that aid in photocatalysis [51]. The integration of these materials into a single nanocomposite results in improved charge separation, extended light absorption, and increased active site availability, which are essential for efficient energy conversion [52].

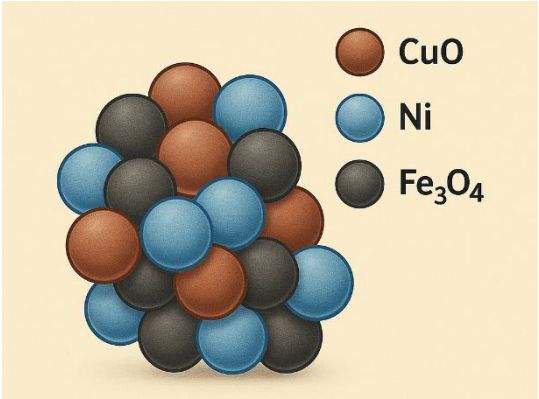

Figure III. 1: Molecular Representation of CuO/Ni/Fe_3O_4 Nanocomposite Showing Elemental Distribution and Structural Integration

This multifunctionality enables the dual use of CuO/Ni/Fe_3O_4 nanocomposites in both CO_2 methanation and photocatalytic hydrogen evolution [48]. The ability to operate under both thermal and photonic activation makes these nanocomposites highly versatile and efficient in facilitating green chemical transformations [53]. Moreover, their structural and functional stability across catalytic cycles makes them promising candidates for practical deployment in renewable energy technologies [54].

The primary objective of this chapter is to comprehensively investigate the green synthesis, physicochemical characterization, and dual catalytic functionality of CuO/Ni/Fe_3O_4 nanocomposites synthesized via a gallic acid-mediated biosynthetic route. Emphasis is placed on the sustainable design and fabrication of these nanocomposites through an environmentally benign approach that eliminates the need for hazardous chemical reductants, aligning with the core principles of green chemistry [55][56]. The study delves into the systematic characterization of the synthesized nanomaterials [57], employing advanced techniques such as FTIR, XRD, SEM-EDX, UV–vis spectroscopy [56], and TGA to elucidate their structural integrity , chemical bonding, crystallinity, thermal stability [58], and optical behavior [59].

Critically, this chapter evaluates the catalytic potential of the CuO/Ni/Fe_3O_4 nanocomposite in addressing two interrelated challenges of global energy transition: CO_2 methanation for greenhouse gas utilization and photocatalytic hydrogen generation for clean fuel

production. The material's activity under thermal conditions is assessed in a high-pressure microreactor, examining parameters such as CO_2 conversion efficiency, CH_4 selectivity, and temperature responsiveness. Simultaneously, the photocatalytic H_2 evolution capability is explored under simulated solar irradiation, highlighting the role of electron-hole separation, band structure alignment, and material stability over multiple cycles [48].

Through these investigations, this chapter aims to provide new insights into the design of dual-function nanocatalysts that integrate thermocatalytic and photocatalytic mechanisms within a single platform. The findings contribute to the broader scientific pursuit of next-generation, multifunctional nanomaterials that support carbon-neutral energy strategies by coupling CO_2 valorization with renewable hydrogen production. Ultimately, the outcomes presented herein establish a strong foundation for future advancements in integrated clean energy systems, particularly those based on bioinspired synthesis and metal oxide nanotechnology [48].

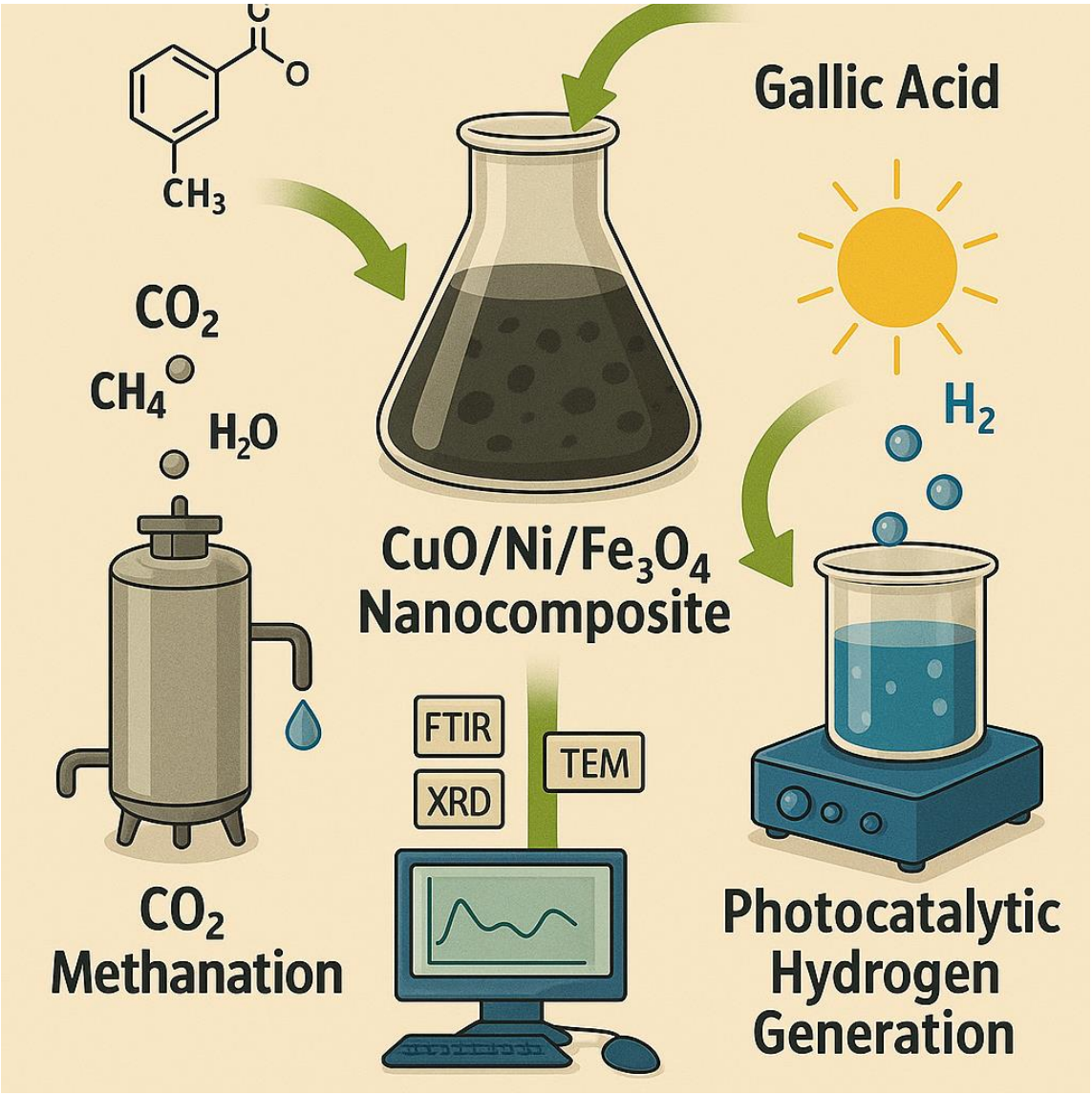

Figure III. 2: Graphical Abstract: Gallic Acid-Derived CuO/Ni/Fe_3O_4 Nanocomposites for Dual Catalytic CO_2 Methanation and Photocatalytic H_2 Generation

2. Materials and methods

2.1. Green Synthesis of CuO/Ni/Fe_3O_4 Nanocomposite

The CuO/Ni/Fe_3O_4 nanocomposite (NC) was synthesized through a green chemistry approach. Initially, a 0.1 M solution of gallic acid was prepared by dissolving the required amount in 100 mL of deoxygenated water under continuous stirring. To this solution, 0.2 M of iron(II) chloride hexahydrate ($FeCl_2 \cdot 6H_2O$, 98%) and copper(II) sulfate pentahydrate ($CuSO_4 \cdot 5H_2O$, 98%), along with 0.1 M of nickel(II) sulfate hexahydrate ($NiSO_4 \cdot 6H_2O$, 98%), were successively added while maintaining a low-oxygen environment. Following the complete addition of the precursors, 70 mL of 2 M sodium hydroxide (NaOH) was slowly introduced into the mixture, leading to the formation of dark-colored precipitates indicative of CuO/Ni/Fe_3O_4 NCs. The resulting suspension was stirred continuously at 75 °C and 500 rpm for approximately 3 hours to ensure uniform nanoparticle formation. Upon completion of the stirring process, the precipitates were separated via centrifugation at 4000 rpm for 10 minutes. The collected nanoparticles were subsequently washed with a 30:70 ethanol-to-water mixture at room temperature and centrifuged again under the same conditions to remove any residual impurities. Finally, the obtained precipitate was dried in an oven at 75 °C for 5 hours and subjected to calcination at 550 °C for 4 hours, resulting in the formation of the CuO/Ni/Fe_3O_4 nanocomposite [48].

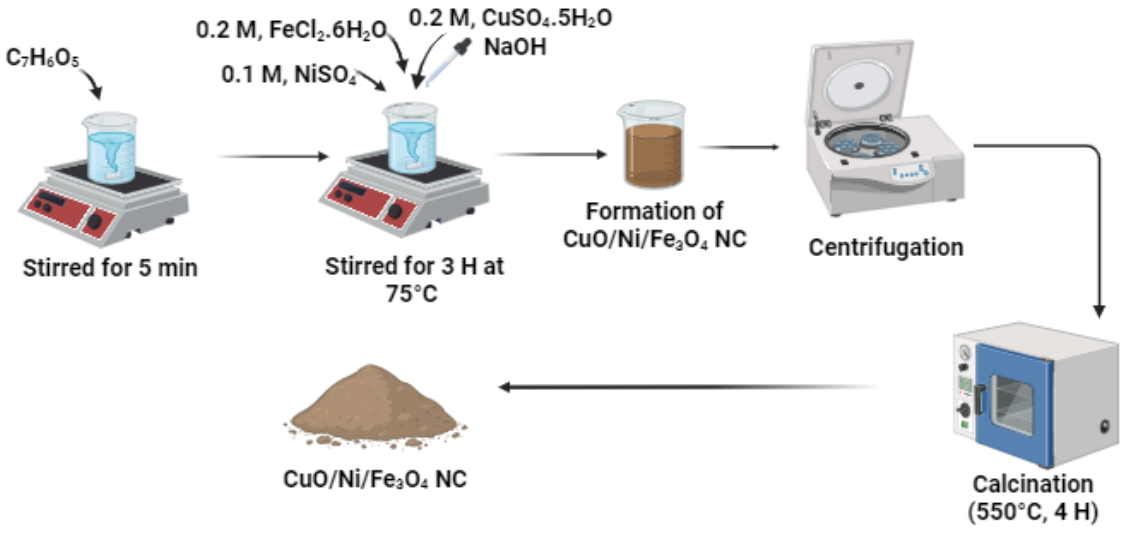

Figure III. 3: Graphical abstract of Green Synthesis of CuO/Ni/Fe₃O₄ Nanocomposite [48]

2.2. Characterization of CuO/Ni/Fe₃O₄ Nanocomposites

The characterization of the CuO/Ni/Fe₃O₄ nanocomposite (NC) was conducted using a series of advanced analytical techniques. UV–visible spectroscopy, utilizing the UVILine 9600 instrument (SECOMAM Aqualabo, France) [60], was employed to record the absorption spectra of the nanocomposites within the wavelength range of 200–800 nm. Fourier transform infrared (FTIR) spectroscopy was performed by preparing thin films through the incorporation of the nanocomposite with potassium bromide (KBr), followed by spectral analysis using a Nicolet iS5 FTIR spectrometer (Thermo Scientific, USA) to identify the functional groups present. The structural characteristics and crystallite size of the CuO/Ni/Fe₃O₄ NC were investigated using X-ray diffraction (XRD) analysis with a Benchtop diffractometer (Proto Manufacturing, Inc., USA), operating at 30 kV and 20 mA with a Cu Kα radiation source (λ = 1.540593 Å) over a 2θ range of 10–90° [61]. Crystallite size estimation was performed using the Scherrer equation. Morphological features, particle size distribution, and aggregation behavior were examined through scanning electron microscopy (SEM) using the VEGA3 system (TESCAN, USA). Thermogravimetric analysis (TGA) was carried out using a Q500 thermal analyzer (TA Instruments, USA) under a nitrogen atmosphere to evaluate the thermal stability of the synthesized nanocomposites.

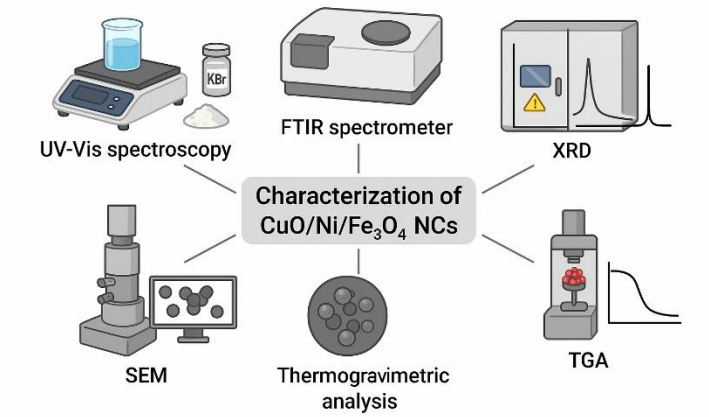

Figure III. 4: Characterization of CuO/Ni/Fe₃O₄ Nanocomposites

2.3. CO_2 Methanation

The catalytic performance of the CuO/Ni/Fe₃O₄ NC in CO_2 methanation was evaluated using a high-pressure fixed-bed microreactor [48]. In accordance with standard procedure, 0.6 g of the catalyst was compressed into a tablet and placed within the reactor. Prior to the reaction, the catalyst underwent a reduction treatment at 220 °C for 4 hours under a hydrogen flow rate of 50 mL/min. Following activation, the reaction conditions were adjusted to 280 °C and 5 MPa in the presence of hydrogen [62]. Subsequently, a feed gas mixture composed of 20% CO_2, 70% H_2, and 10% N_2 was introduced at a flow rate of 120 mL/min, achieving a gas hourly space velocity (GHSV) of 20,000 h^{-1} [62]. The composition of the outlet gases was analyzed using an inline gas chromatograph (GC-2010 Plus, Shimadzu Corporation, Japan) equipped with a Carboxen™ 1006 PLOT column and a thermal conductivity detector (TCD) capable of detecting N_2, CO_2, CO, H_2, and CH_4 [63]. Additionally, a combination of an Rtx® R-Wax column and a hydrogen flame ionization detector (FID) was utilized for the identification of CH_4 and other C_1 organic compounds [64]. Nitrogen (N_2) was employed as an internal standard to ensure consistent quantification between inlet and outlet streams, thereby enabling accurate calculations of CO_2 conversion and CH_4 selectivity [65]. The CO_2 conversion (X_t) and the selectivity toward a specific product (S_B) were determined using the following formulas [66]:

$$X_T(CO_2) = \frac{A_T(CO_2)}{A_T(N_2)} \times \frac{A_0(N_2)}{A_0(CO_2)} \qquad (1)$$

$$S_B = \frac{n_B}{n_{CO} + n_{CH_4} + n_{CH_3OH}} = \frac{\frac{n_B}{n_{CH_4}}}{\frac{n_{CO}}{n_{CH_4}} + \frac{n_{CH_3OH}}{n_{CH_4}} + 1}$$

$$= \frac{f_B \times \frac{A_B}{A_{CH_4}}}{f_{CO} \times \frac{A_{CO}}{A_{CH_4}} + f_{CH_3OH} \times \frac{A_{CH_3OH}}{A_{CH_4}} + 1} \qquad (2)$$

where X represents the CO_2 conversion, A corresponds to the chromatographic peak areas, with subscripts T and 0 denoting the exit and inlet streams, respectively. B indicates the specific product gas, and S represents the product selectivity. The adjustment factors (f) account for differences in detector response for each gas relative to CH_4.

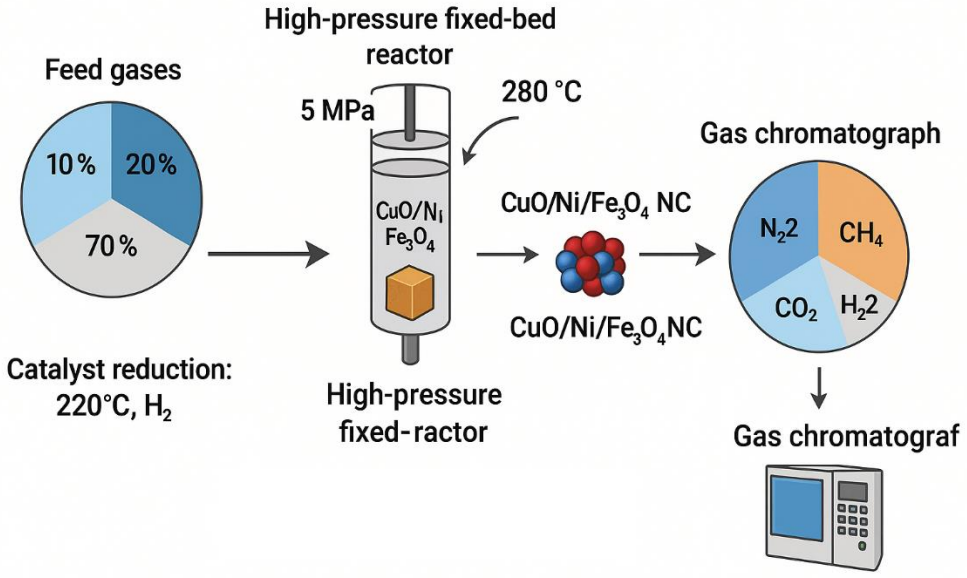

Figure III. 5: CO_2 Methanation using CuO/Ni/Fe₃O₄ Nanocomposites

2.4. Photocatalytic H_2 Production

The photocatalytic hydrogen (H_2) generation performance of the CuO/Ni/Fe₃O₄ nanocomposits was assessed under ambient conditions in a controlled gas environment [48]. Ethanol was employed as a sacrificial agent to enhance the reaction by facilitating electron capture and promoting effective charge separation, thereby improving H_2

production efficiency. In the experimental setup, 20 mg of the photocatalyst was dispersed in a three-necked flask containing a solution composed of 10 mL of methanol and 40 mL of deionized water. The reaction system was irradiated with a 200 W xenon (Xe) arc lamp operating at an intensity of 100 mW/cm². Hydrogen evolution was periodically monitored by sampling the gas phase from the reactor and analyzing it using an inline gas chromatograph (Agilent-8860, United States) [66].

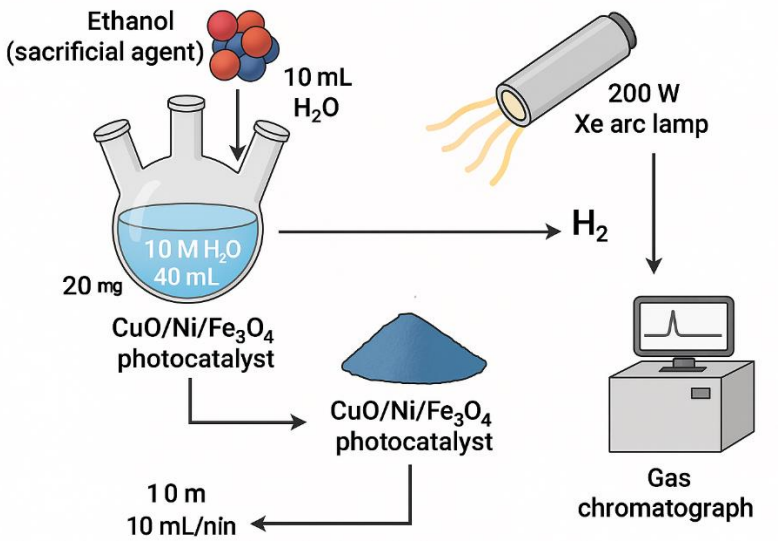

Figure III. 6: Photocatalytic H_2 Production using CuO/Ni/Fe₃O₄ Nanocomposites

3. Structural and Morphological Characterization

3.1. FTIR Analysis

Fourier-transform infrared (FTIR) spectroscopy was employed to identify the functional groups present in the CuO/Ni/Fe₃O₄ nanocomposites synthesized using gallic acid, which acts as a reducing and stabilizing agent during the bioreduction of metal ions and the formation of trimetallic oxide nanoparticles. This analysis was intended to elucidate the molecular species involved in the stabilization and capping of the nanoparticles throughout the synthesis process. The FTIR spectra of the samples are presented in Figure III.7 [48]. A prominent absorption band observed around 3366 cm^{-1} corresponds to O–H stretching vibrations [67], characteristic of phenolic and alcoholic groups [68]. The band detected at 2926 cm^{-1} is attributed to C–H bond stretching [69][51], while the peak at 1467 cm^{-1} is

associated with C=C stretching vibrations of aromatic rings [70]. Additionally, a band at 1348 cm^{-1} indicates O–H bending vibrations related to aqueous-phase synthesis [71], and C–H bending modes were identified at 1257 and 1132 cm^{-1} [49]. A signal at 1082 cm^{-1} suggests the presence of C–O–C stretching vibrations [72], while the absorption near 903 cm^{-1} corresponds to C=C groups typical of alkenes [73]. Furthermore, bands located at 580 cm^{-1} and 461 cm^{-1} were assigned to metal–oxygen bond vibrations, specifically Cu–O, Fe–O, and Ni–O linkages [74][75].

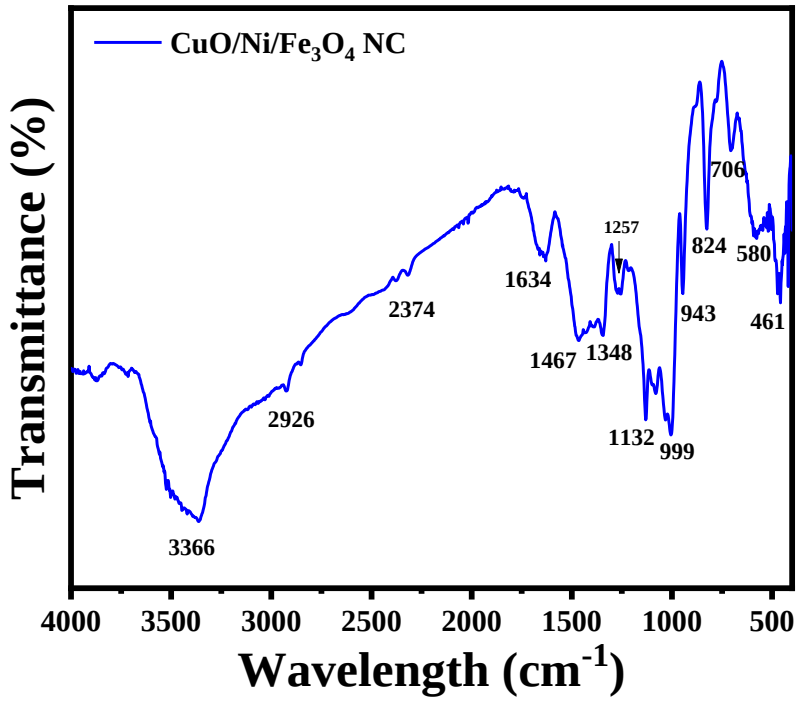

Figure III. 7: FTIR Spectrum of CuO/Ni/Fe₃O₄ Nanocomposite Recorded over the 4000–400 cm^{-1} Range [48]

These results confirm the presence of functional groups derived from active phytochemicals, such as flavonoids, phenolic acids, and aromatic compounds, which play a crucial role in facilitating both the reduction of metal precursors and the stabilization of the resulting trimetallic nanoparticles [76][77].

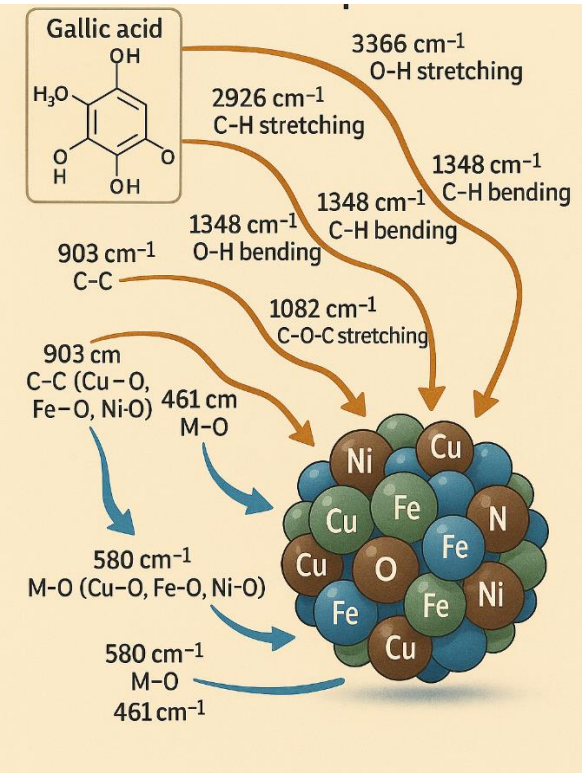

Figure III. 8: Schematic Representation of FTIR Functional Groups and Metal–Ligand Interactions in CuO/Ni/Fe_3O_4 Nanocomposite Synthesized with Gallic Acid

3.2. XRD analysis

The XRD analysis of the CuO/Ni/Fe_3O_4 nanocomposite (Figure III.11) exhibits characteristic diffraction peaks at 2θ values of 44.49°, 51.85°, and 76.38°, corresponding to the (111), (200), and (220) crystallographic planes of Ni nanoparticles, indicative of a cubic crystal structure [48].

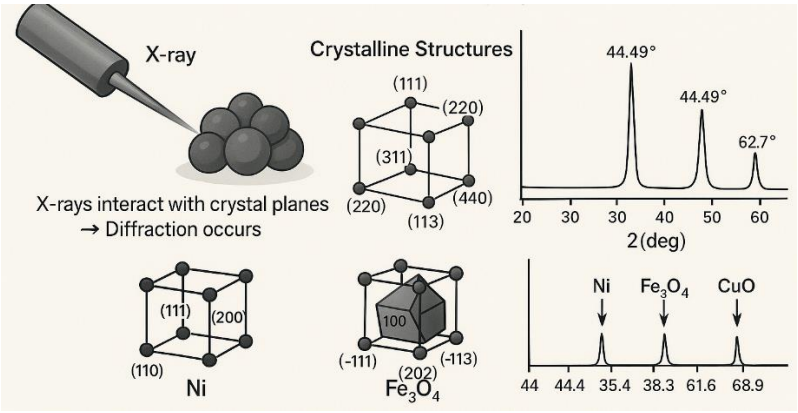

Figure III. 9: Schematic Illustration of XRD Analysis Revealing Crystalline Structures of CuO/Ni/Fe₃O₄ Nanocomposite

These results agree with JCPDS Card No. (01-087-0712). Additionally, the diffraction peaks observed at 2θ values of 18.33°, 30.3°, 35.34°, and 62.67° correspond to the (111), (220), (311), and (440) planes, respectively, confirming the presence of Fe_3O_4 nanoparticles, which also exhibit a cubic structure in line with JCPDS Card No. (01-088-0315). Furthermore, the detection of peaks at 2θ values of 32.5°, 35.6°, 38.7°, 48.8°, 61.6°, and 68.9°, associated with the (110), (-111), (111), (202), (-113), and (-221) planes, respectively, verifies the formation of CuO nanoparticles with a monoclinic crystal structure, consistent with JCPDS Card No. (01-089-2529). The crystallite size, calculated using the Scherrer equation, was approximately 30 nm, indicating the nanocrystalline nature of the CuO/Ni/Fe₃O₄ composite [48].

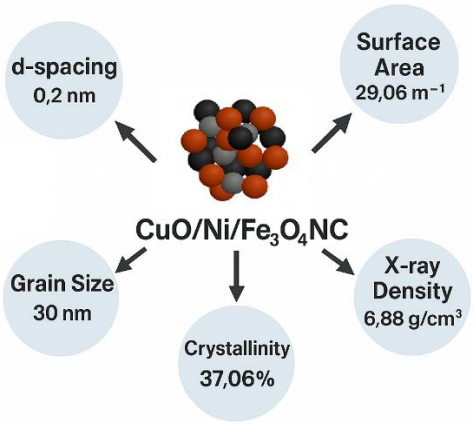

Figure III. 10: Crystallographic Properties of CuO/Ni/Fe₃O₄ Nanocomposite

Moreover, key structural parameters, including X-ray density, d-spacing, lattice parameters, specific surface area, and degree of crystallinity, were evaluated and are summarized in Figure III.10, providing deeper insights into the physical and structural properties of the photocatalysts. Equations (3) and (4) were utilized to estimate the photocatalyst surface area based on grain size (GS) and X-ray density (ρ_x), and to determine the percentage crystallinity by calculating the ratio of the crystalline peak area (Acp) to the total area (Ata) [78], respectively.

$$Surface\ area = \frac{6000}{GS \times \rho_x} \qquad (3)$$

$$Crystalinity\ (\%) = \frac{A_{cp}}{A_{ta}} \times 100 \qquad (4)$$

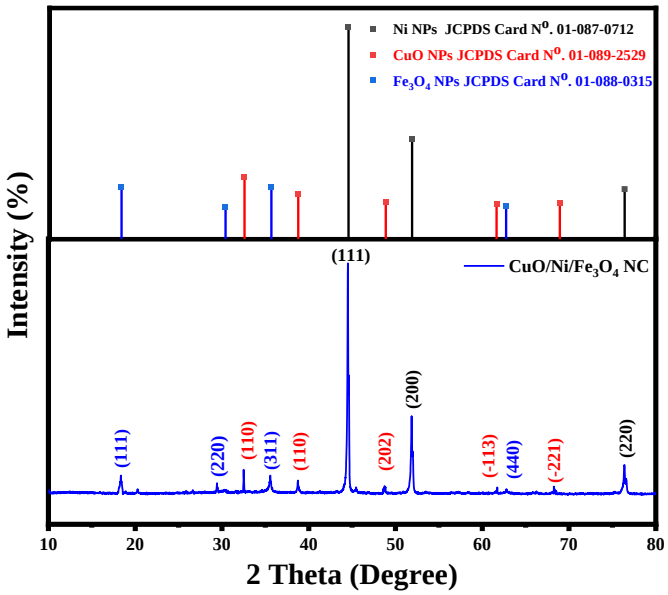

Figure III. 11: X-ray Diffraction Analysis of CuO/Ni/Fe₃O₄ Nanocomposite Structure [48]

3.3. SEM Analysis

The SEM micrograph shown in Figure III.13(a) illustrates the morphological features of the synthesized CuO/Ni/Fe₃O₄ nanocomposite. The image reveals that the material predominantly consists of aggregated spherical nanoparticles, indicating a pronounced tendency for clustering within the composite matrix. Such aggregation behavior is likely

influenced by factors including the synthesis process, surface chemistry, and interparticle forces. Additionally, the particle size distribution analysis (Figure III.13(b)) indicates an average particle size of approximately 40 nm for the CuO/Ni/Fe_3O_4 NC. This relatively narrow size distribution is advantageous for applications such as catalysis and sensing, where uniformity and reproducibility are critical to performance [48].

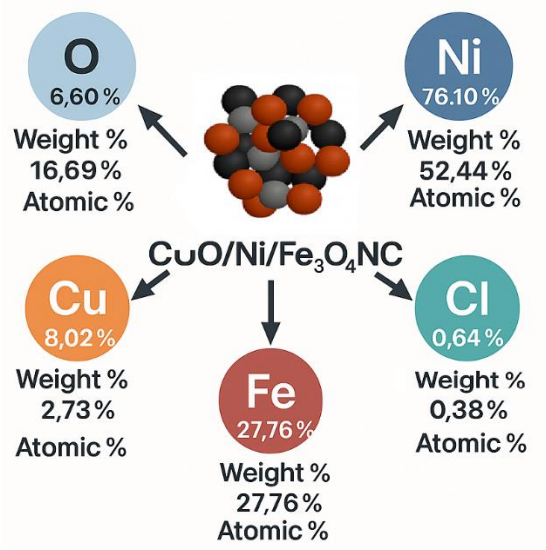

Figure III. 12: Elemental Distribution of CuO/Ni/Fe_3O_4 Nanocomposite

The elemental composition of the nanocomposite, as determined by EDX analysis (Figure III.13(c)), is summarized in Figure III.12. EDX spectrum confirms the presence of Cu, Ni, Fe, and O elements, verifying the successful synthesis of the intended nanocomposite. Notably, nickel (Ni) exhibits the highest contribution, with a weight percentage of 76.10% and an atomic percentage of 52.44%, emphasizing its dominant role within the composite structure. This significant incorporation of Ni is expected to influence the physicochemical properties and functional performance of the CuO/Ni/Fe_3O_4 NC. Furthermore, the minor detection of chlorine (Cl) is likely attributable to residual precursor salts or surface contamination [48].

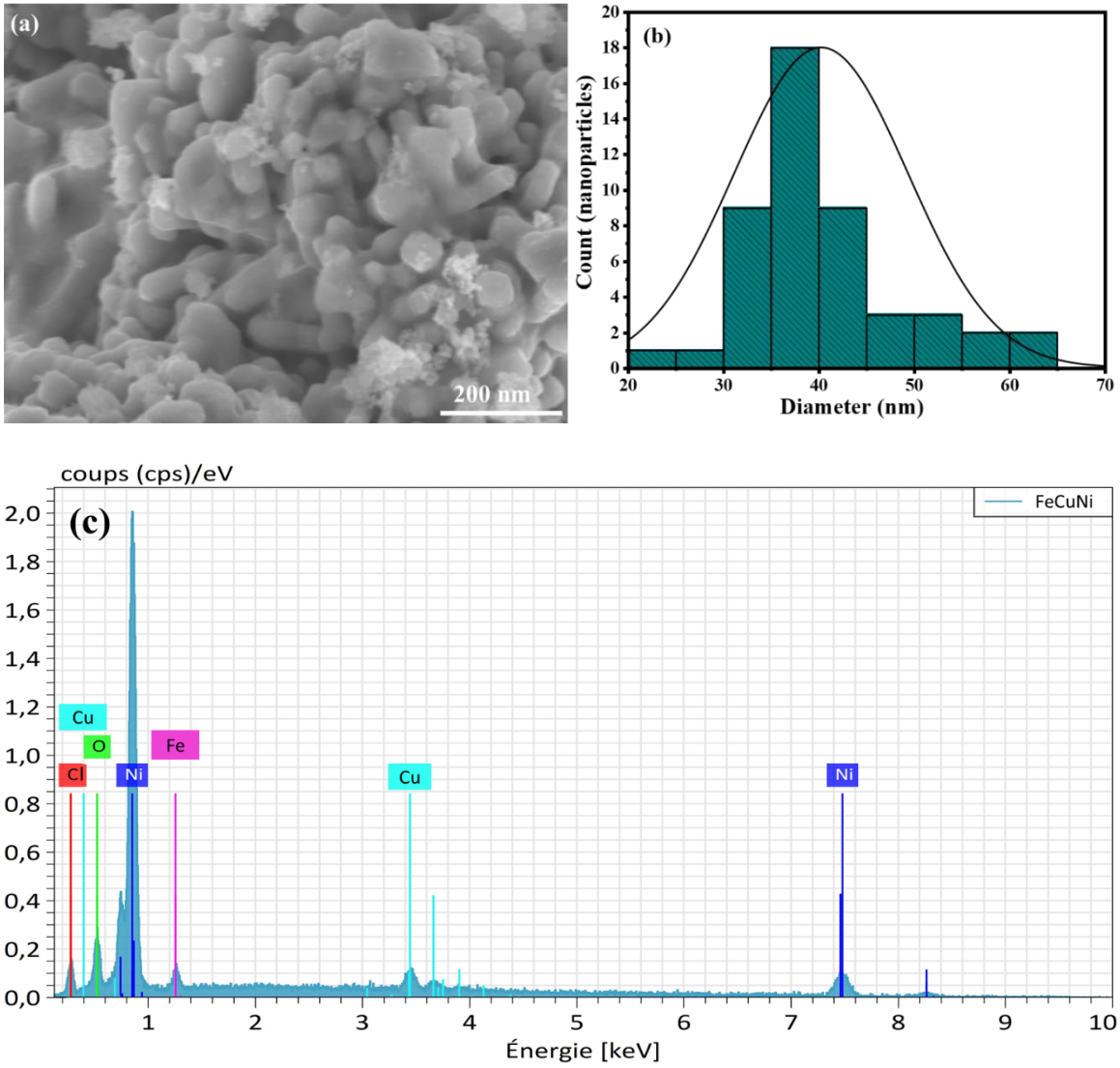

Figure III. 13: (a) Surface Morphology of CuO/Ni/Fe_3O_4 Nanocomposite via SEM Imaging; **(b)** Particle Size Distribution Profile; **(c)** EDX Analysis of Elemental Composition [48].

3.4. Thermogravimetric Analysis

The thermogravimetric (TGA) and differential thermal analysis (DTA) of the CuO/Ni/Fe_3O_4 nanocomposite (NC) provides detailed information regarding its thermal behavior and stability, as depicted in Figure III.15. An initial weight loss of 2.8% was recorded between 85 and 178 °C, attributed to the evaporation of surface-adsorbed water and volatile substances. Such early-stage weight loss is commonly observed in materials synthesized via wet chemical routes, where residual solvents and physically adsorbed moisture are typically present. A more substantial weight reduction of 27.31% was

observed within the 286–512 °C range, corresponding to the decomposition of organic residues or impurities embedded in the composite [48].

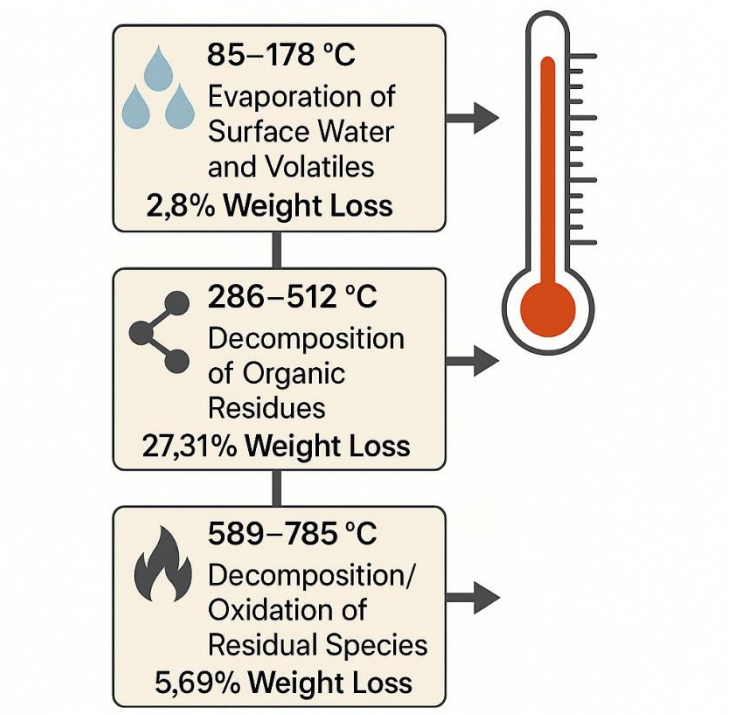

Figure III. 14: Thermal Stability Stages of CuO/Ni/Fe_3O_4 Nanocomposite

This thermal range is characteristic of the degradation temperatures of various organic compounds, implying the presence of synthesis-related residues or unreacted starting materials. Finally, a weight loss of 5.69% occurred between 589 and 785 °C [48], which may be associated with the decomposition or transformation of residual organic species, or potentially with the thermal degradation or oxidation of the composite's structural components at elevated temperatures [79].

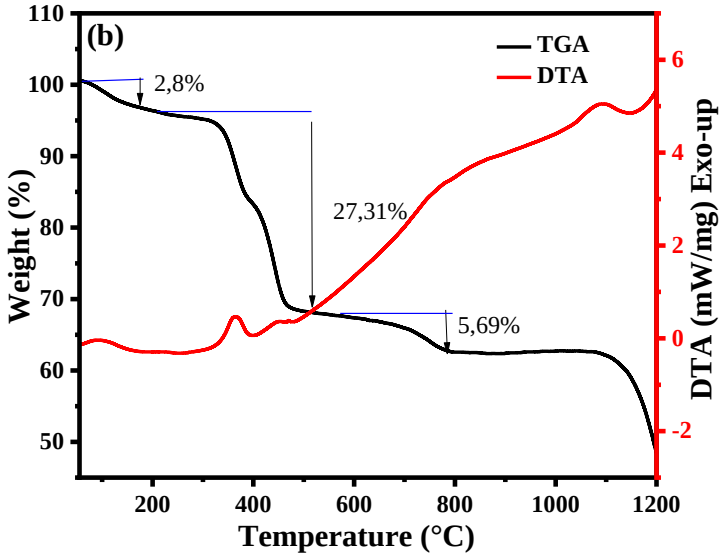

Figure III. 15: Thermogravimetric and Differential Thermal Analysis of CuO/Ni/Fe_3O_4 Nanocomposite [48]

4. Optical Properties and Band Structure

4.1. UV-Visible Analysis

The optical properties of the CuO/Ni/Fe_3O_4 nanocomposite were investigated using UV–visible spectroscopy. The absorption spectrum exhibited a distinct peak at approximately 370 nm (Figure III.16(a)), indicative of electronic transitions within the nanocomposite structure, likely arising from the individual energy levels of the CuO, Ni, and Fe_3O_4 components. To further elucidate the optical behavior, a Tauc plot was constructed by plotting $(\alpha h\nu)^{1/2}$ against photon energy ($h\nu$) [80], where α represents the absorption coefficient. This method enabled the estimation of the optical band gap (E_9).

As shown in Figure III.16 (b), the Tauc plot revealed a band gap energy of approximately 1.26 eV for the CuO/Ni/Fe_3O_4 NC [48].

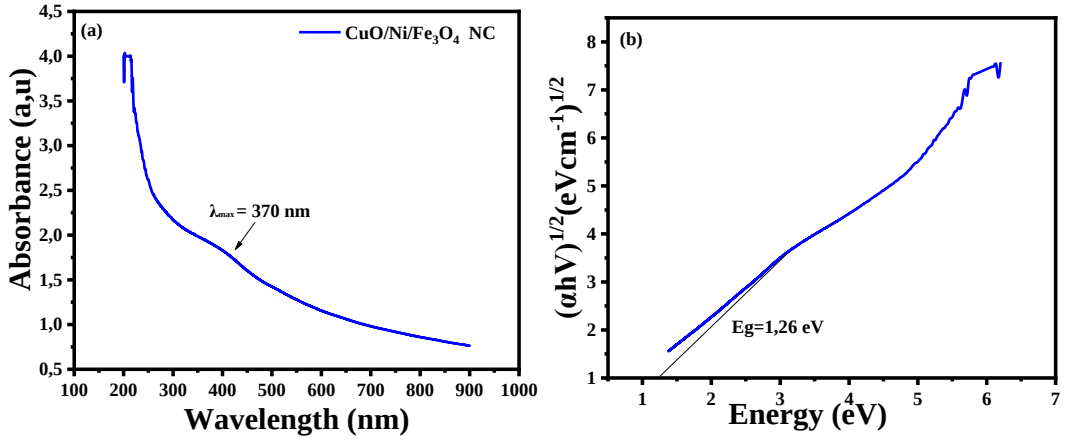

Figure III. 16: (a) UV–Visible absorption spectrum of CuO/Ni/Fe₃O₄ nanocomposite. **(b)** Tauc plot illustrating the energy dependence of $(\alpha h\nu)^{1/2}$ for CuO/Ni/Fe₃O₄ nanocomposite [48]

The relatively narrow band gap suggests that the material possesses favorable semiconductor characteristics [81], making it a promising candidate for applications such as photocatalysis, photovoltaics, and sensing technologies [82].

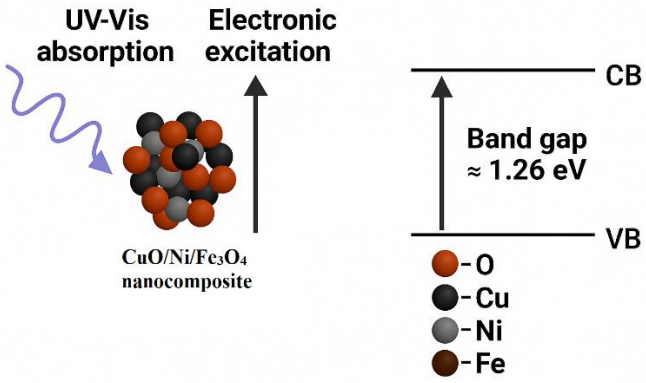

Figure III. 17: Optical Absorption and Band Gap Representation of CuO/Ni/Fe₃O₄ Nanocomposite

4.2. Implications of Band Structure for Photocatalysis

The band structure of semiconductor photocatalysts plays a pivotal role in determining their efficiency in photocatalytic processes. The CuO/Ni/Fe₃O₄ nanocomposite, with a narrow band gap of approximately 1.26 eV as derived from the Tauc plot, exhibits a high capacity for visible light absorption, enabling effective utilization of solar energy. This reduced band gap facilitates the generation of electron–hole pairs under low-energy photon

excitation, promoting redox reactions essential for hydrogen evolution and CO_2 methanation. The conduction band position is suitably aligned for proton reduction to hydrogen, while the valence band provides sufficient potential for the oxidation of sacrificial agents like methanol. Moreover, the heterojunction formed between CuO, Ni, and Fe_3O_4 components enhances charge separation and suppresses recombination, thereby improving photocatalytic activity. These band structure characteristics underscore the potential of the synthesized nanocomposite for sustainable energy conversion applications.

5. Catalytic CO_2 Methanation Performance

5.1. CO_2 Conversion Rate and CH_4 Selectivity

The catalytic methanation of CO_2 was systematically studied to assess the performance of the CuO/Ni/Fe_3O_4 nanocomposite [48]. The experimental outcomes, depicted in Figure III.5, exhibit clear trends in both catalytic activity and selectivity. At an initial reaction temperature of 140 °C, the catalyst demonstrated relatively low activity, achieving a CO_2 conversion rate of 38.1%. As the reaction temperature increased, the conversion significantly improved, reaching a maximum of 94.75% at 420 °C (Figure III.18) [48], thereby confirming that higher temperatures effectively enhance catalytic conversion [83]. In addition, the catalyst showed improved selectivity toward methane as the temperature increased, especially at lower temperature ranges [84][85], suggesting that the incorporation of CuO/Ni/Fe_3O_4 NC favors CH_4 production [48]. Nevertheless, at higher temperatures, the selectivity advantage imparted by the catalyst diminishes[86], likely due to a reduced contribution of side reactions such as the reverse water–gas shift [87].

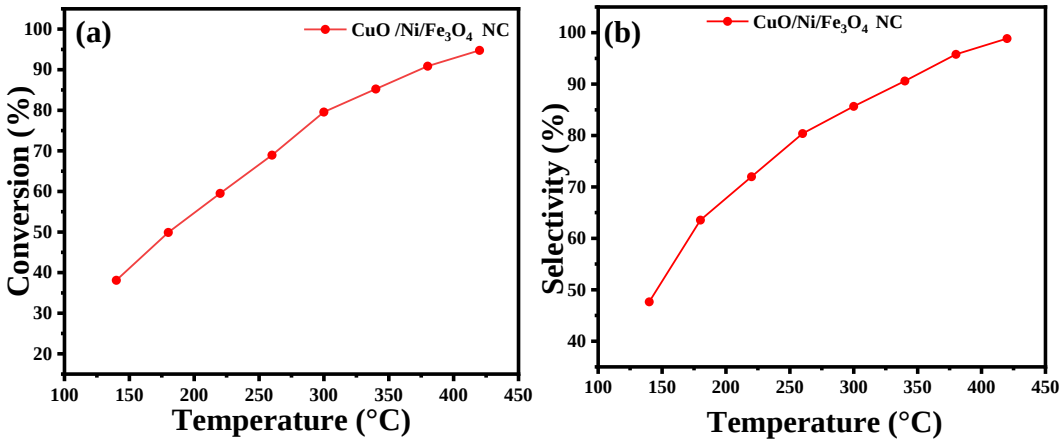

Figure III. 18: Influence of Reaction Temperature on **(a)** CO_2 Conversion and **(b)** CH_4 Selectivity during Catalytic CO_2 Methanation over CuO/Ni/Fe_3O_4 Nanocomposite [48].

5.2. Mechanism of Surface Adsorption and Activation

The mechanism of CO_2 methanation on the catalyst surface involves a series of sequential steps. Initially, CO_2 and H_2 molecules adsorb onto the catalyst surface [88][89]. CO_2 is then activated, dissociating into surface-bound oxygen species (O*) and carbon monoxide radicals (CO*) [90], a process facilitated by hydrogen atoms present on the surface [91]. Concurrently, H_2 molecules also adsorb and dissociate, generating surface hydrogen atoms (H*) [92]. Subsequently, the activated CO* intermediates react with H* atoms to form CH_4 and H_2O [93][94]. The final step involves the desorption of methane and water molecules from the catalyst surface, thereby completing the catalytic cycle [95][96].

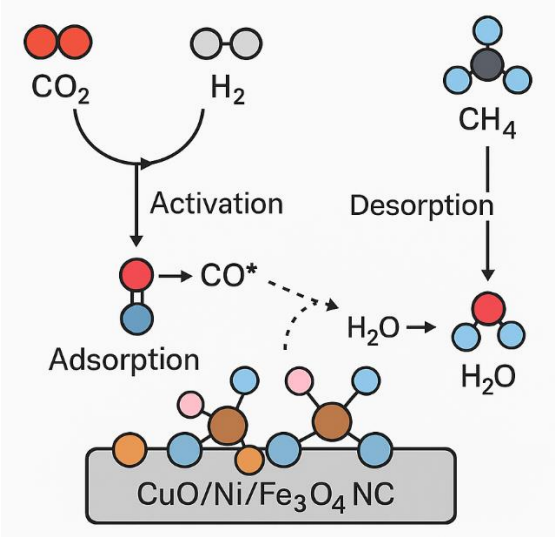

Figure III. 19: schematic of CO_2 Methanation using CuO/Ni/Fe₃O₄ NC

These sequential reactions collectively describe the transformation of CO_2 and H_2 into CH_4 and H_2O, as represented in reaction equation R_4 [97][98].

$$CO_2 \xrightarrow{H*} CO^* + O^* \quad (5)$$

$$H_2 \rightarrow 2H^* \quad (6)$$

$$CO^* + 3H^* \rightarrow CH_4 + H_2O \quad (7)$$

$$CO_2 + 4H_2 \rightarrow CH_4 + 2H_2O \quad (8)$$

The trends in catalytic performance emphasize the effectiveness of CuO/Ni/Fe₃O₄ NCs in CO_2 methanation and underscore the critical role of temperature in optimizing reaction efficiency and selectivity [48].

6. Photocatalytic Activity

6.1. H_2 Production

The photocatalytic H_2 synthesis results offer critical insights into the catalytic performance of CuO/Ni/Fe₃O₄ nanocomposites (Figure III.20) [48]. A progressive increase in H_2 production over time highlights the catalyst's efficiency. After 6 hours of reaction, the CuO/Ni/Fe₃O₄ NC achieved a significantly higher hydrogen yield (741 µmol/g) compared

to the initial generation rate of 165 µmol/g·h (Figure III.20 (a)) [48]. This enhancement is primarily attributed to the role of CuO/Ni/Fe_3O_4 as a surface modifier, promoting better dispersion of active catalytic sites and expanding the effective surface area for the reaction [48]. Furthermore, the nanocomposite improves charge separation efficiency during photocatalysis, thereby boosting overall activity [99][100][101]. The plateau observed in H_2 evolution after 5 hours suggests the system may reach a dynamic equilibrium; however, the slight yet continuous production beyond this point indicates ongoing reaction kinetics [102][103]. Reusability tests over four consecutive photocatalytic cycles demonstrated consistent H_2 production, evidencing the catalyst's stability (Figure III.20 (b)) [48]. XRD analyses of the CuO/Ni/Fe_3O_4 NC before and after photocatalysis showed no significant structural changes, confirming the material's robustness and its potential for repeated use in photocatalytic applications (Figure III.20 (a)) [48].

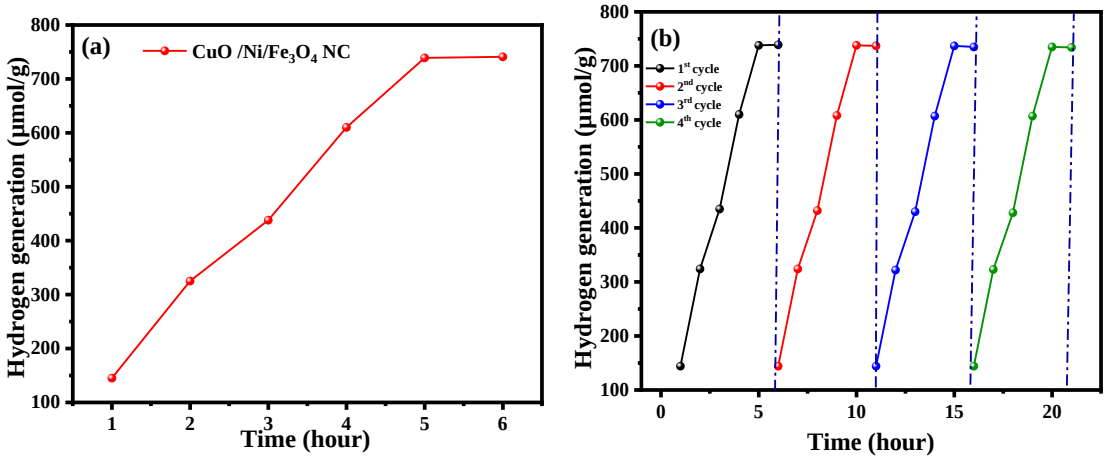

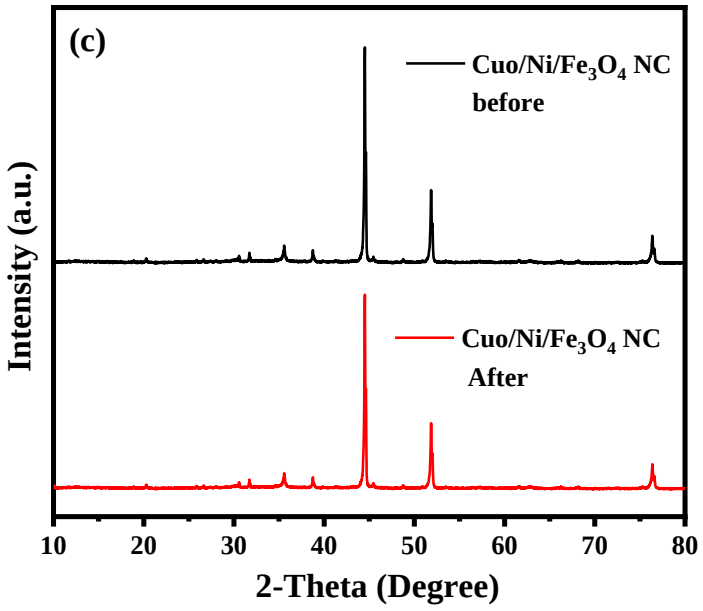

Figure III. 20: (a) Hydrogen generation performance using CuO/Ni/Fe₃O₄ NC photocatalysts; **(b)** Assessment of CuO/Ni/Fe₃O₄ NC stability through successive reusability cycles; **(c)** XRD patterns of CuO/Ni/Fe₃O₄ NC before and after photocatalytic activity [48]

6.2. Potential Mechanism for Photocatalytic H_2 Generation

The photocatalytic generation of hydrogen involves a series of fundamental steps [104][105][106] (Figure III.21). Upon light irradiation, electron–hole pairs are generated within the CuO/Ni/Fe₃O₄ nanocomposite [48], initiating irreversible oxidation reactions of methanol or water. The mechanism describing the use of methanol as a sacrificial agent for hydrogen evolution by CuO/Ni/Fe₃O₄ NCs can be outlined through the following processes [48]:

$$CuO/Ni/Fe_3O_4 \xrightarrow{hv} h_{VB}^{+} + e_{CB}^{-} \qquad (9)$$

The photogenerated holes (h_{VB}^{+}) on the catalyst surface react with hydroxyl groups (OH^-), water (H_2O), or adsorbed methanol (CH_3OH), producing hydroxyl radicals ($OH^{\bullet}$) through well-established pathways [107][82]:

$$OH^- + h_{VB}^{+} \rightarrow OH\cdot \qquad (10)$$

$$H_2O + h_{(VB)}^{+} \rightarrow OH\cdot + H^+ \qquad (11)$$

$$CH_3OH + h^+_{(VB)} \rightarrow CH_3O\cdot + H^+ \quad (12)$$

$$CH_3O\cdot + h^+_{(VB)} \rightarrow CH_2O\cdot + H^+ \quad (13)$$

$$CH_2O\cdot + h^+_{(VB)} \rightarrow CHO\cdot + H^+ \quad (14)$$

$$CHO\cdot + OH\cdot \rightarrow HCOOH \quad (15)$$

$$HCOOH + h^+_{(VB)} \rightarrow HCOO\cdot + H^+ \quad (16)$$

$$HCOO\cdot + h^+_{(VB)} \rightarrow CO_2 + H^+ \quad (17)$$

Methanol thus plays a dual role: efficiently scavenging the photogenerated holes and possibly acting as a hydrogen atom reservoir at the Ni–CuO interface. Subsequently, the protons (H^+) are reduced by the photogenerated electrons to produce molecular hydrogen [108]:

$$2H^+ + 2e^- \rightarrow H_2 \quad (R14)$$

It is important to note that although the energy input required for the lamp exceeds the energy output in the form of hydrogen by approximately six-fold [109], enhancing the catalyst's efficiency is critical for advancing the practical application of solar-driven hydrogen production under visible light irradiation [110][111].

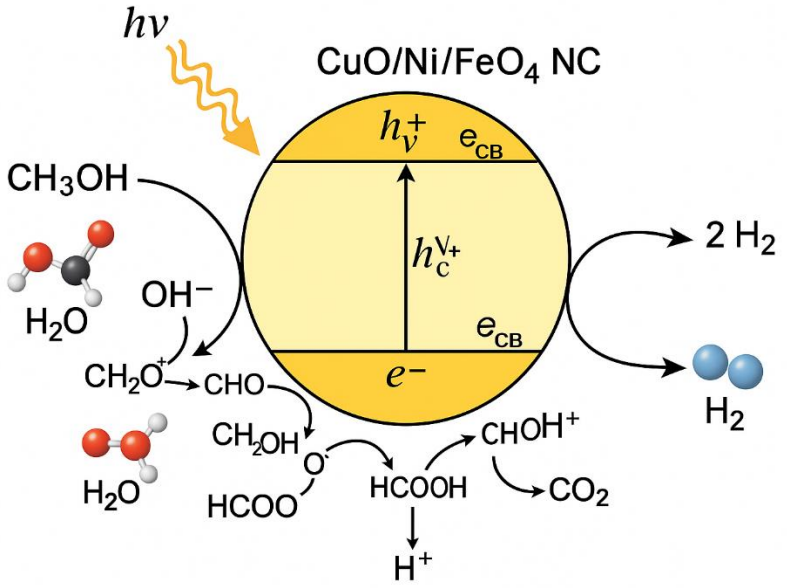

Figure III. 21: Photocatalytic H_2 Generation Mechanism Using CuO/Ni/Fe_3O_4 Nanocomposites

7. Synergistic Role of Trimetallic Design

7.1. Impact of CuO, Ni, and Fe_3O_4 Interfacing on Activity

The integration of CuO, Ni, and Fe_3O_4 within a single nanocomposite architecture imparts a synergistic enhancement in catalytic performance, surpassing the limitations of their individual counterparts [48]. Copper oxide contributes significant redox activity and CO_2 activation capability due to its facile electron transfer characteristics [112]. Nickel (Ni), a well-established hydrogenation catalyst, exhibits strong H_2 adsorption and dissociation properties, thereby promoting efficient hydrogenation of CO_2 intermediates [90]. Meanwhile, Fe_3O_4 provides structural stability [113][114], redox cycling through Fe^{2+}/Fe^{3+} transitions [115], and magnetic separability, facilitating catalyst recovery and reuse. The heterojunction formation at the CuO–Ni–Fe_3O_4 interfaces improves interfacial electron mobility, reduces charge recombination, and increases the density of catalytically active sites [48]. This trimetallic synergy ensures optimal spatial distribution of reactants and intermediates on the surface, resulting in enhanced catalytic activity in both thermocatalytic CO_2 methanation and photocatalytic hydrogen evolution [48].

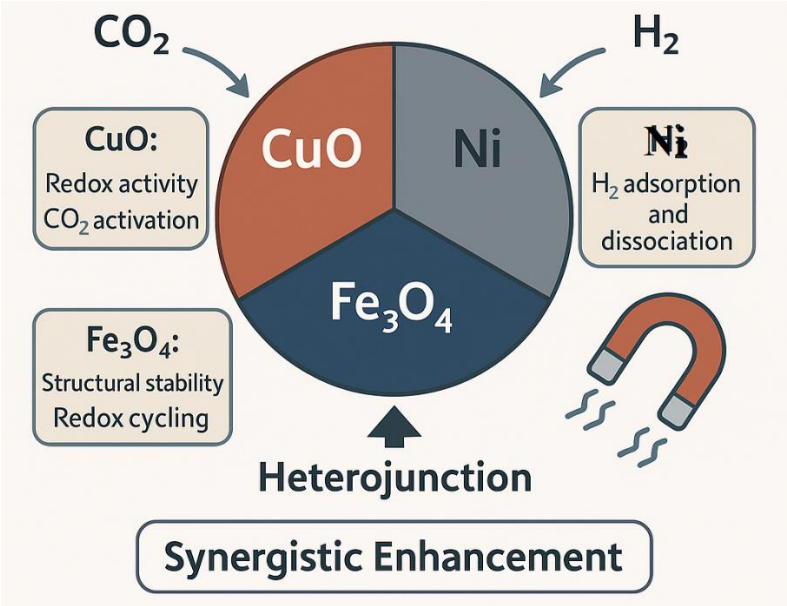

Figure III. 22: Synergistic Interaction of CuO, Ni, and Fe_3O_4 in Trimetallic Nanocomposites Enhancing Catalytic Activity

7.2. Role of Gallic Acid in Reducing and Stabilizing Metal Ions

Gallic acid [116], a naturally occurring trihydroxybenzoic acid [117], plays a pivotal role in the eco-friendly synthesis of the trimetallic nanocomposite by acting simultaneously as a reducing and stabilizing agent [118][119]. Its polyphenolic structure, rich in hydroxyl and carboxyl functional groups, enables effective chelation and reduction of metal ions (Cu^{2+}, Ni^{2+}, and Fe^{2+}/Fe^{3+}) in aqueous media [44]. During the synthesis process, gallic acid facilitates the bioreduction of these metal ions into their corresponding oxide forms [117] while preventing uncontrolled agglomeration through surface capping and steric stabilization [120]. This controlled nucleation and growth pathway promotes the homogeneous dispersion of metal oxide domains throughout the nanocomposite matrix [121], ensuring compositional uniformity and nanoscale phase integration [122]. Moreover, the residual organic moieties from gallic acid may contribute to surface functionalization [123], which can enhance the hydrophilicity and catalytic accessibility of the nanomaterials [124].

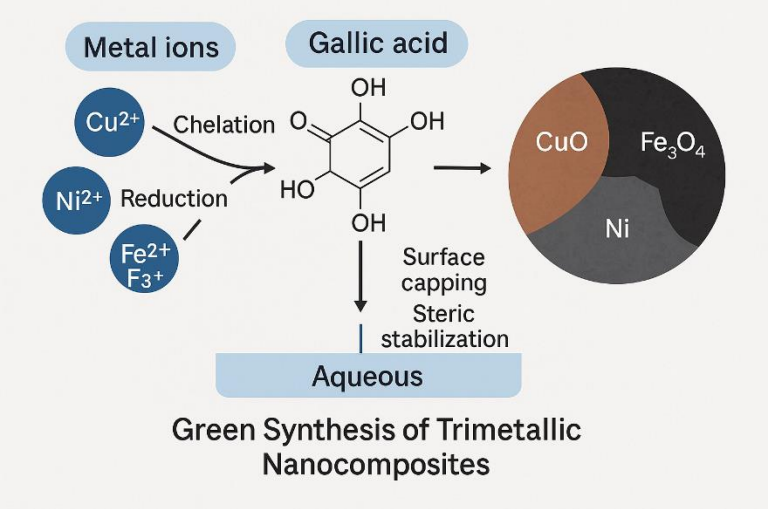

Figure III. 23: Role of Gallic Acid in the Green Synthesis and Stabilization of CuO/Ni/Fe_3O_4 Trimetallic Nanocomposites

7.3. Enhanced Charge Separation and Active Site Distribution

One of the defining advantages of the CuO/Ni/Fe_3O_4 nanocomposite is its superior ability to facilitate charge carrier separation and transport, which is essential for efficient photocatalytic activity [48]. The band alignment among the three metal oxides creates an internal electric field that directs photogenerated electrons and holes away from one another, thereby minimizing recombination losses [125]. CuO, with its narrow band gap, acts as a visible-light absorber and electron donor [126], while Fe_3O_4 and Ni serve as electron acceptors and co-catalytic sites [127]. This heterostructure configuration supports efficient photogenerated charge migration toward reaction sites, promoting reduction and oxidation processes concurrently [34]. Furthermore, the high surface area and uniform active site distribution achieved through gallic acid-mediated synthesis maximize reactant accessibility and interaction with the catalyst surface [128]. These electronic and structural attributes collectively result in improved catalytic kinetics and sustained performance in both CO_2 conversion and H_2 evolution applications [129].

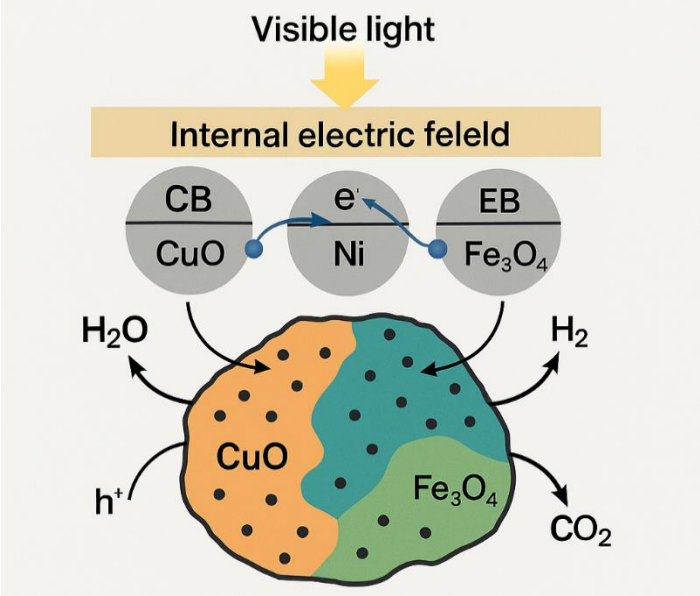

Figure III. 24: Band Alignment and Charge Separation Mechanism in CuO/Ni/Fe_3O_4 Nanocomposites for Enhanced Photocatalytic Activity

8. Environmental and Energy Implications

8.1. CO_2 Valorization in Methanation

CO_2 valorization through catalytic methanation presents a viable strategy for mitigating greenhouse gas emissions while simultaneously producing value-added fuels [130][131]. By converting CO_2 into methane (CH_4), a storable and energy-dense molecule, this process integrates seamlessly with existing natural gas infrastructure [132]. The use of CuO/Ni/Fe_3O_4 nanocomposites enhances this transformation by providing active redox sites, efficient hydrogenation pathways, and high selectivity toward CH_4 under moderate reaction conditions [48]. This not only contributes to the circular carbon economy but also aligns with carbon capture and utilization (CCU) objectives aimed at reducing the atmospheric burden of CO_2 [133]. The implementation of CO_2 methanation technologies on an industrial scale could play a significant role in achieving climate neutrality targets across multiple sectors, including energy, manufacturing, and transportation [134][135].

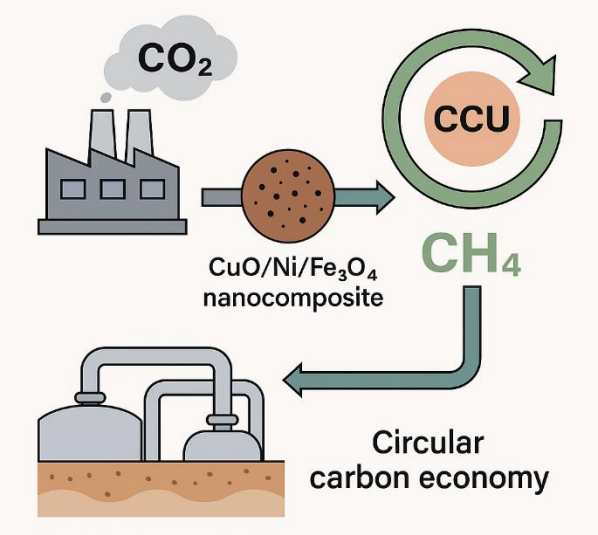

Figure III. 25: CO_2 Valorization via Methanation Using CuO/Ni/Fe_3O_4 Nanocomposites within a Circular Carbon Economy Framework

8.2. Green H_2 Production for Energy Storage

Photocatalytic hydrogen (H_2) generation represents a cornerstone in the development of renewable and storable energy carriers [136][137][138]. Utilizing sunlight to split water or reform alcohols via semiconducting nanocomposites offers a clean and sustainable route to produce hydrogen fuel without emitting CO_2 [139][140]. The CuO/Ni/Fe_3O_4 nanocomposite, owing to its optimized band structure and efficient charge separation, demonstrates notable activity in generating hydrogen under visible-light irradiation [48]. This green H_2 can serve as a zero-carbon energy source for fuel cells, grid storage, and transportation [141]. Furthermore, coupling green hydrogen production with renewable electricity generation can facilitate load balancing in power grids and contribute to long-duration energy storage strategies [142], thus addressing one of the critical challenges in transitioning toward fully decarbonized energy systems [143].

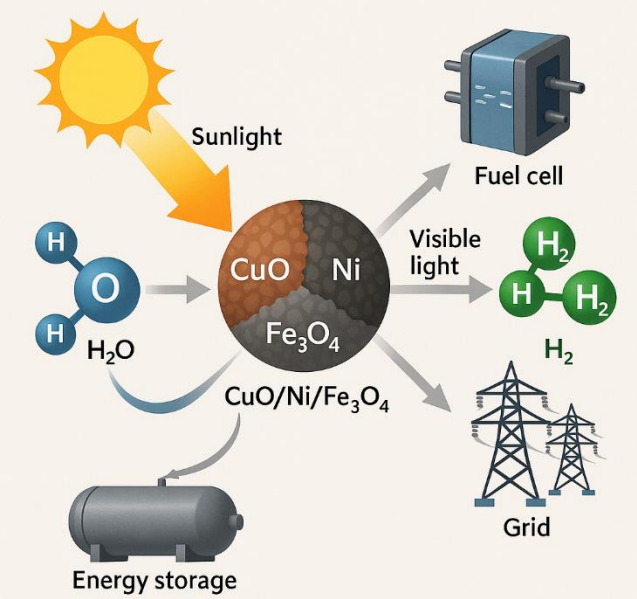

Figure III. 26: Photocatalytic Green Hydrogen Production Using CuO/Ni/Fe_3O_4 Nanocomposites for Renewable Energy Storage and Grid Applications

8.3. Sustainability, Scalability, and Future Applications

The synthesis and application of CuO/Ni/Fe_3O_4 nanocomposites exemplify a sustainable approach to catalyst design [48], particularly through the use of gallic acid as a biogenic reducing agent [45]. This green chemistry pathway minimizes environmental risks [46], eliminates the need for toxic solvents, and supports the scalable production of nanomaterials under mild conditions [45]. The structural robustness, reusability, and magnetic separability of the nanocomposite further enhance its practical viability. Looking ahead, the integration of such multifunctional catalysts into pilot-scale reactors for CO_2 utilization or solar-driven hydrogen generation presents exciting opportunities [10]. Future applications may extend beyond energy, including environmental remediation, photocatalytic disinfection, and solar-to-chemical conversion platforms [136]. Advancing these systems through process optimization and lifecycle analysis will be essential to translating laboratory successes into impactful technologies for global sustainability [137].

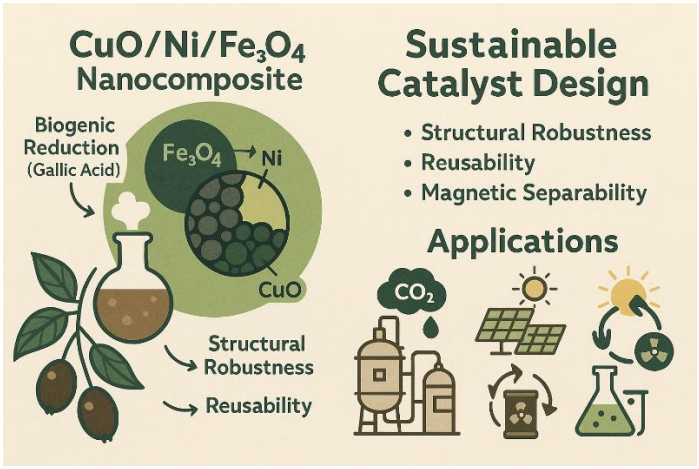

Figure III. 27: Sustainable Synthesis and Multifunctional Applications of CuO/Ni/Fe_3O_4 Nanocomposites via Green Chemistry Approach

9. Conclusion and Future Outlook

This chapter presented an in-depth investigation of the green synthesis, structural characterization, and dual catalytic performance of CuO/Ni/Fe_3O_4 nanocomposites prepared via a gallic acid-mediated bioreduction route. The eco-friendly synthesis process successfully integrated the redox-active CuO, hydrogenation-active Ni, and magnetically separable Fe_3O_4 phases into a trimetallic heterostructure that demonstrated exceptional physicochemical and catalytic properties.

Characterization results confirmed the successful formation of a highly crystalline nanocomposite with distinct CuO, Ni, and Fe_3O_4 diffraction peaks. The average crystallite size was approximately 30 nm, as determined by XRD, while SEM analysis revealed uniform, nearly spherical nanoparticles with an average particle diameter of 40 nm. EDX spectra verified the presence of Cu, Ni, Fe, and O elements, with Ni showing the highest incorporation (76.10 wt.%, 52.44 at.%), confirming its dominant role in the structure. Thermogravimetric analysis (TGA) demonstrated outstanding thermal stability, with only 35.8% total weight loss up to 785 °C, indicative of minimal organic residue and high inorganic content.

Optical characterization revealed a distinct absorption peak at 370 nm and a narrow band gap of 1.26 eV, confirming strong visible-light activity. This narrow band gap and well-aligned band structure facilitated enhanced charge carrier separation and visible-light absorption, which are essential for efficient photocatalysis.

In the CO_2 methanation experiments, the CuO/Ni/Fe_3O_4 catalyst achieved a CO_2 conversion rate of 94.75% at 420 °C and high CH_4 selectivity, highlighting its effectiveness under thermocatalytic conditions. These results demonstrate that synergistic interactions between CuO, Ni, and Fe_3O_4 phases significantly lower the activation barrier and promote CO_2 hydrogenation efficiency.

For photocatalytic hydrogen evolution, the nanocomposite exhibited a high hydrogen generation rate, reaching 741 μmol g^{-1} after 6 hours of illumination under a 200 W xenon lamp (100 mW cm^{-2}). The catalyst showed an initial H_2 generation rate of 165 μmol $g^{-1} \cdot h^{-1}$,

with minimal loss of activity after four consecutive cycles, confirming its excellent reusability and structural integrity, as verified by post-reaction XRD patterns.

These findings collectively demonstrate that the gallic acid-derived CuO/Ni/Fe_3O_4 nanocomposite provides an efficient, stable, and sustainable catalyst platform for dual CO_2 methanation and photocatalytic H_2 production, thanks to its strong interfacial coupling, reduced recombination rate, and robust structural framework.

Future research should target improving visible-light absorption and reaction kinetics through surface sensitization (plasmonic, carbon, or dye coupling) and advanced photoreactor configurations that enhance light distribution. Integrating these catalysts into hybrid CO_2 capture–methanation–hydrogen systems could establish a closed-loop, solar-driven platform for clean fuel production. The outstanding 94.75% CO_2 conversion, 741 μmol g^{-1} H_2 yield, and 1.26 eV band gap position the CuO/Ni/Fe_3O_4 nanocomposite as a high-performance, green catalyst for next-generation clean energy and circular carbon technologies.

References

[1] A. Adewumi, K. A. Olu-lawal, C. E. Okoli, F. O. Usman, and G. S. Usiagu, "Sustainable energy solutions and climate change: A policy review of emerging trends and global responses," *World J. Adv. Res. Rev.*, vol. 21, no. 2, pp. 408–420, 2024.

[2] S. Evro, B. A. Oni, and O. S. Tomomewo, "Carbon neutrality and hydrogen energy systems," *Int. J. Hydrogen Energy*, vol. 78, pp. 1449–1467, 2024.

[3] P. F. Borowski, "Mitigating climate change and the development of green energy versus a return to fossil fuels due to the energy crisis in 2022," *Energies*, vol. 15, no. 24, p. 9289, 2022.

[4] M. Farghali *et al.*, "Strategies to save energy in the context of the energy crisis: a review," *Environ. Chem. Lett.*, vol. 21, no. 4, pp. 2003–2039, 2023.

[5] S. Yi, K. R. Abbasi, K. Hussain, A. Albaker, and R. Alvarado, "Environmental concerns in the United States: Can renewable energy, fossil fuel energy, and natural resources depletion help?," *Gondwana Res.*, vol. 117, pp. 41–55, 2023.

[6] Y. Pan and A. Hashemizadeh, "Circular economy-based assessment framework for enhancing sustainability in renewable energy development with life cycle considerations," *Environ. Impact Assess. Rev.*, vol. 103, p. 107289, 2023.

[7] J. J. Klemeš, P. S. Varbanov, T. G. Walmsley, and A. Foley, "Process integration and circular economy for renewable and sustainable energy systems," *Renewable and Sustainable Energy Reviews*, vol. 116. Elsevier, p. 109435, 2019.

[8] S. O. Jeje, T. Marazani, J. O. Obiko, and M. B. Shongwe, "Advancing the hydrogen production economy: A comprehensive review of technologies, sustainability, and future prospects," *Int. J. Hydrogen Energy*, vol. 78, pp. 642–661, 2024.

[9] S. Tasleem, C. S. Bongu, M. R. Krishnan, and E. H. Alsharaeh, "Navigating the hydrogen prospect: A comprehensive review of sustainable source-based production technologies, transport solutions, advanced storage mechanisms, and CCUS integration," *J. Energy Chem.*, 2024.

[10] S. K. Singh and A. K. Tiwari, "Solar-powered hydrogen production: Advancements, challenges, and the path to net-zero emissions," *Int. J. Hydrogen Energy*, vol. 84, pp. 549–579, 2024.

[11] T. Zhao, Z. Yang, Y. Tang, J. Liu, and F. Wang, "Advances and perspectives of photopromoted CO2 hydrogenation for methane production: catalyst development and mechanism investigations," *Energy & Fuels*, vol. 36, no. 13, pp. 6711–6735, 2022.

[12] U. Ulmer *et al.*, "Fundamentals and applications of photocatalytic CO2 methanation," *Nat. Commun.*, vol. 10, no. 1, p. 3169, 2019.

[13] J. C. Navarro, M. A. Centeno, O. H. Laguna, and J. A. Odriozola, "Policies and motivations for the CO2 valorization through the Sabatier reaction using structured catalysts. A review of the most recent advances," *Catalysts*, vol. 8, no. 12, p. 578, 2018.

[14] S. Khan *et al.*, "Recent advances on photo-thermo-catalysis for carbon dioxide methanation," *Int. J. Hydrogen Energy*, vol. 48, no. 64, pp. 24756–24787, 2023.

[15] A. Hasani, M. Tekalgne, Q. Van Le, H. W. Jang, and S. Y. Kim, "Two-dimensional materials as catalysts for solar fuels: hydrogen evolution reaction and CO 2 reduction," *J. Mater. Chem. A*, vol. 7, no. 2, pp. 430–454, 2019.

[16] G. Chen *et al.*, "From solar energy to fuels: recent advances in light-driven C1 chemistry," *Angew. Chemie Int. Ed.*, vol. 58, no. 49, pp. 17528–17551, 2019.

[17] C. Zou *et al.*, "Industrial status, technological progress, challenges, and prospects of hydrogen energy," *Nat. Gas Ind. B*, vol. 9, no. 5, pp. 427–447, 2022.

[18] H. L. Huynh and Z. Yu, "CO2 Methanation on Hydrotalcite-Derived Catalysts and Structured Reactors: A Review," *Energy Technol.*, vol. 8, no. 5, p. 1901475, 2020.

[19] H. Nazir *et al.*, "Is the H2 economy realizable in the foreseeable future? Part III: H2 usage technologies, applications, and challenges and opportunities," *Int. J. Hydrogen Energy*, vol. 45, no. 53, pp. 28217–28239, 2020.

[20] M. Younas, L. Loong Kong, M. J. K. Bashir, H. Nadeem, A. Shehzad, and S. Sethupathi, "Recent advancements, fundamental challenges, and opportunities in catalytic methanation of CO2," *Energy & Fuels*, vol. 30, no. 11, pp. 8815–8831, 2016.

[21] O. Gohar *et al.*, "Nanomaterials for advanced energy applications: Recent advancements and future trends," *Mater. Des.*, vol. 241, p. 112930, 2024.

[22] N. Farooq *et al.*, "Nanomaterial-based energy conversion and energy storage devices: a comprehensive review," *New J. Chem.*, 2024.

[23] D. Zheng, X. Yang, L. Čuček, J. Wang, T. Ma, and C. Yin, "Revolutionizing dye-sensitized solar cells with nanomaterials for enhanced photoelectric performance," *J. Clean. Prod.*, vol. 464, p. 142717, 2024.

[24] Y. Wang, J. Mao, X. Meng, L. Yu, D. Deng, and X. Bao, "Catalysis with two-dimensional materials confining single atoms: concept, design, and applications," *Chem. Rev.*, vol. 119, no. 3, pp. 1806–1854, 2018.

[25] T. A. Shifa and A. Vomiero, "Confined catalysis: progress and prospects in energy conversion," *Adv. Energy Mater.*, vol. 9, no. 40, p. 1902307, 2019.

[26] M. A. Nadeem *et al.*, "Earth metal doped metal oxide nanomaterials as a potential candidate for energy conversion," *Ceram. Int.*, vol. 50, no. 18, pp. 32542–32548, 2024.

[27] S. Shaheen, I. Sadiq, S. A. Ali, and T. Ahmad, "Bismuth-based multi-component heterostructured nanocatalysts for hydrogen generation," *Catalysts*, vol. 13, no. 2, p. 295, 2023.

[28] A. P. Manuel and K. Shankar, "Hot electrons in TiO2–noble metal nano-heterojunctions: Fundamental science and applications in photocatalysis," *Nanomaterials*, vol. 11, no. 5, p. 1249, 2021.

[29] X. Luo *et al.*, "Trimetallic metal–organic frameworks and derived materials for environmental remediation and electrochemical energy storage and conversion," *Coord. Chem. Rev.*, vol. 461, p. 214505, 2022.

[30] S. Ali *et al.*, "Noble metals based bimetallic and trimetallic nanoparticles: controlled synthesis, antimicrobial and anticancer applications," *Crit. Rev. Anal. Chem.*, vol. 51, no. 5, pp. 454–481, 2021.

[31] S. H. Gebre, "Multi-metallic carbide nanostructures and their electrocatalytic energy storage and conversion applications," *Results Chem.*, vol. 5, p. 100952, 2023.

[32] Y. Zhu, Z. Tang, L. Yuan, B. Li, Z. Shao, and W. Guo, "Beyond conventional structures: emerging complex metal oxides for efficient oxygen and hydrogen electrocatalysis," *Chem. Soc. Rev.*, 2025.

[33] Z. Sun, T. Liao, and L. Kou, "Strategies for designing metal oxide nanostructures," *Sci. China Mater*, vol. 60, no. 1, pp. 1–24, 2017.

[34] C. Xia, H. Wang, J. K. Kim, and J. Wang, "Rational design of metal oxide-based heterostructure for efficient photocatalytic and photoelectrochemical systems," *Adv. Funct. Mater.*, vol. 31, no. 12, p. 2008247, 2021.

[35] X. Wang, S. Song, and H. Zhang, "A redox interaction-engaged strategy for multicomponent nanomaterials," *Chem. Soc. Rev.*, vol. 49, no. 3, pp. 736–764, 2020.

[36] A. E. Kaifer, "Interplay between molecular recognition and redox chemistry," *Acc. Chem. Res.*, vol. 32, no. 1, pp. 62–71, 1999.

[37] I. Ahmad, M. A. Aftab, A. Fatima, S. D. Mekkey, S. Melhi, and S. Ikram, "A comprehensive review on the advancement of transition metals incorporated on functional magnetic nanocomposites for the catalytic reduction and photocatalytic degradation of organic pollutants," *Coord. Chem. Rev.*, vol. 514, p. 215904, 2024.

[38] M. B. Askari, M. T. T. Moghadam, and P. Salarizadeh, "Three-component NiO/Fe3O4/rGO nanostructure as an electrode material towards supercapacitor and alcohol electrooxidation," *Heliyon*, vol. 10, no. 20, 2024.

[39] T. Choudhary, A. Ahlawat, A. Khatri, and P. S. Rana, "Synergistic effect in the structural, optical, and electrical properties of harnessing NiFe2O4/CuO nanocomposite for enhanced

environmental remediation," *Environ. Sci. Pollut. Res.*, vol. 31, no. 2, pp. 2907–2919, 2024.

[40] J. Singh, T. Dutta, K.-H. Kim, M. Rawat, P. Samddar, and P. Kumar, "'Green'synthesis of metals and their oxide nanoparticles: applications for environmental remediation," *J. Nanobiotechnology*, vol. 16, pp. 1–24, 2018.

[41] P. Szczyglewska, A. Feliczak-Guzik, and I. Nowak, "Nanotechnology–general aspects: A chemical reduction approach to the synthesis of nanoparticles," *Molecules*, vol. 28, no. 13, p. 4932, 2023.

[42] H. Duan, D. Wang, and Y. Li, "Green chemistry for nanoparticle synthesis," *Chem. Soc. Rev.*, vol. 44, no. 16, pp. 5778–5792, 2015.

[43] I. Rahmawati *et al.*, "Gallic acid: A promising bioactive agent for food preservation and sustainable packaging development," *Case Stud. Chem. Environ. Eng.*, vol. 10, p. 100776, 2024.

[44] B. Badhani, N. Sharma, and R. Kakkar, "Gallic acid: A versatile antioxidant with promising therapeutic and industrial applications," *Rsc Adv.*, vol. 5, no. 35, pp. 27540–27557, 2015.

[45] M. Ahani and M. Khatibzadeh, "Green synthesis of silver nanoparticles using gallic acid as reducing and capping agent: effect of pH and gallic acid concentration on average particle size and stability," *Inorg. Nano-Metal Chem.*, vol. 52, no. 2, pp. 234–240, 2022.

[46] A. Lunkov *et al.*, "Synthesis of silver nanoparticles using gallic acid-conjugated chitosan derivatives," *Carbohydr. Polym.*, vol. 234, p. 115916, 2020.

[47] Y. Bao *et al.*, "In situ green synthesis of graphene oxide-silver nanoparticles composite with using gallic acid," *Front. Chem.*, vol. 10, p. 905781, 2022.

[48] C. Salmi *et al.*, "Gallic acid assisted synthesis of novel CuO/Ni/Fe3O4 nanocomposite for catalytic CO2 methanation and photocatalytic hydrogen generation," *J. Sol-Gel Sci. Technol.*, pp. 1–13, 2024.

[49] H. R. Naika *et al.*, "Green synthesis of CuO nanoparticles using Gloriosa superba L. extract and their antibacterial activity," *J. Taibah Univ. Sci.*, vol. 9, no. 1, pp. 7–12, 2015.

[50] O. S. Bello, K. A. Adegoke, and O. O. Akinyunni, "Preparation and characterization of a novel adsorbent from Moringa oleifera leaf," *Appl. Water Sci.*, vol. 7, no. 3, pp. 1295–1305, Jun. 2017, doi: 10.1007/s13201-015-0345-4.

[51] R. Ahmad and A. Mirza, "Facile one pot green synthesis of Chitosan-Iron oxide (CS-Fe2O3) nanocomposite: Removal of Pb (II) and Cd (II) from synthetic and industrial wastewater," *J. Clean. Prod.*, vol. 186, pp. 342–352, 2018.

[52] Y. Bai *et al.*, "Metal-organic frameworks nanocomposites with different dimensionalities for energy conversion and storage," *Adv. Energy Mater.*, vol. 12, no. 4, p. 2100346, 2022.

[53] N. Keller, J. Ivanez, J. Highfield, and A. M. Ruppert, "Photo-/thermal synergies in heterogeneous catalysis: Towards low-temperature (solar-driven) processing for sustainable energy and chemicals," *Appl. Catal. B Environ.*, vol. 296, p. 120320, 2021.

[54] N. Linares, A. M. Silvestre-Albero, E. Serrano, J. Silvestre-Albero, and J. García-Martínez, "Mesoporous materials for clean energy technologies," *Chem. Soc. Rev.*, vol. 43, no. 22, pp. 7681–7717, 2014.

[55] B. Ates, S. Koytepe, A. Ulu, C. Gurses, and V. K. Thakur, "Chemistry, structures, and advanced applications of nanocomposites from biorenewable resources," *Chem. Rev.*, vol. 120, no. 17, pp. 9304–9362, 2020.

[56] F. Kurul, B. Doruk, and S. N. Topkaya, "Principles of green chemistry: building a sustainable future," *Discov. Chem.*, vol. 2, no. 1, p. 68, 2025.

[57] A. Kumar and A. Bali, "Development of Advanced Instruments for Spectroscopic Analyses of Nanoparticles/Nanobioparticles," in *Synthesizing and Characterizing Plant-Mediated Biocompatible Metal Nanoparticles*, IGI Global, 2025, pp. 263–286.

[58] D. Sharda, K. Attri, and D. Choudhury, "Characterization Techniques Used for Advanced Materials Describing Physical, Mechanical, Thermal, and Biocompatibility Properties," in *Advanced Materials*, CRC Press, pp. 54–86.

[59] R. D. Prasad *et al.*, "A review on modern characterization techniques for analysis of nanomaterials and biomaterials," *ES Energy Environ.*, vol. 23, p. 1087, 2024.

[60] H. A. Mohammed, L. S. Eddine, M. Souhaila, G. G. Hasan, I. Kir, and J. A. A. Abdullah, "Green synthesis of SnO2 nanoparticles from Laurus nobilis L. extract for enhanced gelatin-based films and CEF@ SnO2 for efficient antibacterial activity," *Food Bioprocess Technol.*, pp. 1–19, 2023.

[61] I. Kir, S. E. Laouini, S. Meneceur, A. Bouafia, and H. A. M. Mohammed, "Biosynthesis and characterization of novel nanocomposite ZnO/BaMg2 efficiency for high-speed adsorption of AZO dye," *Biomass Convers. Biorefinery*, vol. 14, no. 16, pp. 19045–19054, 2024, doi: 10.1007/s13399-023-03985-5.

[62] A. Cárdenas-Arenas, H. S. Cortés, E. Bailón-García, A. Davó-Quiñonero, D. Lozano-Castelló, and A. Bueno-López, "Active, selective and stable NiO-CeO2 nanoparticles for CO2 methanation," *Fuel Process. Technol.*, vol. 212, p. 106637, 2021.

[63] D. De Masi, J. M. Asensio, P. Fazzini, L. Lacroix, and B. Chaudret, "Engineering iron–nickel nanoparticles for magnetically induced CO2 methanation in continuous flow," *Angew. Chemie Int. Ed.*, vol. 59, no. 15, pp. 6187–6191, 2020.

[64] M. A. A. Aziz, A. A. Jalil, S. Triwahyono, and S. M. Sidik, "Methanation of carbon dioxide on metal-promoted mesostructured silica nanoparticles," *Appl. Catal. A Gen.*, vol. 486, pp. 115–122, 2014.

[65] M. A. A. Aziz, A. A. Jalil, S. Triwahyono, R. R. Mukti, Y. H. Taufiq-Yap, and M. R. Sazegar, "Highly active Ni-promoted mesostructured silica nanoparticles for CO2 methanation," *Appl. Catal. B Environ.*, vol. 147, pp. 359–368, 2014.

[66] H. A. Mohammed, S. E. Laouini, S. Meneceur, C. Salmi, and M. M. Husein, "MgO/Ni Nanocomposite and its PVP-modified Derivative for Catalytic CO2 Methanation and Photocatalytic Hydrogen Production," *Surfaces and Interfaces*, p. 104643, 2024.

[67] S. Anwaar *et al.*, "Biogenic synthesis of copper oxide nanoparticles using Eucalyptus globulus Leaf Extract and its impact on germination and Phytochemical composition of Lactuca sativa," *Sci. Rep.*, vol. 14, no. 1, pp. 1–15, 2024.

[68] N. Sofyan, A. M. Jamil, A. Ridhova, A. H. Yuwono, D. Dhaneswara, and J. W. Fergus, "Graphene Oxide Doping in Tropical Almond Fruits Extract Mediated Green Synthesis of Tio2 Nanoparticles for Improved Dssc Power Conversion Efficiency," *Available SSRN 4720043*.

[69] M. Nasrollahzadeh, M. Sajjadi, H. Komber, H. A. Khonakdar, and S. M. Sajadi, "In situ green synthesis of Cu-Ni bimetallic nanoparticles supported on reduced graphene oxide as an effective and recyclable catalyst for the synthesis of N-benzyl-N-aryl-5-amino-1H-tetrazoles," *Appl. Organomet. Chem.*, vol. 33, no. 7, p. e4938, 2019.

[70] H. Assefa, S. Singh, N. Shehata, N. A. Khan, F. E. Olu, and P. C. Ramamurthy, "Green synthesis and characterization of CuO/PANI nanocomposite for efficient Pb (II) adsorption from contaminated water," *Sci. Rep.*, vol. 14, no. 1, p. 30972, 2024.

[71] K. Shameli *et al.*, "Green synthesis of silver/montmorillonite/chitosan bionanocomposites using the UV irradiation method and evaluation of antibacterial activity," *Int. J. Nanomedicine*, pp. 875–887, 2010.

[72] N. T. Baliah, P. Muthulakshmi, P. C. Sheeba, and S. L. Priyatharsini, "Green synthesis and characterization of nanocomposites," *Int. Res. J. Eng. Technol*, vol. 5, pp. 179–186, 2018.

[73] T. U. Rahman, S. Mukhtar, M. A. Zeb, and W. Liaqat, "Green Synthesis, Characterization, and Antibacterial Activity of Metal Nanoparticles and Nanocomposites Using Leaves Extract of Prunus persica L.," *J. Appl. Spectrosc.*, vol. 89, no. 4, pp. 773–779, 2022.

[74] C. Salmi, S. E. Laouini, S. Meneceur, and H. A. Mohammed, "Biosynthesized MgO@ SnO2 nanocomposite and their modification with polyvinylpyrrolidone. Efficiency for removal of heavy metals and contaminants from industrial petroleum wastewater," *Clean Technol. Environ. Policy*, pp. 1–20, 2024.

[75] L. S. Eddine *et al.*, "Biogenic synthesis of Fe3O4/NiO nanocomposites using Ocimum basilicum leaves for enhanced degradation of organic dyes and hydrogen evolution," *J. Porous Mater.*, vol. 31, no. 1, pp. 213–226, 2024.

[76] A. M. El Shafey, "Green synthesis of metal and metal oxide nanoparticles from plant leaf

extracts and their applications: A review," *Green Process. Synth.*, vol. 9, no. 1, pp. 304–339, 2020.

[77] M. Hariram and S. Vivekanandhan, "Phytochemical process for the functionalization of materials with metal nanoparticles: current trends and future perspectives," *ChemistrySelect*, vol. 3, no. 48, pp. 13561–13585, 2018.

[78] A. Laouini *et al.*, "Boosted Antioxidant and Photocatalytic Power: Reusable PEG-Coated Iron Oxide Nanocomposites for Effective Cephalexin and BCB Dye Degradation," *J. Clust. Sci.*, vol. 35, no. 8, pp. 3131–3151, Dec. 2024, doi: 10.1007/s10876-024-02716-8.

[79] K. Pielichowski, J. Njuguna, and T. M. Majka, *Thermal degradation of polymeric materials*. Elsevier, 2022.

[80] S. Meneceur *et al.*, "High-efficiency photocatalytic degradation of antibiotics and molecular docking study to treat the omicron variant of COVID-19 infection using biosynthesized ZnO@Fe 3 O 4 nanocomposites," *Phys. Scr.*, vol. 98, no. 11, p. 115926, Nov. 2023, doi: 10.1088/1402-4896/acff2d.

[81] F. Odobel and Y. Pellegrin, "Recent advances in the sensitization of wide-band-gap nanostructured p-type semiconductors. Photovoltaic and photocatalytic applications," *J. Phys. Chem. Lett.*, vol. 4, no. 15, pp. 2551–2564, 2013.

[82] S. Tasleem and M. Tahir, "Recent progress in structural development and band engineering of perovskites materials for photocatalytic solar hydrogen production: A review," *Int. J. Hydrogen Energy*, vol. 45, no. 38, pp. 19078–19111, 2020.

[83] J. Lin *et al.*, "Enhanced low-temperature performance of CO2 methanation over mesoporous Ni/Al2O3-ZrO2 catalysts," *Appl. Catal. B Environ.*, vol. 243, pp. 262–272, 2019.

[84] K. Stangeland, D. Y. Kalai, H. Li, and Z. Yu, "Active and stable Ni based catalysts and processes for biogas upgrading: The effect of temperature and initial methane concentration on CO2 methanation," *Appl. Energy*, vol. 227, pp. 206–212, 2018.

[85] K. Stangeland, D. Kalai, H. Li, and Z. Yu, "CO2 methanation: the effect of catalysts and reaction conditions," *Energy Procedia*, vol. 105, pp. 2022–2027, 2017.

[86] C. Molinet-Chinaglia, S. Shafiq, and P. Serp, "Low Temperature Sabatier CO2 Methanation," *ChemCatChem*, vol. 16, no. 24, p. e202401213, 2024.

[87] X. Chen *et al.*, "Recent advances in supported metal catalysts and oxide catalysts for the reverse water-gas shift reaction," *Front. Chem.*, vol. 8, p. 709, 2020.

[88] B. Miao, S. S. K. Ma, X. Wang, H. Su, and S. H. Chan, "Catalysis mechanisms of CO 2 and CO methanation," *Catal. Sci. Technol.*, vol. 6, no. 12, pp. 4048–4058, 2016.

[89] C. Mebrahtu, F. Krebs, S. Abate, S. Perathoner, G. Centi, and R. Palkovits, "CO2

methanation: principles and challenges," in *Studies in surface science and catalysis*, vol. 178, Elsevier, 2019, pp. 85–103.

[90] O. E. Medina, A. A. Amell, D. López, and A. Santamaría, "Comprehensive review of nickel-based catalysts advancements for CO2 methanation," *Renew. Sustain. Energy Rev.*, vol. 207, p. 114926, 2025.

[91] S. López-Rodríguez *et al.*, "Elucidating the role of the metal catalyst and oxide support in the Ru/CeO2-catalyzed CO2 methanation mechanism," *J. Phys. Chem. C*, vol. 125, no. 46, pp. 25533–25544, 2021.

[92] A. A. Alkhoori, "CO2 Methanation Reaction: Insights into the Development of Catalysts and Mechanism." Khalifa University of Science, 2023.

[93] S. Ullah, X. Yang, Z. U. Khan, S. Aziz, W. Haider, and H. Ben, "Relationship between Catalyst Structure and Activity in CO2 Methanation of Ru-Based Catalysts: Recent Progress and Future Prospects," *New J. Chem.*, 2025.

[94] A. Mondal, M. Sultana, and A. Paul, "Understanding the Mechanism of CO2 to CH4 Conversion and Hydrogen Evolution Reaction on Mg Nanoparticles in Water under ambient conditions: A DFT Perspective," 2025.

[95] P. Wang *et al.*, "Recent advances and challenges in efficient selective photocatalytic CO2 methanation," *Small*, vol. 20, no. 32, p. 2400700, 2024.

[96] H. Zada, J. Yu, and J. Sun, "Active Sites for CO2 Hydrogenation to Methanol: Mechanistic Insights and Reaction Control," *ChemSusChem*, vol. 18, no. 4, p. e202401846, 2025.

[97] R. Gholizadeh, M. Pavlin, M. Huš, and B. Likozar, "Multiscale Modeling of CO2 Electrochemical Reduction on Copper Electrocatalysts: A Review of Advancements, Challenges, and Future Directions," *ChemSusChem*, vol. 18, no. 1, p. e202400898, 2025.

[98] S. A. Ali, I. Sadiq, M. Estrader, and T. Ahmad, "Atomic-Level Tuning Strategies in Designing Active Catalysts for Heterogeneous CO2 Conversion into Chemical Feedstock," *ChemCatChem*, p. e202500032, 2025.

[99] M. Ismael, E. Elhaddad, and M. Wark, "Construction of SnO2/g-C3N4 composite photocatalyst with enhanced interfacial charge separation and high efficiency for hydrogen production and Rhodamine B degradation," *Colloids Surfaces A Physicochem. Eng. Asp.*, vol. 638, p. 128288, 2022.

[100] Z. Yan *et al.*, "Photocatalysis for synergistic water remediation and H2 production: A review," *Chem. Eng. J.*, vol. 472, p. 145066, 2023.

[101] M. R. Saleh, S. M. Ahmed, S. A. Soliman, and H. M. El-Bery, "Facile construction of self-assembled Cu@ polyaniline nanocomposite as an efficient noble-metal free cocatalyst for boosting photocatalytic hydrogen production," *Int. J. Hydrogen Energy*, vol. 47, no. 9, pp.

6011–6028, 2022.

[102] L. Leone, G. Sgueglia, S. La Gatta, M. Chino, F. Nastri, and A. Lombardi, "Enzymatic and bioinspired systems for hydrogen production," *Int. J. Mol. Sci.*, vol. 24, no. 10, p. 8605, 2023.

[103] S.-I. Giannakandropoulou, "Hydrogen production by anoxic corrosion of steel under gamma radiation." Université Paris-Saclay, 2022.

[104] J. Teng *et al.*, "Coupling photocatalytic hydrogen production with key oxidation reactions," *Angew. Chemie Int. Ed.*, vol. 63, no. 50, p. e202416039, 2024.

[105] Z.-X. Yang *et al.*, "2022 roadmap on hydrogen energy from production to utilizations," *Rare Met.*, vol. 41, no. 10, pp. 3251–3267, 2022.

[106] R. Sharma *et al.*, "Photocatalytic hydrogen production using graphitic carbon nitride (GCN): A precise review," *Renew. Sustain. Energy Rev.*, vol. 168, p. 112776, 2022.

[107] C. M. Perales *et al.*, "From Pollutant Removal to Renewable Energy: MoS_2-Enhanced P25-Graphene Photocatalysts for Malathion Degradation and H_2 Evolution," 2025.

[108] S. Zhang, K. Wang, F. Li, and S.-H. Ho, "Structure-mechanism relationship for enhancing photocatalytic H2 production," *Int. J. Hydrogen Energy*, vol. 47, no. 88, pp. 37517–37530, 2022.

[109] H. A. Maitlo, B. Anand, and K.-H. Kim, "TiO2-based photocatalytic generation of hydrogen from water and wastewater," *Appl. Energy*, vol. 361, p. 122932, 2024.

[110] S. Chen *et al.*, "Photocatalytic glucose depletion and hydrogen generation for diabetic wound healing," *Nat. Commun.*, vol. 13, no. 1, p. 5684, 2022.

[111] L. Schumacher and R. Marschall, "Recent advances in semiconductor heterojunctions and Z-schemes for photocatalytic hydrogen generation," *Top. Curr. Chem.*, vol. 380, no. 6, p. 53, 2022.

[112] S. Ali, A. Razzaq, H. Kim, and S.-I. In, "Activity, selectivity, and stability of earth-abundant CuO/Cu2O/Cu0-based photocatalysts toward CO2 reduction," *Chem. Eng. J.*, vol. 429, p. 131579, 2022.

[113] S. S. AlNeyadi *et al.*, "Hydrophilic magnetic COFs: The Answer to photocatalytic degradation and removal of imidacloprid insecticide," *Heliyon*, vol. 10, no. 20, 2024.

[114] Z. Lu, D. Yu, F. Nie, Y. Wang, and Y. Chong, "Iron nanoparticles open up new directions for promoting healing in chronic wounds in the context of bacterial infection," *Pharmaceutics*, vol. 15, no. 9, p. 2327, 2023.

[115] R. Khoramian, M. Issakhov, P. Pourafshary, M. Gabdullin, and A. Sharipova, "Surface modification of nanoparticles for enhanced applicability of nanofluids in harsh reservoir

conditions: A comprehensive review for improved oil recovery," *Adv. Colloid Interface Sci.*, p. 103296, 2024.

[116] J. Zhao, I. A. Khan, and F. R. Fronczek, "Gallic acid," *Struct. Reports*, vol. 67, no. 2, pp. o316–o317, 2011.

[117] E. Haslam, "Hydroxybenzoic acids and the enigma of gallic acid," *Shikimic Acid Pathw.*, pp. 163–200, 1986.

[118] R. Venkatesan, P. Sivaprakash, I. Kim, A. M. Tawfeek, and S.-C. Kim, "Green synthesis of carbon nanoparticle-reinforced nanocomposites with gallic acid as a crosslinking agent on poly (butylene adipate-co-terephthalate): Preparation, characterization, and performances," *Ind. Crops Prod.*, vol. 209, p. 117949, 2024.

[119] N. Farzaneh, M. A. Chamjangali, N. Goudarzi, and M. Rezakazemi, "Green synthesis of gallic acid–capped gold nanoparticles as novel electro-catalyst for electro-oxidation of ethylene glycol in alkaline media," *Int. J. Hydrogen Energy*, vol. 51, pp. 245–258, 2024.

[120] A. S. Aliero, N. A. Zawawi, N. A. N. N. Malek, M. Helmi Sani, and M. H. Usman, "Biogenic Synthesis of Silver Nanoparticles Using Palm Oil Mill Effluent and its Antioxidant Potential," *Waste and Biomass Valorization*, pp. 1–8, 2025.

[121] M. V Kovalenko *et al.*, "Prospects of nanoscience with nanocrystals," *ACS Nano*, vol. 9, no. 2, pp. 1012–1057, 2015.

[122] A. Fahes, L. Balan, C. Andreazza-Vignolle, C. de Melo, D. Zanghi, and P. Andreazza, "Polymer/AgPt Bimetallic Nanoparticles Synergy: Optimizing Plasmonic Durability through Controlled Synthesis and Matrix Integration," *Nanoscale Adv.*, 2025.

[123] X. Guan, S. Yan, Z. Xu, and H. Fan, "Gallic acid-conjugated iron oxide nanocomposite: An efficient, separable, and reusable adsorbent for remediation of Al (III)-contaminated tannery wastewater," *J. Environ. Chem. Eng.*, vol. 5, no. 1, pp. 479–487, 2017.

[124] C. Sainz-Urruela, S. Vera-López, M. P. San Andrés, and A. M. Díez-Pascual, "Surface functionalization of graphene oxide with tannic acid: Covalent vs non-covalent approaches," *J. Mol. Liq.*, vol. 357, p. 119104, 2022.

[125] E. Pastor, M. Sachs, S. Selim, J. R. Durrant, A. A. Bakulin, and A. Walsh, "Electronic defects in metal oxide photocatalysts," *Nat. Rev. Mater.*, vol. 7, no. 7, pp. 503–521, 2022.

[126] H. Siddiqui, M. R. Parra, P. Pandey, M. S. Qureshi, and F. Z. Haque, "Utility of copper oxide nanoparticles (CuO-NPs) as efficient electron donor material in bulk-heterojunction solar cells with enhanced power conversion efficiency," *J. Sci. Adv. Mater. Devices*, vol. 5, no. 1, pp. 104–110, 2020.

[127] S. De, J. Zhang, R. Luque, and N. Yan, "Ni-based bimetallic heterogeneous catalysts for energy and environmental applications," *Energy Environ. Sci.*, vol. 9, no. 11, pp. 3314–

3347, 2016.

[128] D. Febriantini, A. R. Liandi, and Y. Yulizar, "A comprehensive study on the influence of single and multiple phytochemicals in facilitating green synthesis of ZrO2 nanoparticles," *Nano-Structures & Nano-Objects*, vol. 39, p. 101303, 2024.

[129] S. Zhu *et al.*, "Recent advances in catalyst structure and composition engineering strategies for regulating CO2 electrochemical reduction," *Adv. Mater.*, vol. 33, no. 50, p. 2005484, 2021.

[130] A. Pappa, C. Pham-Huu, S. Papaefthimiou, and S. Zafeiratos, "Catalytic Approaches for CO2 Conversion to Value-Added Products: An Overview of Life Cycle Assessment Studies," *Adv. Energy Sustain. Res.*, p. 2400399, 2025.

[131] R. Estevez, L. Aguado-Deblas, F. M. Bautista, F. J. López-Tenllado, A. A. Romero, and D. Luna, "A review on green hydrogen valorization by heterogeneous catalytic hydrogenation of captured CO2 into value-added products," *Catalysts*, vol. 12, no. 12, p. 1555, 2022.

[132] V. D. Mercader, P. Aragüés-Aldea, P. Durán, E. Francés, J. Herguido, and J. A. Peña, "Optimizing sorption enhanced methanation (sem) of CO2 with Ni3Fe+ lta 5 A mixtures," *Catal. Today*, vol. 453, p. 115262, 2025.

[133] A. S. S. Pinto, L. J. McDonald, J. L. H. Galvan, and M. McManus, "Improving life cycle assessment for carbon capture and circular product systems," *Int. J. Life Cycle Assess.*, vol. 29, no. 3, pp. 394–415, 2024.

[134] Z. O. U. Caineng *et al.*, "Progress, challenge and significance of building a carbon industry system in the context of carbon neutrality strategy," *Pet. Explor. Dev.*, vol. 50, no. 1, pp. 210–228, 2023.

[135] G. Varvoutis, A. Lampropoulos, E. Mandela, M. Konsolakis, and G. E. Marnellos, "Recent advances on CO2 mitigation technologies: on the role of hydrogenation route via green H2," *Energies*, vol. 15, no. 13, p. 4790, 2022.

[136] B. Li, X. Liu, H. Zhu, H. Guan, and R. Guo, "Recent Progress of Round-the-Clock Photocatalytic System in Environmental and Energy Applications: A Review," *ChemPhysChem*, vol. 26, no. 9, p. e202401144, 2025.

[137] S. Rai, N. Sriram, and P. Alva, "Advancing green laboratory practices: A review of sustainability in healthcare," 2024.

Chapter IV:

Green Fabrication of NiO/Ni@PVA Nanofibers for Enhanced Soap Extraction from Biodiesel

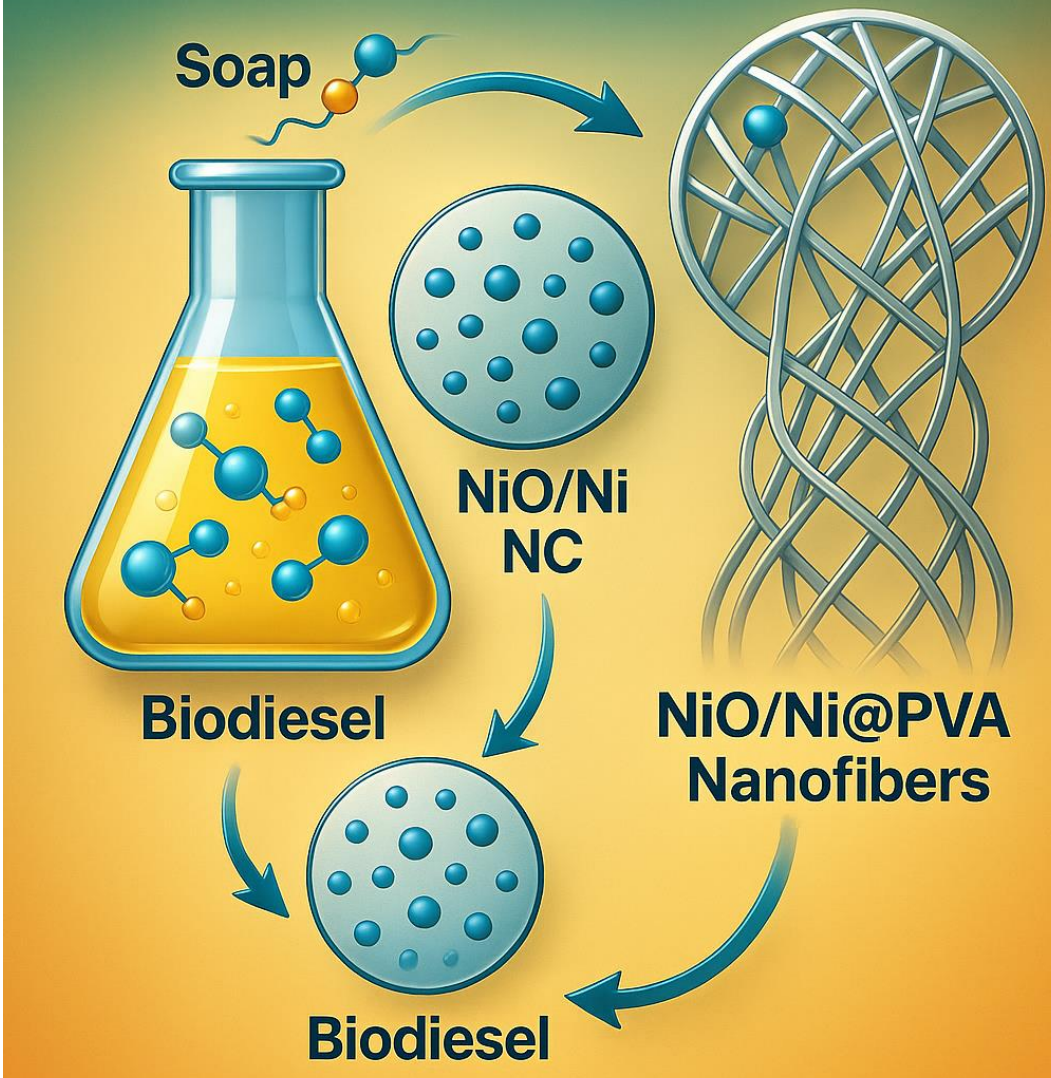

1. Introduction

Biodiesel, a renewable and biodegradable alternative to fossil fuels, has garnered substantial interest as part of the global transition toward sustainable energy [1][2]. Derived primarily from vegetable oils or animal fats through transesterification [3][4], biodiesel offers environmental advantages such as reduced greenhouse gas emissions and enhanced biodegradability [3][5]. However, despite its promise, several challenges persist in its production chain, particularly in post-reaction purification [6][7][8]. Among these, the presence of soap residues formed as byproducts during transesterification poses a significant barrier to achieving fuel-grade biodiesel [9][10], thus necessitating innovative purification strategies to enhance fuel quality and engine compatibility [11][12].

Traditional soap removal techniques such as water washing, adsorption, and solvent extraction have been extensively explored [13][14][15]. Water washing remains the most commonly used method due to its simplicity and effectiveness [16]; however, it generates large volumes of wastewater, increasing operational costs and environmental burdens [17][18]. Solvent extraction, while effective, poses risks related to solvent recovery and toxicity [19]. Adsorption techniques using solid-phase materials are increasingly favored for their efficiency and lower ecological footprint [20], particularly when integrated with recyclable or biodegradable adsorbents [21]. Despite their respective benefits, these methods face limitations in scalability, cost, and environmental compatibility, underscoring the need for more sustainable solutions [22].

The presence of soap residues in biodiesel negatively affects its physicochemical properties, leading to poor combustion performance [23][24], increased particulate emissions, injector fouling, and clogged filters in engines [25][26]. These residues also interfere with accurate fuel characterization and quality testing [27], complicating adherence to international fuel standards such as ASTM D6751 and EN 14214 [28][29]. Therefore, efficient soap removal is essential not only for compliance but also for ensuring long-term engine durability and performance [30][31][32].

Conventional purification methods, though widely used, suffer from several drawbacks [33][34]. Water-based techniques require extensive drying steps post-washing, adding to

the energy burden. Solvent-based approaches often involve hazardous chemicals and are economically impractical at an industrial scale [35]. Additionally, solid adsorbents like activated carbon and ion-exchange resins, while effective, are non-renewable and often non-recyclable [36][37]. These limitations have prompted research into alternative materials and methods that combine efficiency with environmental sustainability [38].

Nanotechnology offers a transformative platform for biodiesel purification[39], leveraging the high surface area, tunable surface chemistry, and enhanced reactivity of nanomaterials [40][41]. Nanomaterial-based adsorbents can provide selective and efficient removal of contaminants like soap, glycerol, and methanol, with improved reusability and lower material requirements [42][43][44]. Their physicochemical properties can be engineered for specific interactions with soap molecules, thereby enhancing purification performance while reducing secondary waste generation [45].

Among various nanomaterials [46], metal oxide-based nanostructures have shown particular promise for biodiesel treatment [47][40]. Their high adsorption affinity [48], catalytic potential, and stability under reaction conditions make them ideal candidates for sustainable purification processes [49][47]. When designed appropriately, these materials can address key operational challenges such as soap selectivity, regeneration efficiency, and compatibility with biodiesel matrices [41][50].

A notable advancement in this domain is the green synthesis of nanocomposites using plant extracts [51][52]. For instance, *Pistacia lentiscus* extract serves as an effective biogenic reducing agent for the formation of NiO/Ni nanostructures [53]. This eco-friendly route avoids the use of hazardous precursors and supports a circular economy by utilizing plant-based resources [54]. The phytochemicals present in the extract not only mediate the reduction process but also impart functional surface groups that enhance adsorption interactions with soap molecules [55].

Nickel-based nanostructures, particularly NiO/Ni composites, offer exceptional performance in adsorption and catalysis due to their amphoteric surface behavior, redox activity, and strong affinity for organic and ionic species [56]. Their magnetic properties also enable easy recovery post-treatment, further supporting their recyclability and cost-

effectiveness [57][58]. When integrated into a polymeric matrix such as polyvinyl alcohol (PVA) [59], these nanostructures form flexible and robust nanofibers with enhanced mechanical and functional properties [60].

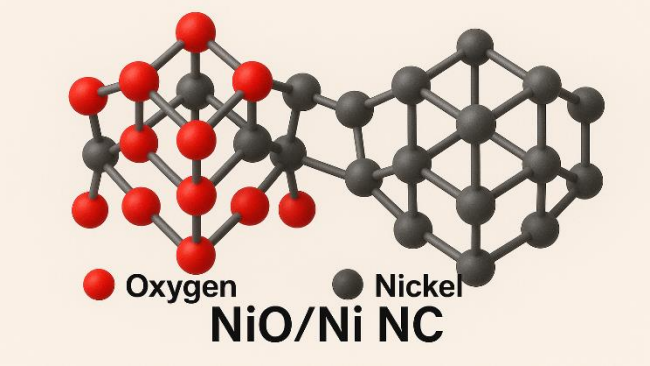

Figure IV. 1: Molecular Structure of NiO/Ni Nanocomposite

Electrospinning has emerged as a versatile technique for fabricating nanofiber membranes from polymer-based matrices [61]. It allows for the controlled deposition of nanoparticles within fibrous networks, enhancing surface area and accessibility of active sites [62][63]. Electrospun nanofibers not only improve adsorption capacity but also facilitate easy handling and regeneration, making them suitable for continuous purification operations in industrial settings [64][65].

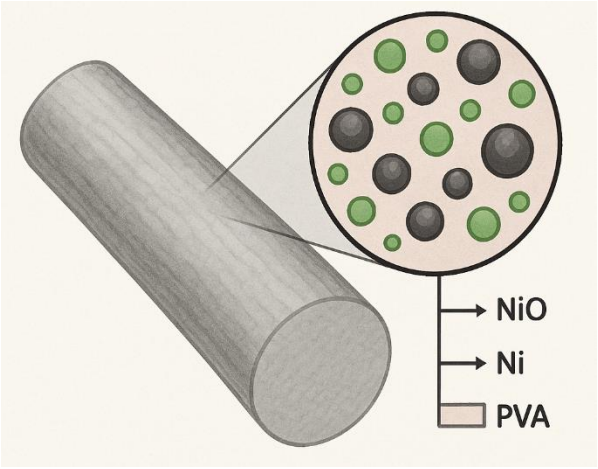

Figure IV. 2: Structural Illustration of NiO/Ni@PVA Electrospun Nanofiber Showing Nanoparticle Dispersion Within the Polymer Matrix

The overarching objective of this chapter is to investigate the green synthesis and electrospinning of NiO/Ni@PVA nanofibers for effective soap removal from biodiesel. Through comprehensive characterization, adsorption experiments, and computational modeling, this study aims to evaluate the structural, functional, and environmental attributes of the developed materials. By integrating green chemistry, nanotechnology, and sustainable engineering principles, this work contributes to advancing eco-efficient purification systems capable of addressing the pressing quality challenges in biodiesel production.

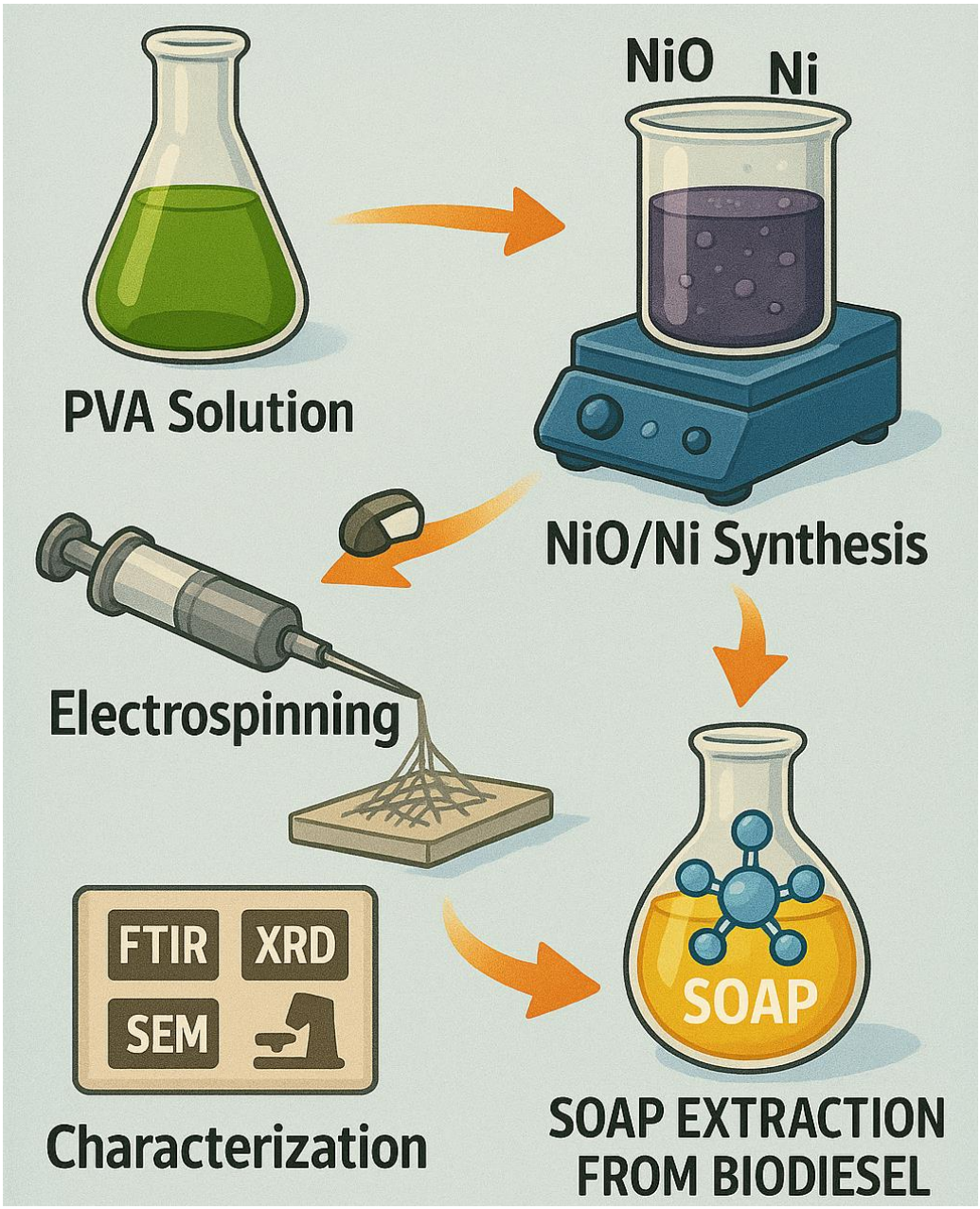

Figure IV. 3: Schematic Illustration of the Green Fabrication and Application of NiO/Ni NC & NiO/Ni@PVA Nanofibers for Efficient Soap Extraction from Biodiesel

2. Experimental Methodology

2.1. Synthesis of NiO/Ni Nanocomposite via Green Chemistry

The green synthesis of NiO/Ni nanocomposites was initiated by dissolving 0.3 M nickel sulfate ($NiSO_4$) in 100 mL of deionized water. The prepared solution was subsequently mixed with 900 mL of *Pistacia lentiscus* leaf extract in an Erlenmeyer flask, ensuring minimal oxygen exposure throughout the process. Thereafter, 70 mL of 2 M sodium hydroxide (NaOH) solution was gradually introduced into the mixture, leading to the formation of dark precipitates, indicative of nanocomposite formation. The suspension was stirred continuously at 70 °C and 700 rpm for approximately 3 hours. The resulting precipitates were separated via centrifugation at 4000 rpm for 10 minutes, followed by washing with distilled water at ambient temperature and an additional centrifugation for 15 minutes. The purified precipitate was dried in an oven at 75 °C for 5 hours and subsequently subjected to calcination at 550 °C for 4 hours, yielding the final NiO/Ni nanocomposite. The overall synthesis procedure is depicted in Figure IV.4.

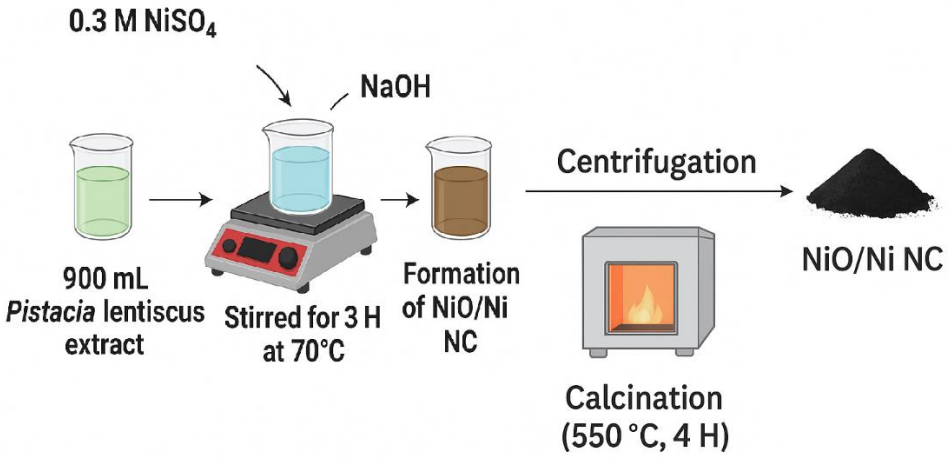

Figure IV. 4: Green Synthesis of NiO/Ni Nanocomposites

2.2. Preparation of NiO/Ni@PVA Electrospun Nanofibers

The fabrication of NiO/Ni@PVA electrospun nanofibers commenced with the preparation of a 12 wt% polyvinyl alcohol (PVA) solution, into which 0.2 g of NiO/Ni nanocomposites (NCs) were incorporated. The resulting mixture was continuously stirred for 2 hours to ensure uniform dispersion of the nanocomposites within the polymer matrix. Subsequently,

the solution was subjected to ultrasonication for 15 minutes to eliminate any entrapped air bubbles, resulting in a clear and homogeneous dispersion. This prepared solution was then loaded into the syringe of an electrospinning apparatus. Electrospinning was conducted using a Nanospider Lab 200 system equipped with a rotating cylinder electrode for membrane fabrication. The process parameters included an applied voltage of 51 kV, an electrode separation distance of 18 cm, and a cylinder rotation speed of 4 rpm. The electrospinning was carried out at a controlled temperature of 23.5 °C and a relative humidity of 38%, with fiber deposition occurring on a polypropylene nonwoven substrate. The detailed schematic representation of the NiO/Ni@PVA nanofiber preparation is presented in Figure IV.5.

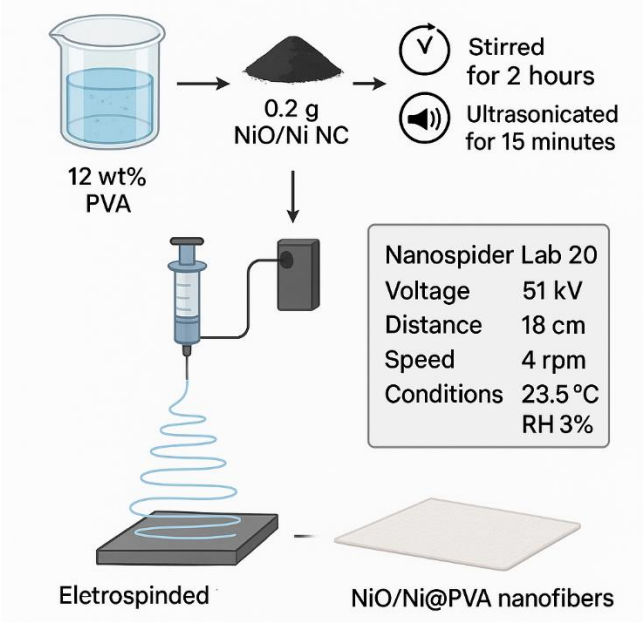

Figure IV. 5: Preparation of NiO/Ni@PVA Electrospun Nanofibers

2.3. Characterization Techniques (UV-Vis, XRD, FTIR, SEM, TGA, XPS)

The optical properties of the NiO/Ni nanocomposites and NiO/Ni@PVA nanofibers were examined using UV-visible spectroscopy, with absorption spectra recorded across the 200–800 nm range utilizing a UVILine 9600 spectrophotometer (SECOMAM Aqualabo, France). Fourier-transform infrared (FTIR) spectroscopy was employed to identify the

functional groups present within the nanocomposites. For FTIR analysis, thin films were prepared by blending the nanocomposites with potassium bromide (KBr) and analyzed using a Nicolet iS5 FTIR spectrometer (Thermo Scientific, USA). The crystallite size was estimated from X-ray diffraction (XRD) patterns using the Scherrer equation. The surface morphology, particle size distribution, and degree of aggregation were assessed through scanning electron microscopy (SEM, VEGA3 model, TESCAN, USA) [66].

Thermogravimetric analysis (TGA) was performed using a Q500 thermal analyzer (TA Instruments, USA) under a nitrogen atmosphere to evaluate the thermal stability of the nanomaterials [67].

Additionally, the chemical composition and surface states were characterized via X-ray photoelectron spectroscopy (XPS) using a VGS ESCALAB 210 system equipped with a monochromatic Mg Kα radiation source. The analysis was conducted under constant pass energy mode, maintaining a chamber pressure of approximately 5×10^{-10} Torr [68].

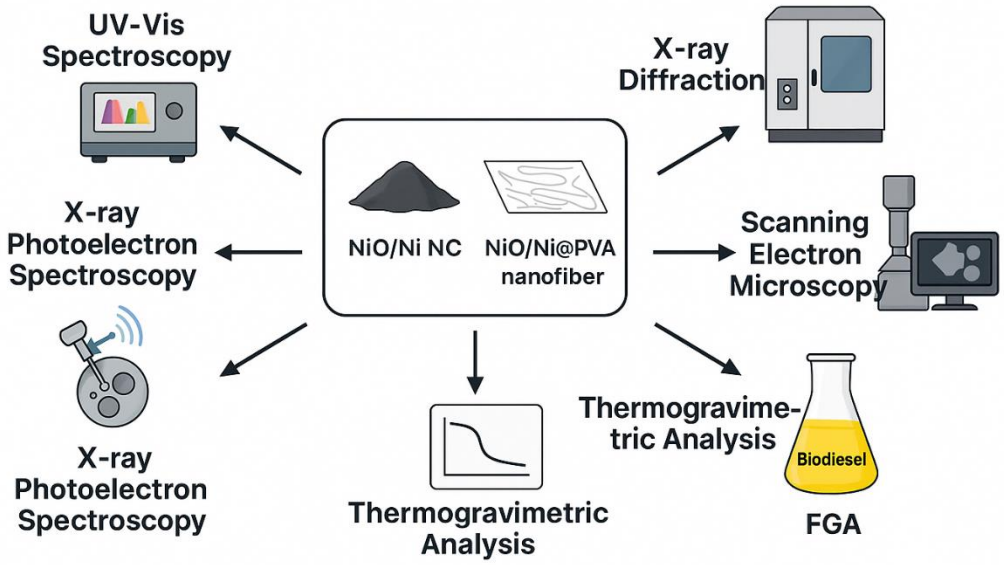

Figure IV. 6: Characterization of NiO/Ni Nanocomposites and NiO/Ni@PVA Nanofibers

2.4. Biodiesel Production from Palm Oil

Biodiesel synthesis was carried out by initially preparing Solution 1, comprising 150 mL of methanol and 4.2 g of potassium hydroxide (KOH) [69]. This mixture was heated on a

hot plate equipped with a magnetic stirrer at a temperature range of 55–60 °C until a homogeneous solution was achieved. In parallel, Solution 2 was prepared by heating 420 mL of palm oil within the same temperature range [70]. Once both solutions attained the target temperature, Solution 1 was gradually added to Solution 2. The combined mixture was stirred continuously at 60 °C for 1 hour at a stirring speed of 250 rpm to facilitate the transesterification reaction. Upon completion, the reaction mixture was transferred into a separation funnel and left undisturbed for 4–5 hours to allow phase separation, resulting in the collection of biodiesel in the upper layer and glycerol in the lower layer [71][72].

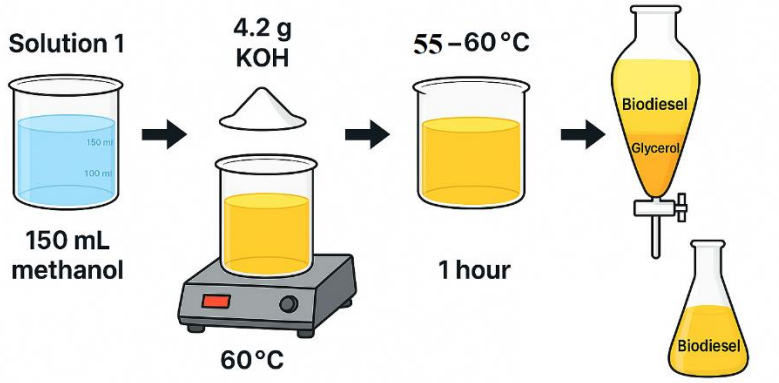

Figure IV. 7: Preparation of Biodiesel

2.5. Soap Removal Experiments: Dosage, Contact Time, Stirring Speed

A screening study was conducted during the solid-liquid extraction stage to determine the most effective nanocomposite for soap removal from biodiesel. For each extraction trial, a conical flask was charged with 0.03 g of the NC (either NiO/Ni powder or NiO/Ni@PVA nanofiber) and 15 mL of biodiesel (as illustrated in Figure IV.3). The mixtures were subjected to orbital shaking at 150 rpm across different contact times (0, 3, 6, 9, 12, 15, and 18 minutes) to ensure thorough homogenization. Upon completion of the extraction, the phases were allowed to separate naturally before soap content was quantified by centrifugation. To evaluate the effect of catalyst dosage, experiments were conducted by varying the catalyst mass (0.01, 0.015, 0.02, 0.025, and 0.03 g per 10 mL of biodiesel), maintaining a constant contact time of 18 minutes and a stirring speed of 150 rpm. Additionally, the influence of stirring speed on the extraction efficiency was assessed by

varying the mixing speeds (30, 60, 90, 120, and 150 rpm). All experiments were performed under ambient temperature conditions.

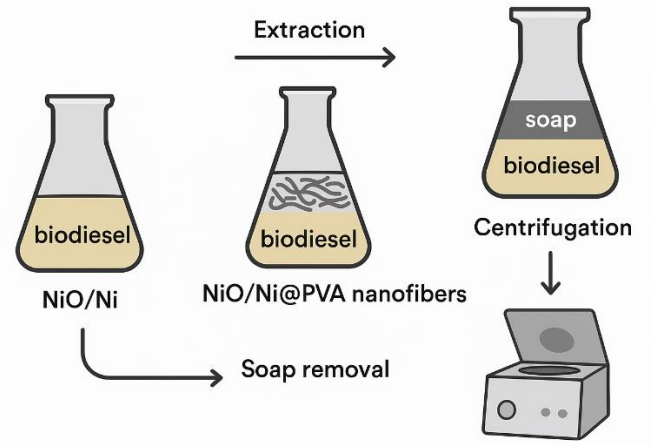

Figure IV. 8: Removal of Soap from Biodiesel Using NiO/Ni Nanocomposites and NiO/Ni@PVA Nanofibers

2.6. Soap Content Analysis (AOCS Titration Method)

The soap content in biodiesel was quantified following the AOCS titration method. Specifically, 2.5 mL of 98% acetone and 97.5 µL of bromophenol blue indicator were added to 40 g of biodiesel. The resulting solution was titrated with a 0.01 M hydrochloric acid (HCl) solution until a color change from blue to yellow was observed. The soap concentration was then calculated using the following equation [13]:

$$soap\ (ppm) = \frac{volume\ of\ titrated\ HCl\ (ml) \times 0.01\ M \times 304400}{wieght\ of\ biodiesel\ (g)} \qquad (1)$$

Furthermore, the extraction efficiency (%) was determined according to the following formula [73]:

$$Extraction\ efficiency\ (\%) = \frac{C_i - C_f}{C_i} \times 100\% \qquad (2)$$

where C_i represents the initial soap concentration (ppm) and C_f denotes the final soap concentration (ppm).

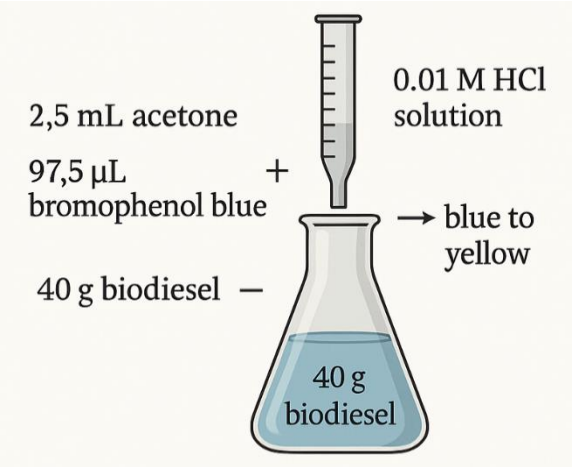

Figure IV. 9: AOCS Titration Method

2.7. Efficiency of Soap Removal from Biodiesel Over Successive Cycles

Following the optimization of operational parameters specifically, a contact time of 18 minutes, a catalyst dosage of 0.03 g, and a stirring speed of 150 rpm the reusability and adsorption efficiency of the NiO/Ni nanocomposites and NiO/Ni@PVA nanofibers were systematically evaluated. In these experiments, 10 mL of biodiesel containing an initial soap concentration of 4671 ppm was treated with 0.03 g of catalyst under the optimized conditions. Soap content was quantified using the AOCS titration method [13]. After each treatment cycle, the catalyst was separated from the biodiesel, thoroughly washed, and subsequently dried at 100 °C. The recovered catalyst was then reused in further cycles by mixing with fresh 10 mL samples of biodiesel, maintaining a constant initial soap concentration of 4671 ppm across all cycles.

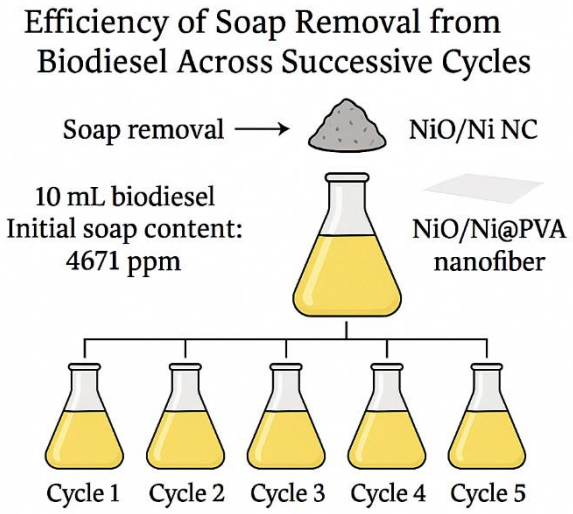

Figure IV. 10: Efficiency of Soap Removal from Biodiesel Across Successive Cycles

2.8. Computational Modeling and Adsorption Energy Calculation

The interaction between soap molecules and the surface of NiO/Ni nanocomposites was investigated through first-principles calculations using the Forcite module. The receptor structure was carefully constructed and refined to accurately preserve the nanocomposites' geometry and dimensions [74]. Initially, NiO nanoparticles were modeled using ChemDraw software, with the surface oriented along the (-100) cleavage plane, and subsequently expanded into a 6×6×1 supercell. The Ni element was likewise modeled and positioned onto the NiO nanoparticle surface. Geometric optimization and electronic property calculations were carried out using Forcite, which maintains crystal symmetry during structural refinement [75]. The ligand structure, representing the soap molecule, was retrieved from the PubChem database (https://pubchem.ncbi.nlm.nih.gov/) and placed on the NC surface. The Monte Carlo Metropolis method was employed to calculate the adsorption energy [76]. The adsorption energy (E_{ad}), representing the strength of interaction between the nanocomposite and the soap molecule, was determined according to the following equation:

$$E_{ad} = E_{\mathrm{NiO/Ni}} - E_{\mathrm{NiO/Ni}-Soap} - E_{soap\ molecule} \qquad (3)$$

Where $E_{NiO\backslash Ni\text{-}Soap}$ is the total energy of the NiO/Ni nanocomposite with the adsorbed soap molecule, $E_{NiO\backslash Ni}$ is the energy of the isolated NiO/Ni nanocomposite, and E_{Soap} represents the energy of the isolated soap molecule in their respective ground states.

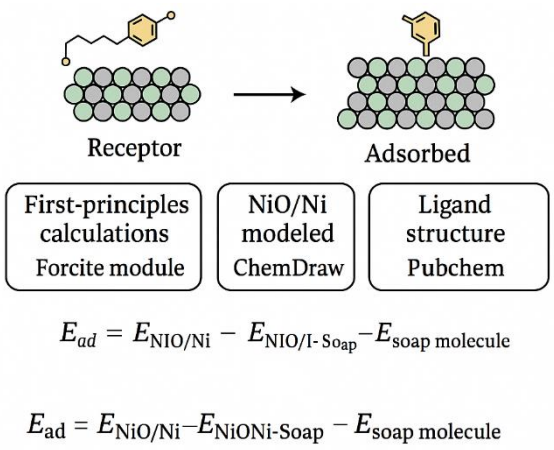

Figure IV. 11: Computational Description Adsorption Energy

3. Characterization of Synthesized Nanomaterials

3.1. Optical Properties and Bandgap Energy (UV-Vis, Tauc Plot)

UV-Visible spectroscopy was employed to elucidate the optical properties of NiO/Ni nanocomposites and NiO/Ni@PVA electrospun nanofibers, providing insight into the effects of nanostructuring and polymer integration on their electronic behavior. The absorption spectra revealed distinct peaks at 290 nm for the NiO/Ni powder and 284 nm for the NiO/Ni@PVA nanofiber (Figure IV.13(a)), corresponding to electronic transitions associated with the NiO and Ni phases. The slight redshift observed in the NiO/Ni@PVA nanofiber relative to the NiO/Ni powder suggests modifications in the electronic environment, likely due to variations in nanoparticle dispersion, surface interactions, or morphological changes induced by the electrospinning process. The incorporation of PVA appears to contribute to a minor bandgap reduction, potentially driven by enhanced interfacial bonding, an increase in defect density, or structural rearrangements, thereby influencing charge carrier dynamics and augmenting optical absorption within the nanofiber composite [77].

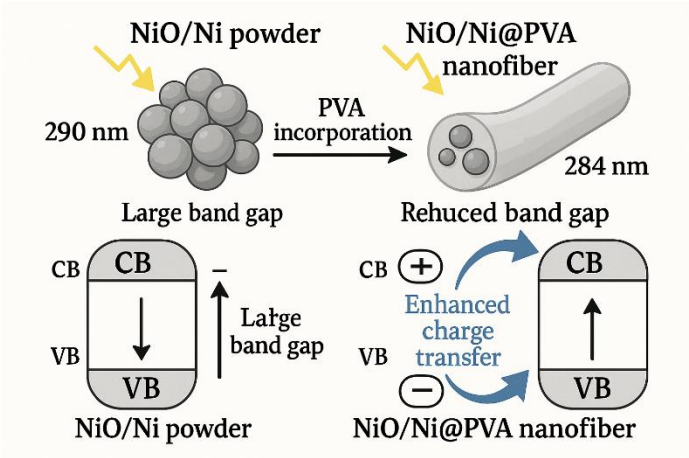

Figure IV. 12: Band Gap Modulation and Charge Transfer Enhancement in NiO/Ni@PVA Nanofibers

Additionally, analysis of the optical band gaps, determined from Tauc plots [67], further differentiates the two samples. The NiO/Ni powder exhibited a band gap energy of 3.83 eV, consistent with values reported in the literature [77], affirming its semiconducting nature (Figure IV.13(b)). Conversely, the NiO/Ni@PVA nanofiber demonstrated a slightly reduced band gap of 3.61 eV, which can be attributed to enhanced electron mobility, improved charge separation, and potential increases in crystallinity induced by the electrospinning process [67]. The observed band gap narrowing implies modifications to the material's density of electronic states, which could be advantageous for applications requiring enhanced electronic and photocatalytic performance.

Moreover, the changes in the optical behavior of the NiO/Ni@PVA nanofibers emphasize the role of polymer integration in tailoring the electronic structure of nanocomposites. The presence of PVA likely facilitates improved charge transfer processes and modifies defect states, contributing to enhanced functionalities in applications such as photocatalysis, sensing, and pollutant adsorption in biodiesel purification [78]. These findings highlight electrospinning as an effective strategy for engineering the optical and electronic properties of nanocomposites, positioning these materials as promising candidates for advanced technological applications.

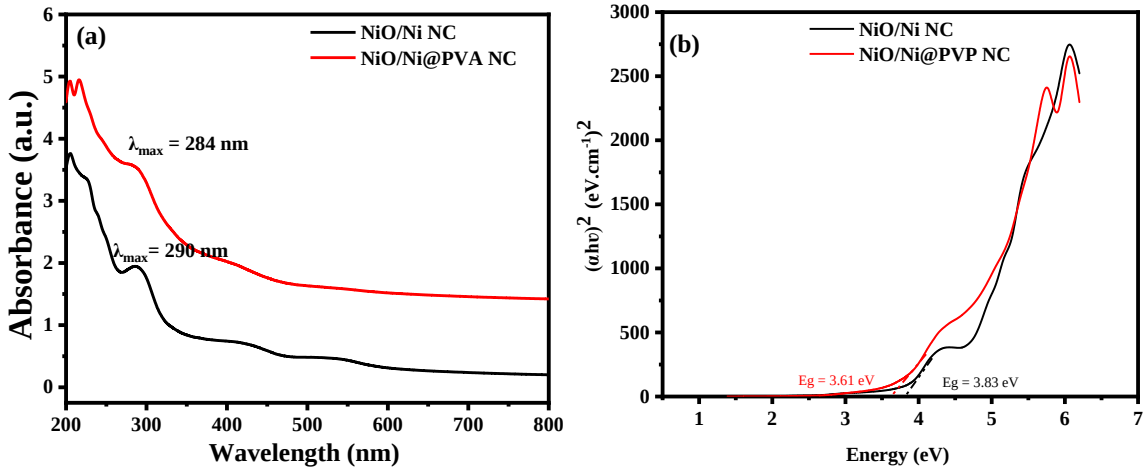

Figure IV. 13: (a) UV–Vis absorption spectra of NiO/Ni nanocomposites and NiO/Ni@PVA electrospun nanofibers. **(b)** Tauc plot analysis depicting the relationship between $(\alpha hv)^{1/2}$ and photon energy (hv) for both NiO/Ni nanocomposites and their PVA-integrated electrospun counterparts.

3.2. Functional Groups Identified by FTIR

Fourier-transform infrared (FTIR) spectroscopy was conducted to characterize the functional groups present on the surface of the NiO/Ni nanocomposite (Figure IV.15). The FTIR spectrum displays distinct absorption bands at approximately 3411 cm^{-1}, 2919 cm^{-1}, 1627 cm^{-1}, and 1105 cm^{-1}, corresponding to O–H stretching [79], C–H stretching [80], and C=O stretching vibrations [81], respectively. The broad absorption feature centered at 3411 cm^{-1} is indicative of hydroxyl groups [82], suggesting a hydrophilic surface nature. This pronounced hydrophilicity is attributed, in part, to the green synthesis approach employing *Pistacia lentiscus* leaf extract, wherein residual phytochemicals, such as polyphenolic compounds, introduce additional O–H and C=O functionalities onto the nanocomposite surface [83]. These bio-derived surface groups not only facilitate nanoparticle reduction and stabilization during synthesis but also enhance the interaction with soap molecules, thereby improving biodiesel purification performance.

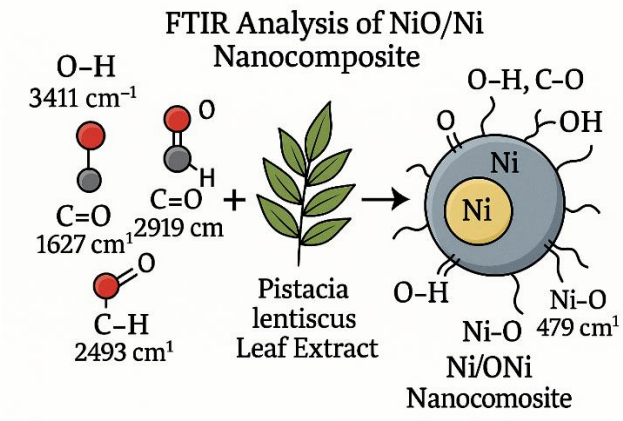

Figure IV. 14: Surface Functionalization of NiO/Ni Nanocomposites via Pistacia lentiscus Extract: FTIR Insights

Furthermore, the absorption band observed around 479 cm^{-1} is assigned to the Ni–O stretching vibrations, confirming the successful formation of the NiO/Ni nanocomposite structure [84]. The incorporation of bioactive compounds from the plant extract significantly modifies the surface chemistry, potentially enhancing the material's adsorption capabilities [85]. Identifying these functional groups is crucial for elucidating the adsorption mechanisms underlying the nanocomposite's activity and for understanding its role in improving biodiesel quality [86].

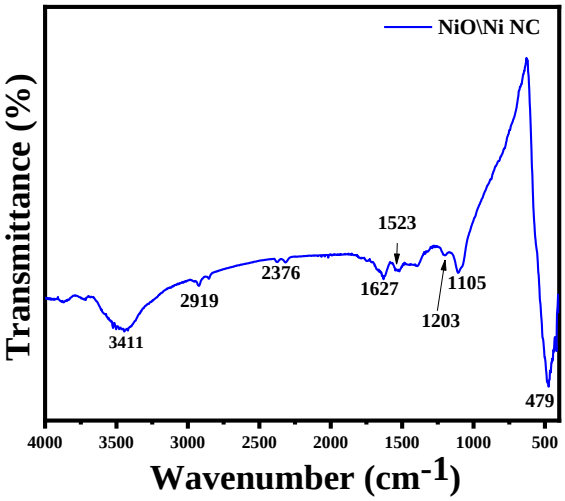

Figure IV. 15: Vibrational Spectral Analysis of NiO/Ni NC via FTIR

3.3. Crystalline Structure Analysis via XRD

X-ray diffraction (XRD) analysis was conducted to investigate the structural properties and crystallinity of both the NiO/Ni nanocomposite and the NiO/Ni@PVA electrospun nanofibers. For the NiO/Ni NC, distinct diffraction peaks were recorded at 2θ values of 37.33°, 43.38°, 63.38°, 75.60°, and 79.61°, corresponding to the (111), (200), (220), (311), and (222) planes of cubic NiO, in accordance with the standard reference code 01-073-1519 (Figure IV.17 (a)). These reflections confirm the formation of a well-crystallized cubic NiO phase. Moreover, the presence of metallic nickel (Ni) is verified by additional peaks at 44.60°, 51.98°, and 76.60°, corresponding to the (111), (200), and (220) planes of cubic Ni, referenced by code 01-070-0989. The sharpness and high intensity of these peaks indicate a high degree of crystallinity for both the NiO and Ni phases within the nanocomposite.

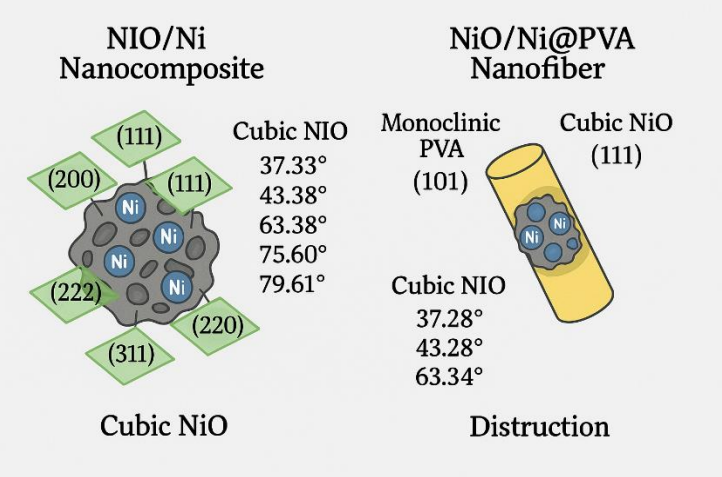

Figure IV. 16: Crystallinity and Phase Analysis of NiO/Ni-Based Materials via XRD

In the case of the NiO/Ni@PVA nanofibers, a pronounced diffraction peak at 2θ = 19.44° is observed, attributed to the (101) plane of the monoclinic structure of polyvinyl alcohol (PVA) [87], [88] (Figure IV.17 (b)). Compared to the NiO/Ni NC, the diffraction peaks corresponding to NiO and Ni exhibit reduced intensity in the nanofibers, likely due to the presence of the PVA matrix, which may cause a partial decrease in crystallinity or a dilution effect. This reduction in peak intensity also suggests a fine nanoscale dispersion of the NiO/Ni phases within the PVA fibers, which influences the crystallographic coherence. Nevertheless, the persistence of the characteristic NiO and Ni reflections indicates that the

crystalline nature of the nanocomposite is retained following its incorporation into the polymer matrix. These XRD findings affirm the successful integration of the NiO/Ni nanocomposite into the PVA nanofibers while highlighting the influence of the polymeric environment on the material's overall crystalline structure.

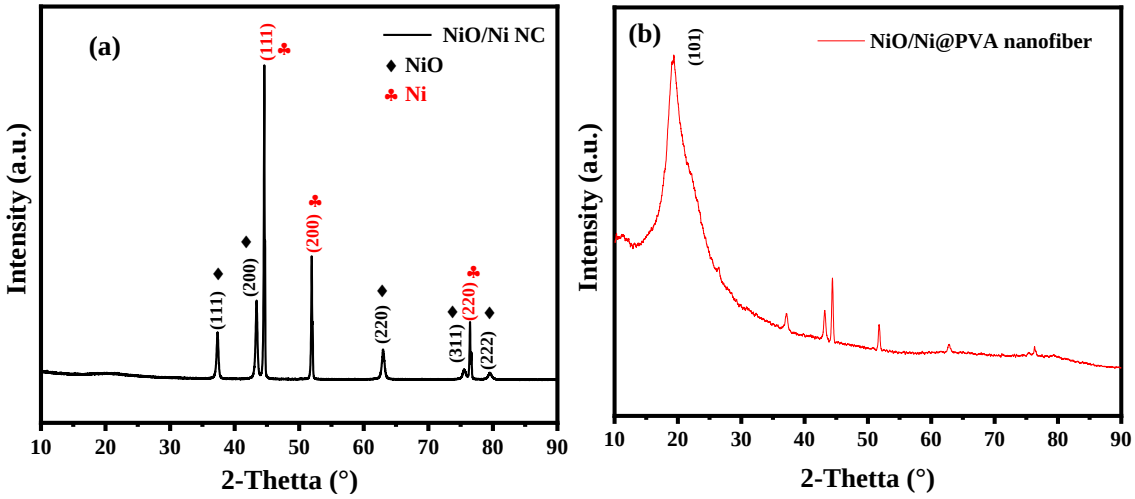

Figure IV. 17: Crystallographic Patterns of **(a)** NiO/Ni NC and **(b)** NiO/Ni@PVA Nanofiber

3.4. Morphological Features (SEM, EDX)

Scanning electron microscopy (SEM) was employed to examine the surface morphology of the NiO/Ni nanocomposite powder and the NiO/Ni@PVA electrospun nanofibers (Figure IV.19 (a,b)). The NiO/Ni NC powder exhibits a relatively homogeneous nanoscale morphology, characterized by slight agglomeration, a common feature of nanoparticles synthesized via green methods. The utilization of *Pistacia lentiscus* leaf extract in the green synthesis process introduces bioactive molecules that serve as stabilizing agents, facilitating controlled nucleation and growth of nanoparticles and effectively minimizing excessive aggregation [89]. This controlled synthesis route leads to the formation of smaller nanoparticles with enhanced specific surface area, attributes that are particularly advantageous for adsorption processes in biodiesel purification applications.

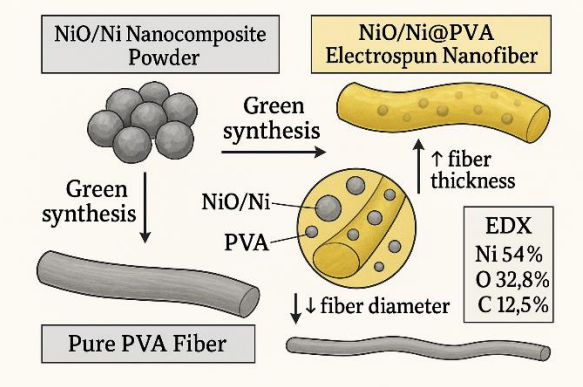

Figure IV. 18: Surface Morphology and EDX Characterization of NiO/Ni@PVA Nanofibers

In the case of the NiO/Ni@PVA electrospun nanofibers, a notable reduction in fiber diameter is observed, decreasing from approximately 280 nm in pure PVA fibers to around 250 nm upon nanocomposite incorporation. This reduction suggests strong interfacial interactions between the NiO/Ni NCs and the PVA matrix, likely driven by surface functional groups introduced during the green synthesis procedure. Furthermore, the structural integrity of the fibers is enhanced, as reflected by the increase in overall fiber thickness from 20 µm in pristine PVA fibers to 30 µm in the NiO/Ni@PVA nanofibers. The uniform dispersion of the NiO/Ni nanocomposite throughout the fiber matrix highlights the effectiveness of the electrospinning process in achieving stable and well-integrated nanostructures.

Energy-dispersive X-ray (EDX) analysis further supports these findings, revealing distinct peaks corresponding to Ni, O, and C elements, with atomic percentages of 54%, 32.8%, and 12.5%, respectively (Figure IV.19 (c)). The presence of these elements confirms the successful embedding of the NiO/Ni NCs within the polymeric network. The green synthesis approach significantly influences the final nanofiber morphology by improving nanoparticle dispersibility, minimizing fiber defects, and enhancing the homogeneity of the electrospun structures. These morphological improvements contribute to increased surface area, superior adsorption capacity, and enhanced mechanical stability, thus positioning NiO/Ni@PVA nanofibers as promising candidates for industrial-scale applications.

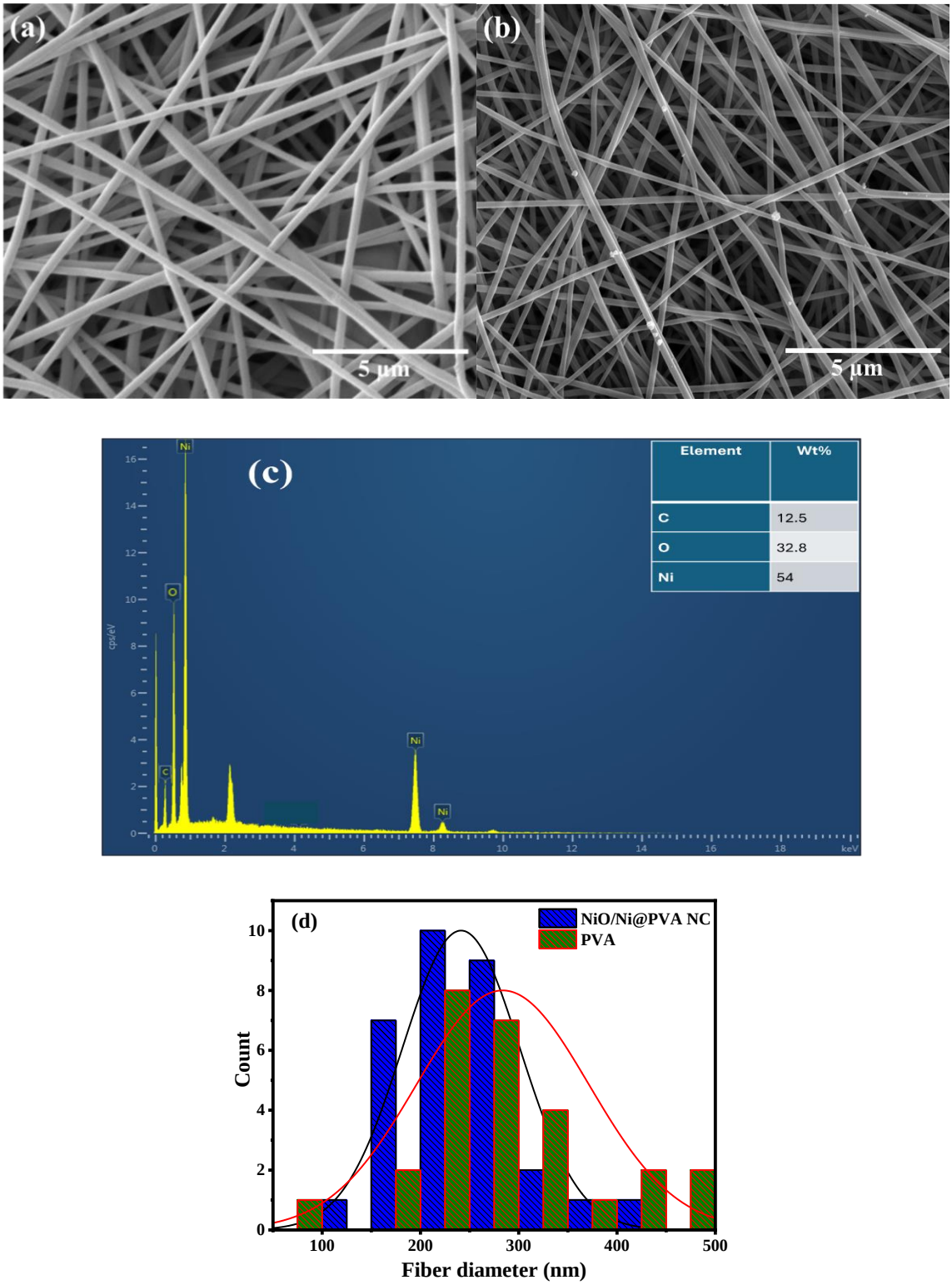

Figure IV. 19: SEM micrographs of **(a)** pristine PVA nanofibers and **(b)** NiO/Ni@PVA nanofibers; **(c)** EDX elemental analysis of NiO/Ni@PVA nanofibers; and **(d)** nanofiber diameter distribution

3.5. Surface Chemistry via XPS

X-ray Photoelectron Spectroscopy (XPS) was employed to investigate the elemental composition and chemical states of the NiO/Ni@PVA electrospun nanofibers. The high-resolution spectra of Ni 2p, O 1s, and C 1s provide critical insights into the surface chemistry of the material.

The Ni 2p spectrum (Figure IV.21 (a)) displays characteristic peaks at binding energies of approximately 855 eV (Ni $2p_{3/2}$) and 873 eV (Ni $2p_{1/2}$), along with prominent satellite peaks, which are indicative of Ni^{2+} oxidation states typical of NiO [90]. The presence of these satellite features, commonly associated with nickel oxides, confirms the formation of NiO and suggests the coexistence of multiple nickel valence states within the nanocomposite. Furthermore, the pronounced intensity and sharpness of these peaks highlight a substantial NiO presence on the surface of the electrospun nanofibers.

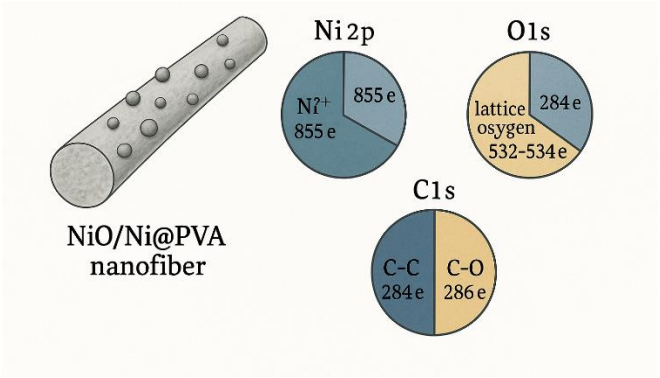

Figure IV. 20: Surface Chemical Composition and Elemental States of NiO/Ni@PVA Nanofibers Revealed by XPS Analysis

The O 1s spectrum (Figure IV.21 (b)) reveals peaks around 530 eV, 532 eV, and 534 eV, corresponding to oxygen atoms in distinct chemical environments [91]. The peak at approximately 530 eV is attributed to lattice oxygen within the NiO structure, while the peaks at higher binding energies are associated with hydroxyl groups or surface-adsorbed oxygen species, suggesting surface oxidation or interactions with atmospheric moisture.

The C 1s spectrum (Figure IV.21 (c)) exhibits binding energy peaks near 284 eV and 286 eV, assigned to C–C and C–O bonds, respectively [90]. These signals confirm the successful incorporation of the PVA matrix within the nanofiber structure, with the C–O

bonds particularly reflecting the presence of oxygenated carbon species derived from the PVA polymer backbone [92].

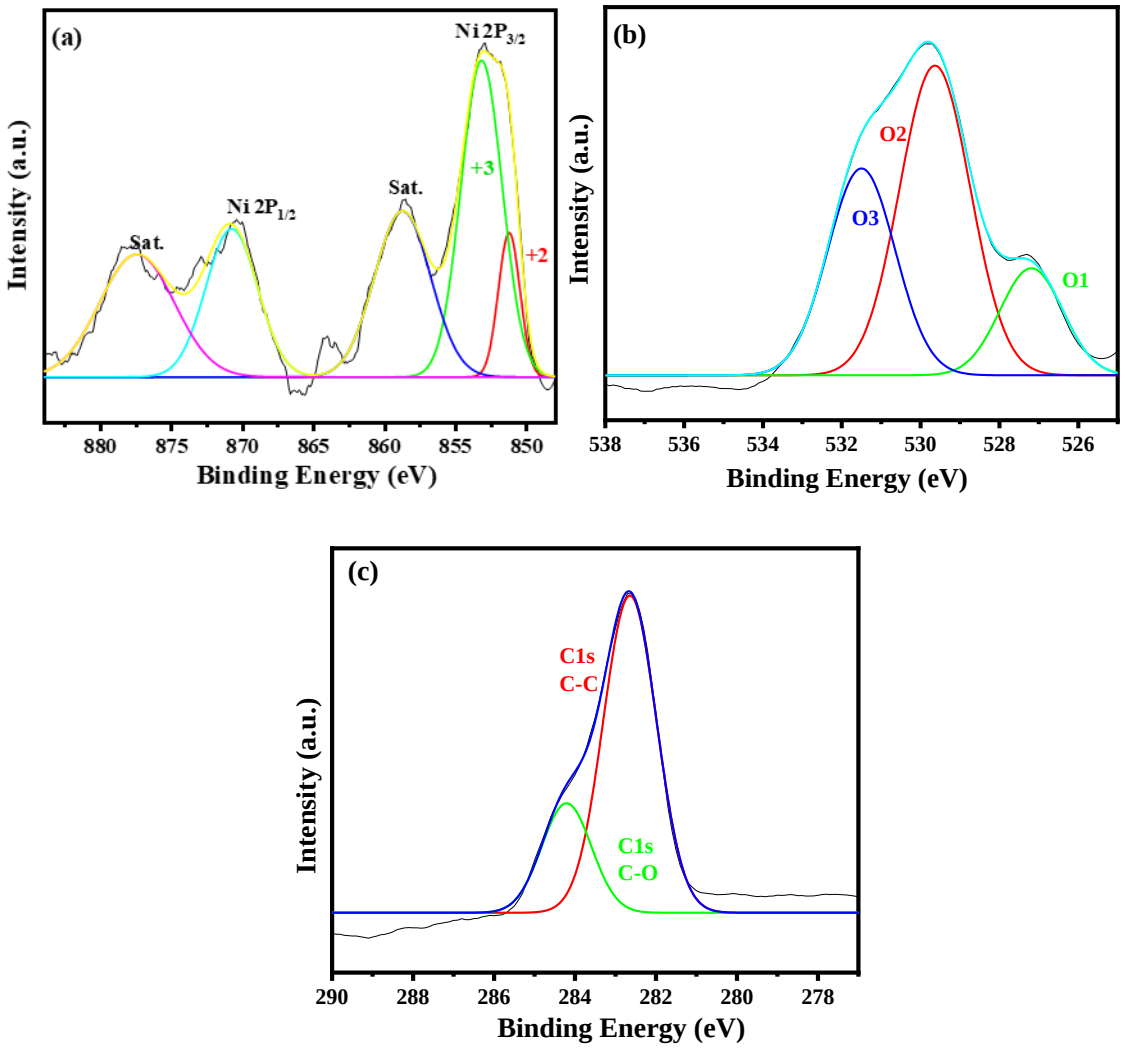

Figure IV. 21: High-Resolution XPS Analysis Showing **(a)** Ni 2p, **(b)** O 1s, and **(c)** C 1s Core-Level Spectra

3.6. Thermal Stability Evaluation (TGA)

Thermogravimetric analysis (TGA) was conducted to evaluate the thermal stability and decomposition behavior of the NiO/Ni nanocomposites and NiO/Ni@PVA electrospun nanofibers. The NiO/Ni NC exhibited minimal weight loss during heating, with a total reduction of only 1.64% up to 800 °C, indicating excellent thermal stability. This slight weight loss is primarily attributed to the removal of residual moisture and volatile organic compounds originating from the synthesis process.

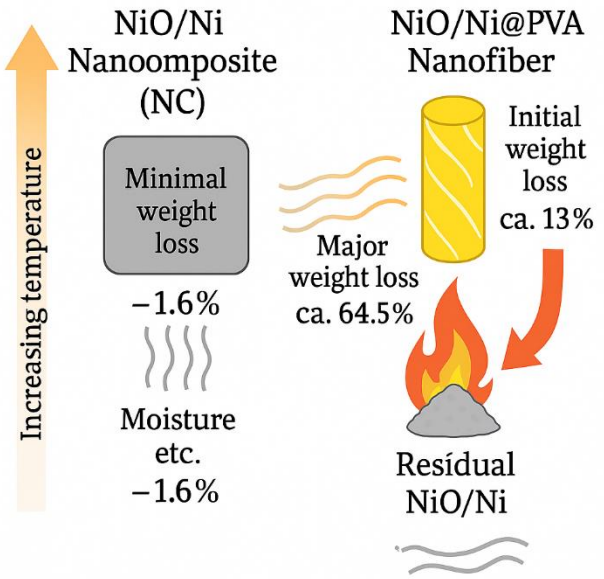

Figure IV. 22: Comparative Thermal Stability of NiO/Ni Nanocomposite and NiO/Ni@PVA Nanofiber Based on TGA Analysis

In contrast, the NiO/Ni@PVA nanofibers demonstrated a significantly greater mass loss, with approximately 64.5% reduction observed by 800 °C [93]. This substantial weight loss is primarily associated with the thermal decomposition of the PVA matrix, as organic polymers are prone to degradation at elevated temperatures. An initial weight loss of about 13% below 200 °C is attributed to the evaporation of physically adsorbed water and residual solvents. The major decomposition event, accounting for most of the weight loss, occurs between 200 °C and 600 °C and corresponds to the breakdown of the PVA polymer structure [94]. Beyond this temperature range, a stable residual mass of approximately 5.4% remains, attributable to the presence of thermally stable NiO/Ni nanoparticles.

Overall, these findings highlight the excellent thermal stability of the NiO/Ni phase within the electrospun nanofiber matrix and demonstrate that the observed mass losses are predominantly due to the degradation of the polymeric component (PVA) at high temperatures.

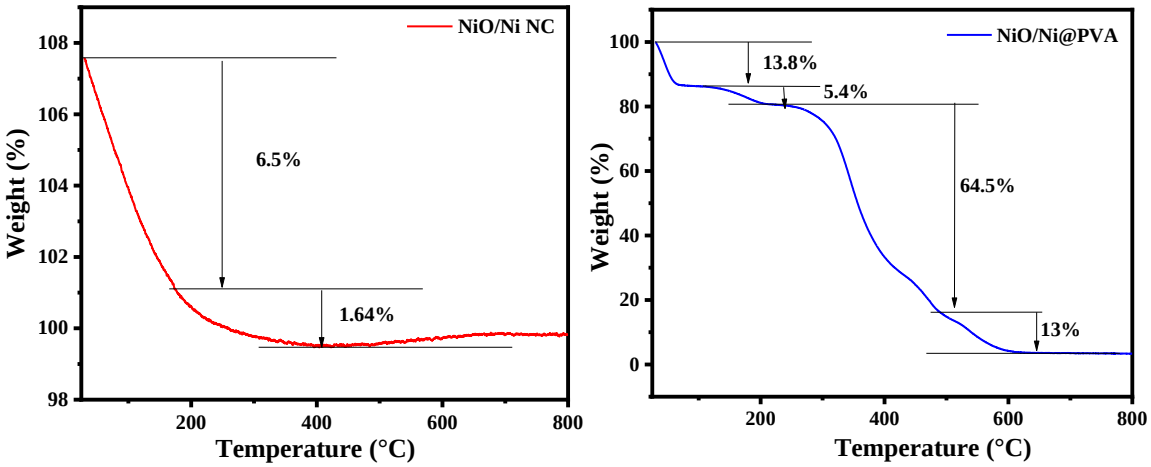

Figure IV. 23: Thermogravimetric and Differential Thermal Analysis (TGA/DTA) of (a) NiO/Ni Nanocomposite and (b) NiO/Ni@PVA Electrospun Nanofiber

4. Biodiesel Purification Efficiency

4.1. Biodiesel Production from Palm Oil

Biodiesel was synthesized from refined palm oil using potassium hydroxide (KOH) as a catalyst and methanol (CH_3OH) as the transesterification reagent, owing to their high efficacy in facilitating the conversion of triglycerides into fatty acid methyl esters (FAME) [72]. A molar ratio of 10:1 (oil to methanol) was employed to enhance the reaction rate and improve biodiesel yield. Although refined palm oil was used as the feedstock, the produced biodiesel exhibited a soap content of 4671 ppm, significantly exceeding the internationally accepted limit of 50 ppm. This elevated soap concentration highlights the necessity for an efficient purification step to ensure the biodiesel meets industrial quality standards.

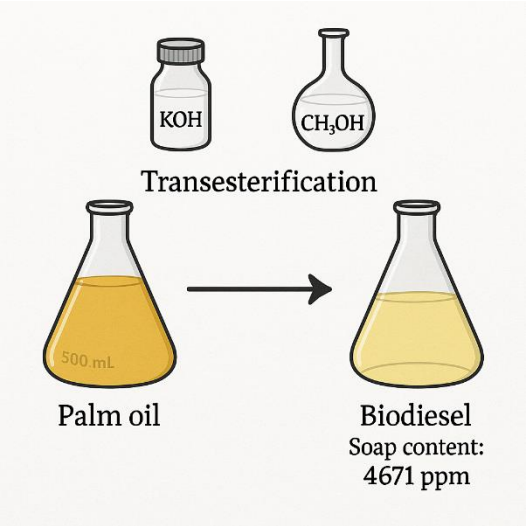

Figure IV. 24: Transesterification Process of Palm Oil into Biodiesel

4.2. Time-Dependent Soap Adsorption Kinetics

The influence of extraction time on the efficiency of soap removal from biodiesel was evaluated using both NiO/Ni nanocomposite powder and NiO/Ni@PVA electrospun nanofibers (Figure IV.26 (a)). The extraction time was systematically varied to determine its impact on adsorption performance. The findings reveal that extending the extraction duration enhances the soap removal efficiency up to an optimal point. Shorter contact times (e.g., 2 to 10 minutes) were found to be inadequate for achieving significant soap reduction, as limited interaction occurs between the soap molecules and the available active sites on the adsorbent surface. With increased extraction time, more soap molecules are adsorbed due to prolonged exposure to active sites, leading to a progressive decrease in soap content [95].

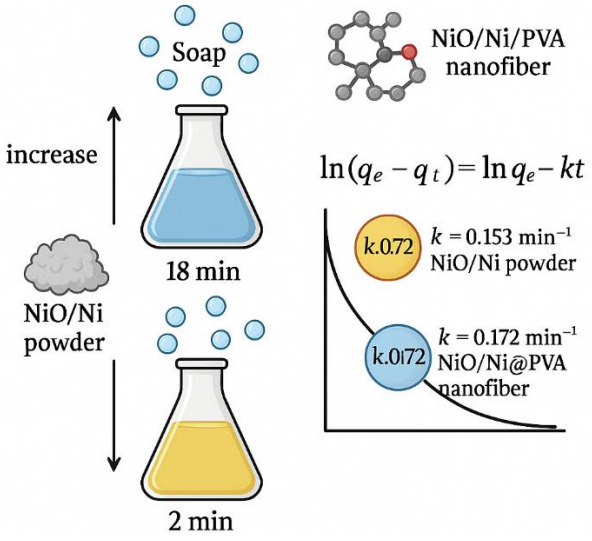

Figure IV. 25: Time-Dependent Adsorption Efficiency of NiO/Ni and NiO/Ni@PVA for Biodiesel Purification

Equilibrium was attained at approximately 18 minutes, beyond which further increases in extraction time did not result in notable improvements in removal efficiency. This plateau indicates the saturation of the adsorption sites and is in line with classical adsorption theory, wherein the initial rate of adsorption is rapid due to the abundance of available binding sites, followed by a gradual decline as these sites become increasingly occupied. Notably, the NiO/Ni@PVA nanofibers outperformed the NiO/Ni powder due to their higher specific surface area and greater density of accessible functional groups, facilitating faster and more efficient adsorption.

Therefore, an optimal extraction time of 18 minutes is recommended for maximizing soap removal while maintaining energy efficiency and process feasibility in industrial biodiesel purification. Prolonging the extraction period beyond this threshold offers negligible benefits and may lead to unnecessary resource consumption.

To further understand the adsorption kinetics, a pseudo-first-order kinetic model was applied (Eq. 4) to describe the time-dependent behavior of soap removal [96]. The calculated rate constants (k) were 0.153 min^{-1} for the NiO/Ni powder and 0.172 min^{-1} for the NiO/Ni@PVA nanofibers (Figure IV.26 (b)), suggesting that although the powder demonstrated a slightly faster kinetic rate, the nanofibers exhibited a higher overall adsorption capacity. This kinetic analysis provides a quantitative understanding of the

enhanced performance of the nanofibers, confirming their suitability for efficient removal of organic contaminants such as soap from biodiesel [97].

$$\ln(q_e - q_t) = \ln(q_e) - k\,t \qquad (4)$$

Where:

- q_e is the equilibrium adsorption capacity (mmol/g),
- q_t is the adsorption capacity at time t,
- k is the pseudo-first-order rate constant (min^{-1}),
- t is the contact time (min).

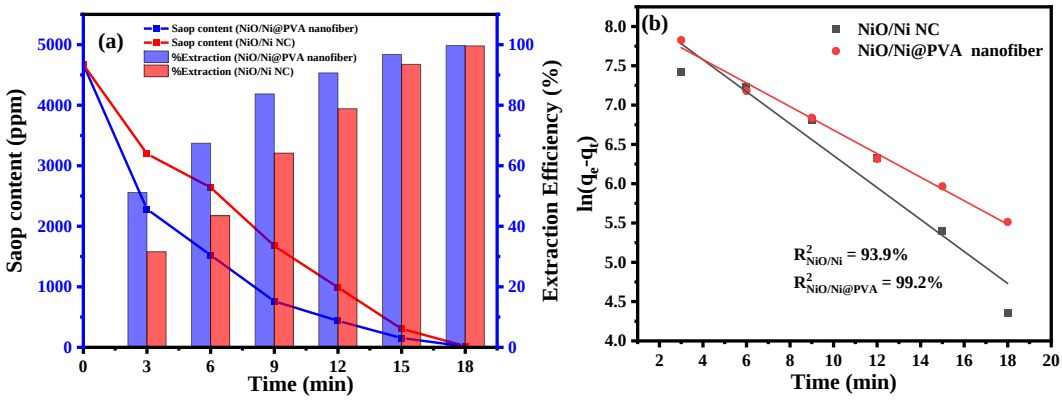

Figure IV. 26: (a) Soap Removal Efficiency and **(b)** Pseudo-First-Order Kinetic Plot [$\ln(C_0/C_t)$] for NiO/Ni Nanocomposite and NiO/Ni@PVA Nanofiber as a Function of Extraction Time

4.3. Dosage Optimization and Adsorbent Comparison

The impact of catalyst dosage on the soap removal efficiency from biodiesel was investigated using NiO/Ni nanocomposites and NiO/Ni@PVA electrospun nanofibers through a solid–liquid extraction method (Figure IV.28). Catalyst quantities ranging from 0.01 to 0.03 g were dispersed in 10 mL of biodiesel and homogenized at 150 rpm for 18 minutes. The results demonstrate that increasing the catalyst dosage significantly enhances soap removal, confirming the effectiveness of the adsorption process. Notably, the NiO/Ni@PVA nanofibers exhibited superior performance, reducing the soap content from

an initial 4671 ppm to 13.5 ppm, whereas the NiO/Ni NC powder achieved a reduction to 19.5 ppm under the same conditions.

The enhanced efficiency of the NiO/Ni@PVA nanofibers can be attributed to several factors. The nanofibers possess a higher surface area, enabling greater adsorption capacity, while the hydroxyl (-OH) functional groups present in the PVA matrix facilitate hydrogen bonding with soap molecules, thereby strengthening molecular interactions. Additionally, the PVA component prevents nanoparticle agglomeration, ensuring improved dispersion and better accessibility of active sites, which collectively contribute to the superior adsorption efficiency [98].

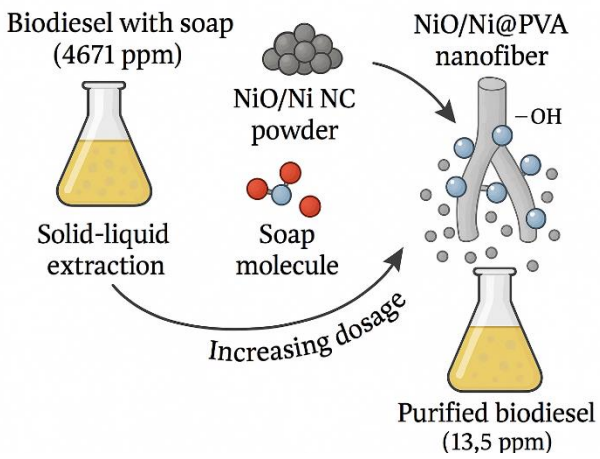

Figure IV. 27: Dosage-Dependent Soap Removal from Biodiesel Using NiO/Ni and NiO/Ni@PVA Adsorbents

The NiO/Ni NC powder, characterized by its smaller particle size, also promotes good dispersion in biodiesel, enhancing contact with soap molecules. Furthermore, the presence of surface oxygen-containing functional groups enhances electrostatic interactions with soap molecules, supporting the adsorption mechanism [99], as detailed in Table 1. The powder form offers operational flexibility by allowing easier adjustment of catalyst dosage and extraction time to optimize purification outcomes.

Despite the favorable properties of the NC powder, the electrospun nanofibers demonstrated a more effective soap removal performance overall. An optimal catalyst dosage of 0.03 g successfully reduced soap concentrations to below the ASTM D6751

standard threshold, thereby improving biodiesel quality while minimizing catalyst consumption. These findings underscore the potential of NiO/Ni@PVA nanofibers as an efficient and sustainable approach for large-scale biodiesel purification applications.

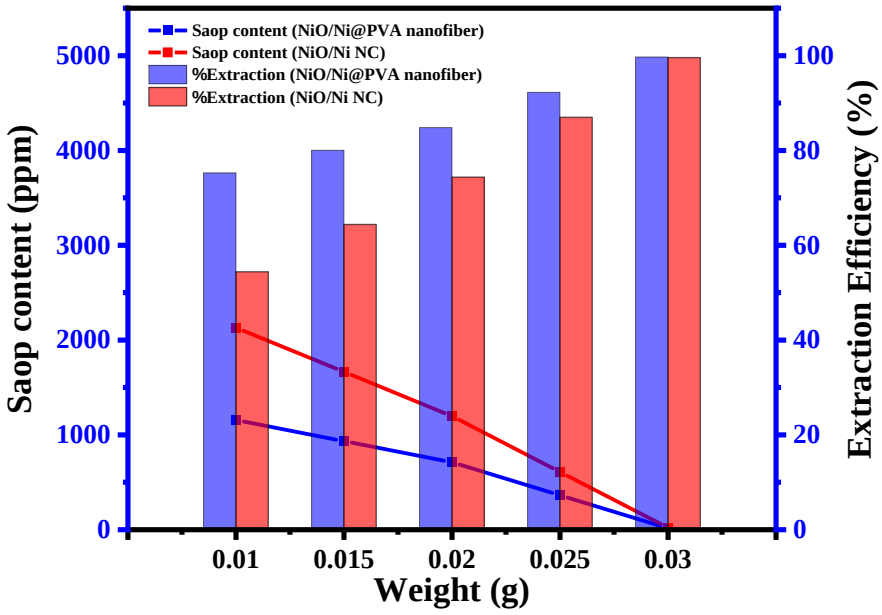

Figure IV. 28: Soap Removal Performance of NiO/Ni-Based Adsorbents as a Function of Catalyst Loading

4.4. Influence of Stirring Speed on Purification Efficiency

The stirring speed during the extraction process plays a crucial role in determining the efficiency of soap removal from biodiesel when using NiO/Ni nanocomposite powders and NiO/Ni@PVA nanofibers (Figure IV.30). In this study, various stirring speeds (30, 60, 90, 120, and 150 rpm) were systematically evaluated while maintaining all other parameters constant. The results demonstrate a clear positive correlation between stirring speed and soap removal efficiency.

At lower stirring speeds (30–60 rpm), soap removal efficiency was relatively poor due to inadequate mixing and limited dispersion of the NC within the biodiesel medium. Insufficient agitation restricted the interaction between the active adsorption sites on the NC and the soap molecules, leading to a reduced collision frequency and lower adsorption rates, thus resulting in higher residual soap concentrations.

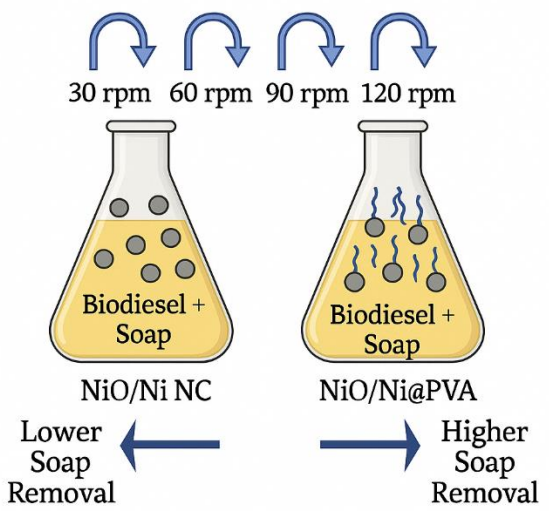

Figure IV. 29: Influence of Stirring Speed on Soap Removal Efficiency Using NiO/Ni-Based Adsorbents

As the stirring speed increased, particularly beyond 90 rpm, a significant enhancement in soap removal efficiency was observed. Higher agitation facilitated better dispersion of the NC throughout the biodiesel, promoting more frequent collisions between soap molecules and the available active sites on the adsorbents. This increased contact led to a greater adsorption rate and improved soap removal performance.

The optimal stirring speed was determined to be 150 rpm, where efficient mixing was achieved without inducing excessive shear forces that could compromise the structural integrity of the NC or trigger undesired secondary reactions [72]. This optimized speed ensures maximum soap adsorption while maintaining the stability of the adsorbent materials, making it a critical operational parameter for effective biodiesel purification.

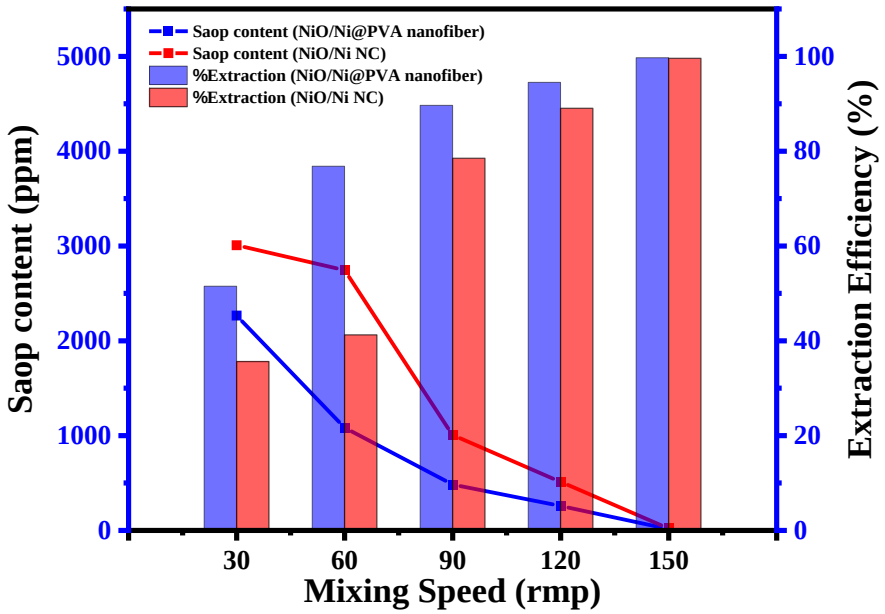

Figure IV. 30: Soap Removal Efficiency of NiO/Ni Nanocomposite and NiO/Ni@PVA Nanofiber as a Function of Stirring Speed

4.5. Reusability and Cyclic Stability of NiO/Ni vs NiO/Ni@PVA

Following the optimization of operational conditions 18 minutes of contact time, 0.03 g catalyst dosage, and a stirring speed of 150 rpm, the reusability and stability of the NiO/Ni NC powder and NiO/Ni@PVA electrospun nanofibers were systematically assessed through multiple recycling cycles (Figure IV.32). In each cycle, 10 mL of biodiesel, initially containing 4671 ppm of soap, was treated under the optimized conditions. The residual soap concentration after each treatment was measured using the AOCS titration method [16]. After each cycle, the catalysts were recovered, thoroughly washed, and dried at 100 °C before reuse in a fresh biodiesel sample.

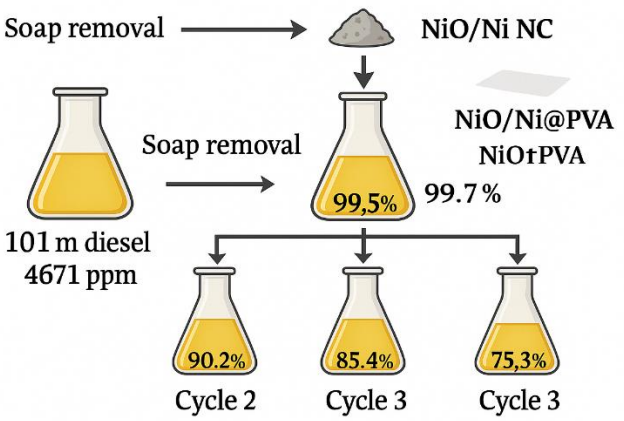

Figure IV. 31: Cycle-Based Performance of NiO/Ni NC and NiO/Ni@PVA Nanofibers in Biodiesel Purification

The results reveal a progressive decline in soap removal efficiency over consecutive cycles for both materials. Initially, the NiO/Ni NC exhibited a soap removal efficiency of 99.5%, while the NiO/Ni@PVA nanofibers achieved a slightly higher efficiency of 99.7%. However, by the fifth cycle, the efficiencies had decreased to 75.3% for the NiO/Ni NC powder and 83.3% for the electrospun nanofibers. This reduction in performance is attributed to the gradual saturation of active adsorption sites and possible structural alterations or degradation of the nanocomposites during repeated use.

These findings highlight the importance of evaluating catalyst durability for practical applications, as long-term stability and reusability are critical parameters for sustainable biodiesel purification.

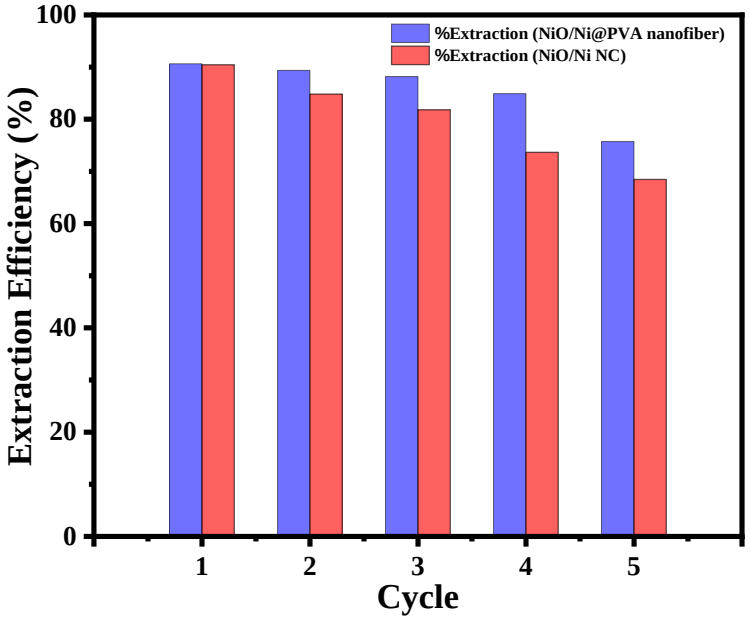

Figure IV. 32: Performance of NiO/Ni-Based Catalysts in Repeated Cycles for Soap Extraction from Biodiesel

5. Molecular docking

5.1. Mechanism of Soap Molecule Adsorption

The adsorption mechanism of soap molecules onto NiO/Ni nanocomposites and NiO/Ni@PVA electrospun nanofibers is governed by multiple interactions, primarily involving electrostatic forces, van der Waals interactions, and hydrogen bonding (Figure IV.33) [74]. Negatively charged soap molecules are attracted to positively charged or neutral active sites on the nanocomposite surfaces, with electrostatic interactions playing a dominant role in facilitating this process [74]. Furthermore, the high surface area and porous structure of the nanocomposites significantly enhance van der Waals forces, providing an abundance of accessible adsorption sites [100].

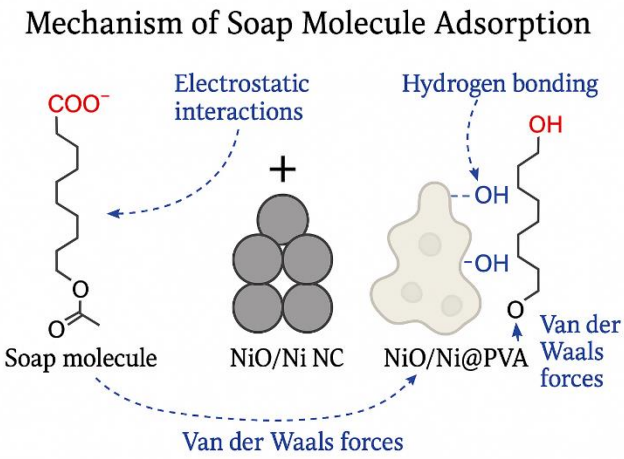

Figure IV. 33: Mechanism of Soap Molecule Adsorption

In addition, functional groups such as hydroxyl and carboxyl groups present on the nanocomposite surfaces enable the formation of hydrogen bonds with soap molecules, further reinforcing the adsorption interactions (Figure IV.34) [101]. The efficiency of these adsorption mechanisms is influenced by operational parameters including contact time, catalyst dosage, and stirring speed, emphasizing the necessity of optimizing these factors during the extraction process to achieve maximum soap removal efficiency.

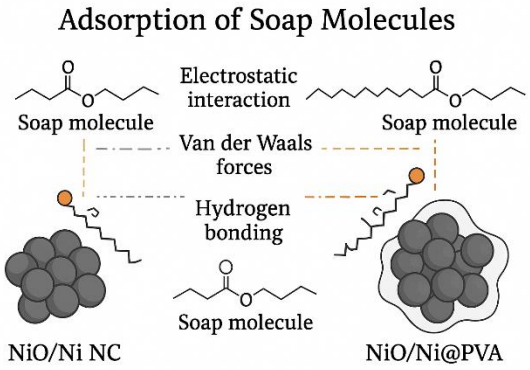

Figure IV. 34: Adsorption of Soap Molecules

Understanding the interplay of these adsorption mechanisms is critical for the effective utilization of NiO/Ni-based nanostructures in biodiesel purification, highlighting their potential for improving biodiesel quality through enhanced contaminant removal.

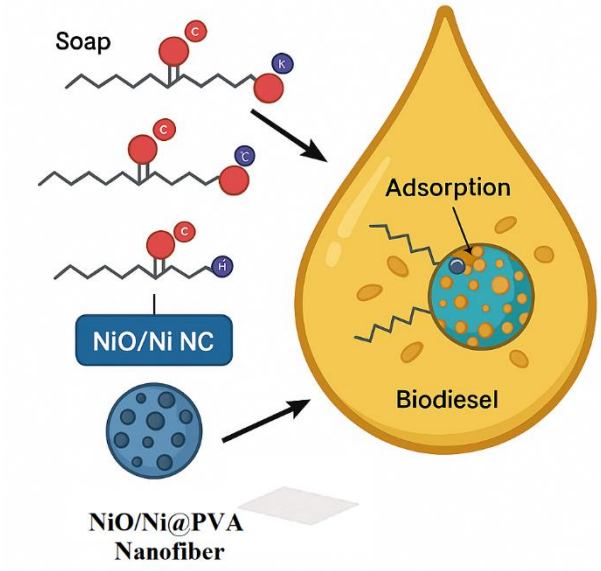

Figure IV. 35: Presentation of Adsorption Phenomena

5.2. Analysis of Adsorption Configuration

Figure IV.36 presents a detailed examination of the adsorption behavior of various dyes onto the optimized NiO/Ni nanocomposite monolayers, emphasizing the underlying intermolecular interactions. In this context, adsorption refers to the accumulation of solute molecules (adsorbates) onto the surface of a solid-phase material (adsorbent), primarily driven by physicochemical interactions between the solute and the porous surface of the solid matrix [74]. While atoms within bulk materials typically achieve stable bonding through covalent, metallic, or electrostatic interactions with neighboring atoms [102], surface atoms possess unsatisfied bonding requirements due to fewer neighboring atoms, thereby enhancing their propensity for adsorption processes [76]. The adsorption mechanism may vary in nature, broadly classified into chemisorption involving stronger electrostatic and covalent interactions and physisorption, which is governed by weaker van der Waals forces [103].

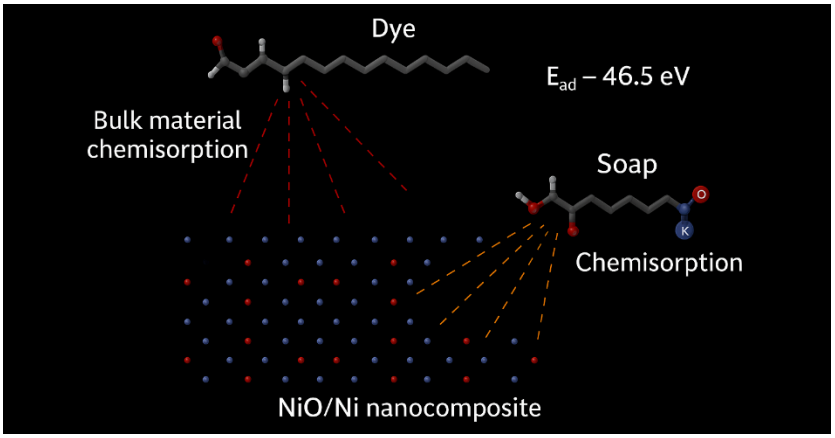

Figure IV. 36: Adsorption Behavior of Dye and Soap on NiO/Ni NC

As illustrated in Figure 13.b, the adsorption configuration between the nanocomposite and soap molecules is characterized by the adsorption energy, a metric indicative of the interaction strength between the ligand (soap) and the adsorbent (NiO/Ni NC). A more negative value of adsorption energy denotes a stronger interaction. In this study, the calculated adsorption energy (E_{ad}) for the soap molecule on NiO/Ni NC was found to be −37.19 eV, suggesting superior adsorption capability exceeding the strength of typical electrostatic interactions and indicating the material's strong affinity for the soap compound. These computational findings align with the experimental data, reinforcing the efficacy of NiO/Ni NC as an effective adsorbent. Furthermore, the results suggest that adsorption behavior can potentially be optimized by adjusting the composition of the metallic components in the nanocomposite.

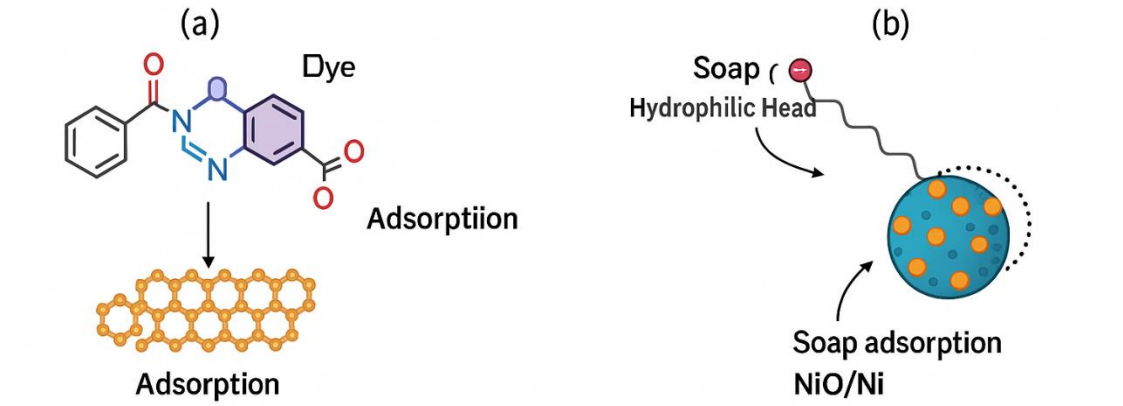

Figure IV. 37: Mechanistic Representation of Dye and Soap Adsorption onto NiO/Ni Nanocomposites

Figure IV.37 outlines the general adsorption mechanism of soap molecules from biodiesel (BD) onto the surface of NiO/Ni nanocomposites. Semiconductor-based nanomaterials, particularly those with engineered heterojunctions, serve as effective adsorbents by providing enhanced active surface areas for pollutant capture. The adsorption efficiency of NiO/Ni NC is further improved through surface modification with compatible materials.

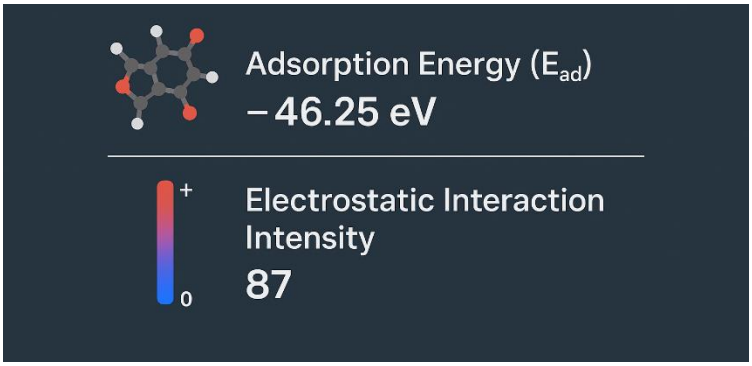

Figure IV. 38: Molecular Interaction Parameters of NiO/Ni Nanocomposites in Soap Adsorption

Simulation results generated using the Material Studio software, along with corresponding adsorption energy values, are summarized in Figure IV.38. The calculated binding energy (E_{ad}) for the NiO/Ni NC was −46.25 eV, reflecting strong electrostatic interaction and significant binding affinity (interaction value: 87). These results indicate that soap molecules exhibit high selectivity and strong affinity for the active sites of the NiO/Ni

surface. Moreover, the reduced free binding energy contributes to the overall structural stability of the nanocomposite during repeated adsorption cycles.

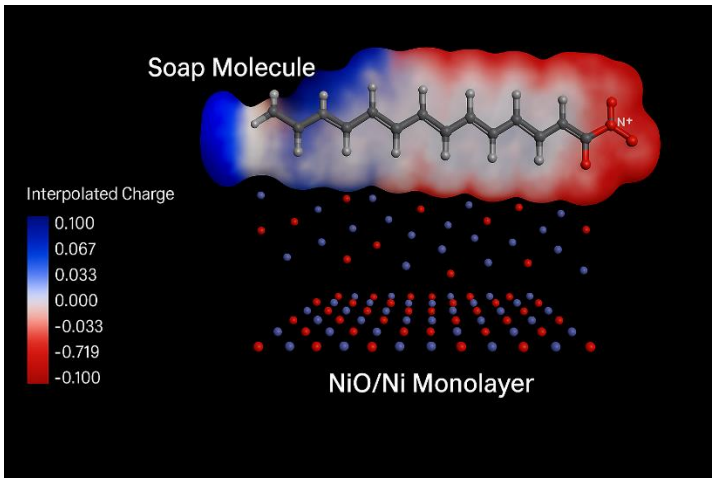

Figure IV. 39: Charge Distribution and Binding Mechanism of Soap Molecule on NiO/Ni Nanostructure

6. Environmental and Practical Implications

6.1. Sustainability of Green Electrospinning Synthesis

The green electrospinning synthesis of NiO/Ni@PVA nanofibers exemplifies a sustainable approach in advanced material fabrication, aligning with the principles of green chemistry. The use of *Pistacia lentiscus* leaf extract as a biogenic reducing agent circumvents the need for hazardous chemicals, offering a safe and eco-friendly synthesis route [104]. This process minimizes environmental risks by avoiding toxic solvents and utilizing aqueous-based media under ambient conditions [105]. Furthermore, the electrospinning technique employed in this study allows for precise control over nanostructure formation with minimal material waste [106]. The resulting nanofibers exhibit high surface area, stability, and enhanced functional group availability, making them suitable for environmentally benign applications such as biodiesel purification. Importantly, this synthesis pathway supports circular material design, using biodegradable polymers like PVA and promoting low-energy processing, thus contributing to cleaner production and reducing the environmental footprint of nanomaterial synthesis.

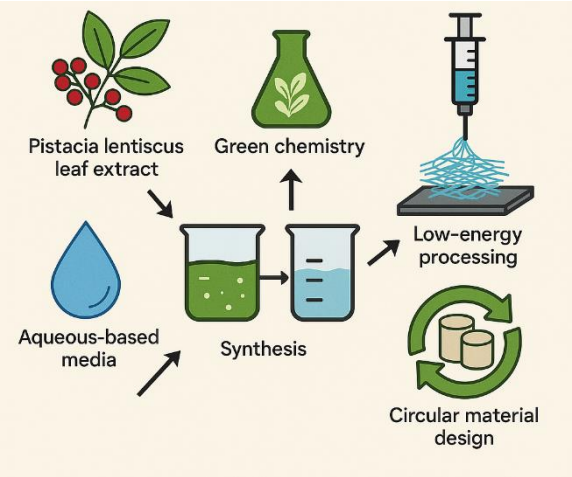

Figure IV. 40: Schematic Representation of the Sustainable Green Electrospinning Synthesis Process for NiO/Ni@PVA Nanofibers

6.2. Reduction in Wastewater Compared to Water Washing

One of the notable environmental advantages of employing NiO/Ni@PVA nanofibers for soap removal from biodiesel lies in the significant reduction of wastewater generation compared to conventional water washing methods. Traditional purification techniques often rely on repeated water wash cycles, leading to the production of large volumes of contaminated effluent that require further treatment and disposal [107]. In contrast, the solid-liquid extraction method utilized in this study eliminates the need for water-intensive processing. By using reusable nanocomposites and nanofibers as adsorbents [108][109], soap removal is achieved efficiently in a closed-loop system [110], dramatically lowering the water demand and associated treatment burdens. This approach not only conserves freshwater resources but also mitigates secondary pollution, enhancing the overall sustainability of biodiesel production.

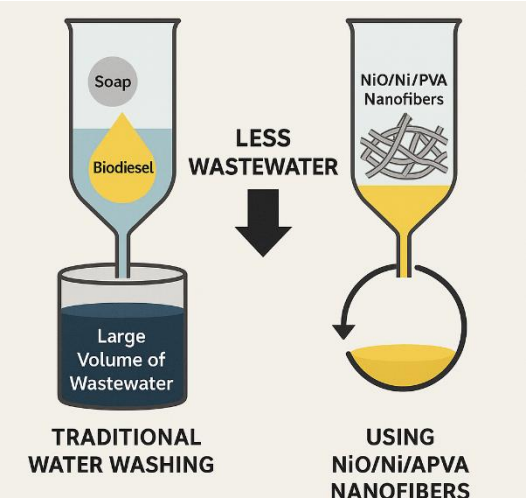

Figure IV. 41: Comparative Illustration of Wastewater Reduction Using NiO/Ni@PVA Nanofibers vs. Traditional Water Washing in Biodiesel Purification

6.3. Potential for Scale-Up and Industrial Application

The scalable potential of the developed NiO/Ni@PVA nanofibers positions them as viable candidates for industrial biodiesel purification processes. The electrospinning setup, especially using systems like the Nanospider Lab 200 [106], supports membrane fabrication at a semi-continuous scale, which can be readily expanded with minimal modifications. Moreover, the mild synthesis conditions, absence of toxic reagents, and relatively low thermal and energy input requirements make the process economically feasible for large-scale deployment [111]. The structural integrity, mechanical stability, and reusability of the nanofibers across multiple purification cycles further reduce operational costs and environmental liabilities [112]. Given their superior performance in removing soap contaminants below regulatory thresholds, these nanofibers have strong commercial potential in biofuel refineries and decentralized purification units.

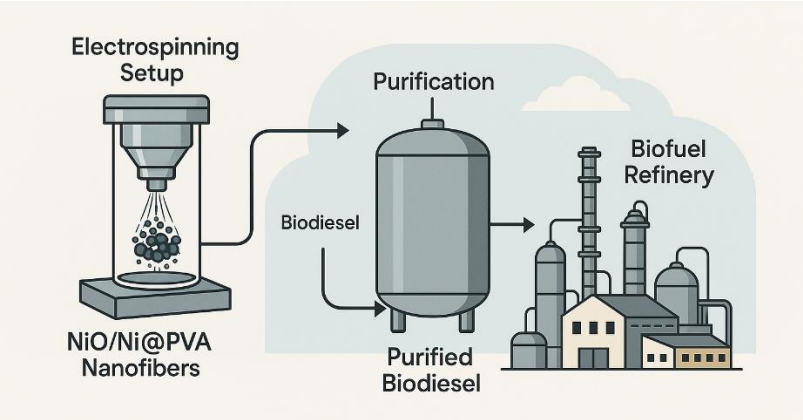

Figure IV. 42: Scalable Integration of NiO/Ni@PVA Nanofibers into Industrial Biodiesel Purification and Refining Systems

7. Conclusion and Future Work

This chapter has presented a comprehensive investigation into the green synthesis and electrospinning fabrication of NiO/Ni@PVA nanofibers for the efficient extraction of soap residues from biodiesel. Through a multidisciplinary approach combining green chemistry, material engineering, and computational modeling, the study provided significant scientific and practical contributions. The integration of Pistacia lentiscus leaf extract in the synthesis process not only eliminated the need for hazardous chemicals but also imparted functional surface groups to the nanocomposites, enhancing their adsorption capacity. The electrospun nanofibers exhibited superior performance in soap removal, achieving concentrations below ASTM standards, and demonstrated excellent reusability over multiple cycles, highlighting their potential for sustainable biodiesel purification.

One of the key strengths of the NiO/Ni@PVA nanofiber system lies in its multifunctional design. The incorporation of NiO/Ni nanocomposites into a PVA matrix resulted in structurally robust, highly porous, and surface-active fibers. These features facilitated enhanced interactions with soap molecules via electrostatic attraction, hydrogen bonding, and van der Waals forces. Compared to the NiO/Ni powder form, the nanofibers exhibited higher adsorption capacity, faster kinetics, improved thermal stability, and greater mechanical integrity. Additionally, the magnetic properties of Ni-based components enabled easy recovery and reuse, thereby reducing material losses and supporting circular economy practices.

Despite these advantages, several limitations must be acknowledged before transitioning to industrial-scale applications. The synthesis process, while green and reproducible at the laboratory scale, requires optimization for large-scale electrospinning systems to ensure consistent nanofiber morphology and quality. Furthermore, the mechanical durability and long-term stability of the nanofibers under continuous flow conditions remain to be fully validated. The adsorption performance may also be influenced by the complexity of real biodiesel matrices containing multiple impurities beyond soap, necessitating further investigation.

Future research should focus on enhancing the surface functionality of the nanofibers through chemical modification or hybridization with other nanomaterials to target a broader range of contaminants. Multi-pollutant removal systems that simultaneously address soap, glycerol, methanol, and trace metals in biodiesel should be developed. Additionally, real-time pilot studies are essential to evaluate performance under industrial conditions, assess regeneration efficiency over extended cycles, and conduct techno-economic and life-cycle assessments. These advancements will pave the way for the large-scale adoption of NiO/Ni@PVA nanofibers in biodiesel refineries and contribute to the broader goals of clean energy and environmental sustainability.

References

[1] R. El-Araby, "Biofuel production: exploring renewable energy solutions for a greener future," *Biotechnol. Biofuels Bioprod.*, vol. 17, no. 1, p. 129, 2024.

[2] R. Estevez *et al.*, "Biodiesel is dead: Long life to advanced biofuels—A comprehensive critical review," *Energies*, vol. 15, no. 9, p. 3173, 2022.

[3] S. M. Farouk, A. M. Tayeb, S. M. S. Abdel-Hamid, and R. M. Osman, "Recent advances in transesterification for sustainable biodiesel production, challenges, and prospects: a comprehensive review," *Environ. Sci. Pollut. Res.*, vol. 31, no. 9, pp. 12722–12747, 2024.

[4] M. A. I. Malik *et al.*, "A review of major trends, opportunities, and technical challenges in biodiesel production from waste sources," *Energy Convers. Manag. X*, p. 100675, 2024.

[5] M. Pydimalla, S. Husaini, A. Kadire, and R. K. Verma, "Sustainable biodiesel: A comprehensive review on feedstock, production methods, applications, challenges and opportunities," *Mater. Today Proc.*, vol. 92, pp. 458–464, 2023.

[6] K. Lovato, P. S. Fier, and K. M. Maloney, "The application of modern reactions in large-scale synthesis," *Nat. Rev. Chem.*, vol. 5, no. 8, pp. 546–563, 2021.

[7] C.-H. Chang, B. K. Paul, V. T. Remcho, S. Atre, and J. E. Hutchison, "Synthesis and post-processing of nanomaterials using microreaction technology," *J. Nanoparticle Res.*, vol. 10, pp. 965–980, 2008.

[8] M. Peters, B. Köhler, W. Kuckshinrichs, W. Leitner, P. Markewitz, and T. E. Müller, "Chemical technologies for exploiting and recycling carbon dioxide into the value chain," *ChemSusChem*, vol. 4, no. 9, pp. 1216–1240, 2011.

[9] R. Govindaraju, S.-S. Chen, L.-P. Wang, H.-M. Chang, and M. Pasawan, "Significance of membrane applications for high-quality biodiesel and byproduct (glycerol) in biofuel industries," *Curr. Pollut. Reports*, vol. 7, pp. 128–145, 2021.

[10] A. Saeed, G. Shabir, and A. Khurshid, "Biofuel Molecules," in *Recent Advances in Industrial Biochemistry*, Springer, 2024, pp. 147–224.

[11] D. Rutz and R. Janssen, "Biofuel technology handbook," *WIP Renew. energies*, vol. 95, 2007.

[12] B. Karmakar and G. Halder, "Green Technologies in Valorization of Waste Cooking Oil to Biodiesel," *Biodiesel Prod. Feed. Catal. Technol.*, pp. 33–48, 2022.

[13] K. M. Abed *et al.*, "Emulsion Liquid Membrane Pertraction of Soap from Crude Biodiesel Using Activated Carbon and Glycol Based Deep Eutectic Solvents," *J. Clean. Prod.*, p. 143404, 2024.

[14] K. M. Abed, A. Hayyan, H. F. Hizaddin, M. A. Hashim, Y.-S. Ng, and W. J. Basirun,

"Integration of deep eutectic solvent and activated carbon in emulsion liquid membrane system for soap removal from crude biodiesel," *Colloids Surfaces A Physicochem. Eng. Asp.*, vol. 673, p. 131786, 2023.

[15] M. K. Ijaz, R. W. Nims, S. de Szalay, and J. R. Rubino, "Soap, water, and severe acute respiratory syndrome coronavirus 2 (SARS-CoV-2): an ancient handwashing strategy for preventing dissemination of a novel virus," *PeerJ*, vol. 9, p. e12041, 2021.

[16] A. Hayyan *et al.*, "Natural and low-cost deep eutectic solvent for soap removal from crude biodiesel using low stirring extraction system," *Biomass Convers. Biorefinery*, pp. 1–9, 2022.

[17] M. Qi *et al.*, "Pollution reduction and operating cost analysis of municipal wastewater treatment in China and implication for future wastewater management," *J. Clean. Prod.*, vol. 253, p. 120003, 2020.

[18] A. Guerrini, G. Romano, L. Carosi, and F. Mancuso, "Cost savings in wastewater treatment processes: the role of environmental and operational drivers," *Water Resour. Manag.*, vol. 31, pp. 2465–2478, 2017.

[19] D. R. Joshi and N. Adhikari, "An overview on common organic solvents and their toxicity," *J. Pharm. Res. Int*, vol. 28, no. 3, pp. 1–18, 2019.

[20] H. Alkhaldi *et al.*, "Sustainable polymeric adsorbents for adsorption-based water remediation and pathogen deactivation: a review," *RSC Adv.*, vol. 14, no. 45, pp. 33143–33190, 2024.

[21] H. Liu *et al.*, "Agricultural biomass/waste-based materials could be a potential adsorption-type remediation contributor to environmental pollution induced by pesticides-A critical review," *Sci. Total Environ.*, p. 174180, 2024.

[22] M. Erakca, M. Baumann, C. Helbig, and M. Weil, "Systematic review of scale-up methods for prospective life cycle assessment of emerging technologies," *J. Clean. Prod.*, p. 142161, 2024.

[23] M. E. M. Soudagar, N.-N. Nik-Ghazali, M. A. Kalam, I. A. Badruddin, N. R. Banapurmath, and N. Akram, "The effect of nano-additives in diesel-biodiesel fuel blends: A comprehensive review on stability, engine performance and emission characteristics," *Energy Convers. Manag.*, vol. 178, pp. 146–177, 2018.

[24] S. Vellaiyan, "Recent advancements in water emulsion fuel to explore efficient and cleaner production from various biodiesels: A retrospective review," *Renew. Sustain. Energy Rev.*, vol. 187, p. 113704, 2023.

[25] A. O. Etim, C. F. Jisieike, T. H. Ibrahim, and E. Betiku, "Biodiesel and its properties," in *Production of biodiesel from non-edible sources*, Elsevier, 2022, pp. 39–79.

[26] A. Gaur, G. Dwivedi, P. Baredar, and S. Jain, "Influence of blending additives in biodiesel on physiochemical properties, engine performance, and emission characteristics," *Fuel*, vol. 321, p. 124072, 2022.

[27] J. Suresh, N. N. Ramlee, S. Toemen, and N. I. Azelee, "Overview and Testing of Fuel Properties of Biodiesel," 2024.

[28] Z. Nazir, K. U. Rehman, I. Hussain, I. M. Mir, R. Aziz, and M. Aslam, "Analytical Techniques for Bio-crude Analysis: Fuel Property and International Standards," in *Biocrude Oil Biorefinery: An Emerging Biorefining Approach*, Springer, 2025, pp. 285–312.

[29] M. Hamood ur Rehman, M. Hussain, P. Akhter, and F. Jamil, "Breaking Barriers in Biodiesel: From Feedstock Challenges to Technological Advancements," *Chem. Africa*, pp. 1–32, 2025.

[30] T. Yu *et al.*, "Diesel engine emission aftertreatment device aging mechanism and durability assessment methods: A review," *Atmosphere (Basel).*, vol. 14, no. 2, p. 314, 2023.

[31] B. B. Xalilovich, "SERVICING OF CAR ENGINES," *Int. J. Adv. Sci. Res.*, vol. 3, no. 11, pp. 205–210, 2023.

[32] K. Ragupathi and I. Mani, "Durability and lube oil contamination study on diesel engine fueled with various alternative fuels: A review," *Energy Sources, Part A Recover. Util. Environ. Eff.*, vol. 43, no. 8, pp. 932–943, 2021.

[33] J. Chen *et al.*, "Review on strategies and technologies for exosome isolation and purification," *Front. Bioeng. Biotechnol.*, vol. 9, p. 811971, 2022.

[34] A. Imtiaz *et al.*, "Challenges, opportunities and future directions of membrane technology for natural gas purification: a critical review," *Membranes (Basel).*, vol. 12, no. 7, p. 646, 2022.

[35] M. Hassanpour, P. Narongdej, N. Alterman, S. Moghtadernejad, and E. Barjasteh, "Effects of post-processing parameters on 3D-printed dental appliances: A review," *Polymers (Basel).*, vol. 16, no. 19, p. 2795, 2024.

[36] J. Bora, R. Hazra, S. Nag, and S. Malik, "Traditional Treatment Methods for Industrial Waste," in *Advanced and Innovative Approaches of Environmental Biotechnology in Industrial Wastewater Treatment*, Springer, 2023, pp. 419–442.

[37] W. M. Kedir, "Bifunctional Heterogeneous Catalysts for Biodiesel Production Using Low-Cost Feedstocks: A Future Perspective," in *Advanced Biodiesel-Technological Advances, Challenges, and Sustainability Considerations*, IntechOpen, 2023.

[38] R. B. Malabadi, K. P. Kolkar, and R. K. Chalannavar, "Industrial Cannabis sativa: Hemp oil for biodiesel production," *Magna Sci. Adv. Res. Rev.*, vol. 9, no. 02, pp. 22–35, 2023.

[39] F. Sher, I. Ziani, M. Hameed, S. Ali, and J. Sulejmanović, "Advanced nanomaterials design

and synthesis for accelerating sustainable biofuels production–A Review," *Curr. Opin. Green Sustain. Chem.*, p. 100925, 2024.

[40] C. S. Damian and Y. Devarajan, "Nanocatalysts in Biodiesel Production: Advancements, Challenges, and Sustainable Solutions," *ChemBioEng Rev.*, vol. 12, no. 2, p. e202400055, 2025.

[41] D. Chettri, M. Boro, A. A. Malik, and A. K. Verma, "Nanotechnology for a greener future: sustainable energy and biofuel advances," *Biofuels*, pp. 1–16, 2024.

[42] T. Rasheed, "Magnetic nanomaterials: Greener and sustainable alternatives for the adsorption of hazardous environmental contaminants," *J. Clean. Prod.*, vol. 362, p. 132338, 2022.

[43] S. S. Ray, R. Gusain, and N. Kumar, *Carbon nanomaterial-based adsorbents for water purification: Fundamentals and applications*. Elsevier, 2020.

[44] B. S. N. Prasad, R. Namdeti, and A. A. Joaquin, "Possibilities and forecast for nanomaterials in the future biorefineries," in *Biomass Conversion through Nanomaterials*, Elsevier, 2025, pp. 55–70.

[45] M. N. S. Azmi *et al.*, "Soap removal from crude biodiesel using industrial polyols," *J. Mol. Liq.*, vol. 422, p. 126972, 2025.

[46] I. M. S. Anekwe, E. K. Tetteh, S. O. Akpasi, and Y. M. Isa, "Current Advances and Potentials of Nanotechnology for Biofuel Production," *Sustain. Eng. Concepts Pract.*, pp. 379–394, 2024.

[47] H. Assad, S. Kaya, P. S. Kumar, D.-V. N. Vo, A. Sharma, and A. Kumar, "Insights into the role of nanotechnology on the performance of biofuel cells and the production of viable biofuels: A review," *Fuel*, vol. 323, p. 124277, 2022.

[48] Y. K. Venkatesh, M. P. Ravikumar, S. Ramu, C. H. Ravikumar, S. Mohan, and R. Geetha Balakrishna, "Developments in Titanium-Based Alkali and Alkaline Earth Metal Oxide Catalysts for Sustainable Biodiesel Production: A Review," *Chem. Rec.*, vol. 23, no. 12, p. e202300277, 2023.

[49] R. Khujamberdiev and H. M. Cho, "Synthesis and Characterization of Nanoparticles in Transforming Biodiesel into a Sustainable Fuel," *Molecules*, vol. 30, no. 6, p. 1352, 2025.

[50] N. R. Khan and A. Bin Rashid, "Carbon-based nanomaterials: a paradigm shift in biofuel synthesis and processing for a sustainable energy future," *Energy Convers. Manag. X*, p. 100590, 2024.

[51] P. G. Bhavyasree and T. S. Xavier, "Green synthesis of Copper Oxide/Carbon nanocomposites using the leaf extract of Adhatoda vasica Nees, their characterization and antimicrobial activity," *Heliyon*, vol. 6, no. 2, 2020.

[52] V. Soni *et al.*, "Sustainable and green trends in using plant extracts for the synthesis of biogenic metal nanoparticles toward environmental and pharmaceutical advances: A review," *Environ. Res.*, vol. 202, p. 111622, 2021.

[53] R. Haddi, A. M. El Kharraz, and M. I. Kerroumi, "Green Synthesis of Zinc Oxide Nanoparticles Using Pistacia lentiscus L. Leaf Extact and Evaluating their Antioxydant and Antibacterial Properties.," *Nano Biomed. Eng.*, vol. 16, no. 2, 2024.

[54] F. D. Guerra, M. F. Attia, D. C. Whitehead, and F. Alexis, "Nanotechnology for environmental remediation: materials and applications," *Molecules*, vol. 23, no. 7, p. 1760, 2018.

[55] M. Bukva, L. C. Soares, L. C. Maia, C. S. D. Costa, and L. V. A. Gurgel, "A review on the design and application of bi-functionalized adsorbents to remove different pollutants from water," *J. Water Process Eng.*, vol. 53, p. 103636, 2023.

[56] H. Lai *et al.*, "Mesostructured NiO/Ni composites for high-performance electrochemical energy storage," *Energy Environ. Sci.*, vol. 9, no. 6, pp. 2053–2060, 2016.

[57] S. Adhikari and G. Madras, "Role of Ni in hetero-architectured NiO/Ni composites for enhanced catalytic performance," *Phys. Chem. Chem. Phys.*, vol. 19, no. 21, pp. 13895–13908, 2017.

[58] M. Liu, J. Chang, J. Sun, and L. Gao, "A facile preparation of NiO/Ni composites as high-performance pseudocapacitor materials," *RSC Adv.*, vol. 3, no. 21, pp. 8003–8008, 2013.

[59] M. Aslam, M. A. Kalyar, and Z. A. Raza, "Polyvinyl alcohol: A review of research status and use of polyvinyl alcohol based nanocomposites," *Polym. Eng. Sci.*, vol. 58, no. 12, pp. 2119–2132, 2018.

[60] Z. Karimzadeh, M. Mahmoudpour, E. Rahimpour, and A. Jouyban, "Nanomaterial based PVA nanocomposite hydrogels for biomedical sensing: Advances toward designing the ideal flexible/wearable nanoprobes," *Adv. Colloid Interface Sci.*, vol. 305, p. 102705, 2022.

[61] Z. Zelca, A. Krumme, S. Kukle, M. Viirsalu, and L. Vilcena, "Effect of Electrode Type on Electrospun Membrane Morphology Using Low-Concentration PVA Solutions," *Membranes (Basel).*, vol. 12, no. 6, p. 609, 2022.

[62] I. S. Chronakis, "Novel nanocomposites and nanoceramics based on polymer nanofibers using electrospinning process—A review," *J. Mater. Process. Technol.*, vol. 167, no. 2–3, pp. 283–293, 2005.

[63] G. Wang, D. Yu, A. D. Kelkar, and L. Zhang, "Electrospun nanofiber: Emerging reinforcing filler in polymer matrix composite materials," *Prog. Polym. Sci.*, vol. 75, pp. 73–107, 2017.

[64] Y. N. Yusoff and N. Shaari, "An overview on the development of nanofiber-based as polymer electrolyte membrane and electrocatalyst in fuel cell application," *Int. J. Energy*

Res., vol. 45, no. 13, pp. 18441–18472, 2021.

[65] M. Toriello, M. Afsari, H. K. Shon, and L. D. Tijing, "Progress on the fabrication and application of electrospun nanofiber composites," *Membranes (Basel).*, vol. 10, no. 9, p. 204, 2020.

[66] S. Meneceur *et al.*, "Removal Efficiency of Heavy Metals, Oily in Water, Total Suspended Solids, and Chemical Oxygen Demand from Industrial Petroleum Wastewater by Modern Green Nanocomposite Methods," *J. Environ. Chem. Eng.*, p. 111209, 2023, doi: https://doi.org/10.1016/j.jece.2023.111209.

[67] H. A. Mohammed, L. S. Eddine, M. Souhaila, G. G. Hasan, I. Kir, and J. A. A. Abdullah, "Green synthesis of SnO2 nanoparticles from Laurus nobilis L. extract for enhanced gelatin-based films and CEF@ SnO2 for efficient antibacterial activity," *Food Bioprocess Technol.*, pp. 1–19, 2023.

[68] P. Prieto, V. Nistor, K. Nouneh, M. Oyama, M. Abd-Lefdil, and R. Díaz, "XPS study of silver, nickel and bimetallic silver–nickel nanoparticles prepared by seed-mediated growth," *Appl. Surf. Sci.*, vol. 258, no. 22, pp. 8807–8813, 2012.

[69] S. O. Kareem, E. I. Falokun, S. A. Balogun, O. A. Akinloye, and S. O. Omeike, "Enzymatic biodiesel production from palm oil and palm kernel oil using free lipase," *Egypt. J. Pet.*, vol. 26, no. 3, pp. 635–642, 2017.

[70] M. W. Mumtaz, H. Mukhtar, F. Anwar, and N. Saari, "RSM based optimization of chemical and enzymatic transesterification of palm oil: Biodiesel production and assessment of exhaust emission levels," *Sci. World J.*, vol. 2014, no. 1, p. 526105, 2014.

[71] B. Salamatinia, H. Mootabadi, S. Bhatia, and A. Z. Abdullah, "Optimization of ultrasonic-assisted heterogeneous biodiesel production from palm oil: A response surface methodology approach," *Fuel Process. Technol.*, vol. 91, no. 5, pp. 441–448, 2010.

[72] K. M. Abed, A. Hayyan, H. F. Hizaddin, W. J. Basirun, and M. A. Hashim, "Lactic acid-based deep eutectic solvents and activated carbon for soap removal from crude biodiesel," *Biomass Convers. Biorefinery*, pp. 1–14, 2023.

[73] K. Mamtani, K. Shahbaz, and M. M. Farid, "Deep eutectic solvents–Versatile chemicals in biodiesel production," *Fuel*, vol. 295, p. 120604, 2021.

[74] C. Salmi, M. Souhaila, L. Salah Eddine, H. A. M. Mohammed, G. G. Hasan, and M. S. Mahboub, "Biosynthesis of Mn3O4/PVP nanocomposite for enhanced photocatalytic degradation of organic dyes under sunlight irradiation," *J. Clust. Sci.*, vol. 35, no. 1, pp. 201–215, 2024.

[75] X. Li, K. Peng, H. Chen, and Z. Wang, "TiO2 nanoparticles assembled on kaolinites with different morphologies for efficient photocatalytic performance," *Sci. Rep.*, vol. 8, no. 1, p. 11663, 2018.

[76] C. Cheng *et al.*, "Advances in preparation, mechanism and applications of graphene quantum dots/semiconductor composite photocatalysts: A review," *J. Hazard. Mater.*, vol. 424, p. 127721, 2022.

[77] A. M. Abd-Elnaiem, M. Rashad, T. A. Hanafy, and N. M. Shaalan, "Improvement of optical properties of functionalized polyvinyl alcohol-zinc oxide hybrid nanocomposites for wide UV optoelectronic applications," *J. Inorg. Organomet. Polym. Mater.*, vol. 33, no. 8, pp. 2429–2444, 2023.

[78] U. K. Panigrahi, P. K. Das, P. D. Babu, N. C. Mishra, and P. Mallick, "Structural, optical and magnetic properties of Ni 1− x Zn x O/Ni nanocomposite," *SN Appl. Sci.*, vol. 1, pp. 1–13, 2019.

[79] D. Arulraj, G. Munuswamy-Ramanujam, A. Karanath-Anilkumar, and T. K. Mistri, "Biofabrication of Silver Nanoparticles from Ormocarpum Cochinchinense Extract and Their Cytotoxic Effects on Thp-1 Leukemia Cells," *Available SSRN 4648483*.

[80] L. F. R. Ferreira, A. Kumar, and M. Bilal, *Recent Advancements In Waste Water Management: Nano-based Remediation*. Elsevier, 2024.

[81] H. Terea, D. Selloum, A. Rebiai, A. Bouafia, and O. Ben Mya, "Preparation and characterization of cellulose/ZnO nanoparticles extracted from peanut shells: effects on antibacterial and antifungal activities," *Biomass Convers. Biorefinery*, 2023, doi: 10.1007/s13399-023-03959-7.

[82] M. F. SHOHUR, Z. Harun, M. R. JAMALLUDIN, S. K. HUBADILLAH, and M. Z. YUNOS, "Antifouling and and antibacterial study of PSf/bio-ZnO nanoparticle (bio-ZnO NP) mixed matrix membrane for humic acid separation," 2024.

[83] T. Paunova-Krasteva *et al.*, "Hybrid chitosan/CaO-based nanocomposites doped with plant extracts from Azadirachta indica and Melia azedarach: evaluation of antibacterial and antibiofilm activities," *Bionanoscience*, vol. 13, no. 1, pp. 88–102, 2023.

[84] M. J. Borah, A. Devi, R. A. Saikia, and D. Deka, "Biodiesel production from waste cooking oil catalyzed by in-situ decorated TiO2 on reduced graphene oxide nanocomposite," *Energy*, vol. 158, pp. 881–889, 2018.

[85] K. Ramesh, G. Bhagavanth Reddy, and M. Noorjahan, "Microwave assisted green synthesis of palladium nanoparticles using dragon fruit peel extract for catalytic reduction of 4-nitrophenol and methylene blue," *React. Kinet. Mech. Catal.*, pp. 1–13, 2024.

[86] W. Yu *et al.*, "Constructing a synergistic catalyst by confining Pd within a MOF using an extended 'bottle-around-ship' protocol," *Microporous Mesoporous Mater.*, vol. 363, p. 112828, 2024.

[87] M. Mousa and Y. Dong, "Strong poly (vinyl alcohol)(PVA)/bamboo charcoal (BC) nanocomposite films with particle size effect," *ACS Sustain. Chem. Eng.*, vol. 6, no. 1, pp.

467–479, 2018.

[88] M. Adamu, M. R. Rahman, and S. Hamdan, "Formulation optimization and characterization of bamboo/polyvinyl alcohol/clay nanocomposite by response surface methodology," *Compos. Part B Eng.*, vol. 176, p. 107297, 2019.

[89] K. Okaiyeto, M. R. Gigliobianco, and P. Di Martino, "Biogenic zinc oxide nanoparticles as a promising antibacterial agent: synthesis and characterization," *Int. J. Mol. Sci.*, vol. 25, no. 17, p. 9500, 2024.

[90] W. Huang *et al.*, "3D NiO hollow sphere/reduced graphene oxide composite for high-performance glucose biosensor," *Sci. Rep.*, vol. 7, no. 1, p. 5220, 2017.

[91] M. Cheng, H. Fan, Y. Song, Y. Cui, and R. Wang, "Interconnected hierarchical NiCo 2 O 4 microspheres as high-performance electrode materials for supercapacitors," *Dalt. Trans.*, vol. 46, no. 28, pp. 9201–9209, 2017.

[92] Y. Bourlier *et al.*, "Investigation of InAlN layers surface reactivity after thermal annealings: a complete XPS study for HEMT," *ECS J. Solid State Sci. Technol.*, vol. 7, no. 6, p. P329, 2018.

[93] H. A. Mohammed, S. E. Laouini, S. Meneceur, C. Salmi, and M. M. Husein, "MgO/Ni Nanocomposite and its PVP-modified Derivative for Catalytic CO2 Methanation and Photocatalytic Hydrogen Production," *Surfaces and Interfaces*, p. 104643, 2024.

[94] M. Gomaa, C. Hugenschmidt, M. Dickmann, M. Abdel-Hamed, E. Abdel-Hady, and H. Mohamed, "Free volume of PVA/SSA proton exchange membrane studied by positron annihilation lifetime spectroscopy," *Acta Phys. Pol. A*, vol. 132, no. 5, pp. 1519–1522, 2017.

[95] P. Boruah, P. Dhar, and V. Katiyar, "8 Nanocellulose-based composites for applications as catalysts and pollutant remediation," *Cellul. Nanocrystals An Emerg. Nanocellulose Numer. Chem. Process.*, p. 229, 2020.

[96] G. Heikal and A. El Shahawy, "Biosorption of phosphorus, total suspended and dissolved solids by dried Phragmites australis: isotherm, kinetic and interactive response surface methodology (IRSM) in oil and soap-derivatives industrial wastewater," *Desalin. water Treat.*, vol. 137, pp. 243–259, 2019.

[97] A. A. A. Darwish, M. Rashad, and H. A. AL-Aoh, "Methyl orange adsorption comparison on nanoparticles: Isotherm, kinetics, and thermodynamic studies," *Dye. Pigment.*, vol. 160, pp. 563–571, 2019.

[98] L.-H. Chen *et al.*, "Preparation and modification of polymer microspheres, application in wastewater treatment: A review," *J. Environ. Manage.*, vol. 366, p. 121807, 2024.

[99] H. Zhao *et al.*, "Effect of oxygen functional groups on competitive adsorption of benzene and water on carbon materials: Density functional theory study," *Sci. Total Environ.*, vol.

863, p. 160772, 2023.

[100] T. Zhang *et al.*, "Removal of heavy metals and dyes by clay-based adsorbents: From natural clays to 1D and 2D nano-composites," *Chem. Eng. J.*, vol. 420, p. 127574, 2021.

[101] C. Li *et al.*, "Soap-free styrene-acrylic/carbon nanotubes composite latex by in situ emulsion polymerization: Preparation, properties and characterizations," *Surfaces and Interfaces*, vol. 25, p. 101204, 2021.

[102] Y. K. Jo, J. M. Lee, S. Son, and S.-J. Hwang, "2D inorganic nanosheet-based hybrid photocatalysts: Design, applications, and perspectives," *J. Photochem. Photobiol. C Photochem. Rev.*, vol. 40, pp. 150–190, 2019.

[103] L. Zhang and M. Jaroniec, "Toward designing semiconductor-semiconductor heterojunctions for photocatalytic applications," *Appl. Surf. Sci.*, vol. 430, pp. 2–17, 2018.

[104] K. Mohamed, K. Zine, K. Fahima, E. Abdelfattah, S. M. Sharifudin, and K. Duduku, "NiO nanoparticles induce cytotoxicity mediated through ROS generation and impairing the antioxidant defense in the human lung epithelial cells (A549): Preventive effect of Pistacia lentiscus essential oil," *Toxicol. reports*, vol. 5, pp. 480–488, 2018.

[105] I. Kir, S. E. Laouini, S. Meneceur, A. Bouafia, and H. A. M. Mohammed, "Biosynthesis and characterization of novel nanocomposite ZnO/BaMg2 efficiency for high-speed adsorption of AZO dye," *Biomass Convers. Biorefinery*, vol. 14, no. 16, pp. 19045–19054, 2024, doi: 10.1007/s13399-023-03985-5.

[106] Z. Zelca, S. Kukle, S. Janceva, and L. Vilcena, "Propolis Integration Methods into Solutions for Highly Loaded Propolis Fibers by Needleless Electrospinning," *Molecules*, vol. 27, no. 7, p. 2311, 2022.

[107] A. Saravanan *et al.*, "Effective water/wastewater treatment methodologies for toxic pollutants removal: Processes and applications towards sustainable development," *Chemosphere*, vol. 280, p. 130595, 2021.

[108] A. S. Ibupoto *et al.*, "Reusable carbon nanofibers for efficient removal of methylene blue from aqueous solution," *Chem. Eng. Res. Des.*, vol. 136, pp. 744–752, 2018.

[109] B. M. Thamer, A. A. Shaker, M. M. A. Hameed, and A. M. Al-Enizi, "Highly selective and reusable nanoadsorbent based on expansive clay-incorporated polymeric nanofibers for cationic dye adsorption in single and binary systems," *J. Water Process Eng.*, vol. 54, p. 103918, 2023.

[110] M. McLaughlin, "Closed-loop cleaner recycling," *Precis. Clean*, vol. 5, pp. 17–24, 1997.

[111] R. S. Varma, "Journey on greener pathways: from the use of alternate energy inputs and benign reaction media to sustainable applications of nano-catalysts in synthesis and environmental remediation," *Green Chem.*, vol. 16, no. 4, pp. 2027–2041, 2014.

[112] S. Peng *et al.*, "Multi-functional electrospun nanofibres for advances in tissue regeneration, energy conversion & storage, and water treatment," *Chem. Soc. Rev.*, vol. 45, no. 5, pp. 1225–1241, 2016.

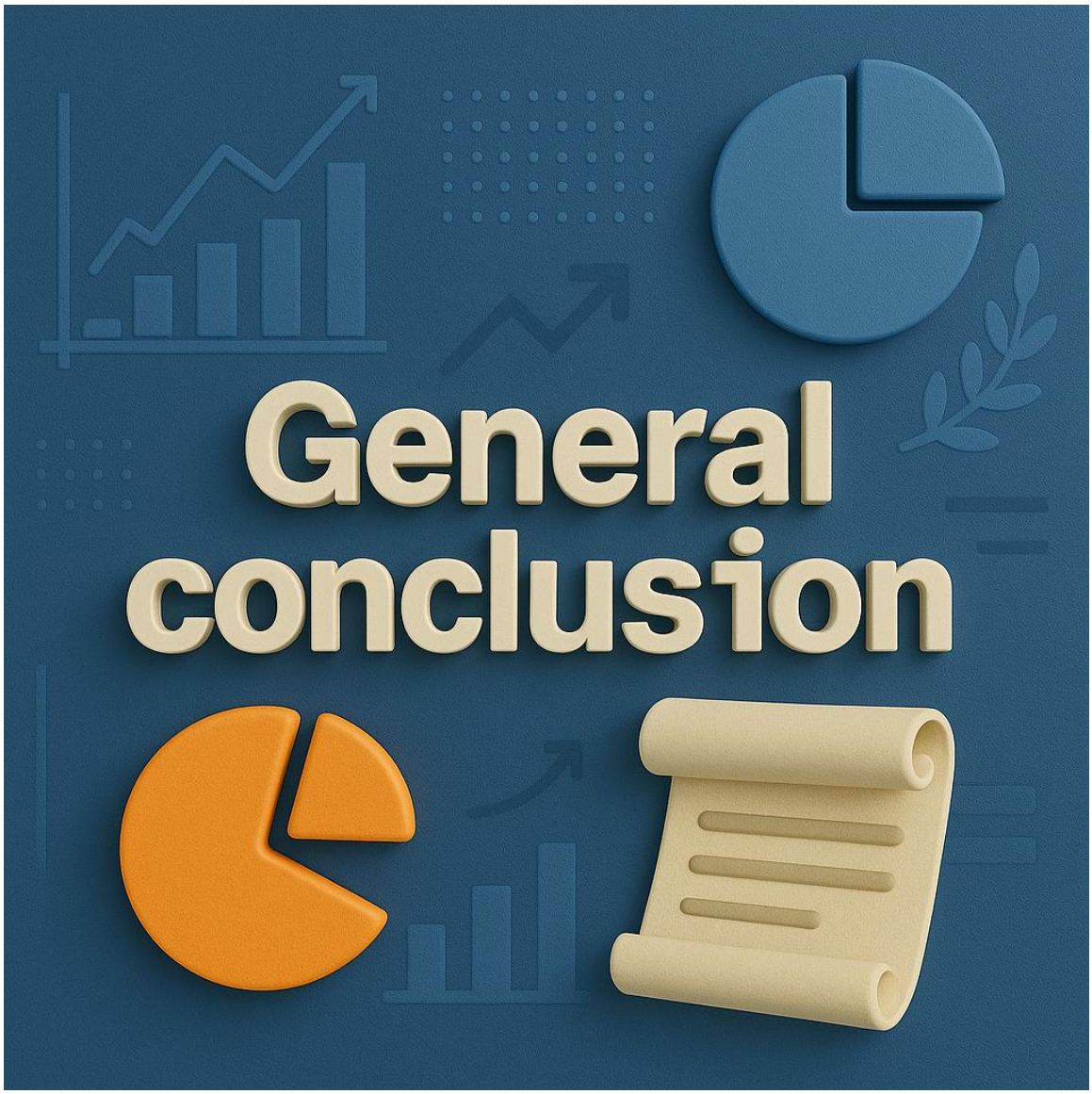
General
conclusion

General Conclusion

This thesis presents a comprehensive investigation into the design, green synthesis, and multifunctional application of polymer-based metal oxide nanocomposites for environmental remediation, renewable energy production, and pollutant degradation. Through an integrated approach combining experimental techniques and computational modeling, the research highlights the synergistic effects of metal oxides and polymeric matrices particularly polyvinylpyrrolidone (PVP) and polyvinyl alcohol (PVA) in enhancing photocatalytic activity, adsorption efficiency, and structural stability.

Four distinct nanocomposite systems were developed using sustainable methods, each tailored to address specific environmental challenges. The Mn_3O_4/PVP nanocomposite demonstrated high sunlight-driven photocatalytic degradation of synthetic dyes, while the MgO@SnO_2 system efficiently adsorbed petroleum-derived pollutants and heavy metals. The CuO/Ni/Fe_3O_4 nanocomposite, synthesized via a gallic acid-mediated route, exhibited dual functionality in photocatalytic hydrogen evolution and CO_2 methanation. The NiO/Ni@PVA electrospun nanofibers showcased enhanced performance in biodiesel purification, supported by kinetic modeling and molecular docking studies to elucidate interaction mechanisms at the nanoscale.

Advanced characterization techniques, including XRD, SEM, FTIR, BET, UV–Vis spectroscopy, TGA, and zeta potential analysis, confirmed the structural integrity, surface properties, and functional efficiency of the synthesized nanomaterials. Moreover, kinetic, isotherm, and thermodynamic analyses provided in-depth insights into adsorption behaviors, while molecular docking simulations offered predictive models for nanocomposite–pollutant interactions.

Collectively, the findings of this research underscore the potential of eco-friendly synthesis routes and polymer-assisted nanocomposites in developing high-performance materials for environmental and energy applications. The incorporation of green chemistry principles and computational tools not only enhances material functionality but also aligns with global sustainability goals.

Future research should explore the scale-up potential of these materials for pilot-scale applications, investigate multi-pollutant removal under real-world conditions, and expand surface modifications to further improve selectivity and reusability. The integration of life cycle assessment (LCA) and techno-economic analysis (TEA) could also provide valuable frameworks for evaluating the feasibility and environmental impact of these systems in practical applications.